

EUROPEAN LUNAR SYMPOSIUM 2014

2014

15/16 MAY

els2014.sservi.nasa.gov

LONDON

EUROPEAN LUNAR SYMPOSIUM

In partnership with the Solar System Exploration Research Virtual Institute

SCIENCE ORGANIZING COMMITTEE

Dr. Mahesh Anand:: Chair
Open University, UK

Prof. Sara Russell:: Co-Chair
Natural History Museum, UK

Ms. Jessica Barnes, Open University, UK

Dr. Neil Bowles, Oxford University, UK

Dr. James Carpenter, ESA

Dr. Ian Crawford, Birkbeck College University of London, UK

Ms. Doris Daou, SServi

Prof. Ralf Jaumann, DLR, Germany

Dr. Katherine Joy, University of Manchester, UK

Mr. Greg Schmidt, SServi

Dr. Romain Tartese, Open University, UK

Prof. Wim van Westrenen, VU University Amsterdam, NL

*Natural
History
Museum*

*Cromwell Rd
London SW7 5BD
United Kingdom*



DELEGATES' HANDBOOK
(LAST UPDATED – 18 APRIL 2014)

Scientific programme

Thursday, 15th May 2014 (Flett Lecture Theatre, NHM)

09.00 Registration

10.00 Welcome/Housekeeping

Session 1: Geomorphology and Remote sensing – Chair TBC

| | | | |
|-------|---------------------------|------|--|
| 10.10 | Donaldson Hanna (Keynote) | p.8 | Characterization of pure anorthosites across the lunar surface: Implications for the evolution of the crust |
| 10.30 | d’Uston | p.10 | Lunar surface compositional and mineralogic properties as seen from orbit (Chandrayaan-1, Kaguya, Smart-1, Clementine) |
| 10.45 | Wilson | p.12 | On the extended distribution of Thorium near the lunar Compton-Belkovich volcanic complex |
| 11.00 | Sinitsyn | p.14 | The hydrogen anomalies in KREEP terrain according to the results of LEND and LPNS neutron spectrometers data |
| 11.15 | Eke | p.16 | The polar water ice inventory – what do we know and how? |
| 11.30 | Saran | p.18 | A new technique for improved mapping of water-ice deposits in the polar cold traps of the Moon |
| 11.45 | Foing | p.20 | Smart-1 impact studies from SPA, basins to Smart-1 bouncing site |
| 12.00 | Bugiolacchi | p.21 | Trends in distribution of small craters in the Apollo 17 region |
| 12.15 | Calzada-Diaz | p.23 | Finding launch sites of meteorites using Lunar Prospector gamma-ray spectrometer datasets |

12.30 Lunch - Provided

Session 2: Geophysics and Near surface environment – Chair TBC

| | | | |
|-------|------------------------------|------|--|
| 13.40 | Greenhagen (Invited keynote) | p.25 | The extreme thermal, thermophysical, and compositional nature of the moon revealed by the Diviner Lunar Radiometer |
| 14.00 | Barabash | p.27 | Investigation of the plasma-surface interaction on the Russian Luna-25/26/27 missions |
| 14.15 | De Angelis | p.28 | Improved models of the Moon radiation environment |
| 14.30 | Dell’Agnello | p.30 | The Moon as a Laser-ranged Test Body for General Relativity and New Gravitational Physics |
| 14.45 | Harker | p.31 | Telerobotic exploration and radio astrophysics from the far side of the moon |
| 15.00 | Bamford | p.32 | A self-consistent demonstration of how the lunar crustal magnetic anomalies produce mini-magnetospheres |

15.15 Tea/coffee - Provided

Session 3: Lunar samples (part 1) - Chair TBC

| | | | |
|-------|---------------------------|------|---|
| 15.40 | Füri (Invited keynote) | p.33 | Origin of lunar water and nitrogen: Constraints from Apollo 17 volcanic glasses |
| 16.00 | Tartèse | p.34 | Water content and H isotopic composition of apatites in lunar KREEP basalts: Clues to indigenous lunar water |
| 16.15 | Barnes | p.36 | Assessing the volatile inventory of apatites in lunar impact melt breccias |
| 16.30 | Curran | p.38 | The Moon’s regolith archive in lunar meteorites |
| 16.45 | Alexander | p.40 | Exotic lithologies at the Apollo 12 site: Examination of fines from the lunar soil samples 12023 and 12003 |
| 17.00 | Elliott (Invited keynote) | p.42 | The significance of similarities and differences in the Mg isotopic composition of the Earth’s mantle and lunar samples |

17.30 Poster session and evening drinks reception (Flett Lecture Theatre Foyer)

Friday, 16th May 2014 (Flett Lecture Theatre, NHM)

Session 3: Lunar samples (part 2) - Chair TBC

| | | | |
|-------|---------------------------|------|---|
| 09.00 | Registration | | |
| 10.05 | Nemchin (Invited keynote) | p.43 | Zircon from the Moon, Earth and Mars |
| 10.25 | Steenstra | p.45 | Core-mantle differentiation in the Moon: constraints from metal-silicate partitioning of moderately siderophile elements in a hydrous magma ocean |
| 10.40 | Rai | p.47 | Lunar core formation: Additional constraints from metal-silicate partitioning of germanium and the highly siderophile elements |
| 10.55 | Kleine | p.48 | Lunar ¹⁸² W and the origin of the Moon |

Session 4: Future missions – Chair TBC

| | | | |
|-------|-------------------------|------|--|
| 11.10 | Kring (Invited keynote) | p.50 | Exploring the lunar south polar region and far side with human and human-assisted sample return missions |
| 11.30 | Irfan | p.52 | Characterisation of a potential landing site of interest in the lunar south polar region |
| 11.45 | Jaumann | p.54 | A dedicated Small Lunar Exploration Orbiter (S-LEO) and Mobile Payload Element (MPE) |

12.00 Lunch - Provided

| | | | |
|-------|-----------|------|--|
| 13.15 | Kramer | p.56 | Why Ingenii is the ideal target for a lunar sample return mission. |
| 13.30 | Lawrence | p.58 | Lunar PLANE: Lunar Polar Low-Altitude Neutron Experiment for High-Spatial Resolution Hydrogen Measurements |
| 13.45 | Coll | p.60 | In situ PYR-GC-MS chemical/isotopic analysis of lunar soil: A ground truth to interpret the analyses of the samples returned from the Moon |
| 14.00 | Barber | p.61 | L-VRAP: the Lunar Volatile Resources Analysis Package |
| 14.15 | Reiss | p.62 | Technological challenges for in-situ investigation of lunar resources |
| 14.30 | Carpenter | p.64 | Lunar exploration and science in ESA |
| 14.45 | Lim | p.65 | Space Architecture for exploration and settlement on other planetary bodies – In-Situ Resource Utilisation (ISRU) based structures on the Moon |

15.00 Tea/coffee – Provided

Session 5: Global partnerships – Chair TBC

| | | | |
|-------|-------------------|------|---|
| 15.25 | Schmidt (Keynote) | p.67 | Developing the Global Exploration Roadmap: Expanding the “Lunar Vicinity” Scenario. |
| 15.45 | Cox | p.69 | The International Lunar Geophysical Year: 2017-2018 |
| 16.00 | Daou | p.70 | NASA's Solar System Exploration Research Virtual Institute” – International partnerships in lunar science |
| 16.15 | Gray | p.71 | Lunar team report from a planetary design workshop at ESTEC |
| 16.30 | Wong | p.72 | Going back to the Moon with the Google Lunar XPRIZE |
| 16.45 | Bussey | p.73 | VORTICES: VOLatiles Regolith Thermal Investigations Consortium for Exploration & Science |

Poster presentations

Thursday, 15th May – 17.30-19.30 (Flett Lecture Theatre Foyer, NHM)

| | | |
|-----------------|-------|--|
| Czelusckhe | p.76 | Re-examination of Apollo 17 LSPE data using new LRO-based coordinates of seismic equipment |
| Harker | p.78 | Inferring the properties of the first stars and galaxies from a radiometer in lunar orbit |
| Harnett | p.79 | The relationship between solar wind particle impacts and spectral maturation through simulations and observations at lunar magnetic anomalies |
| Davenport | p.81 | Let's SPICE things up: Simulating Planetary Igneous Crystallization Environments |
| Marriner | p.83 | Characterisation of a terrestrial low-iron spinel as an analogue to support thermal infrared observations of the moon |
| McDonald | p.85 | The origin and evolution of volatiles in the Earth-Moon system: A halogen perspective |
| Mortimer | p.87 | The Indigenous Volatile Content of the Lunar Interior: Investigating Mare Basalts Using Stepped Heating Technique |
| Joy | p.89 | Global diversity of the lunar crust: science and challenges of lunar sample return |
| Donaldson Hanna | p.91 | Thermal infrared studies of lunar soils: Characterizing spectral effects due to simulated lunar conditions and packing |
| Otto | p.93 | Comparison of mass-wasting features in craters on asteroid 4 Vesta and the Moon |
| Rommel | p.95 | Automatic endmember selection and nonlinear spectral unmixing of terrestrial minerals |
| Grumpe | p.97 | Automatic segmentation of petrographic geologic units based on elemental abundance maps |
| Warren | p.99 | New laboratory measurements to help constrain surface roughness effects in the Lunar Diviner Radiometer dataset |
| Weilding | p.101 | Identification (and misidentification) of dark-halo craters within the taurus-littrow region of the Moon from Moonzoo data |
| Zhang | p.103 | Estimate of lunar TiO ₂ and FeO with M ³ data |
| Bailey | p.105 | NASA's Solar System Exploration Research Virtual Institute: Interdisciplinary science and community development |
| Czelusckhe | p.106 | ROBEX-ASN – A concept study for an active seismic network on the Moon |
| Bauer | p.108 | Reduction, analysis and application of one-way laser ranging data from ILRS ground stations to LRO |
| Reiss | p.109 | Evaluation of small-scale penetrators for lunar subsurface investigation |
| Vrublevskis | p.111 | Potential for lunar exploration using a stirling power conversion system (SPCS) powered by a radioisotopic heat source currently being developed for the European Space Agency (ESA) |
| Hiesinger | p.112 | Assessing safety and potential science of the Luna-Glob landing site in Boguslawsky crater, Moon |

Oral presentations

CHARACTERIZATION OF PURE ANORTHOSITES ACROSS THE LUNAR SURFACE: IMPLICATIONS FOR THE EVOLUTION OF THE CRUST. K. L. Donaldson Hanna^{1,2}, L. C. Cheek³, C. M. Pieters², J. F. Mustard², B. T. Greenhagen⁴, N. E. Bowles¹ ¹Atmospheric, Oceanic and Planetary Physics, University of Oxford, Clarendon Laboratory, Parks Road, Oxford, UK, ²Department of Geological Sciences, Brown University, Providence, RI, USA, ³Astronomy Department, University of Maryland, College Park, Maryland, USA, ⁴Jet Propulsion Laboratory, Pasadena, CA, USA.

Introduction: Recent near-infrared (NIR) observations from the SELENE Spectral Profiler (SP) and Multiband Imager (MI) and the Chandrayaan-1 Moon Mineralogy Mapper (M³) have been used to uniquely identify anorthosite (rocks dominated by Fe-bearing crystalline plagioclase) around impact basins, in massifs in the Inner Rook mountains of Orientale, and in the central peaks, walls, floor and ejecta of craters [e.g. 1-5]. These results are significant because they validate earlier observations [e.g. 6-7] as well as characterize the widespread distribution of crystalline anorthosite across the lunar surface. The identification of crystalline plagioclase in the NIR comes from a broad absorption band at approximately 1.25 μm due to electronic transitions of minor Fe^{2+} in the crystal structure. While previous NIR lab studies have suggested that band depth and center position of the 1.25 μm feature may vary with Fe and An content [8,9], the relationship between NIR spectral properties of plagioclase and its composition (AN#) has yet to be quantified. Regions of nearly pure crystalline plagioclase (<5% olivine and pyroxene) as identified in NIR spectra are ideal areas to investigate the utility of thermal infrared (TIR) data to constrain plagioclase compositions [10-11].

The Diviner Lunar Radiometer Experiment onboard NASA's Lunar Reconnaissance Orbiter has three spectral bands near the 8 μm region chosen specifically to measure the peak of the Christiansen Feature (CF) [10], an emissivity maximum indicative of composition [12]. New lab measurements of varying compositions of the plagioclase solid solution series demonstrate that the CF position is diagnostic of composition and linearly related to AN# when measured under a simulated lunar environment [13].

Here we use M³ NIR global mosaics and

individual data strips to identify the distribution of crystalline plagioclase and integrate those observations with Diviner TIR data to determine plagioclase composition in lunar anorthosites. This integrated NIR and TIR approach is thus focused on relatively pure, crystalline plagioclase exposures across the lunar surface. Examining the local and global distribution of crystalline plagioclase is significant for (1) identifying rock types (ferroan anorthosites versus Mg-suite or Alkali-suite rocks) and (2) determining the crustal depth where crystalline plagioclase is observed. These results may ultimately constrain processes of formation (e.g. lunar magma ocean crystallization versus serial magmatism).

Data and Methods: Low resolution global mosaics of M³ data were prepared for each of the instrument's optical periods for evaluation within the team [15]. To identify crystalline plagioclase in the M³ data, an integrated band depth (IBD) at 1.25 μm was run on these mosaics as well as select full resolution data strips. This 1.25IBD was developed to specifically distinguish crystalline plagioclase-rich areas from mafic-rich areas and the details of its calculation are provided elsewhere [4,11]. Pixels exhibiting prominent Fe-bearing, crystalline plagioclase absorptions will have higher 1.25IBD values (absorption band strengths > 1-2%). M³ spectra are also extracted from each of the high IBD value regions to confirm the identification of pure crystalline plagioclase as well as determine its 'purity' or mafic mineral abundance. Spectra that display only a crystalline plagioclase absorption near 1.25 μm and lack mafic absorptions near 1 and 2 μm are considered "spectrally pure" plagioclase and represent anorthosites with exceedingly low mafic mineral abundances [4,11].

Diviner radiance data for lunar mid-day over 37

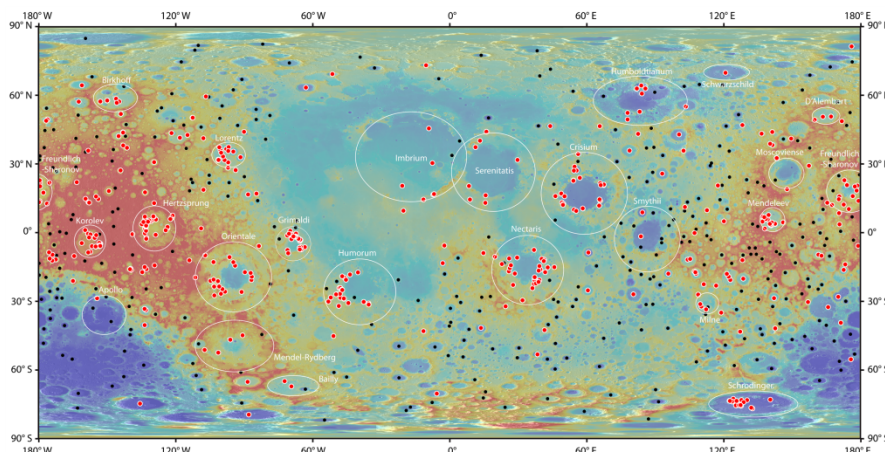


Figure 1: Red circles highlight M³ identifications of pure crystalline plagioclase as identified by high 1.25 μm integrated band depth values. The smaller, black circles identify investigated craters that did not contain pure crystalline plagioclase. The background image is the Lunar Orbiter Laser Altimeter (LOLA) topography [15] overlain on a Lunar Reconnaissance Orbiter Camera (LROC) Wide Angle Camera (WAC) [16] global mosaic

craters that had good Diviner coverage were converted to emissivity and used to generate a CF map. TIR spectra were extracted from Diviner emissivity data and compared to laboratory emissivity spectra of a Ca-rich endmember of plagioclase (An_{96}) measured under simulated lunar conditions.

Results: As seen in Figure 1, pure, crystalline plagioclase is confirmed to be widely distributed across the lunar surface. We identified spectrally pure, crystalline plagioclase in the walls and ejecta of simple craters and in the walls, floors, central peaks, and ejecta of complex craters; most in association with near- and far- side impact basins. Exposures of pure, crystalline plagioclase are clearly associated with the inner and outer rings of larger impact basins like Orientale, Hertzprung, Humorum, Nectaris, and Crisium as well as limited exposures associated with Mendel-Rydberg, Imbrium, Humboldtianum, Serenitatis, Smythii, and South Pole-Aitken (SPA) basins. Pure, crystalline plagioclase is also identified in the peak ring structures of Grimaldi, Korolev, Mendelev, and Schrödinger. Other peak ring basins, such as Coulomb-Sarton, Moscoviense, Schwarzschild, D'Alembert, Milne, and Lorentz have limited identifications of pure plagioclase in their peak rings. All of these identifications are associated with regions of the highest crustal values (as modeled by Wieczorek et al. [17]) surrounding each impact basins.

To better understand the compositional variability of plagioclase globally distributed across the lunar highlands, Diviner CF maps for 37 highland craters that have good Diviner data coverage were analyzed. M^3 and Diviner CF maps of each crater were co-registered in ENVI and units identified as pure plagioclase in M^3 were analyzed further in the Diviner data. For these units, the median, mean and standard deviation CF values were calculated. A histogram is calculated for all pixels for spectrally pure plagioclase regions identified in all 37 highland craters (Figure 2). A single distribution of Diviner CF values is observed in the histogram with a mean CF value of $7.91 \pm 0.05 \mu m$ suggesting that the average composition of plagioclase identified in all of the highlands craters is similar. Plagioclase composition is not the only factor in the width of the CF value distribution as space weathering, topography, and/or minor contributions of mafic minerals can affect the CF value.

The mean Diviner CF can be compared to the wavelength position of the CF of anorthite (An_{96}) measured under simulated lunar conditions to estimate the $An\#$ for the observed pure served plagioclase units. Under simulated lunar conditions, the CF position of anorthite (An_{96}) was measured at $7.84 \mu m$. The mean CF value at $7.91 \pm 0.05 \mu m$ measured by Diviner suggest the

plagioclase composition across the highlands is relatively uniform in composition, highly calcic ($An_{\geq 96}$), and is consistent with plagioclase compositions found in the ferroan anorthosites (An_{94-98}) in the Apollo sample collection. Thus, the plagioclase composition measured in ferroan anorthosites is representative of plagioclase compositions throughout the lunar highlands.

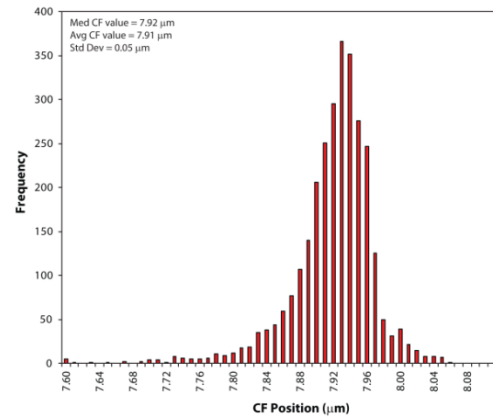


Figure 2: Histogram of CF values for all spectrally pure plagioclase pixels analyzed in all of the 37 craters used in this compositional study. The histogram has a single distribution with a mean CF value of $7.92 \mu m$ and a standard deviation of $0.05 \mu m$.

Conclusions: Our results confirm that spectrally pure anorthosite is widely distributed across the lunar surface and most exposures of the ancient anorthositic crust are concentrated in regions of thicker crust surrounding impact basins on the lunar near- and far-sides. In addition, the scale of the impact basins and the global nature and distribution of pure plagioclase requires a coherent zone of anorthosite of similar composition in the lunar crust supporting its formation from a single differentiation event involving a magma ocean. Our identifications of pure anorthosite will be combined with the GRAIL crustal thickness models to determine crustal thicknesses at which pure anorthosite is observed.

References: [1] Ohtake M. et al. (2009) *Nature*, 461. [2] Matsunaga T. et al. (2008) *GRL*, 35. [3] Pieters C. M. et al. (2009) *LPS XL*, Abstract #2052. [4] Cheek L.C. et al (2013) *JGR*, 118. [5] Yamamoto S. et al (2012) *GRL*, 39. [6] Hawke B. et al. (2003) *JGR*, 108. [7] Tompkins S. and Pieters C. (1999) *Meteoritics & Planet. Sci.*, 34, 25-41. [8] Adams J. and Goullaud L. (1978) *LPS IX*, 2901-2909. [9] Cheek L. et al. (2011) *LPS XLII*, Abstract #1608. [10] Greenhagen B. T. et al. (2010) *Science*, 329, 1507-1509. [11] Donaldson Hanna K. L. et al. (2014) *JGR*, Submitted. [12] Conel J. (1969) *JGR*, 74, 1614-1634. [13] Donaldson Hanna K. L. et al. (2012) *JGR*, 117. [14] Boardman J. W. et al. (2011) *JGR*, 116. [15] Smith D. E. et al. (2010) *GRL*, 37. [16] Robinson M. S. et al. (2010) *Space Sci. Rev.*, 150, 81-124. [17] Wieczorek et al. (2012) *Science*, doi:10.1126/science.1231530.

LUNAR SURFACE COMPOSITIONAL AND MINERALOGIC PROPERTIES AS SEEN FROM ORBIT (CHANDRAYAAN-1, KAGUYA, SMART-1, CLEMENTINE). C. d'Uston¹, P. Pinet¹, S. Chevrel¹, Y. Daydou¹, O. Forni¹, O. Gasnault¹, A. Souchon² ¹Institut de Recherche Astrophysique et Planetologie, 9 Avenue du Colonel Roche, BP 44346, 31028 Toulouse Cedex4, France, ²Space Exploration Institute, 68 Faubourg de l'Hôpital, CH-2002 Neuchâtel, Switzerland.

Introduction: During the past ten years, a series of space missions has been sent to orbit the Moon. At that time, it was realized that even though the APOLLO era had provided unrivaled data on the surface composition, a large part of the Moon surface was still unknown. Starting in the second half of the 1990s, several programs were set up to provide a global coverage of our neighbor celestial body. Behind the observation goals that were assigned to the programs, the objectives are still to test the various scenarios of the Moon formation, and to identify the succession of geological processes which shaped and composed its surface. In this overview presentation, we will present the different methods which were implemented in IRAP and summarize the results of the different missions first in terms of chemical composition and then in terms of mineralogy and surface properties.

Observations using nuclear methods: These methods provide an identification of the elemental composition of a surface layer ~50cm thick, and due to their low levels of emission, they result in regional resolution; the two methods which have been used are the gamma-ray spectrometry (GRS) and the X-ray fluorescence spectroscopy (XRF).

The most recent GRS results were obtained with the Japanese Kaguya mission which embarked a High resolution GRS based on a large crystal of High Purity Germanium provided by the French company Canberra (AREVA group) in Strasbourg [1]. The main results are listed in the following:

- Major elements (O, Mg, Si, Ca, Ti, Fe) and some trace elements (K, Th, U) have been mapped [2,3] with an improved space resolution.

- A global map of the U abundance was derived for the first time which shows a variation up to 2ppm with an average of ~0.3ppm, while the Th abundance was ~1.2ppm [4]. From their analyses, significant variation in U/Th was found in the farside of the Moon. They also suggest that the lunar highland compositions are not uniform. The newly obtained Th map has revealed that two regions near the equator on the farside have the lowest Th abundances. The variation of the Th abundance perfectly correlates with the crustal thickness in the farside and the southern nearside, and it could be a result of the crystallization of the lunar magma ocean [5].

- The first global distribution of Ca on the Moon has also been obtained [6]. While the derived Ca abundance generally confirms the mare-highland dichotomy, the eastern mare regions such as

Crisium, Nectaris, and Fecunditatis exhibit unexpected high Ca abundances. This may be explained by regional concentrations of high-Ca clinopyroxene.

XRF observations were made by C1XS instrument [7,8] on board the Indian Chandrayaan-1 orbiter around the moon, to aid in determining whether regional compositional differences (e.g., the Mg/Fe ratio) are consistent with models of lunar crustal evolution and to also permit geochemical studies of smaller scale features, such as the ejecta blankets and central peaks of large impact craters, and individual lava flows and pyroclastic deposits. As the sun had a very low level of activity during the mission, only very few X-ray fluorescence spectra were measured during several episodes of solar flares. Over a highland region on the southern nearside of the Moon they indicate a composition rich in plagioclase with a slight mafic mineral enhancement and a Ca/Al ratio that is significantly lower than measured in lunar returned samples [9]. Over the region of the Apollo 14 landing site on the Fra Mauro Formation, the quantitative estimates of the MgO/SiO₂ and Al₂O/SiO₂ ratios are inside the range of basaltic samples from the Apollo and Luna collections [10].

Observations using orbital imaging spectroscopy: Combining UVVIS and NIR Clementine spectral data, we characterized the mineralogy of the different volcanic and crustal materials occurring on the Aristarchus Plateau and its close vicinity, in order to investigate their stratigraphic relationships and understand the nature of the crust in this region of the Moon [7]. Implementing an advanced iterative linear mixture modeling, a comprehensive description of the distribution and amount of surface mixture of the units, has been established which documents the stratigraphic relationships in the region of study. Despite the overall regional complexity, the determination of relationships and origin of the different units forming the structure of the Plateau is addressed and proposes a scenario to relate the documented distribution of the surface materials to the Imbrium impact event.

This study, based on the integrated visible–near infrared Clementine dataset, paved the way for high spatial resolution spectroscopic surveys recently carried out by LISM/Kaguya on board Selene and M3 (Moon Mineralogy Mapper) on board Chandrayaan-1.

Observations using orbital spectrophotometry: Based on the SMART-1/AMIE imaging data (European Space Agency), we have been able to derive the single-scattering albedo and phase function, local surface roughness and regolith porosity, and the coherent backscattering, single scattering, and shadowing contributions to the opposition effect for specific lunar mare regions [8].

Also, new results have been produced from the mapping of lunar photometric function parameters using the multiangular AMIE images [9]. The behavior of the photometric function is interpreted in terms of lunar regolith properties. This study reveals photometric anomalies on both small (sub-kilometer) and large (tens of kilometers) scales. In particular, it is shown that basaltic lava flows within Mare Imbrium and Oceanus Procellarum indicate higher regolith porosity for the redder soils due to differences in the chemical composition of lavas.

Observations combining orbital spectrophotometry and imaging spectroscopy: A study of the Lavoisier lunar crater combining photometric data from the AMIE camera (SMART-1 mission) and hyperspectral data from the Moon Mineralogy Mapper M3 (Chandrayaan-1 mission) has been recently completed, with a special emphasis on the pyroclastic deposits considered to be present on the crater floor [10]. The photometric parameters are in agreement with the general photometric behaviors of the lunar regolith, especially the backscattering properties. The assumed pyroclastic materials within Lavoisier present at first order a rather homogeneous photometric behavior, in favor of their surface state homogeneity. However, they are not significantly different from other “non-dark” patches on the crater’s floor, whereas the assumed pyroclastic deposit of Lavoisier F displays clearly different photometric parameters, indicative of distinct physical surface properties from the pyroclastic materials within Lavoisier. Using laboratory data to get hindsight on the reliability of results from orbital datasets [11], we show that the use of more or less depleted phase curves for photometric inversions has a clear impact on the photometric parameters that are derived. The hyperspectral analysis of Lavoisier crater shows that the various pyroclastic deposits present the same mineralogical composition, distinct from the floor of the crater and the mare basalts.

M3 spectra do not differentiate between the pyroclastic deposits within Lavoisier and Lavoisier F. They have the same spectral signatures, share a similar mineralogical composition, and probably the same volcanic origin. Therefore, the differences seen in the photometric analysis from the AMIE observations are indicative of variations in grain sizes, and/or roughness, and/or particles scattering properties, and/or compaction state.

This example demonstrates that a combined mineralogical and photometric analysis is a very useful approach to document the nature of the pyroclastic deposits of the Moon, and possibly of other objects of the Solar System (e.g., Mercury) as the combination of the mineralogy and the physical properties sets constraints on the origin and mode of emplacement of the deposits, and characterizes the eruption styles.

Integrated Analyses and datasets handling: The wealth and the diversity of the results highlighted above plead in favor of a lot more effort in the coming years towards the integration of datasets produced with different observation techniques and from separate lunar missions.

Relying on statistical multidimensional analysis and clustering techniques, a number of powerful tools and methods (see for instance [12, 13] and LPSC abstracts in recent years [14, 15]) have been developed in our group along the years which should be implemented with success for this purpose.

References: [1] Hasebe, N. et al. (2010) *Transaction of space technology Japan*, Vol. 7. [2] Reedy, R.C., et al. (2009) *American Astronomical Society, DPS meeting #41*, #26.06. [3] Kobayashi, S., et al., (2011) *Space Sci. Rev.*, Vol. 154, Issue 1-4, pp. 193-218. [4] Yamashita, N., et al., (2010) *Geophys. Res. Letters*, Vol. 37, Issue 10. [5] Kobayashi, S., et al., (2012) *Earth and Planetary Science Letters*, Vol. 337, p. 10-16. [6] Yamashita, N., et al., (2012) *Earth and Planetary Science Letters*, Vol. 353, p. 93-98. [7] Crawford, I.A., et al., (2009) *Planetary and Space Science*, Vol. 57, Issue 7, p. 725-734. [8] Grande, M. et al. (2009), *Planetary and Space Science*, Vol. 57, Issue 7, p. 717-724. [9] Narendranath, S., et al. (2011), *Icarus*, Vol. 214, Issue 1, p. 53-66. [10] Weider, S.Z., et al. (2012), *Planetary and Space Science*, Vol. 60, Issue 1, p. 217-228. [11] Chevrel, S.D. et al. (2009) *Icarus*, 199, 9–24. [12] Muinonen K. et al. (2011) *Astronomy & Astrophysics*, Vol: 531, A150. [13] Kaydash et al. (2009) *Icarus*, 202, 393-413. [14] Souchon A.L. et al. (2013) *Icarus*, 225, 1–14. [15] Souchon A.L. et al. (2011) *Icarus*, 215, 13–331 [16] Gasnault O. et al. (2002) *JGR Planets*, 107, (E10), 2-1. [17] Chevrel S.D. et al. (2002) *J.G.R. Planets*, 107, E12. [18] Mizzon, H. et al. (2013), *44th LPSC*, abstract #1719, p.2975. [19] Gasnault, O. et al. (2009), *40th LPSC*, abstract #2253

ON THE EXTENDED DISTRIBUTION OF THORIUM NEAR THE LUNAR COMPTON-BELKOVICH VOLCANIC COMPLEX. J. T. Wilson¹, V. R. Eke¹, R. J. Massey¹, R. C. Elphic², B. L. Jolliff³, D. J. Lawrence⁴, L. F. A. Teodoro⁵ ¹Institute for Computational Cosmology, Department of Physics, Durham University, Science Laboratories, South Road, Durham DH1 3LE, UK, ²Planetary Systems Branch, NASA Ames Research Center, MS 245-3, Moffett Field, CA, 94035-1000, USA, ³Department of Earth and Planetary Sciences and the McDonnell Centre for the Space Sciences, Washington University, One Brookings Drive, St Louis, Missouri 63130, USA, ⁴The Johns Hopkins University Applied Physics Laboratory, Laurel, Maryland, USA, ⁵BAER, Planetary Systems Branch, Space Sciences and Astrobiology Division, MS 245-3, NASA Ames Research Center, Moffett Field, CA 94035-1000, USA.

Introduction: The chemical composition of the Moon's surface has been successfully mapped by the Lunar Prospector spacecraft using gamma ray and neutron spectroscopy and these maps have led to an improved understanding of the formation and evolution of the lunar surface and interior [1,2]. Both of these methods of measuring elemental composition have the advantage, over other forms of spectroscopy, of not being sensitive to the mineral form in which the elements occur and of being able to probe composition at depths of a few tens of centimetres rather than only the top few wavelengths, as in UV/VIS/NIR imaging. Further, in the case of gamma ray detection from the natural decay of thorium (Th), uranium and potassium, the inferred abundances do not depend on cosmic ray flux or ground truth but only on having an accurate background subtraction. These chemical elements are particularly interesting because they are large, incompatible atoms that remain in a melt as it cools. Thus their distribution acts as a trace of magmatic activity and differentiation.

Of these three chemical elements Th is the most easily observed as its 2.61 MeV peak in the Moon's gamma ray spectrum is both strong and well separated from others. Examination of the Th abundance maps has, with other data, given rise to the interpretation that the Moon is split into three geologic terrains [2]: The low-Th Feldspathic Highlands Terrane, the moderate Th South Pole-Aitken basin and the high Th Procellarum KREEP Terrane (named after the high potassium (K), rare earth element (REE) and phosphorus (P) minerals that cover much of its surface but which also contains other incompatible elements such as Th).

The classification scheme is broken by one notable anomaly, located between the craters Compton (103.8°E, 55.3°N) and Belkovich (90.2°E, 61.1°N) on the lunar farside. This anomaly is a compositionally unique feature first detected in Lunar Prospector Gamma Ray Spectrometer (LP-GRS) data as an enhancement in Th concentration located at 60°N and 100°E [2]. Further investigation has associated this feature with a topographically elevated, high albedo region containing irregular depressions, cones and domes of varying size, interpreted as a local volcanic complex $\sim 25 \times 35 \text{ km}^2$ in area [3]. It thus became known as the Compton-Belkovich Volcanic Complex (CBVC). The CBVC remains unique in that the high Th region is not

coincident with an elevated FeO terrain (as would be expected from a KREEP basalt); instead the CBVC appears to have a low FeO abundance ($\sim 4\text{--}5\text{ wt.}\%$) that is similar to much of the lunar highlands [1,3]. Crater counting results indicate a possible age of 3.18 Gyr for volcanic resurfacing at the CBVC [4], suggesting that the Th distribution exposed at the CBVC may provide a rare insight into the upper mantle at this relatively late time in the Moon's evolution.

One drawback of gamma ray spectroscopy is the large spatial footprint of the detectors. When the LP-GRS was in an orbit 30 km above the lunar surface the full-width at half-maximum (FWHM) of the detector's footprint was $\sim 45 \text{ km}$. Additional statistical analysis is therefore required to extract information about the elemental composition of sites as small as the CBVC.

Reconstructions: The pixon method has recently been used to reconstruct remotely sensed neutron and gamma ray data and was shown to give a spatial resolution 1.5-2 times that of other methods in reconstructing planetary data sets [5,6,7]. It is an adaptive image reconstruction technique, in which the reconstructed truth is described on a grid of pixons, where a pixon is a collection of pixels whose shape and size is allowed to vary. The pixon sizes are set by requiring the information content of the image, in the pixon basis, to be flat, which maximizes the image entropy.

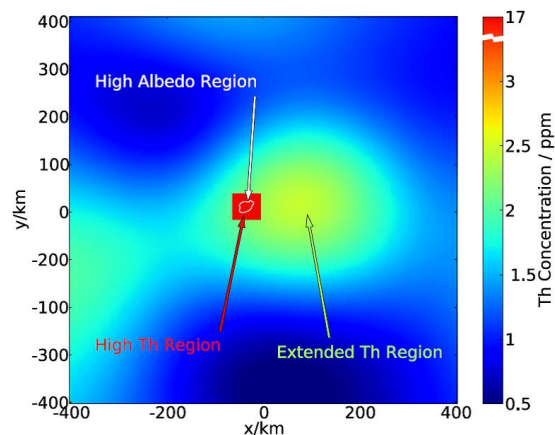


Figure 1: The best-fitting Th distribution in the vicinity of the CBVC. The high Th region is shown in dark red and occupies approximately 5 times the area of the high albedo feature, which is shown with the white contour.

We found that the standard pixon method was over-smoothing the image at the CBVC (due to the low signal to noise ratio), however the data require a sharp variation in the concentration of Th. To solve this problem we allow an area of the image, the ‘high-Th region’, to contain a significantly larger Th concentration than its surroundings, both the area and Th concentration of this region are varied. When the parameters adopted for this region match those giving rise to the LP-GRS data, the best match of data and blurred model should be produced.

The best-fit high-Th region in Fig. 1 is considerably larger than the high albedo region identified in Diviner, WAC and NAC imaging [5]. Additionally there is a broad Th enhancement stretching ~300km east of the CBVC.

The range of parameters allowed for the high-Th region is shown in Fig. 2. It is clear from the plot that a model with a high-Th region as small as the ~25×35km² high albedo region, shown with the black star, is disfavoured. The best-fitting decoupled regions cover 3000-5800km², corresponding to side lengths of ~55-75km and containing Th concentrations of ~20-13ppm.

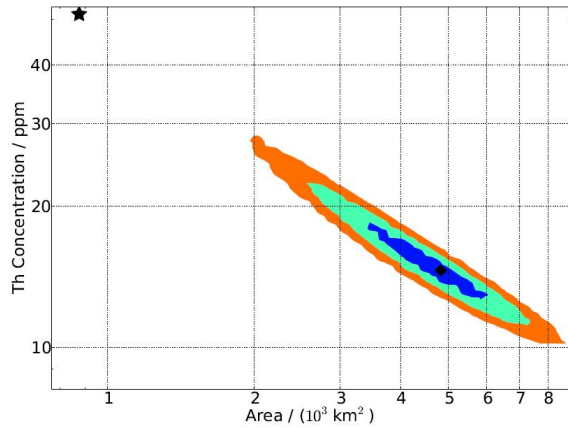


Figure 2: Constraints on the size and Th concentration in the high-Th region. The black diamond shows the best-fit reconstruction with minimum χ^2 . Coloured regions enclose 68%/95%/99.7% confidence limits, determined from $\Delta\chi^2 = \chi^2 - \chi^2_{\min}$. The black star shows the position of the optimum reconstruction under the assumption that the high-Th region coincides with the high albedo feature.

Pyroclastic eruption as a Method of Lunar

Transport: The results of the reconstructions show that the Th is presently distributed more widely than the high albedo region. We considered the effect of sputtering, thermal motion, downslope motion of regolith and regolith transport due to impact processes. The last of these is illustrated in Fig. 3. These results were produced by first assuming that all of the Th was originally in the high albedo region, modelled as a circle with area equal to that of the albedo feature identified by [3]. Following [8], we then assume power laws for the impactor size-

frequency relation and ejecta blanket thickness, and finally calculate the effect of 3.2Gyr of random impacts on the lateral transport of regolith. As can be seen, this process does not provide nearly enough regolith migration to account for the discrepancy between high-Th and high albedo regions. In fact the effect of all processes, post-emplacement, to alter the distribution around the CBVC is insufficient to explain the extent of the Th distribution measured in the reconstructions in Fig. 2. Therefore, we conclude that the Th must initially have been emplaced more widely than the high albedo region.

We hypothesise, following [3], that the mechanism was a highly silicic form of pyroclastic eruption not evident elsewhere on the Moon. Repeated pyroclastic eruptions from the many volcanic features in the CBVC could feasibly give rise to the observed high Th region that extends beyond the high albedo feature.

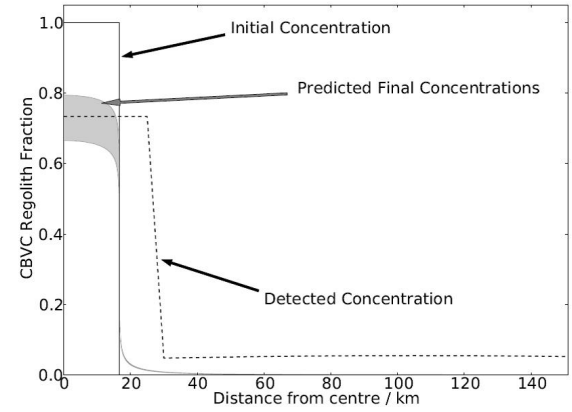


Figure 3: Variation of the fraction of regolith that originated within the CBVC (grey shaded area) with distance from the centre of the CBVC. The detected concentration curve is scaled so that it tends to zero at large distances and matches the model within the CBVC.

References: [1] Lawrence, D. J. et al. (1999), *GRL*, 26, 2681-2684. [2] Jolliff, B.L. et al. (2000), *JGR*, 105, 4197-4216. [3] Jolliff, B. L. et al. (2011), *Nature Geoscience*, 4, 566-571. [4] Shirley, K. A. et al. (2013), *Lunar and Planetary Science Institute Conference Abstracts*, vol. 44, p. 2469. [5] Pina, R. K., and R. C. Puetter (1993), *PASP*, 105, 630-637. [6] Eke, V. (2001), *MNRAS*, 324, 108-118. [7] Lawrence, D. J., et al. (2007), *GRL*, 34, L03201. [8] Li, L., and J. F. Mustard (2005), *JGR(Planets)*, 110, E11002.

THE HYDROGEN ANOMALIES IN KREEP TERRAIN ACCORDING TO THE RESULTS OF LEND AND LPNS NEUTRON SPECTROMETERS DATA. M.P. Sinitsyn, Sternberg Astronomical Institute, Universitetsky prospect, 13, Moscow 119992, Russia (msinitsyn.sai@gmail.com).

Introduction: At the present time, a large amount of data collected by neutron spectrometer LEND [12], mounted on LRO spacecraft. However, only the polar regions subjected to study in sufficient detail. Meanwhile, the spectrometer data covering the entire surface of the moon, including its equatorial regions. This report provides an analysis of epithermal neutron flux [10,11] for the some surface formations located, in KREEP region.

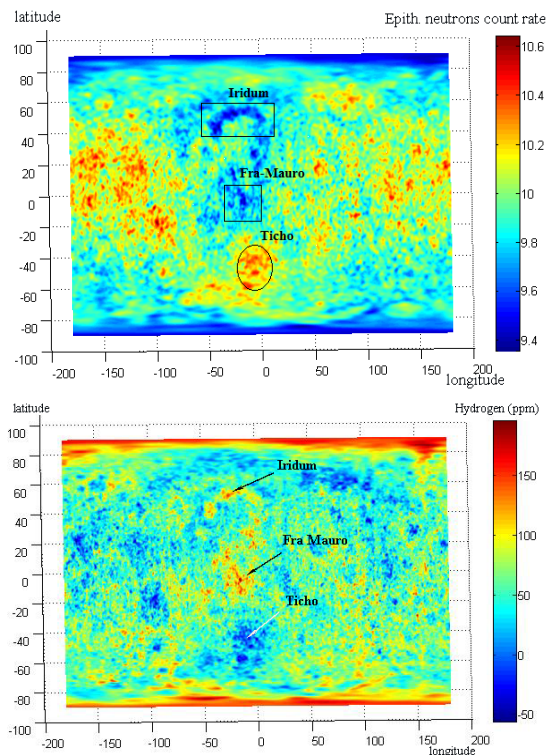


Figure 1: Epithermal neutrons flow distribution around intire equatorial surface (LEND omnidirectional sensor[12], above) and global map of hydrogen concentration (LPNS,below).

The area of KREEP is the vast terrain on the near side. It corresponds to significant suppression of epithermal neutron flux and, accordingly, increase of hydrogen concentration [2]. For estimating changes of neutron flux used so-called suppression factor (δ) [2,17]. The suppression factor indicates a relative difference between an investigated area flow and a flow of selected comparison area. The comparison (reference) area selected like area with maximum neutron flux, which corresponds to the minimum of hydrogen content. The reference zone in the vicinity of crater Tycho is choosed for calculation of suppression factors presented below. Hydrogen content in this area consists of 0-5 ppm by LPNS data (fig.1).

| anomalies | lat | long | δ (%) | stand. error | H (ppm) |
|------------------------------|-------|-------|--------------|---------------|---------|
| 1. Iridum | 50.2 | -29.8 | 6.9 | 49.4 σ | 82.2 |
| 2.Gruithuisen vol. dome | 36.1 | -39.6 | 5.4 | 10.5 σ | 70.7 |
| 3. Fra Mauro | -6.1 | -17.0 | 7.2 | 24.0 σ | 127.5 |
| 4.Aristarchus plateau | 26.7 | -53.3 | 5.4 | 18.2 σ | 77.1 |
| 5.Marius hills | 14.1 | -51.5 | 4.6 | 12.1 σ | 45.6 |
| 6. Hansteen | -15.3 | -43.7 | 5.3 | 30.3 σ | 90.8 |
| 7.Helmet | -8.9 | -28.0 | 4.1 | 26.2 σ | 65.8 |
| 8.Montes Carpatius | 14.6 | -23.7 | 5.9 | 25.6 σ | 92.5 |
| 9.Montes Caucasus | 37.5 | 9.9 | 5.9 | 26.6 | 65.9 |
| 10.Montes Apenninus | 19.9 | 0.0 | 6.2 | 27.9 | 87.4 |
| 11. KREEP terrain | - | - | 4.6 | 39.2 | 62.3 |
| 12.entire equatorial surface | - | - | 3.0 | 25.1 | ~30 |
| 13. Ticho | -43.5 | -11.5 | 0.0 | - | 3.0 |

Table 1: Epithermal neutron suppression factors (δ , LEND) and average hydrogen contents (H, LPNS) for anomalies located on the KREEP terrain. The number 11 corresponds to global KREEP region. The number 12 corresponds to all equatorial surface from -60 deg. To 60 deg.

Distribution epithermal neutron flux around the equatorial region: The tab.1 shows that the characteristic suppression factors for epithermal neutrons of KREEP terrain: $\delta = 3\text{-}7\%$. This is generally a very large value for the equatorial region. Characteristic values for the highland of dark side: $\delta = 0\text{-}3\%$. As can be seen from fig. 1 noticeable suppression of the neutron flux is observed on the both poles and in the area of KREEP on the near side. For comparison, the suppression factor in the vicinity of the crater Cabeus is 17%, which corresponds to the concentration of 470 ppm hydrogen [11].

Increased hydrogen concentrations in the KREEP terrain: The objects under consideration have substantial suppression factors ($\delta = 4.1\text{-}7.2\%$) relatively crater Ticho. The hydrogen content is 45-127 ppm while the average around equatorial surface

is about 30 ppm. The maximum suppression factors (δ) correspond to Fra Mauro and Iridum [20,21] areas (fig.2). As can be seen, the maximum hydrogen concentration reaches 180 ppm for Fra-Mauro anomaly. These areas were formed due to the huge impact that created Mare Imbrium basin [19]. It can be expected that the material making up these formations lifted from quite significant depth. Several of the considered objects (Gruithuisen volcanic dome [21], Aristarchus plateau, Marius hills) are obviously volcanic origin. Moreover, lunar pyroclastic deposits [1,5,6] also have tendency to increased suppression factor [17,18,19]. All this may indicate indigenous lunar origin of that hydrogen compounds. In addition, several recent studies [7,13,14,15,16] point to substantial content of hydrogen (water) on the KREEP surface and in the lunar mantle. For instance, apatite in low titanium mare basalt include 500-15000 ppm of hydroxyl (OH)[13]; the lunar melt inclusions contain 615 to 1410 ppm water [7].

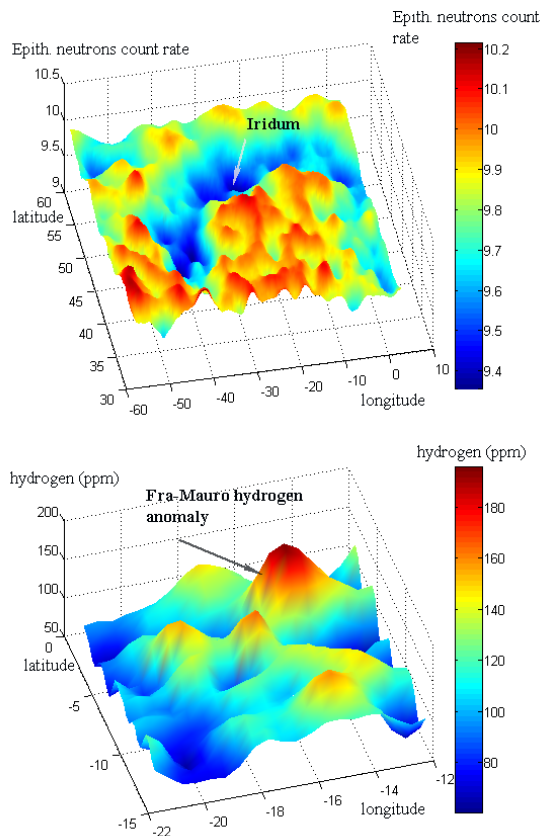


Figure 2: Epithermal neutrons flow distribution around Iridum (LEND omnidirectional sensor[12], above) and hydrogen concentration in the vicinity of Fra-Mauro crater (LPNS,below).

Discussion: One might reasonably question arose whether these hydrogen anomalies are due to internal processes, or by reason of the incorporation of solar wind protons? In this regard, necessary to say that has not yet found clear correlation of hydrogen

content and maturity of the any formations [3,8]. Many immature craters, such as Copernicus and Giordano Bruno did not show significant changes in the epithermal neutron flux. This may mean that lifted fresh material has the same amount of hydrogen as the surface. More difficult question: how inclusion of rare earth elements influence to absorption of epithermal neutrons? On this account there is very few information [4,9], but the results of the hydrogen content according to LPNS are taking into account gadolinium and samarium contents.

Conclusion: The results of two neutron spectrometers independently indicate a correlation between increased concentration of hydrogen (suppression epithermal neutrons flow) and surface formations of KREEP region. Perhaps this indicates the indigenous origin of hydrogen compounds in this territory.

References: [1] Allen C.C. et al. (2012) JGR, 117, E00H28. [2] Boynton G. F. et al. (2012) JGR, 117, E00H33. [3] Feldman W.C. et al. (2001) JGR, 106, 23231-23251. [4] Feldman W.C. et al. (2000) JGR, 105, 20347-20363. [5] Gaddis L.R. et al. (2003) Icarus, 161, 262-280. [6] Gustafson J. O. et al. (2012) JGR, 117, E00H25. [7] Hauri E.H. et al. (2011), Science, 333, 6039, 213-215. [8] Johnson J.R. et al. (2001) 32th LPSC, abstract #1440. [9] Lawrence D.J. et al. (2006) JGR, 111, E08001. [10] Litvak M. L. et al. (2012) JGR, 117, E00H22. [11] Mitrofanov I.G. et al. (2010a) Science, 330, 483-486. [12] Mitrofanov I.G. et al. (2010b) Space Sci. Rev., 150(1-4), 183-207. [13] Tartese R. et al. (2013) Geochimica et Cosmochimica Acta, 122, 58-74. [14] Qin C. et al. (2012) Icarus, 220, 100-105. [15] Saal A.E. et al. (2008) Nature, 454, 170-172. [16] Saal A.E. et al. (2013) Science, 340, 1317-1320. [17] Sinitsyn M.P. et al. (2014) 45th LPSC, abstract #1066. [18] Sinitsyn M.P. et al. (2013) 4th Moscow Solar System Symp., 4MS3-PS14. [19] Taylor S.R. (1975) Lunar Science: A Post-Apollo View. NY: Pergamon Press. 372 p. [20] Wagner R. et al. (2002) JGR, 107, E001844. [21] Wagner R. et al. (2010) JGR, 115, E003359. [22] Wohler C. et al. (2014) 45th LPSC, abstract #1329

THE POLAR WATER ICE INVENTORY – WHAT DO WE KNOW AND HOW? V. R. Eke¹, L. F. A. Teodoro², R. C. Elphic³, W. C. Feldman⁴, D. J. Lawrence⁵ ¹Institute for Computational Cosmology, Durham University, South Road, Durham. DH1 3LE, UK, ²BAER, Planetary Systems Branch, Space Sciences and Astrobiology Division, NASA Ames Research Center, Moffett Field, CA 94035-1000, USA, ³Planetary Systems Branch, Space Sciences and Astrobiology Division, NASA Ames Research Center, Moffett Field, CA 94035-1000, USA, ⁴Johns Hopkins University Applied Physics Laboratory, Laurel, MD 20723, USA, ⁵Planetary Science Institute, 1700 E. Fort Lowell, Suite 106, Tucson, AZ 85719, USA.

Introduction: Knowing how much accessible water ice is present in polar cold traps and at what concentration would greatly inform planning of future lunar missions. The only “ground truth” data taken to date came from the LCROSS experiment, which determined that the regolith in one small region of the Cabeus crater contained $\sim 5 \pm 3$ wt.% water ice [1]. Both neutron spectroscopy and radar sensing offer the possibility of remotely inferring the presence of volumetrically significant water ice deposits over large areas [2,3]. However, in the scientific literature, there is a lack of consensus on the interpretation of the available data from both of these techniques. While the spatial resolution of the hydrogen maps produced by different neutron detectors is a matter that has been debated [4,5], there is uncertainty over whether or not the radar is detecting icy or rough surfaces [6,7].

Two neutron experiments have made maps of the near-surface hydrogen abundance: the Lunar Prospector Neutron Spectrometer (LPNS) and the Lunar Exploration Neutron Detector (LEND). The LPNS was an omni-directional detector flown 15 years ago [2]. Its spatial resolution of ~ 45 km was larger than most permanently shaded polar cold traps, leaving the inferred hydrogen distribution tantalisingly uncertain. Two different approaches have since been attempted to constrain further the location and concentration of these deposits: the software approach and the much more expensive hardware approach.

The former was performed using a pixon image reconstruction algorithm [8] that found a hydrogen distribution that, after blurring with the LPNS response, looked like an unnoisy version of the data. This technique was further employed to show that the hydrogen was typically concentrated into cold traps, increasing the likelihood of it being present as water ice [9]. Using up to date maps of the cold trap distribution, a model to convert neutron count rate to hydrogen concentration [10], and the assumption that all hydrogen was present as water ice, the pixon method applied to data from the LPNS predicted that LCROSS would find water ice at the per cent level in Cabeus [11].

The LEND team chose the hardware solution for making sharper maps of lunar hydrogen, building the Collimated Sensor for EpiThermal Neutrons (LEND CSETN). This detector was placed onto NASA’s Lunar Reconnaissance Orbiter. The effectiveness of

the collimator at blocking out neutrons from outside its tiny field of view was called into question prior to launch [12], and since data have become available, a number of different studies have shown that this concern was well justified [5,13,14,15].

With the influx of data from the Synthetic Aperture Radar experiments Mini-SAR and Mini-RF, the debate over what can be inferred from maps of the Circular Polarisation Ratio (CPR) of returned radar pulses continues. Fresh craters show high CPR both inside and outside their rims as a result of multiple scattering from blocky ejecta. However, some “anomalous” craters with high interior CPR and low CPR values, where their ejecta blankets would be, have also been discovered [6]. If the weathering caused by micrometeorite bombardment is isotropic, then the surface roughness inside and outside craters should decrease at the same rate. One possible inference from the presence of anomalous craters is that something other than a rough surface is responsible for the high CPR within anomalous craters. That something could be water ice.

More recently, anomalous craters have been found in equatorial regions with CPR distributions that are indistinguishable from those at the poles, despite the fact that water ice cannot be responsible for these anomalous craters [7]. Also, there appear to be many more anomalous craters in polar regions, suggesting that temperature is important to some extent [6].

Quantitative Comparison of Neutron Detectors: Both the LPNS and LEND CSETN measure the neutron flux above the lunar poles, so their maps can be directly compared. A good statistic for this purpose, which takes into account the different count rates into these two detectors, is the count rate contrast defined, for pixel \mathbf{x} , via

$$\delta(\mathbf{x}) = \frac{c(\mathbf{x}) - \bar{c}}{\bar{c}},$$

where c represents a count rate and \bar{c} is the mean count rate within the whole map. Both statistical noise and coherent fluctuations can give rise to large contrasts, but only the latter will contribute to the autocorrelation function when averaged over the entire map. For a given separation between pixels, \mathbf{r} , the autocorrelation function is defined by

$$\square(r) = \langle \delta(\mathbf{x})\delta(\mathbf{x} + \mathbf{r}) \rangle,$$

where the brackets denote an average over all pixels separated by a distance r .

From Figure 1, the LPNS map made from the 30 km orbit contains much larger coherent variations than either the LPNS map from 100 km, which has a proportionately larger detector footprint blurring the count rate contrasts, or the LEND CSETN map. One can immediately infer that any small-scale high contrast pixels in the LEND CSETN must be statistical noise. Furthermore, the figure also shows that the pixion reconstruction enhances the amplitude of the small-scale features, as it is designed to do. It is clear that the software solution has enhanced small-scale contrast, whereas the hardware solution has not.

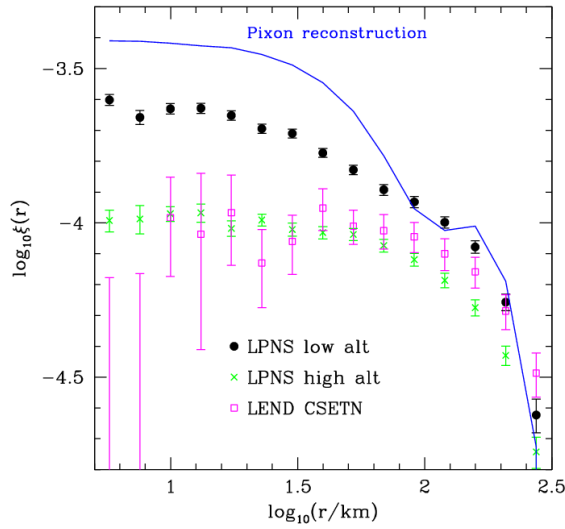


Figure 1: The autocorrelation functions, accounting for spacecraft background, for the LPNS south pole maps using high- and low-altitude data and the LEND CSETN map of the same region. The blue line shows the result for the pixion LPNS reconstruction.

CPR Variation Within Anomalous Craters:

Using Mini-SAR data, the variation of CPR within polar anomalous craters has been studied. If the high interior CPR values were related to ice deposits, then one might expect highest CPR values on pole-facing crater walls and at the bottoms of craters, where the temperatures remain coldest. In fact, the CPR maps are dominated by angle-of-incidence effects, where returns from parts of the surface viewed at grazing incidence have higher CPR than those viewed head on, where specular reflection is stronger. To account for the varying Mini-SAR viewing angle, LOLA topographical data are used.

The CPR in the central, coldest, regions of the craters, shown with the black curve in the Figure 2, is indistinguishable from that outside the crater rims in regions that endure much higher temperatures. This suggests that these monostatic CPR measurements are not picking out ice deposits. After

objectively selecting a set of polar craters, CPR-anomalous craters have relatively small diameter-to-depth ratios and high CPR regions tend to be only on steep crater walls, hinting at yet-to-be-weathered-away surface texture as the reason these craters appear anomalous.

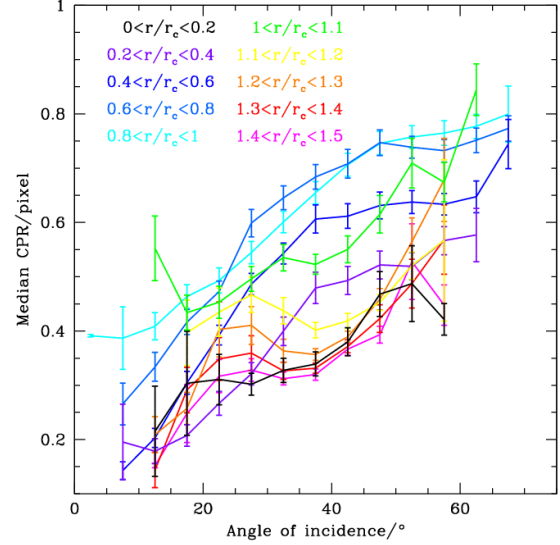


Figure 2: The variation of typical CPR with angle of incidence for polar anomalous craters. The different curves show results within different annuli, out to 1.5 times the crater radius, r_c .

Summary: It seems likely that monostatic radar measurements relate to surface roughness. The LEND CSETN has failed to improve on results from the LPNS. The best polar hydrogen maps come from the pixion reconstruction of the LPNS data.

References: [1] Colaprete A. et al. (2011) *Science*, 330, 463. [2] Feldman W. C. (1998) *Science*, 281, 1496. [3] Nozette S. (1996) *Science*, 274, 1495. [4] Mitrofanov I. G. et al. (2010) *Science*, 330, 483. [5] Lawrence D. J. et al. (2011) *Science*, 339, 292. [6] Spudis P. (2013) *JGR*, 118, 2016. [7] Fa W. and Cai Y. (2013) *JGR*, 118, 1582. [8] Elphic R. C. et al (2007) *GRL*, 3413204. [9] Eke V. R. et al. (2009) *Icarus*, 200, 12. [10] Lawrence D. J. et al (2006) *JGR*, 111, 8001. [11] Teodoro L. F. A. et al. (2010) *GRL*, 3712201. [12] Lawrence D. J. et al. (2010) *AsBio*, 10, 183. [13] Eke V. R. et al. (2012) *ApJ*, 747, 6. [14] Miller R. S. et al. (2012) *JGR*, 117, 11007. [15] Teodoro L. F. A. et al (2014) *JGR*, in press.

A NEW TECHNIQUE FOR IMPROVED MAPPING OF WATER-ICE DEPOSITS IN THE POLAR COLD TRAPS OF THE MOON. S. Mohan¹, S. Saran², A. Das², ¹PLANEX, Physical Research Laboratory, Ahmedabad - 380009, India, ²Space Applications Centre, ISRO, Ahmedabad - 380015, India.

Introduction: Recent investigations of lunar polar regions using remote sensing data suggested the existence of water-ice in permanently dark regions of polar craters (e.g., [1–4]). Radar is regarded as one of the most effective tools for detecting water ice, because as a low dielectric loss medium, water ice could produce Coherent Backscatter Opposition Effect (CBOE) under certain conditions. The key parameter to address this is the radar circular polarization ratio (CPR) and previous studies indicated that if ice in the permanently shadowed areas of the lunar poles has radar characteristics similar to the ice on Mercury, Mars and the Galilean satellites, then they will have substantial radar enhancements characterized by a CPR greater than unity.

Since 2008, two orbital miniature synthetic aperture radars (Mini-SAR and Mini-RF) on Chandrayaan-1 and Lunar Reconnaissance Orbiter (LRO) missions have imaged the lunar surface with the main purpose of detecting the polarimetric signature of ice at the lunar poles [5]. Spudis et al. [1, 4] analyzed radar data for both the poles of the Moon that was acquired by the Mini-RF radars and found that some craters show elevated CPRs in their interiors, but not exterior to their rims. However, elevated CPR values were also observed from the interiors of some non-polar craters, young, fresh polar craters [1, 4] and very rough surfaces such as a rough, blocky lava flow, which has angles that form many small corner reflectors [6]. Thus, elevated CPR values are not a unique signature of water ice deposits. Therefore, additional information related to geological setting and roughness patterns should also be considered while identifying the regions containing water-ice deposits.

In this study, in order to identify a unique signature of water-ice deposits, analysis of radar polarimetric scattering mechanisms in elevated CPR regions at the lunar north pole was carried out. Based on the signatures of diffuse scatterers and radar backscattering coefficient, a scattering mechanism-based algorithm [6] was developed and then tested using Chandrayaan-1 Mini-SAR data. The algorithm showed promising results for identifying craters with water-ice deposits by separating them from young, fresh craters with elevated CPR values.

Methodology: In this study, scattering properties of 20 craters were analyzed; 16 of them are at the north pole and the remaining craters belong to non polar regions of the Moon. Out of the 16 north polar craters, 13 have permanently shadowed regions, while the remaining three are fresh impact craters with their ejecta fields distinctly visible in the

Mini-SAR images. Each of the craters along with its impact ejecta region was analyzed in terms of radar backscatter and scattering mechanism to study the anomalous scattering properties. Mean values of polarimetric parameters CPR, m (degree of polarization) and δ (relative phase) were observed for these regions. The craters are classified into anomalous and fresh (young) according to the mean CPR values observed. Since high CPR regions were to be analyzed, the areas with CPR values greater than 1 at the crater interior were masked out for subsequent analysis.

Scattering mechanism in high CPR regions. Since the relative phase delta (δ) is a sensitive indicator for odd and even bounce scattering, regions showing surface scattering (specular or mirror-like reflections) could be separated from other regions. Therefore, use of CPR in conjunction with δ could give improved understanding of scattering types in a region. For this analysis, CPR values were plotted against δ and the scatter plots were studied. In CPR space, the image pixels for which $\text{CPR} < 1$ were found to be confined to the region of $\delta = -180^\circ$ to $\delta = 0^\circ$, and the upper half of the plane ($\delta = 0^\circ$ to $\delta = 180^\circ$) contained pixels with $\text{CPR} > 1$, which have contributions from both double-bounce and volume scattering. In this way, contribution from surface scattering was eliminated.

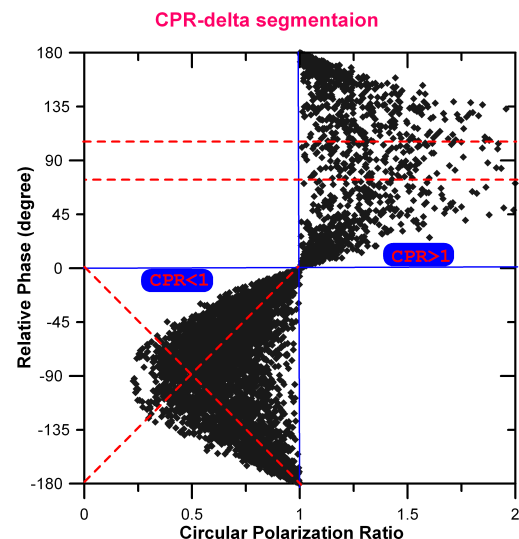


Figure 1: Graphical illustration of CPR-delta segmentation technique. Zones of CPR less than and greater than 1 are indicated. The red dotted lines indicate regions of $\delta = -180^\circ$ to 0° and $\delta = 90^\circ$ to 100° in those zones respectively, which are segregated using this method. The residual regions contribute exclusively to diffuse/volume scattering in the $\text{CPR} > 1$ zone.

As the Mini-SAR transmitted LCP, a dominant double-bounce scattering mechanism will return a left circular polarized wave again, which will be centered at $\delta = +90^\circ$. So the pixels with delta values of $90^\circ \pm 10^\circ$ were removed to separate the regions having contribution from both double-bounce and volume scattering. A graphical representation of this segmentation using CPR and delta values is shown in Figure 1.

Also, as a threshold value of -15 dB (total backscattered power) was chosen based on the observations of mean backscatter at regions of $\text{CPR} > 1$ at the interior of the analyzed craters. This backscatter threshold was applied to mask out two regions: interior of non-polar anomalous craters which mimic the water-ice-like condition and very high backscatter observed at the crater walls which are oriented in the direction of the radar (in the order of $+5$ dB to -8 dB). Based on the above inputs, an algorithm was developed as shown in Fig. 2, which can be used to represent the areas of possible locations of water-ice.

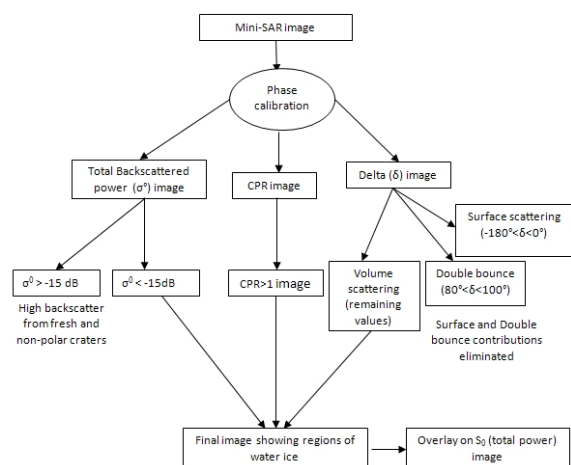


Figure 2: The CPR-delta algorithm for identification of water-ice in lunar polar regions.

Results & Discussion: A decomposition technique based on the parameters m and δ derived from the hybrid polarimetric SAR data was found to be effective in identifying dominant scattering mechanisms associated with a radar resolution cell [7]. But the high CPR regions ($\text{CPR} > 1$) showed contributions from surface, volume and double bounce scattering mechanisms, derived from this method, for all the craters. Thus, high CPR regions exclusively contributed by diffuse/volume scattering were identified using the algorithm described above. The results of the existing decomposition technique and the algorithm developed are shown in example in Fig. 3. The green pixels overlaid on S_0 images indicate the possible locations of water-ice according to the two methods. Clear differences could be observed between the two methods in depicting the possible water-ice regions within the permanently

shadowed regions of the crater interior. Even though some non-polar craters also exhibit anomalous scattering properties, they are characterized by high backscatter values in their interiors (average values around -10 dB) in contrast to the low values of polar anomalous craters, suggestive of diffuse scattering likely due to water-ice particles mixed with the regolith. Thus, CPR-delta method was implemented for detecting regions of water-ice along with a backscatter criterion that helps in differentiating polar anomalous craters from those of non polar origin.

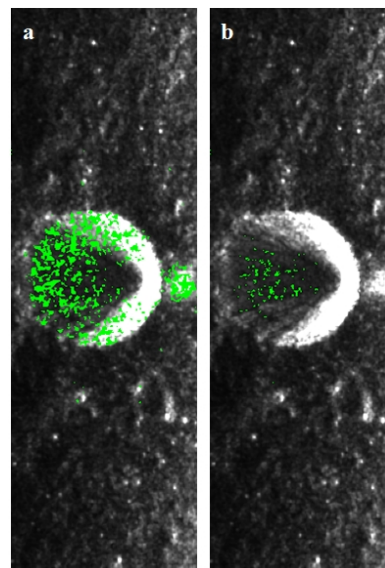


Figure 3: Regions of volume scattering (in green) overlaid on S_0 images of the small crater on the floor of Rozhdestvensky using (a) existing method (regions of $\text{CPR} > 1$) and (b) the algorithm developed.

Conclusion: The CPR-delta approach along with backscatter analysis used in this study provides a better method to identify volume scattering regions and the new algorithm showed promising results for identifying craters with water ice deposits by separating them from young fresh craters with elevated CPR values. The identification of regions which exclusively contribute to volume scattering in the permanently shadowed regions is important in supporting the debate over the possible existence of water-ice in those areas, since a high degree of correlation between the occurrence of high CPR values and the transition from seasonally sunlit to permanently shadowed regions of the crater wall is certainly required.

References: [1] Spudis, P. D. et al. (2010) *GRL*, 37, L06204. [2] Pieters, C. M. et al. (2009) *Science*, 326, 568-572. [3] Colaprete, A. et al. (2010) *Science*, 330, 463-468. [4] Spudis, P. D. et al. (2013) *JGR*, 118, 1-14. [5] Nozette, S. et al. (2010) *Space Sci. Rev.*, 150, 285-302. [6] Mohan, S. et al. (2013) *Curr. Sci.*, 105 (11), 1579-1587. [7] Raney, R. K. (2007) *IEEE Trans. Geosci. Remote Sens.*, 45, 3397-3404.

SMART-1 IMPACT STUDIES FROM SPA, BASINS TO SMART-1 BOUNCING SITE. B. H. Foing¹ and SMART-1 Science & Technology Working Team*, ¹ESA/ ESTEC, Postbus 299 , 2200 AG Noordwijk, The Netherlands (Bernard.Foing@esa.int).

Abstract: We highlight some ESA SMART-1 results on impact processes. We discuss impact basins, the morphology of craters, the properties of central peaks, and the study of specific impact craters of interest to ILEWG community. We also give an update on the results from SMART-1 impact campaign and the search for SMART-1 bouncing site and debris using latest LRO data.

Introduction: ESA SMART-1 mission demonstrated Solar Electric Propulsion for deep space, tested new technologies for spacecraft and instruments miniaturisation, and provided an opportunity for science [1-24] until impact on 3 September 2006. To date, 75 refereed papers and more than 325 conference or technical papers have been published based on SMART-1 (see ADS or SMART-1 scitech website sci.esa.int/smart-1). The SMART-1 data are accessible on the ESA Planetary Science Archive PSA [13]

<http://www.rssd.esa.int/psa>

Studies of impact basins/craters: The South Pole-Aitken Basin was mapped and studied combining data from Clementine, SMART-1, and other missions [24]. Large basins and the relation between impacts, tectonics and volcanism have been studied. The tectonic structure differ in simple impact basins (such as Humorum,) compared to Oceanus Procellarum, suggesting the latter has a different origin. Impact craters in the lunar North and South polar illumination have been mapped [16, 17]. SMART-1 SIR data were used to study the mineral composition of the central peak of craters [22]. SMART-1 could study a large range of impact crater sizes and morphologies, and sites of interest to the international lunar community (ILEWG).

SMART-1 artificial impact: The SMART-1 mission finished in a grazing bouncing impact. The impact flash was observed from Earth, as well as a debris cloud downrange of 50 kms. The SMART-1 impact was modelled using laboratory experiments predicting the size of asymmetric crater and ejecta [23]. We report the analysis of SMART-1 impact campaign and subsequent data from LRO to pinpoint the initial SMART-1 bouncing site and impact debris.

***Acknowledgements :** We acknowledge ESA, member states, industry and institutes for their contribution, and the members of SMART-1 Teams: G.Racca and SMART-1 Project Team, O. Camino

and SMART-1 Operations Team, D. Frew and SMART-1 STOC, B.H. Foing and STWT, B. Grieger, D. Koschny, J.-L. Josset, S. Beauvivre, M. Ellouzi, S.Peters, A. Borst, E. Martellato, M. Almeida, J.Volp, D. Heather, M. Grande, J. Huovelin, H.U. Keller, U. Mall, A. Nathues, A. Malkki, W. Schmidt, G. Noci, Z. Sodnik, B. Kellett, P. Pinet, S. Chevrel, P. Cerroni, M.C. de Sanctis, M.A. Barucci, S. Erard, D. Despan, K. Muinonen, V. Shevchenko, Y. Shkuratov, P. McMannamon, P. Ehrenfreund, C. Veillet, M.Burchell, other Co-Investigators, associated scientists, collaborators, students and colleagues.

Link: <http://sci.esa.int/smart-1/>

References: [1] Foing et al (2001) EMP85-523; [2] Racca et al (2002) EMP85-379; [3] Racca et al. (2002) PSS50-1323; [4] Grande et al. (2003) PSS51-427; [5] Dunkin et al. (2003) PSS51-435; [6] Huovelin et al. (2002) PSS50-1345; [7] Shkuratov et al (2003) JGRE108-E4-1; [8] Foing et al (2003) ASR31-2323; [9] Grande et al (2007) PSS55-494; [10] Pinet et al (2005) PSS53-1309; [11] Josset et al (2006) ASR37-14; [12] Foing et al (2006) ASR37-6; [13] Heather et al, EPSC-DPS 2011-873 [14] Muinonen et al (2011) A&A531-150; [15] Souchon et al EPSC-DPS2011-928, [16] Grieger (2010) cosp38-417; [17] Bussey et al (2011) LPICO-1621-5; [18] Pluchino et al MSAItS 16-152; [19] Qiao (2011) AcASn 52, 539; [20] Vaananen et al (2009) SolarPhys260-479; [21] Alha et al (2012) NIMPA 664, 358; [22] Bhattacharya et al EPSC-DPS2011-1842; [23] Burchell et al (2010) Icarus207-28; [24] Borst, Foing et al (2012) PSS 68, 76;

Public SMART-1 site: www.esa.int/smart-1

ILEWG site: <http://sci.esa.int/ilewg>

SMART-1 Google scholar references & citations:
<http://scholar.google.nl/scholar?&q=smart-1+moon>

Introduction: The Apollo landing sites are the best-studied planetary surfaces outside the Earth. In the last few years, we have witnessed a resurgence of lunar missions, with much of the Moon's surface now photographed to a sub-meter resolution at varying observation conditions. This study is based on Narrow Angle Camera (NAC) [1] images at a spatial resolution of ~ 1.4 m and phase angle ~ 68 degrees. I carried out a census of craters down to a diameter of 5 m within a region centred on Taurus-Littrow valley, site of the Apollo 17 mission. I extended the survey to parts of the surrounding uplands for comparison.

Method: First, boundaries were drawn between terrains with clear differences in morphology, crater distribution, and albedo (Fig. 1). 30,000+ craters (Fig. 2) were then recorded and prominent geomorphologies highlighted (faults and striations).

Data: Fig. 3 compares the (binned) crater size distribution scaled to 100 (%). I noticed distribution trends below 70 m in diameter and focused my attention on this range. The central cluster of craters in the vicinity the A17 Lunar Module has long been interpreted as the product of secondary projectiles from the Tycho impact and dated to around 100 Ma [2]. Their subdued morphology and contemporaneous formation [3] offer a rare opportunity for surveying small craters population accumulation within a known timeframe ("Shallow" craters, red dots in Fig. 1).

Results:

Crater distribution groups. Small crater accumulation frequencies ($D < 70$ m) are remarkably similar within comparable geological environments, such as the uplands (H1,2), in this case with a pronounced peak in the 20-30 m crater size bin (Fig. 3). Mare areas are more complex with three distinct typologies: a central valley type (M3a, M4, M5; green; Fig. 1), a second comparable one (M3b,c; blue), and last, a group with 'intermediate' size distributions (M1, M2, M6; grey).

Cumulative Crater Frequency. The survey of craters within the diameter of "Shallow" ones shows a CCF distribution sitting right on the 15 Ma isochron (with a modelled age of 16.1 ± 1.2 Ma) (Fig. 4). Interestingly, all upland units (especially M2, the Bear Mountain) somewhat follow this trend, whilst mare units do not. Indeed, the latter cannot be easily assigned an age estimate to any size bin (e.g. M1 and M6, Fig. 4).

Discussion and Conclusions: Estimating relative and absolute ages using small crater populations has proved to be a controversial issue [5,6], an approach marred by poor statistics (past low res. images) and concerns about the contribution of

secondary cratering [7]. Here we show that, buried within small-craters surveys, we may find trends (Fig. 3) worth exploring.

In geological terms, the 16 Ma age model, derived from crater size distributions within shallow craters of known formation age [3], offers a tantalising resurfacing estimate matching the dating of a fragment in the breccia 78155 collected not far from SWP (one of the surveyed craters) of 17 ± 1 [8].

Alternatively, the CCF coincidence between craters in highlands and the "in shallow" ones might derive from mechanical properties of the target materials, which would favour the preferential erosion of crater sizes less than ~ 20 m, while preferentially preserving craters up to ~ 60 m (Fig. 3). Is this a localised trend? In either case the implications are intriguing and worth further investigation.

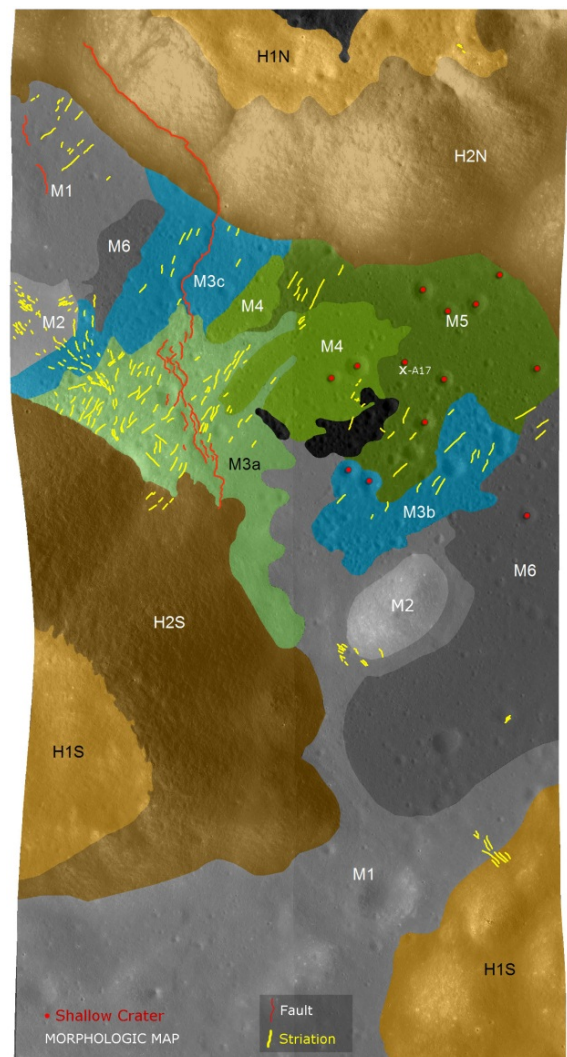


Figure 1: Geologic map of the Taurus-Littrow region. Small blank regions were not included in map due to crater saturation.

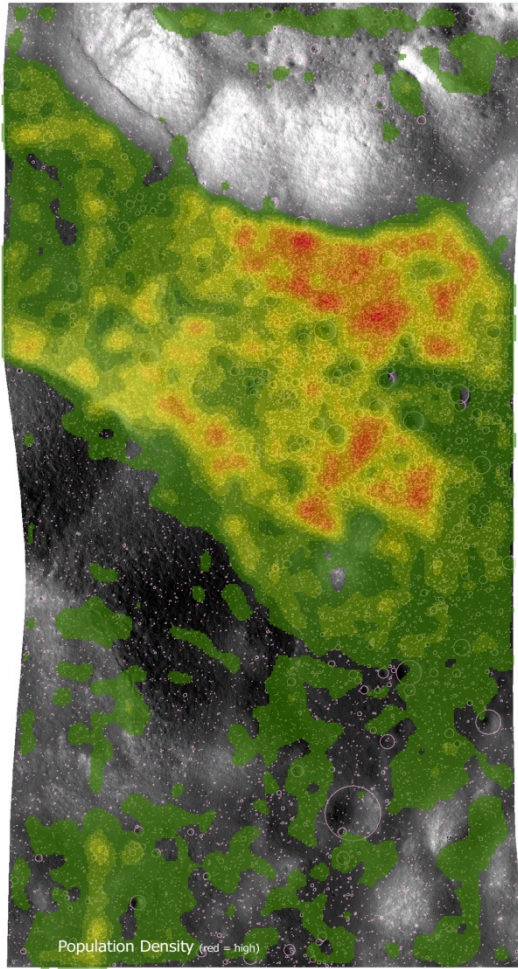


Figure 2: Production density distribution of craters.

Future work: Ideally, large-scale surveys of small craters across other lunar regions would improve our knowledge of their distribution, but they are labour intensive tasks. Likely, help might come from two sources: automated crater surveys (e.g. [9]), and citizen science projects, such as MoonZoo [10], which should bring the large statistical numbers required for studies of this ilk.

Bibliography: [1] Jolliff B.L., et al., and the LROC Targeting Action Team. In *Lunar and Planetary Science XL* Abstr. no. 2345. (2009) [2] Arvidson R. et al., *Proc. 7th Lunar Sci. Conf.*, 2817-2832. (1972) [3] Lucchitta B.K., *Icarus*, 46-50 (1979) [4] Michael G.G. and Neukum G., *EPSL*, (2010) [5] Schultz P.H. et al., *Proc. Lunar Sci. Conf. 8th*, 3539-3564 (1977) [6] Zhiyong X. and Strom R.G., *Icarus*, 220, 254-267 (2012) [7] McEwen A.S. and Bierhaus B.B., *Annu. Rev. Earth Planet. Sci.*, 34:535-567 (2006) [8] Fernandes V.A. et al., *M&PS* 48, Nr 2, 241-269 (2013) [9] Vijayan S. et al., *Icarus* 226, 798-815 (2013) [10] Joy K. H., et al., In *Lunar and Planetary Science XLI*. Abstr. no. 1620. (2010).

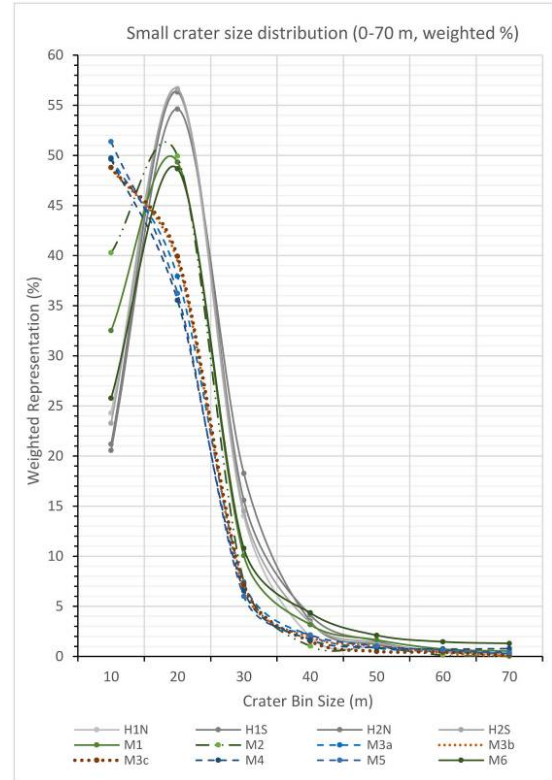


Figure 3: Comparative crater size ($D < 70$ m) distribution within boundaries, as per Fig. 1.

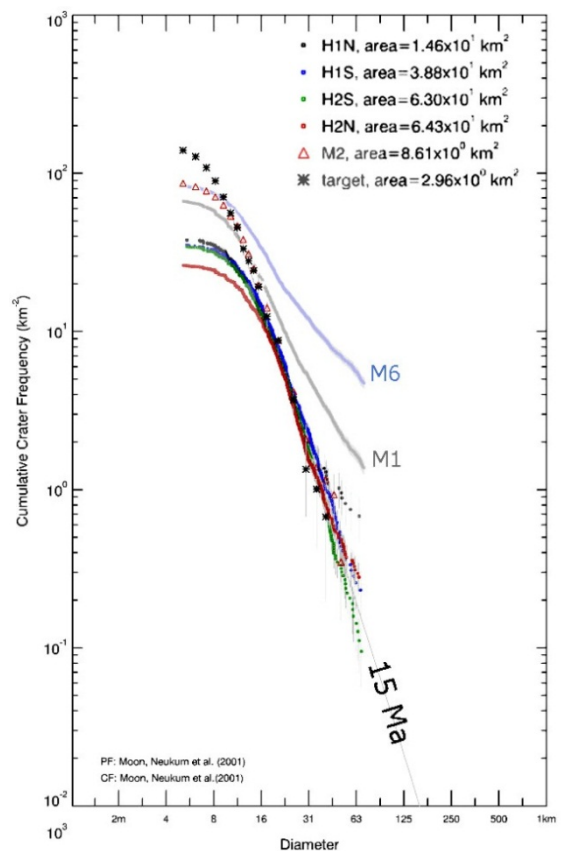


Figure 4: CCF histogram of < 70 m craters in upland regions and 'Shallow craters', here labelled as 'target' ($D/W < 0.15$, [3]). CraterstatsII [4].

FINDING LAUNCH SITES OF METEORITES USING LUNAR PROSPECTOR GAMMA-RAY SPECTROMETER DATASETS. A. Calzada-Diaz¹, K. H. Joy², I. A. Crawford¹, T. A. Nordheim³

¹Department of Earth and Planetary Sciences, Birkbeck College, WC1E 7HX London, UK, ²School of Earth, Atmospheric and Environmental Sciences, University of Manchester, UK, ³Mullard Space Science Laboratory, University College London, UK (acalza01@mail.bbk.ac.uk).

Introduction: Nine lunar localities where sampled during the Apollo and Luna missions. Regolith compositions from those areas were analysed, permitting ground-truth validation for remote-sensing instruments [1-4]. However, the Apollo and Luna missions were very restricted geographically and so do not provide information about the whole Moon.

Lunar meteorites are material ejected from random localities on the Moon in the last 20 million years, the vast majority in the last 10 million years [5]. They originated from small shallow impact craters (less than few km in size) and, therefore, they are sample from the upper part of the lunar surface [6,7]. Lunar meteorites are classified broadly into 3 groups: Impact melt breccias, crystalline mare basalts and regolith breccias [8-10].

Our project aims to use remote sensing datasets to locate the source regions of lunar meteorites so we can better place them into a geological context. Secondary goals are to understand the evolution of the lunar crust and mantle and shed light on the geology of the regions not sampled by the Apollo and Luna missions.

Adapting a method previously applied to lunar meteorites [11,12], we have developed a software application based on Python Programming language that matches input meteorite elemental compositions with the 2 degree per pixel (i.e., 60 km per pixel) LP-Gamma Ray Spectrometer (LP-GRS) dataset, including analytical standard deviations and errors derived from the remote-sensing instrument. The Python application is compatible with ArcGISTM and produces a shapefile layer that allows for convenient visualization of the results.

Apollo and Luna validation: We validated our approach by comparing the compositions of the Apollo and Luna bulk regolith samples [13-19] with the elemental abundance of FeO, TiO₂ and Th reported by LP-GRS. FeO was selected to discriminate between feldspathic and basaltic lithologies, TiO₂ allows us to distinguish different types of basalts, and Th is sensitive to KREEP-bearing materials. We do not include the Mg concentration in our approach due to the poor compositional resolution of the LP-GRS instrument for that element.

We obtain good correlations for most of the landing sites (Figure 1). However, there are small discrepancies related to the spatial resolution of the instrument: our dataset covers a region of 60 km per pixel and therefore heterogeneities in the area, and

the fact that the samples were taken from a much smaller area, may affect our results. In the case of the Apollo 14 landing site, the average Th compositions are larger than those reported in the LP-GRS dataset so we did not obtain any matching results.

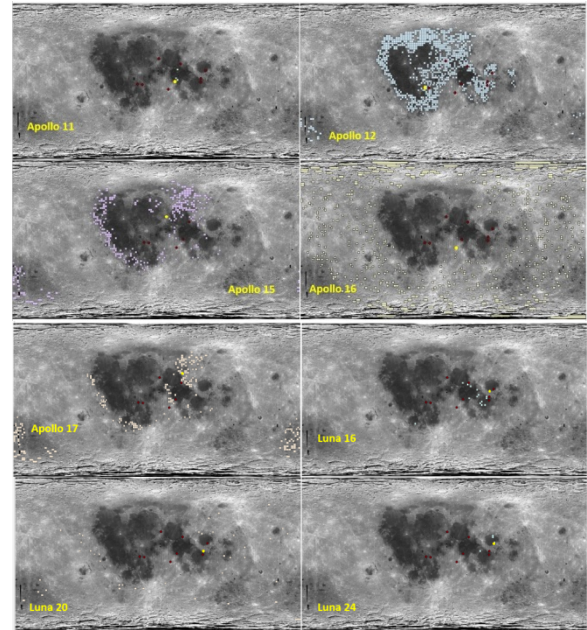


Figure 1: The coloured squares shows the results obtained during our validation exercise. Yellow points designate the landing sites points.

Lunar meteorite results: Previous work has attempted to locate the launch site of certain meteorites [8,11,12,20,21], however this is the first time that this exercise has been done in a systematic manner for all of the meteorites with reported bulk compositions. We create a dataset with the bulk element composition of 85 meteorites and for each of these we calculated the analytical standard deviation of averaged measurements. Some examples are described below:

Impact melt breccia. Dhofar 489 (Dho 489) is a feldspathic impact melt breccia that includes clasts of magnesian anorthosite (MAN). The low-Fe and Th content and the high-#Mg have suggested they may derive from the Anorthositic Feldspathic Highland Terrain (FHT) on the lunar central far side [22-24]. However, based on Fe, Ti and Th content, our software also returns matches on the nearside Outer FHT terrain (Figure 2a).

Crystalline basalt. LaPaz Icefield 02205 (LAP 02205) is a crystalline basalt with low Ti content [25-27]. Our results show mainly two regions as

possible source regions: the Serenitatis Basin and the western area of Oceanus Procellarum (Figure 2b). Studies indicate that this meteorite crystallised at ~ 3 Ga [28] enabling us to restrict its launch site to lava flows in the western Oceanus Procellarum where lavas of this age outcrop.

Incompatible trace element (ITE)- rich mingled regolith breccia. Northwest Africa 4472 (NWA 4472) is a regolith breccia with high content on KREEP elements such as Th (up to 7 ppm) [8,12]. It is thought to be part of Imbrium ejecta deposits both from composition and age (3.92 Ga). Our approach return Mare Frigoris or the surroundings of Mons Caucasus as probably launch sites for this meteorite (Figure 2c).

Basaltic mingled regolith breccia. Calalong Creek is a basaltic-bearing anorthositic regolith breccia [29]. Our results show that the western boundary of Oceanus Procellarum and the eastern area of Mare Frigoris should be considered as possible source regions (Figure 2d). This meteorite had been hypothesized to originate from the South Pole-Aitken impact basin [30] so our results shed doubt on this previous hypothesis.

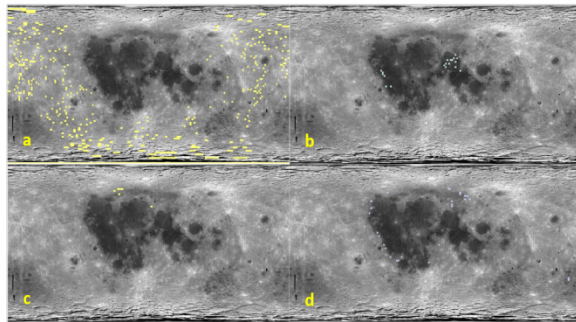


Figure 2: Image showing the places where the analytical FeO, TiO₂ and Th compositions matches the regolith measurements reported by LP-GRS (coloured squares). Meteorites plotter are: a Dho 489; b LAP 02205; c NWA 4472 and d Calalong Creek.

Discussion: Although we have successfully validate our approach against the Apollo localities, several additional factors should be taken into account: the spatial resolution and the measurement uncertainty in the remote sensing data.

The spatial resolution of the LP-GRS dataset used in this work is 2 degrees (i.e., 60 km per pixel). It was chosen due to a combination of an adequate compositional accuracy and an acceptable spatial resolution. Nonetheless, geologically, terrain varies significantly across 60 km, and samples of lunar material are collected or launched from a discrete point, which may lead to some of the small discrepancies seen in our results.

Measurement uncertainties of the LP-GRS instrument also limits the use of some elements such as Mg. Enhanced maps with minimised errors will

allow us to include more elements and improve the results.

Future work: The next step will be to integrate chronology where possible, as well as explore other remote-sensing datasets for better constrain the results.

References: [1] Gillis, J.J., Jolliff, B.L. & Korotev, R.L. (2004). *Geochimica et Cosmochimica Acta*, 68(18), pp.3791–3805. [2] Isaacson, P.J. et al.(2013). *Journal of Geophysical Research: Planets*, 118(3), pp.369–381. [3] McEwen, A.S. & Robinson, M.S. (1997). *Advances in Space Research*, 19(10), pp.1523–1533. [4] Pieters, C.M. et al. (2008). [5] Korotev, R.L. (2005). *Chemie der Erde*, 56, pp. 297-346. [6] Warren P.H. (1994). *Icarus*, 111, pp. 338-363. [7] Basilevsky A.T., Neukum G. & Nyquist L. (2010), *Planetary & Space Science*, 58(14-15), pp. 1900-1905. [8] Korotev, R.L. et al. (2009). *Meteoritics & Planetary Science*, 1322(9), pp.1287–1322. [9] Mercer, C.N., Treiman, A.H. & Joy, K.H. (2013). *Meteoritics & Planetary Science*, 48(2), pp.289–315. [10] Joy, K.H. & Arai, T. (2013). *Astronomy & Geophysics*, 54(4), pp.4–28. [11] Joy, K.H. et al. (2010). *Meteoritics & Planetary Science*, 45(6), pp.917–946. [12] Joy, K., et al. (2011). *Geochimica et Cosmochimica Acta*, 75(9), pp.2420–2452. [13] Morris, R. V et al. (1983). *Handbook of lunar soils*. [14] Rhodes, J.M. & Blanchard, D.P. (1981). *Proceedings Lunar Planetary Science*, 12(B), pp.607–620. [15] McKay, G., Wagstaff, J. & Yang, S.-R. (1986). *Journal of Geophysical Research*, 91(B4), pp.229–237. [16] Korotev, R.L. (1997). *Meteoritics & Planetary Science*, 32, pp.447–478. [17] Simon, S.B. et al. (1985). *Journal of Geophysical Research*, 90(Supplement), pp.D75–D86. [18] Jerde, E.A. et al. (1987). *Journal of Geophysical Research*, 92(B4). [19] Jerde, E.A., Morris, R. V. & Warren, P.H. (1990). *Earth and Planetary Science Letters*, 98(1), pp.90–108. [20] Kuehner, S.M. et al. (2007). *Lunar and Planetary Science XXXVIII*. [21] Arai, T. et al. (2010). *Geochimica et Cosmochimica Acta*, 74(7), pp.2231–2248. [22] Korotev, R.L., Zeigler, R.A. & Jolliff B.L. (2006). *Geochimica et Cosmochimica Acta*, 70, pp.5935–5956. [23] Takeda H. et al. (2006), *Earth and Planetary Science Letter*, 247, pp.171-184. [24] Demidova S.I. et al (2007) *Petrology*, 15(4), pp.416-437. [25] Zeigler, R.A. et al (2005). *Meteoritics & Planetary Science*, 40(7), pp.1073-1101. [26] Righter K., Collins S.J. & Brandon A.D. (2005), *Meteoritics & Planetary Science*, 40(11), pp. 1903-1722. [27] Anand M. et al (2006), *Geochimica et Cosmochimica Acta*, 70, pp. 246-264. [28] Fernandes V.A., Burgess R. & Morris A. (2009) *Meteoritics & Planetary Science*, 44(6), pp.805-821. [29] Hill D.H. & Boynton W.V. (2003) *Meteoritics & Planetary Science*, 38(4), pp. 595-626. [30] Corrigan C.M. et al. (2009) 72nd Annual Meteoritical Society Meeting. Abstract #5375.

THE EXTREME THERMAL, THERMOPHYSICAL, AND COMPOSITIONAL NATURE OF THE MOON REVEALED BY THE DIVINER LUNAR RADIOMETER. B. T. Greenhagen¹, D. A. Paige², E. Sefton-Nash², N. E. Bowles³, the Diviner Science Team ¹Jet Propulsion Laboratory, California Institute of Technology, Pasadena, CA, USA, ²Dept. of Earth, Planetary, and Space Sciences, University of California, Los Angeles, CA, USA, ³Atmospheric, Oceanic, and Planetary Physics, University of Oxford, Oxford, UK (Benjmain.T.Greenhagen@jpl.nasa.gov).

Introduction: After nearly five years in operation, and well into its extended science mission, the Diviner Lunar Radiometer has revealed the extreme nature of the Moon's thermal environments, thermophysical properties, and surface composition. This presentation will highlight contributions from members of the Diviner Science Team addressing a diverse range of scientific questions from the extended science mission.

Diviner Lunar Radiometer: The Diviner Lunar Radiometer is a nine-channel, pushbroom mapping radiometer that was launched onboard the Lunar Reconnaissance Orbiter in June 2009. Diviner measures broadband reflected solar radiation with two channels, and emitted thermal infrared radiation with seven infrared channels [1]. Generally, the three shortest wavelength, narrowband thermal infrared channels near 8 μm are used to constrain surface composition [2] and the four longer wavelength, broadband channels that span the mid- to far-infrared between 13 and 400 μm and are used to characterize the lunar thermal environment and thermophysical properties [3,4].

Diviner is the first multispectral thermal instrument to globally map the surface of the Moon. To date, Diviner has acquired observations over nine complete diurnal cycles and five partial seasonal cycles (the local time of day processes slowly relative to seasons such that Diviner is typically near a noon-midnight orbit around solstices). Diviner daytime and nighttime observations (12 hour time bins) have essentially global coverage, and more than 80% of the surface has been measured with at least 6 different local times.

The spatial resolution during the mapping orbit was ~ 200 m and now ranges from 150 m to 1300 m in the current elliptical "frozen" orbit. Calibrated Diviner data and global maps of visible brightness temperature, bolometric temperature, rock abundance, nighttime soil temperature, and silicate mineralogy are available through the Planetary Data System (PDS) Geosciences Node.

Diviner Foundation Dataset: A major effort during the extended science mission has been to create a "Foundation Dataset" (FDS) to improve the quality and usability of Diviner data available in PDS. To improve the radiometric accuracy, we reexamined Diviner's pre-flight ground calibration and revised the in-flight calibration methodology [5]. Diviner level 1b activity and quality flags have been modified based on critical reviews from Diviner data users. Finally, we used the new level 1 data to produce a wide range of level 2 and 3 gridded datasets that are more accurate, better organized, and include important geometric and observational backplanes [e.g. 6]. Delivery of the Diviner FDS to PDS is expected to begin in 2014.

Thermal Environments: Diviner was designed to accurately measure temperatures across a broad temperature range [1] from midday equatorial regions such as the Apollo landing around 400K, typical nighttime temperatures of less than 100K at night [3], and extreme permanent shadowed regions colder than 50K (Figure1) [5, 7]. The coldest multiply-shadowed polar craters may have temperatures low enough to put constraints on lunar heat flow. Diviner data have also been used to estimate the thermal properties of non-polar permanently shadowed regions [8].

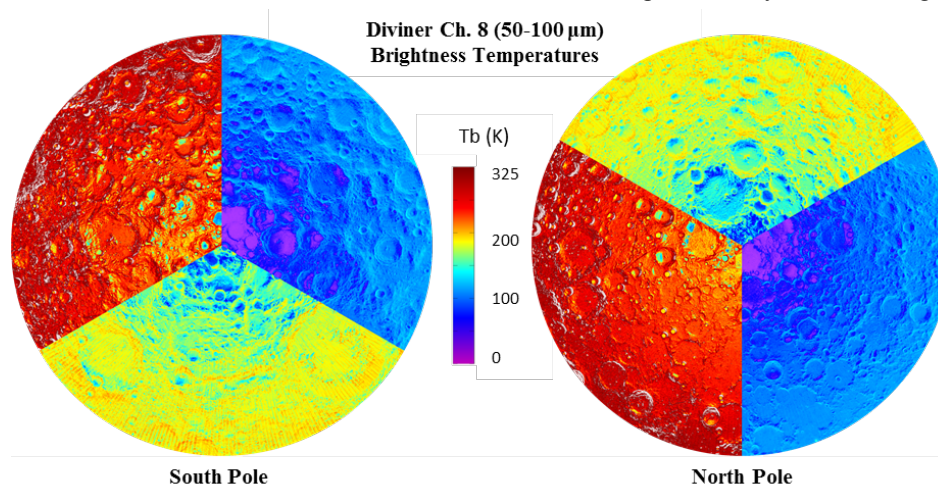


Figure 1: The temperature maps above (pole to 70 degrees) demonstrate the extreme thermal environment of the Moon. Minimum observed Tb are shown 0E to 120 E, average Tb 120E to 240E, maximum Tb 240E to 360E.

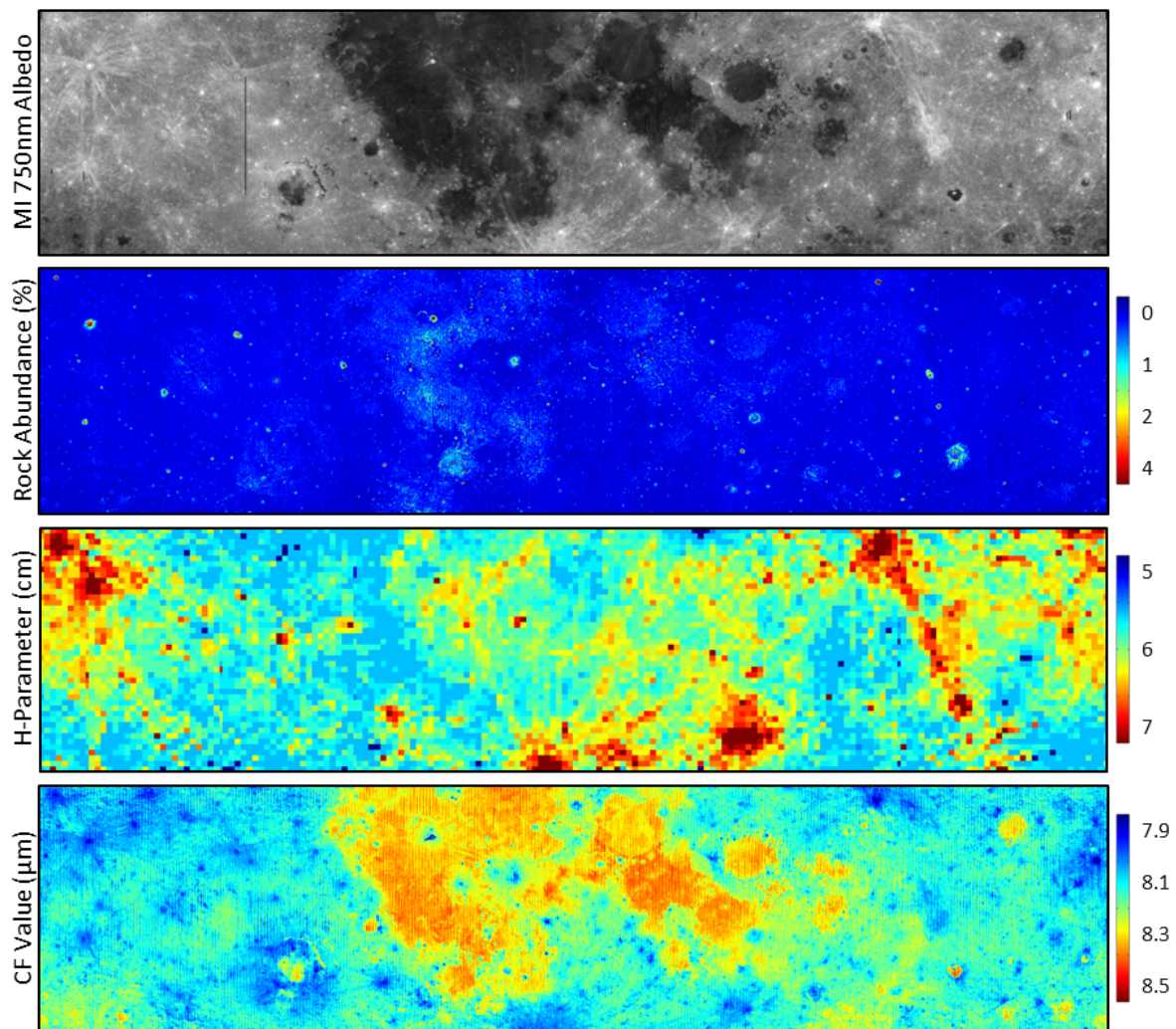


Figure 2: Diviner maps of rock abundance, H-parameter (regolith insulating layer), and Christiansen Feature value. Rock abundance and CF maps are from PDS. SELENE Multiband Imager 750 nm albedo map provided for context.

Thermophysical Properties: Diviner is directly sensitive to the thermophysical properties of the lunar surface including nighttime soil temperature, rock abundance, and surface roughness (Figure 2) [3,4]. During the extended science mission we have produced higher fidelity maps of these properties and used them to investigate anomalous rock abundances [9], “cold spots” with fluffier surface layers [10], regolith formation and evolution [11], and surface roughness [12].

Surface Composition: Diviner was designed to characterize the Christiansen Feature (CF) and constrain lunar silicate mineralogy (Figure 2) [2]. Recent efforts in this area have focused on improving the quality of Diviner’s mid-infrared “photometric” correction, groundtruthing Diviner observations to Apollo soils [13], using Diviner’s longer wavelength channels to improve constraints on olivine [14], and combining Diviner with visible and near-infrared datasets to enhance interpretations of pyroclastic deposits [15], plagioclase-rich regions

[16], high silica regions [17], and space weathering [18].

References: [1] Paige D.A. et al. (2010) SSR, 150. [2] Greenhagen B.T. et al. (2010) Science, 329, 1507. [3] Vasavada A.R. et al. (2012) JGR, 117. [4] Bandfield J.L. et al. (2011) JGR, 116. [5] Aye K.-M. et al. (2013) LPSC XLIV #3016. [6] Sefton-Nash E. et al. (2014) LPSC XLV #2737. [7] Paige D.A. et al. (2010) Science, 330, 479. [8] McGovern J.A. et al. (2013) Icarus, 223, 566. [9] Greenhagen B.T. et al. (2013) LPSC XLIV #2987. [10] Bandfield J.L. et al. (2013) Icarus, submitted. [11] Hayne P.O. et al. (2013) LPSC XLIV #3003. [12] Bandfield J.L. et al. (2014) LPSC XLV #1519. [13] Greenhagen B.T. et al. (2012) AGU Fall Meeting, #P42A-04. [14] Arnold J.A. et al. (2013) LPSC XLIV #2972. [15] Allen C.C. et al. (2013) LPSC XLIV #1220. [16] Donaldson Hanna K.L. et al. (2013) JGR, submitted. [17] Ashley J.W. et al. (2013) LPSC XLIV #2504. [18] Lucey P.G. et al. (2013) LPSC XLIV #2890.

INVESTIGATION OF THE PLASMA-SURFACE INTERACTION ON THE RUSSIAN LUNA-25/26/27 MISSIONS. S. Barabash¹, Y. Futaana¹, M. Wieser¹, A. Grigoriev², A. Shestakov², O. Vaisberg², W. Schmidt³, E. Kallio³, K. Szego⁴, S. Szalai⁴, P. Wurz⁵, M. Collier⁶, T. Zhang⁷, K. Asamura⁸ ¹Swedish Institute of Space Physics, Box 812, SE-98128 Kiruna, Sweden, ²Space Research Institute, 117997, Profsoyuznaya 84/32, Moscow, Russia, ³Finnish Meteorological Institute, Box 503 FIN-00101 Helsinki, Finland, ⁴Institute for Particle and Nuclear Physics, Wigner Research Centre for Physics, Konkoly Thege Miklós út 29-33, H-1121 Budapest, Hungary, ⁵Physikalisches Institut, University of Bern, Sidlerstrasse 5, CH-3012 Bern, Switzerland, ⁶Code 612.2 - Heliospheric Physics, NASA/Goddard Space Flight Center, Greenbelt, Maryland 20771, ⁷Space Research Institute, Schmiedlstraße 6, 8042 Graz, Austria and Univ. of Science and Technology of China, Hefei, China, ⁸Institute of Space and Astronautical Science, 3-1-1 Yoshinodai, Sagami-hara, Japan (stas@irf.se)

Introduction: The Moon does not possess a global magnetic field and collisional atmosphere but only a surface –bound tenuous exosphere. The lunar surface is thus exposed to the solar wind. The interaction of the solar wind particles with the lunar regolith is by far more complex process than simple absorption [1]. The backscattering of the solar wind particles results in the production of fast neutrals (energetic neutral atoms, ENA), protons, and possibly even negative ions. Sputtering of the regolith materials results in the release of few eV atoms. All these particles carry information on the microphysics of the interaction [2], which is important for understanding the implantation processes and protolysis of the regolith materials to water.

Roscosmos (Russia) is currently preparing 3 three missions to the Moon Luna-Glob-lander/Luna-25 (2016), Luna-Resource-orbiter/Luna-26 (2018), and Luna-Resource-lander/Luna-27 (2019). The missions will carry instrumentation for the ENA detection on the surface and from orbit as well an ion and electron analyzer for studies near-surface plasma developed at the Swedish Institute of Space Physics, (IRF-Kiruna) in the close cooperation with groups from Russia, Europe, US, Japan, and China (see the affiliation list).

Configuration: Luna-25 will carry a single-pixel ENA detector XSAN (eXtra Small Analyzer of Neutrals, contribution under consideration). A large geometrical factor high angular resolution Lunar

Neutrals Telescope (LNT) will fly onboard Luna-26. Luna-27 will carry the package LINA (Lunar Ions and Neutrals Analyzer) including XSAN and a combined ions and electron analyzer LPA (Lunar Plasma Analyzer). LINA-XSAN is accommodated on a scanning platform to allow pointing to different surface areas.

Instrument description: XSAN is based on the miniature ion analyzer developed and built at IRF-Kiruna for such missions as Chandrayaan-1 [3], BepiColombo [4], Phobos-Grunt, Yinghuo, PRISMA. The analyzer entrance is equipped with an effective neutral-to-positive-ion converter and a charge particle deflector. LNT is the following-on of the CENA (Chandrayaan-1 Energetic Neutrals Analyzer) instrument built by IRF-Kiruna for the Indian Chandrayaan-1 mission [3]. It is this instrument discovered the strong ENA emissions from the lunar surface [1]. The CENA ion optics is further optimized to increase geometrical factor and angular resolution. LPA is a new development, using the ion – surface interaction for the ion mass identification. The performance of these three instruments is summed below.

References: [1] Wieser M. et al. (2009), *Planet. Space Sci.*, 57, 2132–2134, [2] Wieser M. et al. (2010) *Geophys. Res. Lett.*, 37 (5), doi:10.1029/2009GL041721. [3] Barabash S. et al. (2009) *Current Science*, 96, 526–532. [4] McComas D. J. et al. (2009) *Geophys. Res. Lett.*, 36, doi:10.1029/2009GL038794.

| Parameter | XSAN | LNT | LINA-LPA |
|-------------------------------|---|---|---|
| Measured particles | ENA, ion ⁺ | ENA | ion ⁺ , ion ⁻ , el ⁻ |
| Energy range | 10 eV – 15 keV | 10 eV – 3.3 keV | 1 eV – 40 keV |
| Resolution, $\Delta E/E$ | 15-20% (ENA), 7% (i) | 50% | 12% |
| Mass range, amu | 1 - >16 | 1 - 60 | 1 - 70 |
| Mass resolution, $\Delta M/M$ | 2 ($M = 1, 2, 4, 8, >16$) | H, O, Na/Mg-,K/Ca-group, Fe | 2 and 30 (2 channels) |
| FoV | 15° x 30° | 15° x 20° | 90° x 360° (< 25 keV) |
| Ang. pixel | 10° x 15° ^a | 5° x 5° ^a | 5.5° x 19.5° ^a |
| G-factor | 5·10 ⁻² cm ² sr eV/eV | 1.5·10 ⁻¹ cm ² sr eV/eV | 6·10 ⁻⁴ cm ² sr eV/eV (pixel) |
| Instrument mass | 650 g | 3.8 kg | 3.8 kg (inc. XSAN) |
| Total power, W | < 3W | < 12 W | < 16 W |

^aFull Width at half Max (FWHM)

Introduction: Radiation protection is one of the two NASA highest concerns priorities [1]. In view of manned missions targeted to the Moon [2], for which radiation exposure is one of the greatest challenges to be tackled [3], it is of paramount importance to be able to determine radiation fluxes and doses at any time on, above and below the lunar surface [4]. With this goal in mind, models of radiation environment due to Galactic Cosmic Rays (GCR) and Solar Particle Events (SPE) on the Moon have been developed, and fluxes and spectra hereby computed [5]. The work is described [6] as models of incoming cosmic ray [7-9] and solar primary particles [6] impinging on the lunar surface, transported through the subsurface layers, with backscattering taken into account, and interacting with some targets described as material layers. Time dependent models for incoming particles for both GCR and SPE are those used in previous analyses as well as in NASA radiation analysis engineering applications [10]. The lunar surface and subsurface has been modeled as regolith and bedrock, with structure and composition taken from the results of the instruments of the Luna, Ranger, Lunar Surveyor and Apollo missions, as well as from groundbased radiophysical measurements (see discussion in [4-6], [10]). The lunar-like atmosphereless body surface models are used to develop models for the surfaces of Martian satellite Phobos [11]. Also the radiation environment for the transit phase from the Earth to the Moon have been modeled. These results for the Moon Radiation Environment as well as for the cruise phase have been obtained in the framework of the RADOM investigation that is onboard the CHANDRAYAAN-1 mission by the Indian Space Agency ISRO. The RADOM investigation and preliminary results are described in another LPSC 2009 paper by Ts.P. Dachev.

Results - Moon: In order to compare results from different transport techniques, particle transport computations have been performed with both deterministic (HZETRN) [12] and Monte Carlo (FLUKA) [13] codes with adaptations for planetary surfaces geometry for the soil composition and structure of the Apollo 12 Oceanus Procellarum landing site [14,15], with a good agreement between the results from the two techniques [6,10]: GCR-induced backscattered neutrons are present at least up to a depth of 5 m in the regolith, whereas after 80 cm depth within regolith there are no neutrons due to SPE [6,10]. Moreover, fluxes, spectra, LET and doses for many kinds of particles, namely protons, neutrons, alpha particles, heavy ions, pions, muons etc., for various other lunar soil and rock compositions have been obtained with the

deterministic particle transport technique (see Fig. 1 and 2) [6]. Results have in particular been obtained for orbital scenarios, for surface (i.e. landers, habitats and rover) scenarios, for subsurface scenarios, and for lunar polar locations, with regards to ways to infer and detect locally the presence of water and/or volatiles. The results from this work can only be compared in literature with previous versions of the same models or with very simplistic models [4-6,10], as also mentioned in [16]. These models have been then rescaled to be tested against spacecraft instruments data (e.g. RADOM onboard the CHANDRAYAAN-1 spacecraft from ISRO). The models have been set to a 100 km altitude circular orbit, to the actual mission time frame (both punctual and averaged data), and to the actual environmental shielding inside the spacecraft. The detailed comparison between models and data is currently underway, along with better trajectory analyses. As a preliminary comparison, RADOM data at 100 km altitude around the Moon give a mean flux for 100 MeV protons of 2.29 particles/cm².sec with a mean dose of 8.77 μ Gy/h. If for the comparison the above model is used, rescaled for CHANDRAYAAN-1 orbital conditions, with a shielding pattern of 0.45 g/cm² on the 2π solid angle before the detector and more shielding (10 g/cm²) on the other 2π solid angle at the back side of the detector, a value for 100 MeV protons of 2.55 particles/cm².sec is this way obtained.

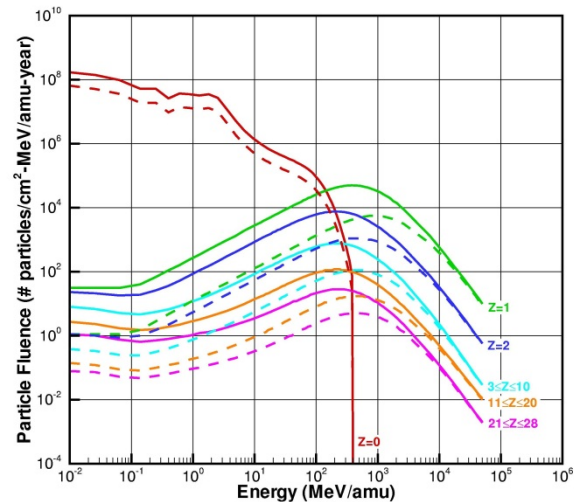


Figure 1: GCR particle environment during the 1977 solar minimum (full lines) and the 1990 solar maximum (dashed lines) at an altitude of 100 km above the lunar surface (results from the deterministic technique).

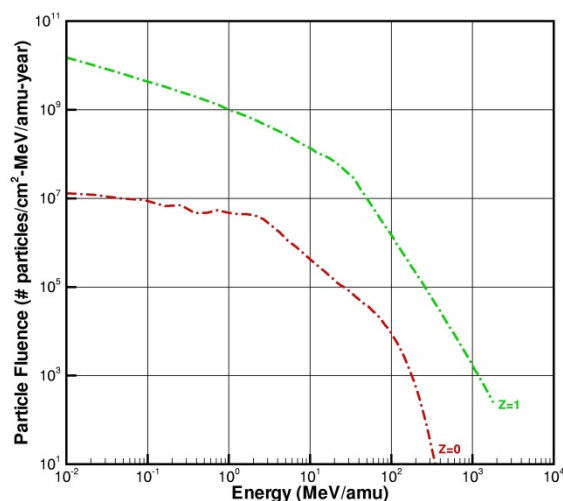


Figure 2: The radiation environment at 100 km altitude from the lunar surface due to the September 1989 SPE (results from the deterministic technique).

Results – Cruise Phase: A tool for radiation shielding analysis developed for manned deep space missions [17] has been used. The tool allows obtaining radiation dose and dose rates for different interplanetary mission scenarios, composed of at least one out of three main segments, namely the launch and the interplanetary cruise phase, the planetary approach /departure and orbit insertion/escape phase, and the planetary surface phase. For each individual phase the respective radiation environment is taken into account, along with its variations with time. Only Galactic Cosmic Rays (GCR) and Solar Particle Events (SPE) are considered during the interplanetary cruise phase, trapped radiation belts, where present, are also considered in the planetary approach phase, and the planetary environments (atmospheres, where present, and surfaces) effects are taken into account in the third phase. Some examples of analysis results for space missions are given in [18].

Conclusions: Models for the radiation environment to be found on the Moon (on, above and below the surface) due to GCR, SPE and backscattering effects have been developed. A good agreement has been found between results from deterministic and Monte

Carlo transport techniques. The quite large differences in the time and effort involved between the deterministic and Monte Carlo approaches deeply favor the use of the deterministic approach in computations for scientific and technological space radiation analysis. This approach looks promising for comparisons studies with spacecraft data. These models are being tested with the data from RADOM experiment onboard the CHANDRAYAAN-1 spacecraft.

Model Improvements: The model has been updated by using a new lunar topography model

obtained from data of the NASA LRO spacecraft, obtained from stereo imagery and laser altimetry data, with a spatial resolution of the order of 100 m and an altitude resolution of about 20 m or better. This new dataset provides a way of obtaining a much finer grid for radiation patterns which allows more detailed analyses and evaluations. Values for various kinds of doses have been obtained for mission scenarios and shielding patterns above, on and below the Moon surface.

References: [1] O’Keefe, S. (2002)

<http://www.spaceflightnow.com/news/n0203/27okeefe> [2] Duke M.B. et al. (2003) NASA TP2003-212053. [3] Cucinotta F.A. et al. (2001) *Radiat. Res.*, 156, 682-688. [4] De Angelis G. et al. (2002) *J. Radiat. Res.*, 43, 41-45. [5] De Angelis G. et al. (2002) *Proc.Lunar Plan. Sci. Conf. XXXIII*, pp. 1417-1418. [6] De Angelis G. et al. (2007) *Nucl.Phys. B*, 166, 169-183. [7] Badhwar G. D. et al. (1994) *Radiat. Res.*, 138, 201-208. [8] Badhwar G. D. and O’Neill P. M. (1996) *Adv. Space Res.*, 17, 7-17. [9] Wilson J. W. et al. (1999) NASA TP-209369. [10] De Angelis G. et al. (2005) *SAE-2005-01-2831*, pp. 1-11. [11] De Angelis G. et al. (2007) *Nucl.Phys. B*, 166, 184-202. [12] Wilson J. W. et al. (1995) NASA TP-3495. [13] Fassò A. et al. (1993), *Nuc. Instr. & Meth. Phys. Res., A*, **332**, 459-470. [14] ‘Apollo 12 Preliminary Science Report’ (1970) NASA SP-235. [15] Warner J. (1970) ‘Apollo 12 Lunar Sample Information’, NASA TRR-353. [16] ‘Space Radiation Hazards and the Vision for Space Exploration: Report of a Workshop’ (2006) SSB, NCR. [17] De Angelis G. et al. (2003) *Proc. Space Technol. Appl. Int. Forum ‘STAIF-2003’*, pp. 972-983. [18] De Angelis G. et al. (2004) *Adv. Space Res.*, 34, 1395-1403.

THE MOON AS A LASER-RANGED TEST BODY FOR GENERAL RELATIVITY AND NEW GRAVITATIONAL PHYSICS. S. Dell’Agnello¹, D. Currie² ¹INFN – Laboratori Nazionali di Frascati (LNF), Via E. Fermi 40, Frascati (Rome) 00046, Italy (simone.dellagnello@lnf.infn.it) ²University of Maryland, John S. Toll Building, Regents Drive, College Park, MD 20742-4111, USA (currie@umd.edu).

Introduction: Since the 1970s Lunar Laser Ranging (LLR) to the Apollo/Lunokhod Cube Corner Retroreflector (CCR) Arrays [1] supplied some of the best tests of General Relativity (GR): possible changes in the gravitational constant, gravitational self-energy (PPN parameter beta), weak and strong equivalence principle, geodetic precession, inverse-square force-law. Secondly, LLR has provided significant information on the composition of the deep interior of the Moon. LLR physics analysis also allows to set constraints on extensions of GR (like spacetime torsion) and, possibly, on new gravitational physics which may explain the gravitational universe without Dark Matter and Dark Energy (like, for example, Non-Minimally Coupled gravity, NMC). LLR is the only Apollo/Lunokhod experiment still in operation, since 45 years. In the 1970s Apollo/Lunokhod LLR Arrays contributed a negligible fraction of the ranging error budget. Since the ranging capabilities of ground stations of the International Laser Ranging Service (ILRS [2]) improved by more than two orders of magnitude, now, because of the lunar librations, Apollo/Lunokhod CCR arrays dominate the error budget. With the US/Italy project “LLRRA21/MoonLIGHT (Lunar Laser Ranging Retroreflector Array for the 21st century / Moon Laser Instrumentation for General relativity High accuracy Tests)”, University of Maryland and INFN-LNF developed and tested a next-generation LLR payload made by a single, large CCR (100 mm diameter), unaffected by the effect of librations [3] [4] [5]. In fact, we will show that MoonLIGHT reflectors will improve the LLR accuracy by a factor of ten to one hundred in a few years. INFN-LNF also developed a laser retroreflector micropayload to be deployed on the lunar surface to be laser-ranged by lunar orbiters. The latter micropayload will further extend the physics reach of Apollo, Lunokhod and MoonLIGHT CCRs to improve all precision tests of GR and new gravitational physics using LLR data. As an added value for the LLR and SLR (Satellite Laser ranging) disciplines INFN-LNF built and is operating a unique ground infrastructure, the SCF_Lab (Satellite/lunar/GNSS laser ranging and altimetry Characterization Facilities Laboratory) and created a new industry-standard test procedure (SCF-Test) to characterize and model the detailed thermal behavior and the optical performance of CCRs in accurately laboratory-simulated space conditions for science (like LLR) and for industrial applications (for example to the Galileo and Copernicus European flagship space programs, as well as for

other GNSS constellations) [6]. Our key experimental innovation is the concurrent measurement and modeling of the optical Far Field Diffraction Pattern (FFDP), Wavefront Fizeau Interferometry (WFI) and the temperature distribution of laser retroreflector payloads under thermal conditions produced with up to two close-match AM0 solar simulators. The SCF-Lab includes infrared cameras for non-invasive thermometry, thermal control and real-time payload movement to simulate satellite orientation on orbit with respect to solar illumination and laser interrogation beams. These capabilities provide: unique pre-launch performance validation of the space segment of LLR/SLR; retroreflector design optimization to maximize ranging efficiency and signal-to-noise conditions in daylight. Negotiations are underway to propose the LLRRA21/MoonLIGHT payload and SCF-Test services for precision gravity and lunar science measurements with next robotic lunar landing missions. The latter include the 2019 LUNA-27 mission of the Russian lunar program, also in the framework of the ESA-ROSCOSMOS-IKI partnership (see also <http://congrexprojects.com/2014-events/14c05a/introduction>). Results on analysis of Apollo LLR data and search of new gravitational physics with LLR, Mercury Radar Ranging, SLR of LAGEOS (Laser GEodynamics Satellite) will also be presented [7] [8].

References: [1] Alley, C. O.; Chang, R. F.; Currie, D. G.; Mullendore, J.; Poultney, S. K.; Rayner, J. D.; Silverberg, E. C.; Steggerda, C. A.; Plotkin, H. H.; Williams, W.; Warner, B.; Richardson, H.; Bopp, B., *Science*, Volume 167, Issue 3917, pp. 368-370 01/1970. [2] Pearlman, M. R., Degnan, J. J. and Bosworth, J. M. (2002), *Advances in Space Research*, 30, 135-143. [3] D. Currie, S. Dell’Agnello, G. Delle Monache, *Acta Astron.* 68, 667– 680 (2011). [4] S. Dell’Agnello et al., *Planetary and Space Science* 74 (2012) 276–282. [5] S. Dell’Agnello et al, Phase A Study for ASI’s Call for Small Missions, *Exp. Astron.* (2011) 32:19–35, DOI 10.1007/s10686-010-9195-0 (2010). [6]. S. Dell’Agnello et al, *Advances in Space Research*, 47, Issue 5, 1 March 2011, 822–842. [7] R. March, G. Bellettini, R. Tauraso, S. Dell’Agnello, *Phys. Rev D* 83, 104008 (2011). [8] R. March, G. Bellettini, R. Tauraso, S. Dell’Agnello, *Gen Relativ Gravit* (2011), 43:3099–3126 DOI 10.1007/s10714-011-1226-2.

TELEROBOTIC EXPLORATION AND RADIO ASTROPHYSICS FROM THE FAR SIDE OF THE MOON. G. J. A. Harker¹, J. O. Burns², ¹Marie Curie Fellow, Dept. of Physics and Astronomy, University College London, UK (g.harker@ucl.ac.uk), ²Center for Astrophysics and Space Astronomy, University of Colorado Boulder, USA (jack.burns@colorado.edu).

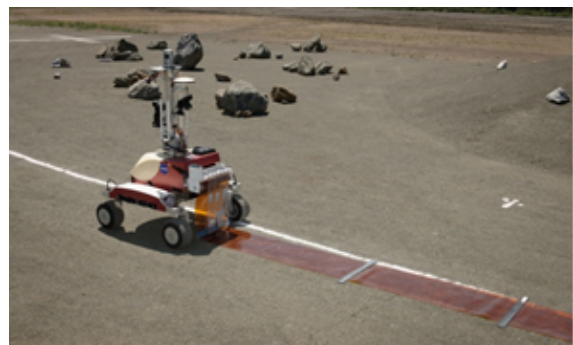
Introduction: Earth-Moon libration points provide both an avenue to develop expertise needed for longer-duration missions and a platform to help discover answers to critical scientific questions concerning the origin and evolution of our solar system and the first stars and galaxies [1]. In the latter case this could build on low-frequency radio observations of the early Universe made by a satellite in a low lunar orbit [2].

An Orion L2 Farside Mission: We have defined two primary science objectives for such a mission. The first would be to return to Earth multiple rock samples from the South Pole – Aitken (SPA) basin. A sample return from SPA was designated as a priority science objective in the US National Research Council (NRC) Planetary Sciences Decadal Survey. The second objective would be to deploy a low radio frequency telescope, where it would be shielded from human-generated radio-frequency interference (RFI) from the Earth and free from ionospheric effects, allowing us to explore currently unobserved primitive epochs of the early Universe. Such observations were recently identified as one of the top science objectives in the NASA Astrophysics Roadmap.



Rover tests. To demonstrate the feasibility of such a mission, we have recently conducted the first surface telerobotics engineering tests using the K-10 rover at the NASA Ames Roverscape under the command of astronauts aboard the ISS. During three 3.5-hr ISS crew sessions in the summer of 2013, Kapton film strips were successfully unrolled from the back of the K-10 rover (see photo). These ISS crew sessions achieved a number of ‘firsts’, including the first real-time teleoperation of a planetary rover from the ISS, the first astronaut to interactively control a high-fidelity planetary rover in an outdoor analogue testbed, and the first realistic simulation of a hum-robot ‘Waypoint’ mission concept.

The Dark Ages Radio Explorer (DARE): We are proposing to build a sensitive, low-frequency radiometer to detect the collective signal from the Universe’s hydrogen during the epoch in which the first stars, galaxies and black holes formed. This would make use of the pristine radio environment (while above the far side) and lack of ionosphere in low lunar orbit without requiring equipment on the lunar surface or permanently stationed above the farside, and hence represents the best (perhaps only) chance to study this crucial epoch in the next few years.



Ground-based prototype. A field test of the *DARE* system (antenna, receiver) was deployed in Green Bank, WV at the end of February (see picture), and is being used to gather data on the ionosphere and RFI environment, and to constrain the foregrounds which present the main challenge for a lunar farside measurement. This also allows us to develop and test a novel calibration approach, which is needed to reach the extreme dynamic range required to detect the faint cosmological signal in the presence of bright, nearby, astrophysical foregrounds.

References: [1] Burns, J. O., Kring, D.A., Hopkins, J. B., Norris, S., Lazio, T. J. W. and Kasper, J. (2013) *Adv. Space Res.*, 52, 306-320. [2] Burns, J. O., Lazio, T. J. W., Bale, S., Bowman, J., Bradley, R., Carilli, C., Furlanetto, S., Harker, G. J. A., Loeb, A. and Pritchard, J. R. (2012) *Adv. Space Res.*, 49, 1070-1084.

A SELF-CONSISTENT DEMONSTRATION OF HOW THE LUNAR CRUSTAL MAGNETIC ANOMALIES PRODUCE MINI-MAGNETOSPHERES. R. A. Bamford¹, A. P. Alves², B. Kellett¹, L. Silva², R. Bingham³ ¹RAL Space, Rutherford Appleton Laboratory, Chilton, Didcot, OX11 0QX, UK, ²Instituto Superior Tecnico, 1049-00, Lisboa, Portugal, ³University of Strathclyde, Glasgow, Scotland, UK (Ruth.Bamford@stfc.ac.uk).

Introduction: The observational evidence from in-situ spacecraft measurements has clearly shown that the Lunar crustal magnetic anomalies [1] form collisionless shocks in the plasma of the solar wind [e.g.2,3,4]. The signatures of collisionless shocks include ion reflection and downstream lower hybrid waves and turbulence, electron heating, particle and magnetic field pile-up across a narrow barrier region (of the order of the electron skin depth typically ~ 1 -2km). On the other side of the barrier region ion density is slowed and depleted. The entire structure forms mini-magnetospheres which, unlike planetary magnetospheres, are observed to extend as little as 10-20km above the Lunar regolith from magnetic fields determined to be about 200-400nT at the surface.

Simple bending of the incoming ions about the magnetic field, or magnetic mirroring of the ions at the converging magnetic field of a pole, cannot account for the abrupt change in the ion density, temperature, cavity formation or downstream turbulence. However plasma kinetic theory that includes the interlinked role of the electron and ion distributions can account for all the observational data [5].

Simulation: Figure 1 shows the results from the OSIRIS[6] plasma code. The 2D simulation shows a magnetic field being impacted by a collisionless hydrogen plasma flowing from right to left. The bottom panel shows the ion density within which wave structure (at lower hybrid frequencies) can be seen. The cavity in the density, formed by the self-consistently generated electric field shown in the middle panel, is clearly visible in the lower panel

Table 1 shows that the quantified values compare very well with the observational data. The width of the pile-up region of the transition into the cavity (L) and the possibility that this can occur at very low altitude (R_s) are all accounted for. The efficiency of the ion deflection is illustrated by the electric field calculation that predicts an opposing electrostatic potential, comparable with the incoming ion energy of 2keV.

The simulation results agree with the previous laboratory experiments [7].

Lunar swirls: Regardless of the controversy as to precisely what the Lunar Swirls are [e.g.. 8], and how they form [9,10], mini-magnetospheres do exist above the discolourations. It is likely that the explanation of these beautiful formations is going to require a combination of plasma physics and selenology.

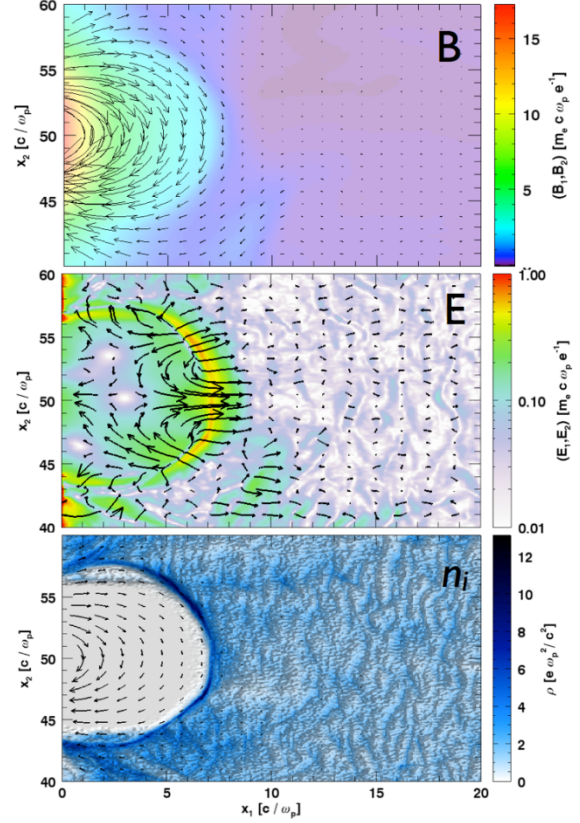


Figure 1: A particle-in-cell plasma code simulation of the interaction of a magnetic field (intensity) (top) interacting with a flowing plasma (ion density shown in bottom panel). The middle panel shows the resulting self-consistent electric field. All units are dimensionless plasma parameters.

Table 1: The calculated stand-off distance (R_s), barrier width (L) and electric field at the barrier (E_r) for a typical quiet time solar wind ($T_e=5\text{eV}$, $B_{IMF}=10\text{nT}$), impacting at normal incidence to the Lunar surface of a crustal magnetic anomaly with a surface magnetic field of 400nT. Total potential difference $\Phi = L \cdot E_r$.

| V_{sw} | N_{sw} | R_s | L | E_r | ΦL |
|----------|------------------|-------|-----|-------|----------|
| 440km/s | cm^{-3} | km | km | V/m | kV |
| 2 keV | 5 | 21 | 2.4 | -0.2 | -0.6 |

References: [1] P. J. Coleman, PLPSC (1972). [2] Lin, R.P., *Science*, (1998). [3] Wieser, M., GRL., (2010). [4] Saito, Y., *EPS*, 2012. [5] Bamford, R.A., *PRL* (2012). [6] Fonseca, R. A., *Lec. Notes in Comp. Sci.*, (2002). [7] Bamford, R.A., *Plasma Phy Cont. Fus.* (2007). [8] Blewett, 2011, *JGR* [9] Kramer, G.Y., *JGR*. (2011). [10] Pieters, C. M., *LPSC #1408* (2014).

ORIGIN OF LUNAR WATER AND NITROGEN: CONSTRAINTS FROM APOLLO 17 VOLCANIC GLASSES. E. Füre¹, B. Marty¹, E. Deloule¹, A. Gurenko¹ ¹CRPG-CNRS BP20, 54501 Vandoeuvre-lès-Nancy, France (efueri@crpg.cnrs-nancy.fr).

Introduction: The discovery of water trapped in lunar volcanic glasses (LVGs) [1, 2], melt inclusions [3], and apatites [4-8] has revealed that the lunar interior is not completely anhydrous. In addition, trace amounts of indigenous nitrogen have been detected in various primitive lunar samples [9-11]. This may imply either that the material that formed the Moon was not completely devolatilized, or, alternatively, that volatile-rich chondritic or cometary material was delivered to the lunar magma ocean (LMO) after the Moon-forming impact.

The caveat in the search for indigenous lunar volatiles (e.g., H₂O and N) is that any sample collected at the Moon's surface likely also contains volatiles implanted by solar wind (SW) irradiation, as well as certain volatile element isotopes (e.g., D, ¹⁵N) produced by spallation reactions. Therefore, in our study [12], we used noble gases (He, Ne, Ar) as a tool to separate the volatiles trapped in individual Ti-rich Apollo 17 LVGs into constituent components, since solar and cosmogenic noble gas components are characterized by distinct isotope and/or elemental abundance signatures.

Experimental approach: First, we handpicked large (~300-400 µm in diameter) single LVGs from 13 cm depth of the Apollo 17 74002 drive tube. The LVGs represent droplets from a primitive melt with ~8.9 wt.% TiO₂ and 14.5 wt.% MgO. We assessed the proportion of solar, cosmogenic, and indigenous water (hydrogen) trapped in each individual LVG by coupling SIMS measurements of water abundances and D/H ratios with CO₂ laser extraction-static mass spectrometry analysis of noble gases (He, Ne, Ar). Secondly, we extracted nitrogen from different grain size fractions by CO₂ laser heating.

Results and discussion: Our He-Ne-Ar results show that the Apollo 17 LVGs have been exposed at the lunar surface for ~28 Myrs, on average, and that they contain less than 5% implanted SW-derived noble gases. Hydrogen abundances are equivalent to between 6.5 and 54.3 ppm H₂O. Since the SIMS measurements were carried out away from the grain surfaces, the contribution of hydrogen implanted by the SW is negligible. Spallogenic deuterium, in contrast, represents up to 17 % of the total deuterium content. Based on the noble gas exposure ages, the correction of measured δD values for the cosmogenic contribution ranges from -254‰ to -5‰. Corrected δD values vary between +38‰ and +809‰ and are anti-correlated with the water content, consistent with extensive hydrogen isotope fractionation during kinetic H₂ loss from a lunar melt with an inferred initial isotope signature of the order of -100‰ and a water content of 100-300 ppm. We conclude that the lunar mantle source that generated the 74002 LVGs contains up to 92 ppm H₂O with a

hydrogen isotope composition similar to that of chondritic meteorites.

A nitrogen component with a δ¹⁵N value of +4.4 ± 7.8 ‰ relative to air is released from the grain surfaces. This value is assumed to reflect the isotope composition of N-bearing volcanic vapor that condensed onto the surface of the LVGs, and suggests that the isotopic composition of indigenous nitrogen in the lunar mantle is comparable to the δ¹⁵N values observed in carbonaceous chondrites (e.g., [13]).

Conclusions: Our results further confirm that the lunar mantle contains a significant amount of water (hydrogen) and nitrogen, in disagreement with the notion of a largely devolatilized Moon. The inferred isotopic composition of lunar hydrogen and nitrogen is similar to the isotope signature of these volatiles trapped in Earth's mantle or in chondritic meteorites. These findings may imply that the material that formed the Moon was not completely degassed, even though the temperatures reached after the giant impact were high enough to achieve the volatilization of large amounts of material [14]. In this scenario, the isotopic resemblance between terrestrial and lunar volatiles may be the result of post-impact equilibration of the terrestrial magma ocean and lunar-forming material [15]. Alternatively, if the giant impact resulted in extensive devolatilization of the material that formed the Moon, water and nitrogen must have been added to the LMO after the Moon-forming impact but before solidification of the isolating lunar crust. In this case, since the low δD and δ¹⁵N values we infer for the lunar mantle rule out Oort cloud comets as major contributors to the lunar volatile budget, lunar volatiles must originate from the accretion of chondritic matter.

References: [1] Saal A. et al. (2008) *Nature* 454, 192-196. [2] Saal A. et al. (2013) *Science* 333, 1-7. [3] Hauri E. et al. (2011) *Science* 333, 213-215. [4] Boyce J.W. et al. (2010) *Nature* 466, 466-469. [5] McCubbin F.M. et al. (2010) *PNAS* 107(25), 11223-11228. [6] Greenwood J.P. et al. (2011) *Nat. Geosci.* 4, 79-82. [7] Tartèse R. and Anand M. (2013) *EPSL* 361, 480-486. [8] Tartèse R. et al. (2013) *GCA* 122, 58-74. [9] Becker R.H. et al. (1976) *Proc. 7th Lunar Sci. Conf.*, 441-458. [10] Kerridge J.F. et al. (1991) *Proc. 21st Lunar Sci. Conf.*, 291-299. [11] Mathew K.J. and Marti K. (2001) *EPSL* 184, 659-669. [12] Füre E. et al. (2014) *Icarus* 229, 109-120. [13] Kerridge J.F. (1985) *GCA* 49, 1707-1714. [14] Canup R.M. (2004) *Annu. Rev. Astron. Astrophys.* 42, 441-475. [15] Pahlevan K. and Stevenson D.J. (2007) *EPSL* 262, 438-449.

WATER CONTENT AND H ISOTOPIC COMPOSITION OF APATITES IN LUNAR KREEP BASALTS: CLUES TO INDIGENOUS LUNAR WATER. R. Tartèse¹, M. Anand^{1,2}, F. M. McCubbin³, I. A. Franchi¹ ¹Planetary and Space Sciences, The Open University, Walton Hall, Milton Keynes, MK7 6AA, UK, ²Department of Earth Sciences, The Natural History Museum, Cromwell Road, London, SW7 5BD, UK, ³Institute of Meteoritics, University of New Mexico, 200 Yale Blvd SE, Albuquerque, NM, 87131, USA (Romain.Tartese@open.ac.uk)

Introduction: It is well established that significant amounts of indigenous H-bearing species (henceforth referred to as “water”) are present in lunar volcanic glasses, in olivine-hosted melt inclusions within volcanic glasses [1-4], in nominally anhydrous minerals from the lunar highlands [5], and in the mineral apatite from nearly all lunar lithologies [6-13]. However, the significance of some of these measurements into directly translating into a volatile-rich lunar interior has recently been questioned, especially the estimates derived from analysis of mineral apatite [14].

On the other hand, the H isotopic composition of water present in lunar minerals and melts provides clues to its origin. Greenwood et al. [9] first reported H isotopic composition for lunar apatites and interpreted their elevated D/H ratios as signatures of comet-derived water. Subsequently, Tartèse and Anand [15] proposed that indigenous lunar water could have been characterized initially by CI chondrite-like D/H ratios, and the elevated D/H ratios measured in apatites from mare basalts could have resulted from magmatic degassing of H₂. Recent studies have indeed measured chondritic D/H ratios in volcanic glasses and their melt inclusions [1,4], and H₂ degassing is now considered a likely mechanism to explain some elevated lunar D/H ratios [1,13,15-16]. Finally, recent analyses carried out in apatites from the Mg-suite norites, representing some of the oldest samples of the lunar highlands, yielded D/H ratios comparable to terrestrial values (δD ranging from ~ 0 to -200 ‰ [7]).

To gain further insights into the origin(s) and evolution of lunar water, we are investigating the apatite water content and its H isotopic composition in the relatively rare lunar rock types represented by KREEP basalts, which have not been previously studied extensively for their H₂O and D/H systematics.

Results: H₂O content and H isotopic composition were measured in apatites using the Cameca NanoSIMS 50L at the Open University, following established protocols [e.g., 6,13] and all data have been corrected for spallogenic production of H and D using published cosmic-ray exposure ages. Apatites in sample 72275 are characterized by large H₂O variations between ~ 50 and 850 ppm, with homogeneous δD values (weighted average = -113 ± 62 ‰, 2σ) (Fig. 1). H₂O contents in apatites

in the olivine gabbro (OG) lithology of NWA 773 range from ~ 500 to 2800 ppm and δD values between -273 ± 139 ‰ and 184 ± 140 ‰ (Fig. 1). In sample 15386, apatite H₂O contents range from ~ 100 to 800 ppm, with δD values displaying very large variations between 89 ± 99 ‰ and 778 ± 123 ‰ (Fig. 1).

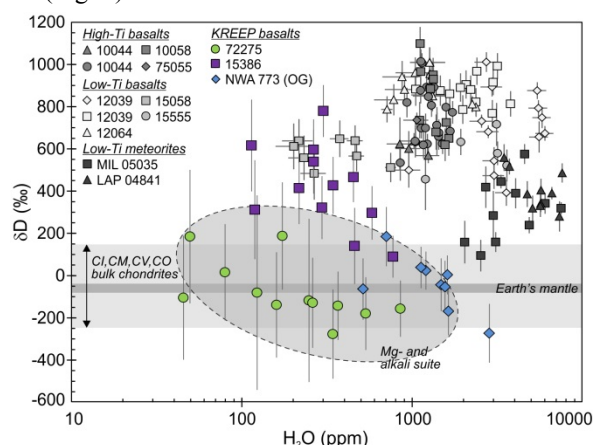


Figure 1: δD (‰) vs. H₂O (ppm) in apatites from KREEP basalts (literature data are from [6-7,9,13], δD value for terrestrial mantle (-60 ± 20 ‰) is from [17] and for bulk CI-chondrites is from [18].

Discussion:

Degassing of H₂. Apatites in 15386 and in NWA 773 display a trend of increasing δD with decreasing H₂O (Fig. 1). This trend can result from several processes such as (i) incorporation of solar wind (SW) hydrogen implanted in the lunar regolith during magma ascent and eruption, (ii) post-crystallisation diffusive loss of OH from apatites or (iii) degassing of H₂ from the magma during apatite crystallisation. Simple binary mixing between a low-H₂O and high δD indigenous end-member and a SW-type composition ($\delta D \sim -997$ ‰) is not consistent with the data. To test the possibility of diffusion-induced H₂O- δD variations, NanoSIMS imaging of ¹H and ¹⁹F was carried out on an assemblage containing an apatite grain in contact with late-stage quenched melt (glass). Profiles of ¹H and ¹⁹F variations show that the transitions between the apatite and the glass is very sharp ($\sim 1-2$ μm), precluding significant diffusive exchange and re-equilibration of apatite. Finally, the H₂O- δD relationship defined by apatites in NWA 773 and 15386 matches very well with theoretical calculation of D/H increase caused by H₂ degassing. In addition, petrological observations, such as the fact that the

apatite grain with the highest H₂O content and the lowest δ D analysed in 15386 is enclosed within an early-formed pyroxene crystal, strongly suggest that the observed H₂O- δ D relationship in NWA 773 and 15386 resulted from crystallization during magmatic degassing of H₂ [13,15].

H₂O content in the lunar interior: a KREEP basalt perspective. Tartèse et al. [13] estimated ~ 50-500 ppm H₂O for the typical low-Ti basalt source regions. Such estimates for water contents were strikingly similar to those for mantle sources of pyroclastic products (~ 50-400 ppm H₂O; [2]), as well as those of terrestrial (~ 60-400 ppm H₂O [19]) and martian basalts (~ 100-300 ppm H₂O [20]). KREEP basalts are enriched in P (P₂O₅ ~ 0.5-0.7 wt.% [21]) compared to typical mare basalts [22]. Phosphate saturation thus likely occurred earlier in the crystallisation history of KREEP basalts, after around 85-90 % crystallisation [23], compared to > 95 % crystallisation for typical mare basalts [24]. Taking this into account, back-calculations yield estimates of ~ 100-2500 ppm H₂O for the primitive KREEP basalt melts. If one considers that the KREEPy component of these basalts is a feature characteristic of their mantle source regions, these source regions would have contained ~ 10-400 ppm H₂O, overlapping with previous estimates mentioned above for different lunar lithologies. On the other hand, these water contents in primitive KREEP basalts could also result from en route assimilation of 0.7 to 18 % of an urKREEP component by “dry” magmas, considering that urKREEP had ~ 1.4 wt.% H₂O [5].

Can we really use apatite to assess the volatile inventory of magmatic liquids?

Boyce et al. [14] recently cautioned the use of apatite to derive estimates of magmatic water content. They showed that (i) partitioning of H₂O, F and Cl in apatite does not follow trace element Henrian behaviour as these volatiles are essential structural constituents in apatite, their abundances being therefore related to stoichiometric constraints. As a result, the volatile inventory in apatite depends on the relative abundances of these species in the melt, not on their absolute abundances. On top of that, a crystallising apatite strongly favors F > Cl > H₂O. Therefore, relative abundances of these species in a melt will be dramatically affected by apatite crystallisation itself, and it appears possible in fact to crystallise almost pure hydroxylapatite from a melt with low H₂O content. All the published estimates of magmatic water contents in lunar magmas based on apatite analyses have been made using Henrian-type partition coefficients [6-8,10,13]. As a result, previous studies may have overestimated the actual volatile contents of lunar magmas. On the other hand, NanoSIMS imaging of the late-stage quenched

melt and apatite assemblage in 15386 shows that the melt is definitely enriched in water compared to the apatite, the calculated partition coefficient being consistent with those determined experimentally. In any case, the complicated relationship between melt and apatite volatile contents merit innovative experimental work in order to get better constraints on this topic.

H isotopic composition of lunar water. Putting aside the question of volatile abundances, apatite studies still provide valuable insights on indigenous volatiles, notably through studies of their H and Cl isotope characteristics. Whichever process was responsible for producing the large H₂O variations seen in apatites in KREEP basalt 72275, it was not accompanied by H₂ degassing, as associated δ D values are relatively constant over a range of H₂O contents, yielding a weighted δ D value of -113 ± 62 ‰ (n = 12; MSWD = 1.3). Such terrestrial-like H isotopic compositions are consistent with a common origin for terrestrial and lunar indigenous water [1,4,13,15].

Acknowledgements: We thank NASA CAPTEM for allocation of Apollo samples. This research was funded by a STFC research grant to MA (Grant no. ST/I001298/1). NanoSIMS access was provided through UKCAN (STFC grant ST/I001964/1).

References: [1] Füre E. et al. (2013) *Icarus*, 229, 109-120. [2] Hauri E. H. et al. (2011) *Science*, 333, 213-215. [3] Saal A. E. et al. (2008) *Nature*, 454, 192-196. [4] Saal A. E. et al. (2013) *Science*, 340, 1317-1320. [5] Hui H. et al. (2013) *Nature Geosci.*, 6, 177-180. [6] Barnes J. J. et al. (2013a) *Chem. Geol.*, 337-338, 48-55. [7] Barnes J. J. et al. (2014) *Earth Planet. Sci. Lett.*, 390, 244-2525. [8] Boyce J. W. (2010) *Nature*, 466, 466-469. [9] Greenwood J. P. et al. (2011) *Nature Geosci.*, 4, 79-82. [10] McCubbin F. M. et al. (2010a) *P. Natl. Acad. Sci.*, 27, 11223-11228. [11] McCubbin F. M. et al. (2010b) *Am. Mineral.*, 95, 1141-1150. [12] McCubbin F. M. et al. (2011) *GCA*, 75, 5073-5093. [13] Tartèse R. et al. (2013) *GCA*, 122, 58-74. [14] Boyce J. W. et al. (2014) *Science*, doi:10.1126/science. 1250398. [15] Tartèse R. and Anand M. (2013) *Earth Planet. Sci. Lett.*, 361, 480-486. [16] Sharp Z. D. et al. (2013) *Earth Planet. Sci. Lett.*, 380, 88-97. [17] Lécuyer C. et al. (1998) *Chem. Geol.*, 145, 249-261. [18] Alexander C. M. O'D. et al. (2012) *Science*, 337, 721-723. [19] Saal A. E. et al. (2002) *Nature*, 419, 451-455. [20] McCubbin F. M. et al. (2012) *Geology*, 40, 683-686. [21] Taylor G. J. et al. (2012) *Met. Planet. Sci.*, 47, 861-879. [22] Hallis L. J. et al. (2014) *GCA*, in press. [23] Harrison T. M. and Watson E. B. (1984) *GCA*, 48, 1468-1477. [24] Sha L. K. (2000) *GCA*, 64, 3217-3236.

ASSESSING THE VOLATILE INVENTORY OF APATITES IN LUNAR IMPACT MELT BRECCIAS.
J. J. Barnes^{1,2}, R. Tartèse¹, M. Anand^{1,2}, I. A. Franchi¹, N. A. Starkey¹, S. S. Russell² ¹Planetary and Space Sciences, The Open University, Milton Keynes, MK7 6AA, UK, ²Department of Earth Sciences, The Natural History Museum, Cromwell Road, London, SW7 5BD, UK (jessica.barnes@open.ac.uk).

Introduction: The recent discoveries of hydrogen (H) bearing species on the lunar surface and in samples derived from the lunar interior have necessitated a paradigm shift in our understanding of the water inventory of the Moon. The Moon was considered to be ‘bone-dry’ following the Apollo missions. However, since then estimates of interior lunar water have varied from ‘dry’ (few ppm) to ‘wet’ (several 100s ppm) [1-4].

Most recent sample-based studies have attempted to characterise the source(s) of lunar water, which is present in melt inclusions, glass beads, and the mineral apatite [1-12]. A number of sources have been suggested ranging from cometary [10], to chondritic [13], to the Proto-Earth [4,9].

Since the Moon is a heavily impacted planetary body, it is important to investigate if impact processes could affect the volatile budget of lunar samples such as pyroclastic glasses or apatite in rocks. A recent study has investigated the volatile inventory of apatite in ancient (> 4.0 Ga old) lunar highlands samples [9] that had been exposed to extensive impact processing. This study concluded that shock didn’t seem to affect/disturb the volatile inventory nor the H-isotopic composition of apatite in the highlands samples studied [9].

In order to gain further insight into potential effect of impacts on volatile inventory of lunar apatites, we examined two impact melt breccias (IMB) 15405 and 65785 for their volatile abundances and hydrogen isotopic composition.

Samples: 15405 is a clast-bearing IMB. The clasts in the breccia are predominately KREEP basalts and granites. The rock also contains a large proportion of mineral fragments. The impact melt (IM) itself is very fine-grained and composed of intergrown plagioclase, pyroxene and ilmenite crystal laths with a groundmass composition similar to that of KREEP basalts [14]. Although our polished section of this sample contained different clasts, all of the analysed apatites were located within the IM itself. Their scalloped and partially resorbed crystal edges suggest that they are ‘relict’ grains of pre-existing target material.

65785 is also classified as an IMB although the IM itself is somewhat coarser-grained than that in 15405. The IM is composed predominately of plagioclase intergrown with olivine, minor pyroxene, and other accessory phases such as spinel and apatite. The IM protolith is suspected to be QMG/felsite like with a KREEP component [15].

Methods: Polished sections of samples were mapped for their elemental abundances using an FEI

Quanta 3D Dual beam Scanning Electron Microscope at The Open University, using a 0.6 nA and 20.05 kV electron beam. Two protocols were used for performing NanoSIMS ion probe analyses at The Open University 1) D/H-OH measurements and 2) volatile abundance measurements following the protocols described in [8,9,11,12].

Results: We report the measured OH contents as water equivalent to make them comparable to previous studies. We analysed a total of five apatite grains from the two samples. In sample 15405 apatite H₂O contents range from 40 to 120 ppm with corresponding δ D of between \sim 300 and \sim -500 ‰ (Fig. 1). The H₂O content of apatites in 65785 ranges between \sim 20 and 30 ppm with δ D values of 620 and 710 ‰ (Fig. 1).

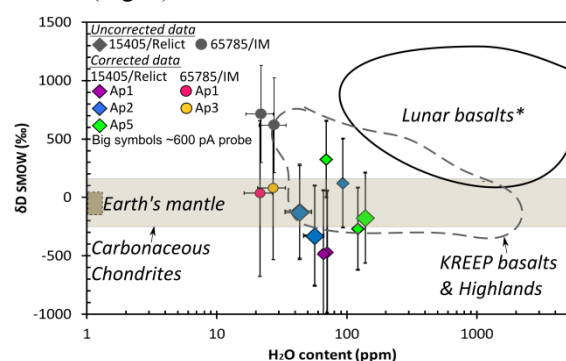


Figure 1: Plot showing both the measured (grey symbols) and spallation corrected H₂O contents and δ D values of apatites in samples 15405 and 65785. Uncertainties are the combined 2σ analytical error and uncertainties associated with the CRE ages. Plotted for comparison are the available literature data for H₂O- δ D values of lunar basalts (* = Apollo mare basalts & lunar basaltic meteorites [8,10,11]), KREEP basalts [12] and lunar highlands samples (norites and granite, [9]), range in Earth’s mantle δ D [19 and references therein] and range in δ D for CI, CM, CV, and CO chondrites [20].

Discussion: Before using the measured H-isotopic composition of apatites to identify potential sources for H in IMB apatites it is important to apply appropriate corrections for spallogenic production of both H and D [e.g., 4]. This correction is negligible for 15405 as this sample has a relatively short (11 Ma, [16] cosmic ray exposure (CRE) age. However, 65785 has a relatively long CRE age (271 Ma, [17]) and hence the correction is large yielding corrected δ D values between 37 and 81 ‰.

One of the characteristics of apatite in these breccias is that they are relatively dry (< 150 ppm H₂O). It is attractive to relate this feature to

dehydration during breccia formation, especially given the temperatures (up to ~ 2000 °C) invoked for impact-melt formation [e.g., 18].

To a first order, the spread in δD values for IMBs is similar to that observed for lunar highlands and KREEP basaltic samples (Fig. 1). The range in δD spans from non-terrestrial (i.e. elevated values up to ~ 400 ‰) to terrestrial-like or carbonaceous chondrite-like values and extend towards even lower δD values (~ -500 ‰), albeit with large uncertainties.

It is perhaps not surprising that apatites in 15405 yield almost identical signatures to those of KREEP basalts and lunar highlands samples (e.g. granite 14303) given that the clasts in this breccia are KREEP basalts and granites, and that the IM itself has a bulk composition characteristic of KREEP suggesting a KREEP-like protolith [14]. Despite the range in δD for apatite in this sample, the H₂O content remains uniform within and between grains. NanoSIMS abundance measurements performed on apatites 2 and 5 in sample 15405 also revealed that these apatites are dry. Interestingly the F contents are similar between grains (3 wt.% versus 3.5 wt.%) whilst the Cl contents differ in the two grains by almost two orders of magnitude (1 wt.% versus 0.05 wt.%). This may suggest that these grains have retained their primary volatile heterogeneities. However, in order to fully assess the potential for dehydration of the apatite and likely reaction of the apatite with the impact melt (textural modification) it is important to also investigate the volatile inventory of the IM surrounding apatite grains. However, these measurements are extremely challenging and require further development of existing analytical protocol. Nevertheless, such measurements will also help evaluate any potential involvement of solar wind derived H in the IM.

In contrast to 15405 the texture of IMB 65785 suggests that the apatite in this sample crystallised from the IM. If true then it could be speculated that the consistent δD of apatites in 65785 represents the δD signature of the homogenized melted target lithology [18] which incidentally has a composition (δD ~ 40 to 80 ‰) similar to that of some carbonaceous chondrites and other highlands lithologies (Fig. 1).

Clearly further work is required on apatites in these samples and other IMBs in order to fully assess the behaviour of H in response to impact-related thermal metamorphism.

Acknowledgements: CAPTEM are thanked for allocation of Apollo samples. STFC is thanked for a PhD studentship to JJB, a research grant to MA (grant No. ST/I001298/1), and NanoSIMS access was through UKCAN by the STFC-funded grant ST/I001964/1.

References: [1] Boyce, J. W. et al. (2014) *Science* DOI: 10.1126/science.1250398. [2] Saal, A. E. et al. (2008) *Science* 454, 192-195. [3] Hauri, E. H. et al. (2011) *Science* 333, 213-215. [4] Saal, A. E. et al. (2013) *Science* 340, 1317-1320. [5] Boyce, J. W. et al. (2010) *Nature* 466, 466-470. [6] McCubbin, F. M. et al. (2010) *PNAS* 107, 11223-11228. [7] McCubbin, F. M. et al. (2011) *GCA* 75, 5073-5093. [8] Barnes, J. J. et al. (2013) *Chem. Geol.* 337-338, 48-55. [9] Barnes, J. J. et al. (2014) *EPSL* 390, 244-252. [10] Greenwood, J. P. et al. (2011) *Nat. Geosci.* 4, 79-82. [11] Tartèse, R. et al. (2013) *GCA* 122, 58-74. [12] Tartèse, R. et al. (2014) *Geology* 42, 363-366. [13] Tartèse, R. et al. (2013) *EPSL* 361, 480-486. [14] Ryder, G. (1976) *EPSL* 29, 255-268. [15] Keil, K. et al. (1975) *GRL* 2, 369-372. [16] Drozd, R. J. et al. (1976) *Proc. LSC VII*. [17] Schaeffer, G. A. and Schaeffer, O. A. (1977) *Proc. LSC VIII*. [18] French, B. M. (1998) *Tech. Report, LPI-Contrib-954* 1. [19] Lécuyer, C. et al. (1998) *Chem. Geol.* 145, 249-261. [20] Alexander, C. M. O'D. et al. (2012) *Science* 337, 721-723.

Overview: A number of lunar regolith meteorites have been selected to assess the impact flux on the lunar surface through time. We will assess the surface maturity and calculate the cosmic ray exposure (CRE) ages of each sample to determine their regolith history. Our sample suite includes samples of feldspathic highland breccias, mare basalts and mixed feldspathic-basaltic breccias, some have never previously been analysed for their complete cosmogenic noble gas inventory.

Surface Maturity and CRE Ages: The surface of the Moon is a very dynamic environment. As the Moon has no atmosphere, the regolith is exposed to bombardment from micrometeorites (<1 mm), particles from the sun (solar wind, SCRs – solar cosmic rays) and the wider galactic environment (GCRs – galactic cosmic rays) [1]. Micrometeorites and solar wind particles only interact with the immediate surface (top few mm) and increased exposure to these particles results in the maturation of the regolith [2]. Trapped noble gases (e.g., ³⁶Ar) correlate well with other maturity indices such as the I_s/FeO index (the intensity of ferromagnetic resonance normalised to the bulk Fe content) (Fig. 1), which has been shown to be proportional to the duration of surface exposure [2, 3]. Only for three lunar meteorites (MAC 88104/5, ALHA 81005 and QUE 93069) have I_s/FeO values been published [4, 5] and the technique is not currently used. Therefore, determination of the trapped gases in the meteorites will be critical to assessing the maturity of the samples. In contrast to micrometeorites and solar wind, SCRs and GCRs penetrate up to a few cm to meters into the regolith, respectively [1]. Cosmogenic isotopes are produced during this interaction and the CRE age is defined as the duration the sample has been exposed to these cosmic rays, in the lunar regolith or during transfer as a meteoroid in space. To calculate this age, the production rates for each cosmogenic nuclide is needed, which depends mainly on the chemistry and depth of the target rock [6, 7]. The trapped noble gases and CRE age can be determined to understand the history of the sample during its lifetime in the lunar regolith.

Lunar regolith meteorites are ejected from random localities across the Moon, by asteroidal and cometary impacts [8, 9]. All lunar meteorites have experienced some exposure to cosmic rays either while residing in the top few meters of lunar regolith (2π irradiation), during transit to Earth (4π irradiation), or both [8, 10]. As a result, lunar meteorites provide the opportunity to look at the exposure history and regolith archive on a global

scale, compared with the Apollo and Luna sample collection [11].

Analytical Technique: We have developed a micro-furnace technique to analyse the noble gas isotope concentrations of small (1-10 mg) bulk lunar rock chips and soils. A low volume resistance filament furnace, for higher sensitivity and low blanks, is connected to a VG5400 noble gas mass spectrometer. Noble gases are released in temperature steps (from ~600°C up to ~1500°C) to distinguish the surface-correlated trapped gases from the volume-correlated cosmogenic gases. This technique is being applied to determine: (i) the cosmic ray exposure age, (ii) the shielding depth, (iii) the closure age and (iv) the duration of surface exposure (i.e., maturity) of each meteorite.

The petrology and mineral chemistry of the samples are assessed using polished blocks made from sub-splits of each sample (~3-6 mg). A Philips FEG-SEM with EDAX Genesis EDS system is used to produce back-scatter electron images and false-colour element maps and a Cameca SX 100 EMPA was used to determine mineral chemistry. These data will be used to test the consistency of the mineral chemistry with the reported bulk rock chemistry. Production rates of cosmogenic noble gas isotopes can then be determined from bulk rock compositions and used to calculate the cosmic ray exposure age of samples.

Apollo Regolith Record: Regolith breccias collected at different Apollo landing sites generally fall into two categories: young and ancient breccias (as measured by the antiquity indicator ⁴⁰Ar/³⁶Ar_{tr}) [12, 13]. The ancient breccias have closure ages (breccia formation ages) of >3.5 Ga and are from immature (i.e., low I_s/FeO, ³⁶Ar_{tr}) soils with exposure ages of only a few million years (Fig. 2) [12]. Younger regolith breccias <3.5 Ga typically exhibit greater degrees of maturity (i.e., high I_s/FeO, ³⁶Ar_{tr}) with a range of CRE ages (Fig. 2). The difference between the types of regolith breccias is possibly associated with the changing impact flux on the lunar surface through time. The ancient regolith breccias relate to a period of intense large-scale basing-forming events and rapid overturn of the regolith [12, 13]. Whereas the younger regolith breccias have been exposed to more or less energetic but more frequent impacts (e.g., micrometeorites) and reprocessed on a smaller scale over a longer period of time.

Scientific Goals: Our goal is to test if lunar meteorites display the same or similar link between their level of maturity and their breccia formation age. Assessing the impact flux at different periods in

lunar history can provide an archive of regolith processes through time [14, 15].

The initial results of our noble gas study will be presented at this meeting and added to the current growing data-set from lunar meteorites providing new constraints on the global context of the evolution of the lunar regolith.

Acknowledgements: Thank you to Dr John Cowpe and Bev Clementson for all their help, advice and expertise in the lab. We would also like to thank the NASA Meteorite Working Group for loaning us the samples and STFC for project funding.

References: [1] Lucey P. et al. (2006) *Rev. Mineral. Geochem.*, 60, 83-220. [2] Morris R. V. (1978) *Proc. LPS IX*, 2287-2297. [3] Morris R. V. (1976) *Proc. LPS VII*, 315-335. [4] Morris R. V. (1983) *Geophys. Res. Lett.*, 10, 807-808. [5] Lindstrom M. M. (1995) *Proc. LPS XXVI*, 849-850. [6] Reedy R. C. et al. (1983) *Science*, 219, 127-135. [7] Leya I. et al. (2001) *Meteoritics & Planet. Sci.*, 36, 1547-1561. [8] Lorenzetti S. et al. (2005) *Meteoritics & Planet. Sci.*, 40, 315-327. [9] Joy K. H. and Arai T. (2013) *Astronomy & Geophysics*, 54, 4.28-4.32. [10] Eugster O. (2003) *Chemie Der Erde*, 63, 3-30. [11] Korotev R. L. (2005) *Chemie der Erde*, 65, 297-346. [12] McKay D. S. (1986) *JGR*, 91, D277-D303. [13] Joy K. H. et al. (2011) *GCA*, 75, 7208-7225. [14] Fagen A. et al. (2013) *LPSC XXXV*, abstract #1907. [15] Fagen A. et al. (2014) *Earth Moon and Planets*, *In press*.

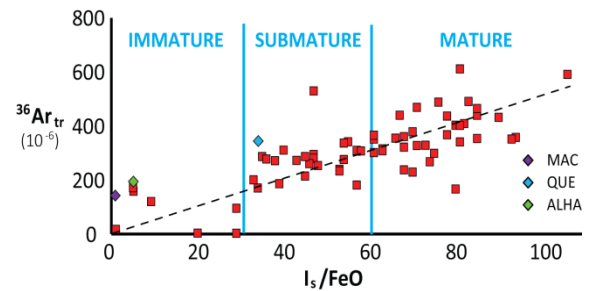


Figure 1: Apollo soil literature data for the maturity indices I_s/FeO and trapped ^{36}Ar . Increased maturity is associated with increased surface exposure (top few mm). Data for lunar meteorites MAC 88104/5, QUE 93069 and ALH 81005 are also shown [4, 5].

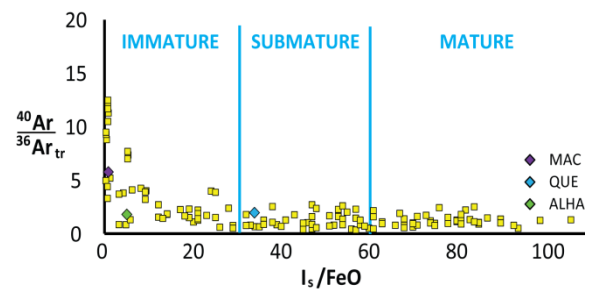


Figure 2: Apollo soil and breccia literature data for the maturity indices I_s/FeO and trapped $^{40}Ar/^{36}Ar$ values. Data for lunar meteorites MAC 88104/5, QUE 93069 and ALH 81005 [4, 5, 15] are also shown.

EXOTIC LITHOLOGIES AT THE APOLLO 12 SITE: EXAMINATION OF FINES FROM THE LUNAR SOIL SAMPLES 12023 AND 12003. L. Alexander^{1,2}, J. F. Snape^{2,3}, K. H. Joy^{2,4}, I. A. Crawford^{1,2}, H. Downes^{1,2} ¹Department of Earth and Planetary Science, Birkbeck College, University of London, UK, ²Centre for Planetary Sciences, UCL-Birkbeck, London, ³Planetary and Space Sciences, The Open University, Milton Keynes, UK, ⁴SEAES, University of Manchester, Manchester, UK (l.alexander@bbk.ac.uk).

Introduction: The Apollo 12 mission landed in the Eastern region of Oceanus Procellarum (Mare Cognitum). Crater size-frequency distribution measurements by [1] indicate that some of the youngest lava flows on the Moon occur within the Oceanus Procellarum region and it is, therefore, possible that some younger, exotic fragments have been sampled by the Apollo 12 mission. Most basalts from the Apollo 12 site can be grouped into three main basaltic suites: olivine, ilmenite and pigeonite, based on their mineralogy and bulk composition [2,3,4]. An additional suite of feldspathic basalts consists of one sample only [4]. However, care needs to be taken with classification based on bulk chemical properties as many small samples are not representative of their parent rocks [4].

As part of a larger study of the diversity of basalts at the Apollo 12 site, we present petrological and geochemical results for basaltic chips from the Apollo 12 soil samples 12003 and 12023 with an emphasis on variations in major, minor and trace element mineral chemistry in order to identify samples which are representative of local flows and samples which are likely to be exotic material introduced by impacts.

Methods: All samples were cut in half for radioisotope dating and mounted in epoxy resin. Samples 12003,308 and 12023, 155 consisted of a variety of chips which were labelled accordingly (e.g. 12023,155_1A, 2A etc). Samples were analysed with a JEOL JXA-8100 electron microprobe with an Oxford Instrument INCA energy dispersive system (EDS) to produce back scattered electron (BSE) images and elemental maps (Fig. 1). Bulk chemical compositions were calculated from multiple EDS raster beam analyses (RBA) and corrected for differences in phase densities in accordance with [5]. This method has been previously tested on known compositions and found to be in good agreement [6].

Results:

Bulk Chemistry. With the exception of 3 coarse-grained, possibly non-representative, fines, all samples are low-Ti basalts (bulk rock 1-6 wt% TiO₂), which are typical of lava flows sampled at the Apollo 12 site [7]. The bulk compositions of most of the samples are consistent with those of olivine, pigeonite and ilmenite basalts. Four samples (12023, 155_4A and 5A, and 12003, 308_1A and 314_D) are compositionally similar to feldspathic basalts given the high concentrations of Al₂O₃.

Chemistry of mineral phases. The pyroxene grains show a range of compositions (En₀₋₆₇Fs₁₅₋

₉₀Wo_{3.7-41}) with zoning from Mg-rich cores to progressively Fe-rich rims, with extreme Fe-rich pyroxferroite rims in some samples. Plagioclase feldspar is mostly anorthitic (An₇₇₋₉₄). Olivine compositions typically range from Fo₃₄₋₇₄, but the widest range and the lowest Fo contents are seen in 12003,308_2A (Fo₃₋₇₃). Olivine Ti/V ratios are similar for most samples (2 to 3), although higher values are seen for coarser grained samples due to generally lower V contents. Spinel compositions range from chromite to ulvöspinel (2Ti₁₀₋₉₇Al₂₋₂₉Cr_{0.4-69}) following a typical mare basalt fractionation trend [8].

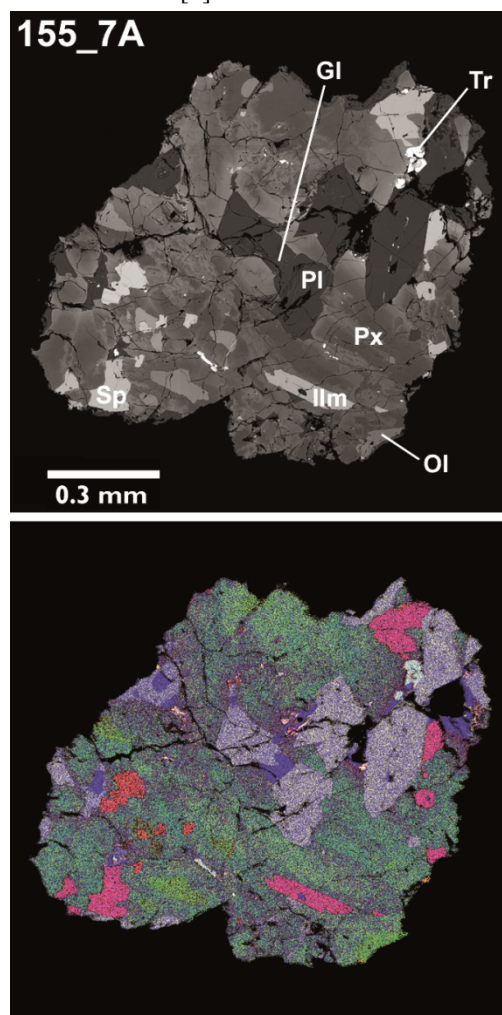


Figure 1: Back-scattered electron (BSE) image and false colour element map of sample 12023,155_7A, one of the samples which may be exotic to lava flows at the Apollo 12 site. Colours represent concentrations of different elements: Si = blue, Fe = red, Mg = green, Ca = yellow, Al = white, Ti = pink and Cr = orange. Annotations are: Px

= pyroxene, Ol = Olivine, Ilm = ilmenite, Pl = plagioclase, Sp = spinel, and Gl = glass.

Discussion: The small sizes of the samples means that they may not be representative of their parent rock and their bulk chemical properties cannot be relied on for classification or comparison, particularly in the case of the coarse grained samples. Where samples are fine-grained or vitrophyric, we can reconstruct the equilibrium parent melt Mg# using the composition of the most primitive olivine [9, 10, 11] and appropriate mineral-melt Kd values [12]. Other methods can help to categorise the samples. It has been suggested [13] that olivine trace element compositions, and particularly Ti/V ratios discriminate between the basalt groups. While most samples have bulk compositions, modal mineralogies and mineral chemistries consistent with the previously identified olivine, pigeonite or ilmenite Apollo 12 basalt lithological groups, there are several notable exceptions:

Samples 12003,308_3A, 12003_316 and 12003_311 have high modal abundances of olivine and low modal abundances of pyroxene, although the coarse grain size (up to ~0.8 mm) indicates that they may not be representative. However, in addition these samples have olivine with higher Ti/V ratios and lower Co concentrations than other Apollo 12 samples and may represent material contributed by a separate lava flow.

Sample 12023,155_1A has unique mineral compositions in olivine and spinel which indicates that it is not related to the other samples. The olivine grains analysed have lower concentrations of Cr₂O₃ at high Mg#, with low Ni and Mn concentrations (41 to 55 ppm Ni, 2400 to 2556 ppm Mn). Plagioclase compositions are less anorthitic and the spinel grains have higher Al₂O₃ concentrations. Ti/V ratios in olivines are high (Fig. 1), which indicate that this sample is similar to Apollo 12 ilmenite basalts [13]. However, compositional equilibration is believed to have affected the chemistry in this coarser-grained sample. Given the differences in mineral composition, we believe that 155_1A may originate from a different parent melt to other Apollo 12 basalts.

Three samples (12003,314_D; 12023,155_4A and ,155_5A) are identified as potential feldspathic basalts. Given that other feldspathic basalt fragments from the Apollo 12 site have been identified [14, 15], these may represent additions to this lithological group. If this is the case, then it indicates that feldspathic basalts may not be exotic to the Apollo 12 site [4] but may instead represent a local flow, possibly underlying the landing site [15]

Sample 12023,155_7A (Fig. 1) shows a wider range of plagioclase compositions (An₇₆₋₉₃Or₀₋₄) and a different crystallisation trend of Mg# vs. An# in

plagioclase to the other samples. This sample is most similar to the ilmenite basalts in terms of its bulk chemistry (after [4]) and Ti/V ratio of olivine (after [13]) but it has distinctly different plagioclase chemistry and crystallisation trends to the other samples. It shows similarities to Apollo 14 high-Al basalts in terms of An# in plagioclase [16, 17], and Fo#, Ti/V ratios and Sc, Ni and Co concentrations in olivine [13]. This sample is tentatively identified as an exotic fragment which may represent a lithology more similar to the Apollo 14 basalts than the Apollo 12 basalts.

Sample 12023,155_11A contains pyroxene that is compositionally distinct from other samples. Although the pyroxene is zoned (En₀₋₄₃Fs₄₀₋₈₅Wo₁₂₋₃₃), no Fe-poor pyroxene is present (Mg# <50 in all measurements). Due to the similarity in crystallisation trends and mineral chemistries to those of Fe-rich late-stage minerals in other samples, we conclude that sample 155_11A is likely to represent a more fractionated Apollo 12 basaltic melt, rather than being exotic to the Apollo 12 site.

Future work: Further work, including Ar-Ar dating of the remaining samples (see [18, 19] for initial results) will further help to constrain the origin of these samples and others analysed as part of our wider study.

Acknowledgments: We are grateful to Dr. Andy Beard for his assistance with electron microprobe analyses and to Dr. Martin Rittner for his assistance with LA-ICP-MS analysis.

References: [1] Hiesinger, H. et al. (2003) *JGR*, 108, E7. [2] James O. B. and Wright T.L. (1972) *Bull. Geol. Soc. Am.*, 83, 2357-2382. [3] Rhodes J. M. et al. (1977) *LPS IIX*, 1305-1338. [4] Neal C. R. et al. (1994) *Meteoritics*, 29, 334-348. [5] Warren P.H. (1997) *LPS XXVIII*, Abstract 1497. [6] Snape, J. F. et al. (2011) *LPS XLII*, Abstract 2011. [7] Neal C. R. and Taylor (1992) *GCA*, 56, 2177-2211. [8] Reid, Jr. J.B. (1971) *EPSL* 10: 351-356 [9] Roeder, P.L. and Emslie, R.F. (1970) *Contrib. Mineral. Petrol.* 29, 275. [10] Dungan, M. A. and Brown, R. W. (1977) *LPS VIII*, 1339-1381. [11] Joy, K. H. et al. (2008) *GCA*, 72, 3822-3844. [12] Longhi, J. et. al. (1978) *GCA*, 42, 1545-1548. [13] Fagan, A. L. et. al. (2013) *GCA*, 106, 429-455. [14] Korotev, R.L., Joliff, B.L., Zeigler, R.A., Seddio, S.M., Haskin, L.A. *GCA* 75: 1540-1573, 2011. [15] Snape, J.F., Alexander, L., Crawford, I.A.C., and Joy, K.H. *LPSC XLIV* #1044. [16] Neal, C.R., and Kramer, G.Y. *Am. Mineral.* 91: 1521 – 1535, 2006. [17] Hui, H., Oshrin, J.G., and Neal, C.R. *GCA* 75: 6439 – 6460, 2011. [18] Snape J. F. Burgess R. Joy K. H. Ruzie L. Crawford I. A. *LPSC XLV* #1974. [19] K. H. Joy, R. Burgess, L. Ruzie, P. Clay, J.F. Snape, L. Alexander, I.A. Crawford. (2014) *Goldschmidt 2014* #1429.

THE SIGNIFICANCE OF SIMILARITIES AND DIFFERENCES IN THE MG ISOTOPIC COMPOSITION OF THE EARTH'S MANTLE AND LUNAR SAMPLES. T. Elliott¹, Y.-J. Lai^{1,2}, M. Willbold^{1,3}, P. Pogge von Strandmann^{1,4}, A. Walker⁵, M. Anand⁶, H. Chen¹, C. Coath¹ ¹Bristol Isotope Group, School of Earth Sciences, University of Bristol, UK, ²Institut für Geochemie und Petrologie, ETH, Zürich, Switzerland, ³School of Earth, Atmospheric and Environmental Sciences, University of Manchester, UK, ⁴Department of Earth Sciences, University College London, UK, ⁵School of Earth and Environment, University of Leeds, UK, ⁶CEPSAR, The Open University, UK.

Introduction: The striking isotopic similarity between the Earth and Moon has played an important role constraining models of lunar formation. The canonical, Giant Impact model of Moon formation [1] predicts a dominance of impactor in the Moon. This is incompatible with the irrevocable mass independent oxygen and titanium, radiogenic tungsten and mass dependent silicon isotope measurements of Earth and Moon. As a result, two recent studies [2,3] have further explored collisions which satisfy these compositional criteria. Given subsequent loss of excess angular momentum by resonant despinning, successful solutions range from impacting two near equal sized bodies to a much smaller impactor hitting a larger proto-Earth. It would be useful to have geochemical tests of these different scenarios.

Mg isotope measurements: Here we explore the new perspectives provided on lunar evolution from mass-dependent Mg isotope measurements (typically expressed as $\delta^{26}\text{Mg}$, or parts per thousand deviation from the DSM-3 standard). There are existing lunar $\delta^{26}\text{Mg}$ data but they are contradictory, so we have used a new double-spiking approach with the aim of removing the influence of matrix effects on the analyses. We have measured to high precision a range of lunar basalts and assume, from terrestrial analogy, that there is no isotopic fractionation during melting. We find that all low-Ti basalts studied have $\delta^{26}\text{Mg}$ within error ($\sim 0.05\%$) of the terrestrial mantle. In contrast, high-Ti basalts are $\sim 0.2\%$ isotopically lighter. Of the divergent results published in the literature, our findings are in agreement with the recent work of Sedaghatpour et al [4]. Significantly, our work also shows that the terrestrial mantle and therefore also the low-Ti basalts are super-chondritic by $\sim 0.05\%$.

Implications: The contrast between high and low-Ti basalts echoes measurements seen in a number of isotopic systems. Others have argued that the high-Ti basalts are contaminated with material produced during the latter stages of magma ocean crystallisation. A likely phase to cause the isotopic fractionation of Mg is ilmenite. The Mg isotope measurements potentially provide a new means of quantifying the involvement of this phase

pending experimental calibration of its magmatic isotope fractionation.

Unlike the mass-independent isotope ratios used to compare the composition of Earth and Moon, it is possible that $\delta^{26}\text{Mg}$ is fractionated by vapour-liquid partitioning during lunar genesis. For example, homogenisation of mass independent O, Ti and W isotopic signatures in the aftermath of a Giant Impact has been used as an alternative explanation of the isotopic similarity of Earth and Moon. The consequences of such a model for the Si isotopic composition of the Moon are reported by Pahlevan et al [5] and an extension of this model to $\delta^{26}\text{Mg}$ is an important next step. However the similarity Earth and Moon to better than 0.05% likely places a valuable bound on the plausibility of such a re-equilibration model.

Perhaps the most significant aspect of the lunar Mg isotopic measurements is that they are non-chondritic. Thus the Moon needs to have been derived from a body or part of a body that had a non-chondritic composition. We have explored means to generate magmatic fractionation of Mg isotopes during crystallization of a magma ocean, potentially formed during previous accretionary impacts. Mg-perovskite has significant potential to fractionate Mg, forming a major host of Mg during differentiation with a different co-ordination environment to the melt. We have used density functional theory to estimate the magnitude of Mg isotopic fractionation by Mg-perovskite and conclude that this is a plausible means to generate radial differences in Mg isotopic composition in a differentiated planetary body. If Mg-perovskite is key to generating superchondritic Mg-isotopic compositions on Earth, this has important implications for the sizes of the bodies involved in Moon forming impact. Producing a magnesium-perovskite derived signature is much more difficult to explain in two bodies of half-Earth mass than in a more massive one (later impacted by a smaller one).

References: [1] Canup R. and Asphaug E. (2001) *Nature*, 412, 708-712. [2] Cuk M. and Stewart S. (2012) *Science*, 338, 1047-1052. [3] Canup R. (2012) *Science*, 338, 1052-1055. [4] Sedaghatpour et al. (2013) *GCA*, 120, 1-16., 1344-1345. [4] Pahlevan (2011) *EPSL*, 301, 433-443.

Introduction: Zircon's unique chemical characteristics, notably its enrichment in U, HREE and Hf, create an opportunity to constrain the origin and age of its source rocks. The remarkable physical resistance of zircon also ensures that these characteristics are preserved and accessible for study even when it is separated from its host, for example in sedimentary rocks on the Earth or impact and regolith breccias as well as soils on the Moon and Mars.

This presentation aims to compare the isotopic and trace element signatures preserved in zircon grains from the Moon, Mars and Earth. Such a comparison can help to reconcile existing diverse interpretations of individual zircon suites, which remain highly controversial.

Zircon grains with ages exceeding 3.9 Ga have been known to exist in some metasedimentary rocks in Western Australia since the early 1980's [1] and have been extensively studied during the last decade to gain information about the early stages of Earth's evolution [2-4]. These studies, although still a subject of substantial debate, have resulted in some profound changes in our understanding of Earth's history.

The first lunar zircon grains were also analysed in the early 1980's [e.g. 5] and since then more have been found in a significant number of lunar highland breccia samples, where they are commonly associated with a variety of rock clasts ranging in composition from troctolites and anorthosites to quartz-monzodiorites and granites.

Discovery of Martian zircon grains in the meteorite sample NWA 7533 interpreted as regolith breccia was reported last year. Zircon present in this sample is found both as separate mineral fragments and included in monzonite clasts.

U-Pb ages: The oldest terrestrial zircon grain was found in the detrital population from a conglomerate sample collected at Jack Hills (Western Australia) and reported to be 4404 ± 8 Ma [2]. However, this age is based on a single analysis within a single zircon grain and a more reliable age estimate of the oldest terrestrial zircon, obtained using several grains from the same detrital population is 4370 Ma. Remarkably 4370 Ma also marks the start of one of the major peaks in the zircon age distribution pattern of lunar zircons, although four grains from the Moon appear to be older with ages between 4.40 and 4.42 Ga. A similar age of 4428 ± 25 Ma was determined for the oldest Martian zircon [6]. The overall age distribution patterns of lunar and terrestrial zircons show broad similarities, comprising several major peaks, that, while not coinciding precisely, indicate extensive magmatic activity on both Moon and Earth. While

the Martian zircon pool is more restricted, the variability of their ages [6, 7] suggests a possibility of similar activity on Mars. Finally an important characteristic of terrestrial zircon grains is the variability of ages recorded within individual crystals, which suggests multiple periods of ancient reworking during metamorphism and/or partial melting, resulting in preservation of inherited cores with multiple complex overgrowths and recrystallization domains. Similar features are absent in lunar zircon, where the possible presence of inherited grains has not been demonstrated convincingly so far; limited examples where different parts of individual grains show different ages are interpreted as a reflection of impact related modification of these grains [8]. In turn unambiguous evidence for impacts has not (yet) been observed in the ancient terrestrial populations. On Mars partial Pb loss towards 1.4-1.7 Ga [6, 7] is recorded in some zircon grains, while others define upper intercept ages close to 1.4 Ga, tentatively interpreted as the age of a major impact that consolidated the host breccia sample. However, more work is needed to determine if these ages are true representation of an impact or can reflect new magmatic (or metamorphic) growth or even some low temperature Pb loss from zircon fragments residing for a long time in the Martian regolith.

Regardless of remaining questions, it is becoming increasingly clear that by about 4.4 Ga Earth, Moon and Mars had formed geochemically distinct enriched reservoirs capable of generating melts, which can crystallise zircon after some degree of fractionation. On the Moon this reservoir is identified as KREEP, a residuum of magma ocean fractionation, which is perhaps uniquely linked to the specific crystallisation sequence resulting in the formation of mafic cumulates followed by flotation of anorthositic crust and separation of Ti-rich phases. On Mars, the early crust sampled by NWA 7533 clast-laden melt rock particles and crystalline matrix of the sample, is compositionally similar to alkali basalt [6]. It was successfully modelled by low (<4%) degree partial melting of a garnet bearing Martian mantle and did not require a specific K, REE, P-enriched reservoir in the early Martian mantle [6]. While the source of the Jack Hills zircon is unknown, discovery of Martian grains of similar age (or slightly older) and also with very similar chemical and isotopic characteristics, indicates that zircons on Earth could have been formed as a result of remelting of similar, evolved basaltic crust rather than continental crust comparable to that existing on the Earth today.

Ti-temperatures: Temperature estimates for Martian zircon are at the higher end or slightly above

the range recorded in the Jack Hills grains. However, they indicate that both planets have conditions (i.e. water) that could have produced low temperature melts. The observed difference can readily be explained by the slight difference in the host rocks on Mars and Earth. Martian zircon is related to monzonite, which explains the somewhat elevated temperature of their crystallisation. While the source of Jack Hills zircon remains elusive, slightly lower temperatures, ranging between about 600 and 700°C, indicate the possibility of more granite-like differentiates as their host rocks. In contrast, all lunar zircon grains indicate formation temperatures in excess of 900°C, with the majority showing Ti-temperatures between 1000 and 1200°C.

REE patterns: The overall REE patterns of the three groups of zircon grains generally reflect the ability of zircon to incorporate different trivalent ionic radius REE into its lattice and are therefore mostly similar and characterised by enrichment in heavy REE and significant depletion in light REE. However, a significant difference between terrestrial and Martian zircon on the one hand and lunar grains on the other is shown by Ce behaviour, which can exist either as Ce(III) or Ce(IV), the latter partitioning very favourably into zircon. The Ce anomaly in the Jack Hills zircons has been interpreted as evidence of an oxidised environment during their formation [9]. Similarly, REE patterns of Martian grains indicate oxidising conditions during their crystallisation. However, the majority of lunar zircon do not show a Ce-anomaly, which is taken as a confirmation of reducing conditions that exist on the Moon. Nevertheless, several zircon grains from lunar breccia samples exhibit a clear positive Ce-anomaly, suggesting that the concentration of Ce in zircon is a factor of very localised change in oxidation conditions, rather than feature that can be used to infer global oxidation state of major planetary reservoirs. Consequently, it is not possible to determine whether the source of the monzonitic melt crystallising zircon on Mars was oxidized or instead, oxidising conditions were a result of melt formation and fractionation. Chlorine-rich volatile degassing, water dissociation and hydrogen escape are processes capable of strongly affecting the oxygen fugacity during magmatic differentiation [10-13]. Similarly, the presence of Ce-anomaly in terrestrial zircon should not be taken as *a priori* evidence of oxidizing conditions existing on the Earth during the early history of the planet

O isotope compositions: The observed variability of oxygen isotope compositions indicates that Mars was not homogenised with respect to oxygen, resulting in variable $\Delta^{17}\text{O}$ in different zircon grains. In addition within grain variation of $\delta^{18}\text{O}$ exceeds range that can be formed as a result of magmatic fractionation, with some estimates as heavy as 7-8‰ and one even up to 10‰. A similar spread in $\delta^{18}\text{O}$ in the Jack Hills zircon suite has been

interpreted as a primary feature indicative of sediment recycling and presence of surface water on the Hadean Earth. However, study of oxygen isotope compositions in Martian zircon shows that variations of $\Delta^{17}\text{O}$ and $\delta^{18}\text{O}$ are not correlated and while one can be an indication of assimilation of surface materials by the magma during the zircon formation, the other has to be related to the reaction of metamict zircon with a low temperature fluid near the surface, significantly long after the zircon crystallisation. This also suggests that perhaps some of heavy oxygen compositions in the Jack Hills grains could be a result of very late alteration of these zircons during an intense lateritic weathering of the Australian continent. This possibility is also supported by U-Pb systems of investigated Martian and terrestrial grains. Both show clear evidence of secondary disturbance of their U-Pb system resulting in formation of discordia arrays on Concordia diagrams. On Mars the discordia has a lower intercept at 1.7-1.6 Ga, while Jack Hills zircon grains are affected by a recent Pb loss. Sample NWA7533 is interpreted as an impact breccia, therefore it is likely that the secondary disturbance of the U-Pb system is induced by impact or impacts at about 1.7-1.6 b.y. In contrast, in terrestrial zircon it is related to the regolith development in Australia. Consequently it is also possible that the surface weathering is at least partly responsible for the observed Pb loss on Mars and the planet could have developed regolith and weathering processes, similar to those currently occurring in Australia, prior or close to 1.7-1.6 Ga.

Contrary to the variability of oxygen isotope compositions observed in Martian and terrestrial zircon, lunar grains show an isotope composition of oxygen that is very restricted and mantle-like, consistent with the high temperature, low fluid concentration melts and an absence of post-crystallisation surface processes involving water, chemical weathering and sedimentary transportation.

References: [1] Froude, D. O. *et al.* (1983) *Nature* 304, 616–618, [2] Wilde, S.A. *et al.* (2001) *Nature* 409, 175-178, [3] Harrison, T.M. *et al.* (2005) *Science* 310, 1947-1950, [4] Peck, W.H. *et al.* (2001) *Geochim Cosmochim Acta* 65, 4215-4229, [5] Compston W. *et al.* (1984) *J. Geophys. Res.*, 89, B525-B534, [6] Humayun, M. *et al.* (2013) *Nature*, 503, 513-516, [7] Yin, Q.Z. *et al.* (2014) 45th LPSC., Abstract #1320, [8] Nemchin, A.A. *et al.* (2009) *Nature Geoscience*, 2, 133-136, [9] Trail, D. *et al.* (2011) *Nature*, 480, 79-82, [10] Sato M., and Wright T.L., (1966) *Science* 153, 1103–1105, [11] Candela P.P. (1986) *Geochim Cosmochim Acta*, 50, 1205–1211, [12] Mathez E.A. (1984) *Nature* 310, 371-375, [13] Bell A.S. and Simon A. (2011) *Geology* 39, 499- 502.

CORE-MANTLE DIFFERENTIATION IN THE MOON: CONSTRAINTS FROM METAL-SILICATE PARTITIONING OF MODERATELY SIDEROPHILE ELEMENTS IN A HYDROUS MAGMA OCEAN. E. S. Steenstra¹, N. Rai², W. van Westrenen¹ ¹Faculty of Earth and Life Sciences, VU University Amsterdam, The Netherlands (e.s.steenstra@student.vu.nl), ²Department of Earth and Planetary Sciences, Birkbeck University of London, UK (n.raï@ucl.ac.uk).

Introduction: Most planetary differentiation models derive constraints on core formation conditions based on the abundance pattern of siderophile elements in planetary mantles [1-5]. These abundance patterns are used to derive conditions at which liquid metal and liquid silicate equilibrated during core formation through experimental metal-silicate partitioning data. Virtually all experiments used to link abundance patterns to core formation models were performed in nominally dry conditions. Although water is known to play a critical role in early planetary evolution [6-8], only two metal-silicate partitioning studies were performed in hydrous systems [9,10]. Because of this lack of data the effect of water on metal-silicate partitioning is very poorly constrained. This was not thought to be an issue in core formation models for the Moon, because until recently it was widely accepted that the Moon accreted dry and never contained any interior water. However, several recent studies have now shown that the Moon did contain indigenous water [11-14]. As current predictive models for metal-silicate partitioning (D) are based on experimental data in anhydrous systems, they may not be appropriate for constraining conditions of core-mantle differentiation of the Moon. This study aims to quantitatively assess the effect of water abundance on metal-silicate partitioning of moderately siderophile elements at lunar relevant pressure-temperature conditions.

Approach: We performed high pressure (1.0-2.5 GPa) and high temperature (1623-1850K) experiments to assess the effect of water abundance on metal-silicate partitioning of Fe, Mn, Cr, P, W, Co, Ni, Mo and Ti. Experiments were conducted with two silicate compositional series consisting of synthetic analogs of the basaltic Apollo 15C green glass [15] and a lunar granite [16]. Silicates were mixed with Fe-powder doped with 1.5 wt. % Ni, Co, Mo, W, P. Experiments were performed at either constant composition, pressure (P) or temperature (T), to reduce the number of variables. Abundances of major elements were assessed with electron microprobe analysis (EMPA) and trace element were measured by electron microprobe and laser ablation inductively coupled mass spectroscopy (LA-ICPMS). In this abstract we only discuss electron microprobe data. After careful calibration and procedures to reduce Na-loss and Al-Si grow-in according to [17], water contents were approximated via EMPA deficiencies from 100%. Raman

spectroscopy was applied to investigate the speciation of water in our experiments. The dependence of metal-silicate partition coefficients on P, T, fO_2 and silicate melt structure and composition can be characterized to derive the following expressions [5]:

$$\log D = a + b(\Delta IW) + c(nbo/t) + d(1/T) + e(P/T) + f \ln(1-X_c) + g(C-O-H) \quad (1)$$

$$\log D = a + b(\Delta IW) + \sum c_i X_i + d(1/T) + e(P/T) + f \ln(1-X_c) + g(C-O-H) \quad (2)$$

In Eqs. (1,2), X_c is the molar value of carbon in the metallic phase, X_i is the mole fraction of oxide i in the silicate phase and C-O-H is the C-O-H abundance in the silicate (in wt.%). All metal-silicate partitioning data obtained in this study were corrected to common reference points of Eqs. (1,2) [4,5]. This approach allows us to isolate the effect of water abundances on element distribution.

Results: Run products show well segregated Fe-rich metallic blobs in a silicate glass matrix. Time series experiments show that a 2 minute run duration at peak conditions is sufficient for attaining equilibrium in hydrous systems (Figure 1).

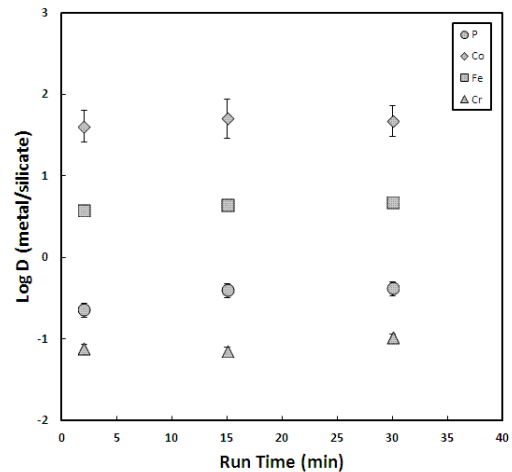


Figure 1: Log $D^{\text{met-sil}}$ of green glass experiments obtained at 1.5 GPa and 1773K as a function of run duration. Errors are maximum errors.

After careful calibration, electron microprobe analysis of hydrous experimental charges shows consistent deficiencies in totals of both silicate and metallic phases, corresponding to dissolved C-O-H species and carbon, respectively [17,18]. The

presence of C-O-H species is confirmed by Raman analysis, which showed broad peaks at $\pm 3400\text{--}3650\text{ cm}^{-1}$ corresponding to the vibration of OH⁻ bonds [19]. Another notable feature is the increase of depolymerisation of the silicate melt with C-O-H contents, also proposed by [9,19,20].

Comparing measured D's from the green glass series with anhydrous D's obtained by predictive equations based on dry data only [5], we observe that some elements appear to be completely unaffected (e.g. Co, Fe). Other elements including P and W do show an effect of water on D values. D(W) are consistently higher in hydrous systems than predicted anhydrous values. Experiments performed in the lunar granite composition also show higher hydrous D(P) relative to predicted anhydrous values at higher water contents.

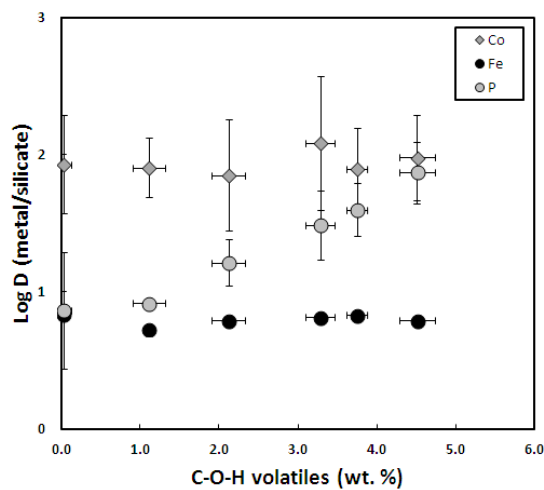


Figure 2: Log $D^{\text{met-sil}}$ of lunar granite experiments obtained at 1.5 GPa and 1623-1773K as function of C-O-H abundance. D's are parameterized to common reference points of T, Xc, NBO/t and $f\text{O}_2$. Horizontal errors are two standard deviations and vertical errors are maximum errors.

Parameterization of obtained experimental data to specifically isolate C-O-H effects show that P (Figure 2) and possibly Mo are indeed more preferentially incorporated in the metallic phase with C-O-H contents. The increase of P is consistent with previous work [10] and is believed to be related to the higher valence state of P relative to the other low valence siderophiles. Preliminary modelling results suggests low valence D(Fe), D(Mn), D(Cr), D(Co) as well as oxygen fugacity are largely unaffected by volatile presence (Figure 2). Despite the difference between hydrous and anhydrous D(W) and increase of D(Mo) with C-O-H contents, preliminary data does not allow us to quantify this effect until we obtain LA-ICPMS measurements.

Discussion: Our preliminary findings suggest that the observed effect of water on the metal-silicate

partitioning behaviour of siderophile elements will yield different interpretations of P-T settings of lunar core formation relative to anhydrous models. Taking into account the distinctive partitioning behaviour of P and possibly Mo and W between hydrous and anhydrous conditions together with the unaffected behaviour of low valence Fe, Ni, Co, Cr and Mn, the areas in P-T space where the lunar mantle abundances of all these elements are simultaneously reproduced could be different from anhydrous models [5].

Outlook: As recent studies point to a hydrous lunar interior [11-14], previously derived conditions of lunar core-mantle equilibration under anhydrous conditions will have to be reconsidered. Future work should be primarily focused on obtaining additional hydrous metal-silicate partitioning data for both moderately and highly siderophile elements. Data obtained with LA-ICPMS analysis (ongoing) and additional Raman analysis of our experiments will be reported at the meeting.

References: [1] Wade J and Wood B.J. (2005) *EPSL*, 236, 78-95 [2] Cottrell E et al. (2009) *EPSL*, 281, 275-287 [3] Siebert J et al. (2012) *EPSL*, 321-322, 189-197 [4] Rai N and van Westrenen W (2013) *JGR, Planets* 118, 1195-1203 [5] Rai N and van Westrenen W (2014) *EPSL*, 388, 343-352 [6] Fukai Y and Suzuki T (1986) *JGR*, 91, 9222-9230 [7] Righter K et al. (1997) *V.M. Goldschmidt Conf.*, 176 [8] Righter K (2003) *Annu. Rev. Earth Planet. Sci.*, 31, 74-135 [9] Jana D and Walker D (1999) *Geochim. Cosmochim. Acta.*, 63, 2299-2310 [10] Righter K and Drake M.J. (1999) *Earth Planet.Sci.Lett.*, 171, 383-399 [11] Saal A.E. et al. (2008) *Nature*, 454, 192-196 [12] Hauri E.H. et al. (2011) *Science*, 333, 213-215 [13] Hui et al. (2013) *Nature Geoscience*, 6, 177-180 [14] Saal A.E. et al. (2013) *Science*, 340, 1317-1320 [15] Delano J.W. (1986) *Proc. Lunar Plan. Sci. Conf. 16th Pt. 2*, *JGR*, 91, D201-D213 [16] Warren P.H. et al. (1983) *Earth Planet.Sci.Lett.*, 64, 175-185 [17] Morgan VI G.B. and London D (1996) *Am. Min.*, 81, 1176-1185 [18] Nash W.P. (1992) *Am. Min.*, 77, 453-457 [19] Mysen B.O. and Yamashita S (2010) *Geochim. Cosmochim. Acta.*, 74, 4577-4588 [20] Dasgupta R et al. (2013) *Geochim. Cosmochim. Acta.*, 102, 191-212.

LUNAR CORE FORMATION: ADDITIONAL CONSTRAINTS FROM METAL-SILICATE PARTITIONING OF GERMANIUM AND THE HIGHLY SIDEROPHILE ELEMENTS. N. Rai^{1,2}, W. van Westrenen² ¹Centre for Planetary Sciences, Birkbeck-UCL, London, UK, ²Faculty of Earth and Life Sciences, VU University, Amsterdam, The Netherlands (n.raai@ucl.ac.uk).

Introduction: A major result of core-mantle differentiation in the terrestrial planets is that the bulk of the siderophile elements are strongly partitioned into the iron-rich metallic core, leaving the silicate mantle and crust relatively depleted in those elements. Since the partitioning of these elements into metallic phases is governed by their metal/silicate partition coefficients (D) and the pressure-temperature-composition-redox conditions during core-mantle differentiation, the measured or estimated abundances of these elements in a planet's silicate reservoirs can in principle be used to constrain core formation conditions [1-4]. Re-analyses of Apollo era seismograms using advanced array processing methods suggest the presence of a small, at least partially molten Fe-rich metallic core in the Moon [5]. Combining measurements of the metal-silicate partitioning behavior of Ni, Co, W, Mo, P, V and Cr with the estimated depletions of those elements in the silicate mantle of the Moon, we modeled the physical and chemical conditions during lunar core formation [1]. We used published metal-silicate partitioning data for Ni, Co, W, Mo, P, V and Cr in the lunar pressure range (1 atm–5 GPa) and characterized the dependence of the metal/silicate partition coefficients (D) on temperature, pressure, oxygen fugacity and composition of the silicate melt and the metal. If the core is assumed to consist of pure iron, core-mantle equilibration conditions that best satisfy lunar mantle depletions of five siderophile elements—Ni, Co, W, Mo and P—are a pressure of 4.5(±0.5) GPa and a temperature of 2200 K. The lunar mantle depletions of Cr and V are also consistent with metal-silicate equilibration in this pressure and temperature range if 6 wt% S is incorporated into the lunar core. Our results therefore suggest that metal-silicate equilibrium during lunar core formation occurred at depths close to the present-day lunar core-mantle boundary. This provides independent support for both the existence of a deep magma ocean in the Moon in its early history and the presence of significant amounts of sulfur in the lunar core.

Approach: Here, we extend our previous work by including additional elements into our lunar core formation model [1]. We test whether the lunar mantle depletions in the moderately siderophile and moderately volatile element Ge [6] and the highly siderophile elements (HSEs) including Re, Os, Ir, Ru, Pt and Re [7,8] can be accounted for by metal-silicate equilibration in a magma ocean scenario. In the widely popular model for the formation of the Earth-Moon system, the Moon formed as a by product of a giant impact [9,10] between a Mars-sized planetesimal and the proto-Earth. However,

this model produces a Moon that is predominantly composed of the impactor and not the proto-Earth [11]. Considering the isotopic similarities [12-14] between the Earth and the Moon and latest dynamical models [15,16] that can produce the Moon from the proto Earth, we also test whether the model outcome for conditions of lunar core formation [1] would change if the BSE (Bulk silicate Earth) composition was assumed as the bulk Moon composition. For modeling the data we follow the same methodology as [1].

Results: Results indicate that the estimated lunar mantle abundance of Ge can be explained by metal-silicate equilibration at conditions of 4.5(±0.5) GPa, 2200 K and under redox conditions of $\Delta IW-2$, consistent with our previous results [1]. We find that the estimated lunar mantle abundances of the highly siderophile elements Os, Ir, Ru, Pt, Pd and Re could not be matched under these conditions. Our calculations show that unless the lunar mantle abundances for these elements are overestimated by orders of magnitude, it is impossible to account for the lunar mantle depletions of these elements by core-mantle equilibration in a magma ocean. Our results support the hypothesis of the subsequent addition of primitive, HSE-rich undifferentiated materials to the lunar mantle after core segregation which can explain both the absolute and relative abundances of the HSEs in the lunar mantle [7,8].

References: [1] Rai N. and van Westrenen W. (2014) *EPSL*, 388, 1-10. [2] Righter K. and Drake M. J. (1996) *Icarus*, 124, 513-529 [3] O'Neill H. S. C. (1991) *GCA*, 55, 1135-1157 [4] Walter M. J. et al. (2000) In *Origin of the Earth and Moon*, U of A Press, Tucson, 265-289 [5] Weber R.C. et al. (2011) *Science*, 331, 309-312 [6] Righter K. et. al. (2011) *EPSL*, 304, 379-388. [7] Dale C. W. et al. (2012) *Science*, 336, 72-75. [8] Day J. M. D. et al. (2007) *Science*, 315, 217-219. [9] Cameron A. G. W. and Ward W. R. (1976) *The origin of the Moon*. In: Merrill, R.B., et al. (Eds.), *Proc. 7th Lunar Planet. Sci. Conf.*, LPI, Houston, pp. 120-122. [10] Hartmann W. K. and Davis D. R. (1975) *Icarus*, 24, 504-515. [11] Canup R. M. (2008) *Icarus*, 196, 518-538. [12] Clayton, R. N. & Mayeda, T. K. (1996) *Geochim. Cosmochim. Acta*, 60, 1999-2017. [13] Touboul M. et. al. (2007) *Nature*, 450, 1206-1209. [14] Armytage R. M. G. et. al. (2012) *Geochim. Cosmochim. Acta*, 77, 504-514. [15] Čuk M. and Stewart S. T. (2012) *Science*, 338, 1047-1052. [16] Canup, R. M. (2012) *Science*, 338, 1052-1055.

Introduction: The most widely accepted model for the formation of the Moon involves a giant impact onto proto-Earth near the end of Earth's accretion. Some of the most important constraints on lunar origin are provided by the similar O, Ti and W isotope compositions of the Earth and Moon, indicating that the Moon predominantly consists of material derived from the proto-Earth's mantle [1-3]. The most recent simulations of the Moon-forming impact are consistent with this [4-6]. The similar $^{182}\text{W}/^{184}\text{W}$ ratios of the bulk silicate Earth (BSE) and Moon are particularly important, because ^{182}W is the decay product of now-extinct ^{182}Hf . The $^{182}\text{W}/^{184}\text{W}$ of the bulk silicate portion of a planetary body mainly depends on the timescale and conditions of core formation, such that it is very unlikely that two distinct bodies have identical W isotope compositions. If the Moon contains a large fraction of impactor mantle material it would, therefore, be expected to have a $^{182}\text{W}/^{184}\text{W}$ different from that of the BSE.

Recently, small ^{182}W heterogeneities have been identified in the Earth's mantle. These have been interpreted to reflect the W isotope composition of Earth's mantle prior to addition of the late veneer [7] or to result from metal-silicate fractionation processes during accretion and differentiation of the Earth prior to the Moon-forming impact [8]. This raises the question as to whether the Moon has the same $^{182}\text{W}/^{184}\text{W}$ as the pre-late veneer BSE. Precisely constraining the $^{182}\text{W}/^{184}\text{W}$ of the Moon is difficult, however, due to cosmic-ray induced neutron capture (NC) reactions modifying ^{182}W abundances [9]. We have recently shown that non-radiogenic Hf isotopes are well suited as a neutron dosimeter for lunar samples [10], making it possible to identify samples devoid of NC effects and to determine the neutron fluence for a given sample. Here we present new high-precision W and Hf isotope data for KREEP-rich samples, which are used to precisely determine the pre-exposure $^{182}\text{W}/^{184}\text{W}$ of the Moon (i.e., the $^{182}\text{W}/^{184}\text{W}$ unaffected by any NC effects). This value is then used to constrain the age and origin of the Moon.

Samples and analytical methods: To identify samples devoid of significant neutron capture effects we investigated the non-radiogenic Hf isotope composition of 20 lunar samples including 6 KREEP-rich whole rocks, 8 low-Ti-, and 6 high-Ti mare basalts. These data are published in [10]. For the present study some of the KREEP-rich samples were selected for high-precision W isotope analyses. Isotope analyses were conducted on the Neptune Plus MC-ICPMS at the University of Münster using

our established techniques [e.g., 11]. The W isotope data are reported as $\epsilon^{182}\text{W}$ values, which is the part per 10^4 deviation from the $^{182}\text{W}/^{184}\text{W}$ of the terrestrial standard. Hafnium isotope data are given as ppm deviations (μ -values) from terrestrial Hf.

Results: The selected KREEP-rich samples exhibit variable NC effects with $\mu^{180}\text{Hf}$ values ranging from *ca.* 0 to *ca.* -300. The same samples exhibit variable $\epsilon^{182}\text{W}$ from *ca.* 0.3 to *ca.* 1.8. In a plot of $\epsilon^{182}\text{W}$ vs. $\mu^{180}\text{Hf}$ the investigated samples define a single correlation line, whose intercept at $\mu^{180}\text{Hf} = 0$ provides the pre-exposure $\epsilon^{182}\text{W} = 0.31 \pm 0.10$ for KREEP (Fig. 1). This value is mainly defined by two of the samples—14321 and 68815—which show no resolved NC effect on their Hf isotope compositions.

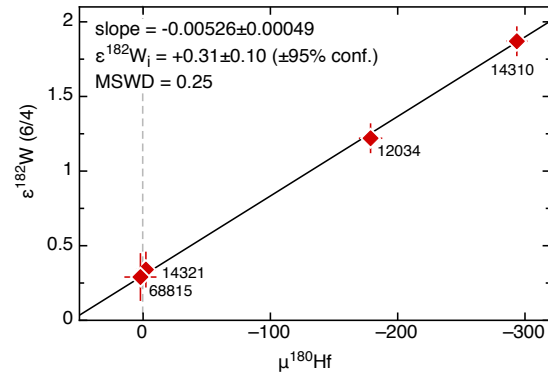


Figure 1: $\epsilon^{182}\text{W}$ vs. $\mu^{180}\text{Hf}$ for KREEP-rich samples investigated in the present study. The intercept $\epsilon^{182}\text{W}$ at $\mu^{180}\text{Hf} = 0$ defines the pre-exposure $\epsilon^{182}\text{W}$ of KREEP. Hf isotope data from [10].

Discussion: $\epsilon^{182}\text{W}$ of the Moon. Touboul et al. [1] showed that there are no radiogenic ^{182}W isotope variations among different lunar samples, indicating that the crystallization of the lunar magma ocean occurred after extinction of ^{182}Hf , i.e., more than *ca.* 60 million years (Ma) after solar system formation. This is consistent with other evidence for differentiation of the Moon *ca.* 150 Ma after solar system formation. The pre-exposure $\epsilon^{182}\text{W}$ of KREEP, therefore, also represents that of the bulk silicate Moon and most likely also that of the bulk Moon (see below).

Comparison to Earth. The $\epsilon^{182}\text{W}$ value of the bulk silicate Moon of $+0.31 \pm 0.10$ determined in the present study is slightly higher but not resolved from small ^{182}W excesses identified in samples from the Isua supracrustal belt [7] and in some komatiites [8]. Willbold et al. [7] have argued that the elevated $\epsilon^{182}\text{W}$ of $+0.13 \pm 0.04$ they determined for Isua samples reflects the W isotope composition of the

BSE before addition of the late veneer. The fraction of late accreted material in the Isua source is not known, however. The source of the Kostomuksha komatiites contains about *ca.* 80% of late accreted material, and has $\epsilon^{182}\text{W} = +0.15 \pm 0.05$ [8]. However, Komati komatiites, which derive from a source containing only *ca.* 40% of late accreted material, show no resolved ^{182}W anomaly [8].

Fig. 2 shows the calculated effect of late accretion on the $\epsilon^{182}\text{W}$ value of the BSE, and illustrates that the $\epsilon^{182}\text{W}$ value of the pre-late veneer BSE probably is between *ca.* 0.1 and *ca.* 0.3, depending on the total mass of the late accreted material. Thus, the $\epsilon^{182}\text{W}$ of the bulk silicate Moon overlaps with that of the pre-late veneer BSE.

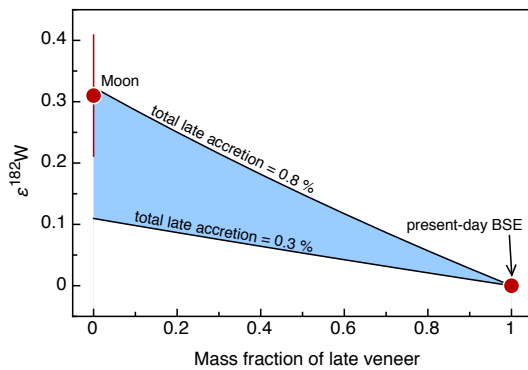


Figure 2: $\epsilon^{182}\text{W}$ vs. mass fraction of late accreted material. The present-day BSE has $\epsilon^{182}\text{W} = 0$. For the late accreted material a W concentration of 200 ppb and $\epsilon^{182}\text{W} = -1.9$ were assumed.

Implications for the origin of the Moon. There is now abundant evidence for the existence of a small lunar core, and the common interpretation is that the lunar core probably consists of impactor core material. The Moon, therefore, is a mixture of three components: impactor mantle, impactor core, and proto-Earth's mantle. These three components most likely were characterized by distinct $\epsilon^{182}\text{W}$ values. Due to early metal segregation, the impactor core almost certainly was characterized by an deficit in ^{182}W , while the impactor mantle had an ^{182}W excess. The proto-Earth's mantle also had an ^{182}W excess, which probably was different from that of the impactor mantle.

Given the presence of three components having distinct $\epsilon^{182}\text{W}$ in the Moon, it is remarkable that the pre-exposure $\epsilon^{182}\text{W}$ of the bulk silicate Moon is so similar to that of the pre-late veneer BSE. The most straightforward interpretation of this similarity would be that the Moon almost entirely consists of terrestrial mantle material. This interpretation would be consistent with the similar Ti and O isotope compositions of the Earth and Moon [2,3], but cannot easily account for the presence of a small lunar core. An alternative interpretation is that the particular mixture of impactor mantle, impactor core

and proto-Earth's mantle making the Moon by coincidence has similar $\epsilon^{182}\text{W}$ than the pre-late veneer BSE. Although such a scenario cannot be excluded, it seems highly unlikely. Note, however, that the inferred $\epsilon^{182}\text{W}$ of bulk silicate Mars of $+0.45 \pm 0.15$ [12] also is very similar to the value inferred here for the bulk silicate Moon. This may indicate that $\epsilon^{182}\text{W}$ values of *ca.* 0.3-0.4 are a common outcome of the terrestrial planet formation process [see 13]. Finally, the similar $\epsilon^{182}\text{W}$ of the Moon and pre-late veneer BSE may also be a direct outcome of the Moon-forming process itself. In this case, the similar $\epsilon^{182}\text{W}$ values would indicate efficient mixing of impactor and proto-Earth's mantle during the impact, such that the *bulk* Moon and the proto-Earth's mantle would have the same $\epsilon^{182}\text{W}$. Such efficient, large-scale mixing would require a very large impact, such as in the proposed collisions between two half-Earths [4].

Implications for the age of the Moon. The similar $\epsilon^{182}\text{W}$ of the bulk silicate Moon and the BSE imply that the Moon formed after extinction of ^{182}Hf , *i.e.*, more than 50 Ma after solar system formation. If the Moon would have formed earlier, when ^{182}Hf was still extant, then the $\epsilon^{182}\text{W}$ of the bulk silicate Moon would be different from that of the bulk Moon (because the lunar core would have an ^{182}W deficit compared to the mantle). If this was the case, then the similar $\epsilon^{182}\text{W}$ of the bulk silicate Moon and the BSE would be entirely coincidental, which seems highly unlikely.

Conclusions: The $\epsilon^{182}\text{W}$ of the Moon is slightly elevated to that of the present-day bulk silicate Earth, but is indistinguishable from the composition of the bulk silicate Earth prior to addition of the late veneer. This similarity is unlikely to be coincidental, but provides important constraints on lunar origin. Either the Moon almost entirely is derived from terrestrial mantle material, or there was efficient mixing of impactor mantle, impactor core and proto-Earth's mantle during the giant impact. In either case, the W isotope data are best accounted for if the Moon formed 'late', *i.e.*, more than 50 Ma after solar system formation.

References: [1] Touboul M. et al. (2007) *Nature*, 450, 1206-1209. [2] Wiechert U. et al. (2001) *Science*, 294, 345-348. [3] Zhang J.J. et al. (2012) *Nature Geoscience*, 5, 251-255. [4] Canup R.M. (2012) *Science*, 338, 1052-1055. [5] Cuk M. and Stewart S.T. (2012) *Science*, 338, 1047-1052. [6] Reufer A. et al. (2012) *Icarus*, 221, 296-299. [7] Willbold M. et al. (2011) *Nature*, 477, 195-199. [8] Touboul M. et al. (2012) *Science*, 335, 1065-1069. [9] Leya I. et al. (2000) *EPSL*, 175, 1-12. [10] Sprung P. et al. (2013) *EPSL*, 380, 77-87. [11] Kruijer T.S. et al. (2013), *EPSL*, 361, 162-172. [12] Kleine T. et al. (2009) *GCA*, 73, 5150-5188. [13] Nimmo F. et al. (2010) *EPSL*, 292, 363-370.

EXPLORING THE LUNAR SOUTH POLAR REGION AND FAR SIDE WITH HUMAN AND HUMAN-ASSISTED SAMPLE RETURN MISSIONS. D. A. Kring^{1,2} ¹Center for Lunar Science and Exploration, USRA-Lunar and Planetary Institute, 3600 Bay Area Blvd., Houston, TX 77058 USA, ²Solar System Exploration Research Virtual Institute (kring@lpi.usra.edu).

Introduction: There is broad international consensus that exploration of the Moon can address fundamentally important scientific questions (e.g., [1,2]) while providing a credible path that carries exploration beyond low-Earth orbit (e.g., [3]). Yet, we have never explored the lunar polar regions or the lunar far side with a lander, rover, or sample return mission. The polar regions and the far side remain *luna incognita*.

Intriguingly, orbital assets, supplementing the insights gained through the Apollo and Luna programs, indicate the Moon is the best and most accessible place in the Solar System to deduce processes associated with planetary accretion, differentiation, formation of primitive planetary crust, and impact modification of that crust.

One of the most comprehensive studies of lunar exploration objectives [1] outlined eight scientific concepts and thirty-five prioritized investigations. A series of summer studies, spanning five years, were conducted to identify every location on the lunar surface where those investigations could be addressed. The final summary of those studies [4] concluded that the majority of the objectives could be addressed in the South Pole-Aitken basin if exploration was limited to that region; that Schrödinger basin, which is within the South Pole-Aitken basin, is the scientifically-richest site; and that Amundsen crater, along the margin of the South Pole-Aitken basin, may be a better location to study volatiles than Shackelton crater.

Schrödinger Basin: This ~320 km diameter impact basin is the second youngest basin and the best preserved of its size. It is located in the modification zone of the South Pole-Aitken basin, the oldest recognizable basin on the Moon. A sample return mission to Schrödinger has the potential of determining the duration of the basin-forming epoch and testing the lunar cataclysm hypothesis [5,6], effectively addressing the two highest science priorities of [1].

In addition, because the basin is so well preserved, it is a perfect target for discerning the geological processes of basin-size impacts.

Those processes uplifted material from great depth, producing a peak ring of crystalline massifs that expose lithologies that can be sampled to test the lunar magma ocean hypothesis. That material, when combined with material exposed in the basin walls and that survives as clasts within impact breccias, can be used to reconstruct a cross-section of the lunar crust. The Schrödinger impact melt can be used to derive the bulk composition of that crust.

Long after the impact melt had solidified, magmas rose through the basin and erupted on the basin floor, producing mare basalt flows and an immense pyroclastic vent. Both of those volcanic products can be used to probe the thermal evolution of the lunar interior.

The pyroclastic vent (Figure 1) is a potential *in situ* resource utilization (ISRU) target and, for that reason, was one of the sites observed during the human-precursor exploration phase of the Lunar Reconnaissance Orbiter mission. The vent may provide volatile deposits and fine-grained material that is easily excavated, transported, and processed for a sustainable exploration effort.

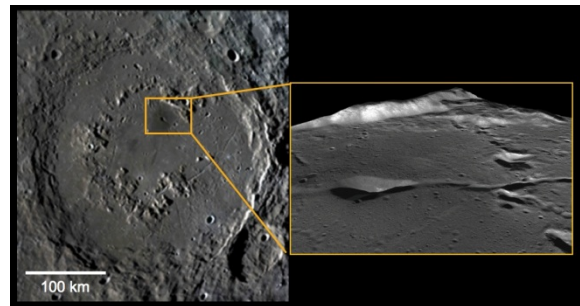


Figure 1: An immense pyroclastic vent on the floor of the Schrödinger basin that was targeted for its ISRU potential by the Exploration Systems Mission Directorate's portion of the Lunar Reconnaissance Orbiter mission.

Because Schrödinger is so well preserve and the diversity of geological processes so broad, a majority of the issues outlined in [1] can be addressed with sample return missions to/from this structure [4].

Studies have identified several landing sites and geologic stations for human sample return missions [5,7]. Studies have also identified several landing sites for human-assisted sample return missions [8-10]. In the latter context, a robotic asset on the surface would be coordinated with crew in an Orion vehicle in an orbit around the Earth-Moon L2 point [11] or in a distant retrograde orbit.

Schrödinger basin is also a good location for the deployment of a low-frequency radio antenna to address astrophysical science objectives [11].

Amundsen Crater: If one instead focuses on the scientific and exploration issues associated with volatiles, then Amundsen Crater is an alternative location for sample return. Studies [12] suggest that all of the investigations of [1] associated with volatile elements in lunar polar regions can be conducted at this site.

Portions of the crater are on the nearside, providing the option of direct communications with

Earth, although access to far side stations might enhance the scientific return of any mission. Amundsen has a broad flat floor suitable for safe landings. It is also often illuminated, providing power to surface assets. Robotic or crewed rovers can drive into permanently shadowed regions (PSRs) to conduct analyses and collect samples in the coldest and potentially volatile-rich regions. Thermal gradients between a sunlit landing site and the PSRs allow for tests of transport and depositional mechanisms.

Also, a traverse across the basin floor will provide access to impact melt samples that can be used to determine the crater's age if returned to Earth and, thus, help calibrate impact flux rates to the Earth-Moon system. Moreover, if a traverse reaches the central peak, then samples of the deep crust can be analyzed and/or recovered.

Mission Options: To adequately address most lunar objectives of [1], sample return missions are required. The best results will be obtained by trained crews on the lunar surface. In the Constellation Program, those activities could have involved crews of four and at least one Lunar Electric Rover for mobility. A human-rated lander and rover, however, are no longer being developed, so alternative architectures involving integrated human and robotic systems are being developed.

Specifically, it may be possible for crew with a NASA Orion vehicle and ESA service module to tele-operate rovers on the surface (Figure 2) and/or provide a communication relay to mission control assets on Earth. In that type of scenario, samples could either be delivered by an ascent vehicle to the Orion spacecraft or, with a return capsule, directly to Earth. Both of these options are being examined in the context of missions to the Schrödinger basin and other areas within the South Pole-Aitken basin (e.g., [11,13]).

A sample return mission to Amundsen would also produce the great insights, but, in that case, meaningful in situ studies of volatiles are another option. Because volatile components can be manipulated with relatively low-temperature transformations, chemical abundances, molecular species, and isotopic measurements can be made on the lunar surface.

Conclusions: The diversity of geologic exposures in the Schrödinger basin provides several interesting mission scenarios and options for multiple sample return missions. If the focus was entirely on the issue of volatiles, then Amundsen crater is a good alternative landing site. Both would produce extraordinary science and provide an opportunity to develop capabilities that will sustain the exploration of space beyond low-Earth orbit.

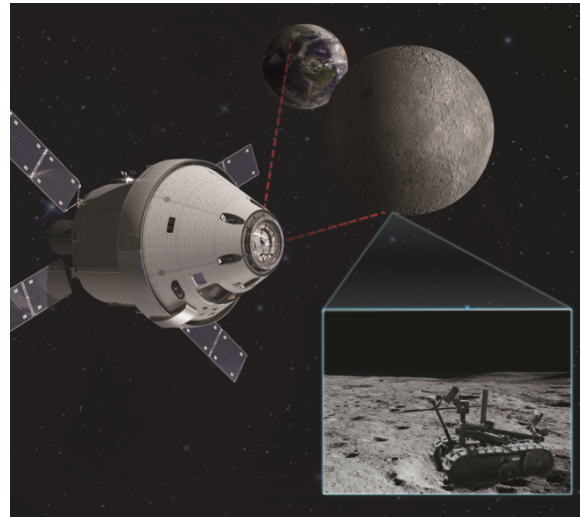


Figure 2: Illustration of the NASA Orion vehicle and ESA service module in the Earth-Moon L2 location above the lunar far side, from where crew can tele-operate a sample-collecting rover and maintain communications between surface assets and mission control on Earth.

References: [1] National Research Council (2007) *The Scientific Context for Exploration of the Moon*. [2] Crawford I.A. et al. (2012) *Planet. Space Sci.*, 74, 3-14. [3] International Space Exploration Coordination Group (2011) *The Global Exploration Roadmap*. [4] Kring D. A. and Durda D. D. (2012) *LPI Contrib.* No. 1694, 688 p. [5] O'Sullivan K. M. et al. (2011) *GSA Spec. Pap.*, 477, 117-127. [6] Hurwitz D. A. and Kring D. A. (2014) *Lunar Planet. Sci. XLV*, Abstract #1398. [7] Bunte M. K. et al. (2011) *GSA Spec. Pap.*, 483, 533-546. [8] Curran N. M. et al. (2014) *Lunar Planet. Sci. XLV*, Abstract #1475. [9] Gullickson A. L. et al. (2014) *Lunar Planet. Sci. XLV*, Abstract #2082. [10] Potts N. J. et al. (2014) *Lunar Planet. Sci. XLV*, Abstract #1835. [11] Burns J.O. et al. (2013) *J. Adv. Space Res.*, 52, 306-320. [12] Runyon K. D. (2012) *Lunar Planet. Sci. XLIII*, Abstract #1619. [13] Hopkins J. B. et al. (2013) *International Astronautical Congress*, 64th, paper A5.1.4, 22 p.

CHARACTERISATION OF A POTENTIAL LANDING SITE OF INTEREST IN THE LUNAR SOUTH POLAR REGION. H. Irfan^{1,2}, I. A. Crawford^{1,2}, P. M. Grindrod^{1,2}, D. De Rosa³, J. D. Carpenter³

¹Department of Earth and Planetary Sciences, Birkbeck, University of London, Malet Street, London, WC1E 7HX, UK, ²Centre for Planetary Sciences, UCL/Birkbeck, London, WC1E 6BT, UK, ³European Space Agency, Estec, Keplerlaan 1, 2200 AG, Noordwijk ZH, The Netherlands (huma.irfan.09@ucl.ac.uk).

Introduction: The objective of this study is the detailed investigation and characterisation of a potential landing site of interest in the lunar South Pole, which is being conducted in collaboration with the European Space Agency (ESA). A prospective region of ~30 x 40 km, centred at 82.7°S, 33.5°W (Fig. 2) is being examined for these studies, which is located on the western limb of the Scott crater in the lunar South Pole, this location has been highlighted previously as an example of a possible site of interest in light of the Russian Luna-Resurs mission. The aim is to investigate and characterise smaller sub-sites of ~3 x 3 km within this locality that satisfy the criteria for the landing site selection, which take into account a risk assessment perspective and proximity to the scientifically interesting features that include: favourable illumination conditions, safe topography, technical constraints for spacecraft landing precision, and a proximity to the scientifically significant features which hint of a possible presence of water ice and/or volatiles and any latent scientifically interesting mineralogy.

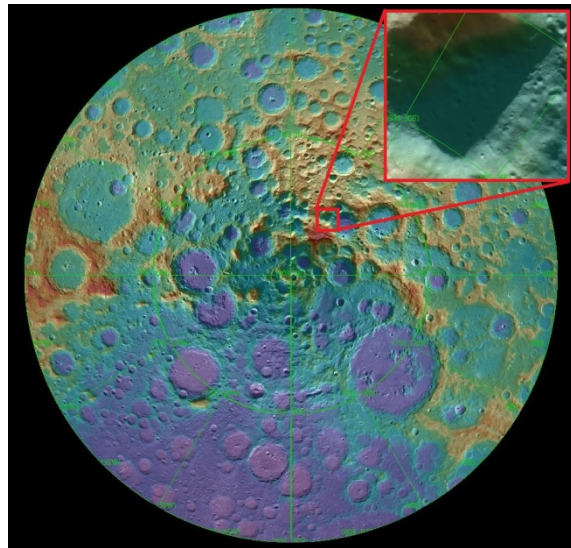


Figure 1: Lunar South Polar region, potential landing site of interest.

The lunar South Pole is a scientifically interesting region for future landing missions, within which, cold regions containing crater cold-traps have been suggested by the Diviner Lunar Radiometer Experiment data surface-temperature observations, where the temperatures can reach as low as 38 K in the permanently shadowed regions [1]. It is thought that within these crater cold-traps, cryogenically trapped water ice and/or volatiles of a primitive

origin may have been derived from impacts and believed to have been preserved for billions of years. Suitable temperatures for volatile stability may also be found in the subsurface in some illuminated areas. In the light of these observations and assumptions, the site considered for this study presents interesting possibilities which are being investigated in detail in this study.

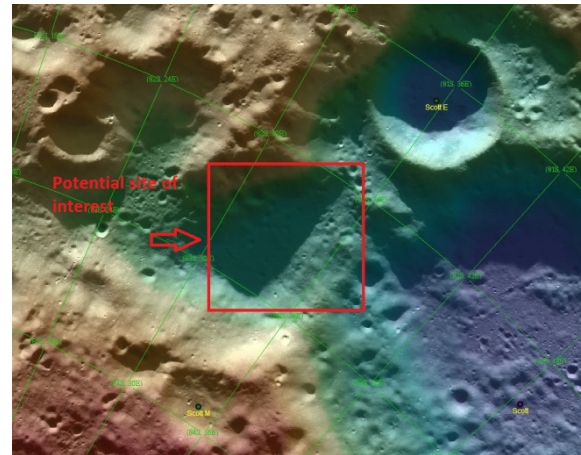


Figure 2: Potential landing site of interest, shown on LROC WAC Colour Shaded Relief map.

Datasets and Methodology: For a comprehensive analysis of this region and the sub-sites within it, various lunar remote sensing datasets have been utilised to ascertain the merit of the potential landing site based on the aforementioned criteria. The Lunar Reconnaissance Orbiter Camera (LROC) Narrow Angle Camera (NAC) images, Lunar Orbiter Laser Altimeter (LOLA) datasets, and NASA's Moon Mineralogy Mapper (M3) data aboard the Chandrayan I mission are being utilised. USGS Integrated Software for Imagers and Spectrometers (ISIS) and SOCET SET software are used to process images and generate DTMs. Topography and surface features, hazard maps including crater and boulder size-frequency distributions, slope and roughness maps, permanently shadowed regions and illumination conditions are simulated using the DTMs in ArcGIS software.

Digital Terrain Models (DTMs). The Lunar Reconnaissance Orbiter Camera (LROC) Narrow Angle Camera (NAC) stereo images of 0.5 to 2 m per pixel resolution are used to generate DTMs. ISIS software routines process the images and perform radiometric correction, which are then imported into SOCET SET for further operations. SOCET SET's

Multi-sensor triangulation (MST) algorithm or bundle adjustment is performed for improved registration of the images [2], and a pair-wise rectification of images is implemented. SOCET SET's Next Generation Automatic Terrain Extraction (NGATE) algorithm is used to generate the DTMs. Lunar Orbiter Laser Altimeter (LOLA) datasets are used to address the accuracy assessment of the DTMs.

Ongoing and Future Work: The Landing Site Risk Analysis software framework (LandSAfe) is a software tool developed by ESA for the analysis and selection of landing sites on the lunar surface [3], which is also being used to generate and compare results for products obtained from other software as described. Furthermore, NASA's Moon Mineralogy Mapper (M3) hyperspectral data of scale 140 m per pixel resolution are also used to investigate the latent scientifically important mineralogy of these sub-localities using the Envi software suite.

References: [1] Paige, D. A. et al. (2010) *Science*, 330, 479-482. [2] Tran, T. et al. (2010) *41st LPSC*, Abstract#2515. [3] Schmidt, R. et al. (2012) *XXII ISPRS Congress*, Vol XXXIX-B4, 506-510.

A DEDICATED SMALL LUNAR EXPLORATION ORBITER (S-LEO) AND MOBILE PAYLOAD ELEMENT (MPE). R. Jaumann^{1,2}, H. Hoffmann¹, N. Schmitz¹ and the Lunar Exploration Orbiter and Mobile Payload Element Study Team ¹Institute of Planetary Research, German Aerospace Center (DLR), Berlin, Germany, ²Freie Universität Berlin, Inst. of Geosciences, Planetology and Remote Sensing, Rutherfordstr. 2, 12489 Berlin, Germany (ralf.jaumann@dlr.de).

The Moon is an integral part of the Earth-Moon system, it is a witness to more than 4.5 b. y. of solar system history, and it is the only planetary body except Earth for which we have samples from known locations. The Moon is thus a key object to understand our Solar System. The Moon is our closest companion and can easily be reached from Earth at any time, even with a relatively modest financial budget. Consequently, the Moon was the first logical step in the exploration of our solar system before we pursued more distant targets such as Mars and beyond. The vast amount of knowledge gained from the Apollo and other lunar missions of the late 1960's and early 1970's demonstrates how valuable the Moon is for the understanding of our planetary system (e.g. Hiesinger and Head, 2006; Jaumann et al., 2012). Even today, the Moon remains an extremely interesting target scientifically and technologically, as ever since, new data have helped to address some of our questions about the Earth-Moon system, many questions remained. In particular, water at the lunar poles, water and hydroxyl bearing surface materials and volatiles changed our view of the Moon as well as the discovery of young volcanism. Therefore, returning to the Moon is the critical stepping-stone to further exploring our immediate planetary neighborhood. Here, we present scientific and technological arguments for a Small Lunar Explorations Orbiter (S-LEO) dedicated to investigate so far unsolved questions and processes. S-LEO is designed to improve our understanding of the lunar environment in terms of composition, surface ages, mineralogy, physical properties, and volatile and regolith processes. S-LEO will carry an entire suite of innovative, complementary technologies, including high-resolution camera systems, several spectrometers that cover previously unexplored parts of the electromagnetic spectrum over a broad range of wavelengths, and a communication system to interact with landed equipment on the farside. The Small Lunar Explorations Orbiter will gather unique, integrated, interdisciplinary data sets that are of high scientific interest and will provide an unprecedented new context for all other international lunar missions.

The most visible mission goal of S-LEO will be the identification and mapping of lunar volatiles to understand their origin and evolution with high spatial as well as spectral resolution. Therefore, in addition to mapping the geological context in the sub-meter range, a screening of the electromagnetic spectrum within a very broad range will be

performed. In particular, spectral mapping in the ultraviolet and mid-infrared will provide insight into mineralogical and thermal properties so far unexplored in these wavelength ranges. The determination of the dust distribution in the lunar orbit will provide information about processes between the lunar surface and exosphere supported by direct observations of lunar flashes. Measuring of the radiation environment will finally complete the exosphere investigations. Combined observations based on simultaneous instrument adjustment and correlated data processing will provide an integrated geological, geochemical and geophysical database that enable

- the exploration and utilization of the Moon in the 21st century;
- the solution of fundamental problems of planetology concerning the origin and evolution of terrestrial bodies;
- understanding the uniqueness of the Earth-Moon System and its formation and evolution.
- the absolute calibration of the impact chronology for the dating of solar system processes.
- deciphering the lunar regolith as record for space environmental conditions.
- mapping lunar resources.

S-LEO is featuring a set of unique scientific capabilities w.r.t. other planned missions including: (1) dedicated observation of volatiles (mainly H₂O and OH), their formation and evolution in direct context with the geological and mineralogical surface with high spectral and spatial resolution (< 1m/px). (2) Besides the VIS-NIR spectral range so far uncovered wavelengths in the ultraviolet (0.2 – 0.4 μm) and mid-infrared (7 - 14 μm) will be mapped to provide mineralogical context for volatile processes (e.g. sources of oxygen). (3) monitoring of dust and radiation in the lunar environment and its interaction with the surface.

In addition a Mobile Payload Element (MPE) can assist a lunar lander mission. The MPE is under study in Germany with the goal to collect uncontaminated and undisturbed samples outside the lander area. The MPE shall acquire samples of regolith with landing-induced contamination being below the detection limit of the associated volatile-seeking instruments; subsurface regolith sampling is preferable

to understand the concentration of volatiles as a function of depth. Chances for encountering elevated volatile concentrations in regolith are dramatically increased if samples are acquired from permanently shadowed patches of terrain; these may be found close to the lander under overhangs of large boulders; moreover, also regolith directly underneath sufficiently large (meter-sized) boulders will have been efficiently 'shadowed' for long periods of time and will be at lower average temperature than the surrounding surface soil which is favorable for preservation of volatiles; thus, regolith from under boulders may be samples of choice for the MPE, provided there is a way to access it. The MPE shall make the samples accessible to analyses by instruments capable of measuring volatiles. Additional benefits for the overall science accomplished by a lunar lander mission could be obtained if the MPE were to conduct 'field geology' type observations and measurements along its traverses, such as geochemical and mineralogical in situ investigations with dedicated instruments on rocks, boulders and regolith. This would dramatically expand the effective area studied by the ESA Lunar Lander mission. As both the lander-based instruments are conceived to ingest regolith, one unique scientific aspect of the MPE could be the in situ study of rocks, boulders and lithic (rock) fragments which otherwise would only be amenable to measurements using any instrument heads mounted on the lander robotic arm (provided any rocks were within reach of the arm). Rocks and rock fragments carry unique, individual histories of igneous, impact and volcanic events from local and distant sources.

References: H. Hiesinger, J.W. Head, New Views of the Moon (B.L. Jolliff et al. eds.) *Rev. Min. Geochem.*, 60, 1- 81 (2006). R. Jaumann et al., 2012, Geology, geochemistry, and geophysics of the Moon: Status of current understanding, *Planet. and Space Sci.*, 74, 15-41.

WHY INGENII IS THE IDEAL TARGET FOR A LUNAR SAMPLE RETURN MISSION. G. Y. Kramer¹ ¹Lunar and Planetary Institute, 3600 Bay Area Blvd, Houston, TX 77058, USA (kramer@lpi.usra.edu).

Ingenii Basin is located on the lunar farside at 33.25 S, 164.83 E. It is Pre-Nectarian in age and has an inner rim diameter of ~325 km. Basalts only partially fill the basin, but flood two large, adjacent impact craters (Thompson, ~120 km and Thompson M, ~100 km in diameter; Fig. 1a) both of which fit neatly within the basin perimeter.

Ingenii is just one of several lunar swirl regions, any of which would be excellent for a sampling mission because of the specific attributes of swirls. A robotic or human mission to Ingenii will help answer questions of interest to planetary science and the broader scientific community. Here I will explain as many as possible in the size constraints of this abstract.

Lunar Swirls. Lunar swirls are bright, optically immature, curvilinear surface features found in discrete locations across the Moon's surface, and all are associated with a local magnetic anomaly. The magnetic field deflects incoming ions, which would otherwise impact the surface and alter the lunar regolith through the creation of agglutinates and microphase iron [1, 2]. These incoming particles may be completely deflected away from the surface or they may be deflected to other regions on the surface. Dark lanes, regions of very low albedo adjacent to swirls, may correspond to locations of enhanced particle flux associated with the nearby particle deflection [2, 3]. The swirls are a laboratory to study the solar wind, space weathering, and complex electromagnetic interactions in the solar system.

Lunar Magnetic Fields. Every swirl is associated with a magnetic anomaly. In addition, it has been shown that the brightest part of a swirl or group of swirls is correlated with the location of magnetic field peak intensity [3, 4]. Models of the distributions of the magnetic source material, when constrained by the observed albedo pattern produce fields that are consistent with magnetometer measurements [5]. Specifically, strongly horizontal surface fields generate bright swirls, while vertical surface fields result in dark lanes. The more intricate swirl morphologies could be used to infer small-scale structure in the near-surface magnetic field as well as the depth and orientation of the magnetic source material.

Space Weathering. The optical properties of the on-swirls surfaces compared with off-swirl and non-swirl surfaces demonstrates the specific ways the surface material is altered by solar wind ions versus micrometeorite impacts [2, 6] – the two agents of space weathering. Not only is space weathering on the swirls retarded, the dark lanes mature much faster than a non-swirl surface.

Since the swirls are weathered almost exclusively by micrometeorites, in situ analysis and returned

samples can be used to study their isolated effect on the maturation process. This is particularly relevant to studies of asteroids. Retardation of the weathering process on the swirls indicates the solar wind is the dominant form of weathering at the Earth-Moon distance. However, at the Asteroid Belt it may be micrometeorites that dominate due to the decreased density of solar wind particles per unit area at that distance from the Sun. The specific spectroscopic differences between asteroid and lunar surfaces due to composition and proximity to the Sun have kept this controversial [7].

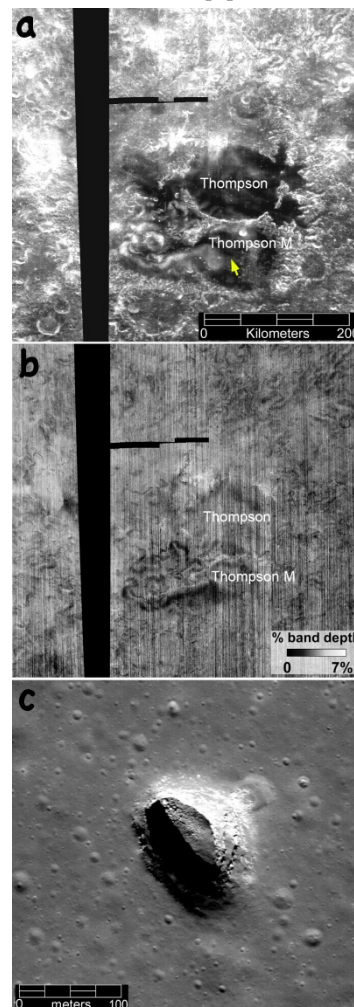


Figure 1: Mare Ingenii (a) M3 750 nm reflectance; (b) OH parameter map (band depth at 2820 nm); (c) Lava pit in Thompson M (location indicated by yellow arrow in (a)).

Sampling Fresh Material. Since the swirls are regions of retarded space weathering with regions of accelerated and/or "standard" space weathering directly adjacent, the opportunity to sample materials of same age, but variable maturity, and vice versa, is available, even to a lander or rover of limited mobility. In a small area one can sample material formed at the same time (e.g., by volcanism, by impact), and/or exposed by impact gardening at the same time, while also sampling fresh material and its weathered counterpart. In addition to better understanding the effect that space weathering has

on different materials, such samples will help pull apart the dominance of magnetic versus electrostatic deflection of solar wind charged particles.

Lunar water. The high albedo swirl markings appear dark in OH and H₂O maps (Fig. 1b) indicating that the swirls are depleted in these volatiles relative to their surroundings [6]. This is consistent with the solar wind deflection model for the swirls [1]. The creation of OH and H₂O is spatially controlled by the magnetic anomalies, making swirls ideal places to study the surface hydration phenomenon and potentially providing locations for extracting this resource.

A flat place to land. The swirls impart no topography, they simply drape whatever existing topography over which they lay. In addition, stereo camera, thermal, and radar imaging of lunar swirls shows that the surface and subsurface roughness of swirls is no different than their surroundings [8, 9]. So one would not need to worry about unexpected uneven surfaces when landing on a swirl/dark lane interface.

Electrical potential. It has been argued [10, 11, 12] that in a plasma wake, such as on the nightside of a planetary body or the shadowed side of a crater bowl, there is a dearth of positive ions to counteract the buildup of negative static electricity on an astronaut's suit or robotic equipment, and thus pose a danger to sensitive instrumentation. However, such a phenomenon may be controlled by the geometry of the magnetic anomalies in useful ways; either through protection and/or as an energy resource. The strength of such an electric field is not dependent on the overall size of the magnetic anomaly, but is related to the local gradient in the magnetic field strength. Locations where the gradient is steep, identified by a sharp bright swirl/dark lane interface, may be a small, but still viable voltage potential to exploit for surface operations.

Plasma physics. The swirls are a place to observe charged particle interactions with a magnetic field involving complex geometries. In particular, the swirls provide a laboratory for studying these interactions in a vacuum on a unique scale – larger than a vacuum chamber [13], yet smaller than a global magnetic field.

Heliophysics. How effective the magnetic anomalies are at deflecting the bulk solar plasma can be studied for both light and heavy ions and for a range of particle fluxes (from the change in incident solar wind angles) with instruments placed at the swirls. Variations in the magnetic field intensities, even at regional magnetic anomaly locations, provide an opportunity to determine whether there are conditions in which only electrons are deflected or other specific controls on particle mass [2, 14]. If the magnetic anomalies formed at an early age and have been protecting the surfaces from the solar wind ever since, the swirls may be a great location to sample the ancient solar wind.

Energy resources. Although the magnetic anomalies alone are sufficient to deflect solar wind ions, retard space weathering, and explain the optical nature of the swirls [2, 14], it has been proposed that an electric field, generated as a consequence of charge separation by the magnetic field [1, 15], may control the movement [15] and structure [16] of dust, and thereby be responsible for the optical nature of lunar swirls and dark lanes.

However, Mare Ingenii has other attributes that make it desirable to a greater range of interests.

South Pole–Aitken (SPA) is a high priority lunar exploration and target for a sample return mission because determining its age will anchor the basin forming epoch, test the terminal cataclysm hypothesis, and SPA impact melt will provide insight into lunar mantle and large impact melt differentiation. Ingenii is located in the northwest corner of SPA making it an ideal location to sample quenched SPA melt, differentiated SPA melt, and potentially the excavated crust. The magnetically shielded regions may yield relatively fresh SPA material. In addition, the magnetic anomalies may be beacons for the locations of the SPA impactor [17].

Basin antipode effects. Imbrium Basin is centered at 34.72 N, 345.09 E - antipodal to Ingenii. Ingenii Basin is surrounded by unusual furrowed terrain, which is attributed to the convergence of seismic waves [18, 19]. Some of these blocks may be uplifted portions of the SPA differentiated melt sheet.

Utilizing a skylight. Mare Ingenii is one of the few location where a collapsed pit, or skylight, has been identified in the lunar maria (Fig. 1c). Skylights have been proposed as ideal features for use as a habitat for a sustained human presence, which can protect astronauts from solar storms and prolonged exposure to cosmic rays.

References: [1] Hood, L.L. & Schubert, G. (1980) *Science*, 208; [2] Kramer G.Y. et al. (2011) *JGR*, 116, E04008; [3] Hood et al. (2000) *LPSC*, abstract #1251; [4] Blewett D T. et al. (2011) *JGR*, 116, E02002; [5] Hemingway, D. & Garrick-Bethell, I. (2012) *JGR*, 117, E10012; [6] Kramer, G.Y. et al. (2011) *JGR*, 116, E00G18; [7] Vernazza et al. (2009) *Nature*, 458, 993; [8] Neish, C.D. (2011) *Icarus*, 215, 186; [9] Glotch T. (2014) *Nat. Comm.*, in press; [10] Farrell et al. (2008) *GRL*, 35, GL034785; [11] Zimmerman M. et al. (2014) *Icarus*, in press; [12] Jackson et al. (2014) *LPSC*, abstract #2154; [13] Bamford, R.A. et al. (2012) *Phys. Rev. Lett.*, 109, 081101; [14] Harnett and Kramer (2014) *Euro. Lun. Sym.*; [15] Garrick-Bethell, I. et al. (2011) *Icarus*, 212, 480; [16] Pieters, C.M. et al. (2014) *LPSC*, abstract #1408; [17] Wiczorek, M.A. et al. (2012) *Science*, 335, 1212; [18] Schultz, P.H. & Gault, D.E. (1975) *Moon*, 12, 159; [19] Richmond, N.C. et al. (2005) *JGR*, 110, 5011.

LUNAR PLANE: LUNAR POLAR LOW-ALTITUDE NEUTRON EXPERIMENT FOR HIGH-SPATIAL RESOLUTION HYDROGEN MEASUREMENTS. D. J. Lawrence¹, P. N. Peplowski¹, M. Ozimek¹, C. Scott¹ ¹Johns Hopkins University Applied Physics Laboratory, Laurel, MD, USA (David.J.Lawrence@jhuapl.edu).

Introduction: Permanently shaded regions (PSRs) are fascinating solar system environments. The type locations for PSRs are craters located at both poles of the Moon and Mercury. The interiors of these craters are not illuminated by sunlight and consequently their temperatures are very cold ($T < 100\text{K}$). One of the most important aspects of PSRs is that they serve as cold traps for volatiles (e.g., water). Predictions dating back to the 1960s and 1970s proposed that lunar PSRs would have enhanced water concentrations [1,2]. Subsequent spacecraft and Earth-based measurements using various techniques (radar, neutron spectroscopy, spectral reflectance) have provided abundant evidence to support these predictions with enhanced volatiles at both the Moon and Mercury [e.g., 3-9]. The characteristics of these regions and the processes that take place in PSRs have implications for a variety of topics such as the history of solar system volatiles [10], synthesis of organic materials [11,12], as well human exploration.

Despite the fact that initial measurements of PSRs have been made, many aspects of PSRs are not known or understood. In particular, our knowledge of the spatial distribution of hydrogen concentrations at the lunar poles is tantalizingly incomplete. The topic of this study is to investigate the extent to which a low-cost, low-resource orbital mission can achieve significant improvements in our knowledge of the lunar polar hydrogen distribution. A better knowledge of the polar hydrogen spatial distribution will have multiple benefits as it can provide key input to studies of PSR volatile processes by isolating individual craters that host enhanced hydrogen. In addition, data from such a mission will be valuable for future landed missions that seek to target landing sites with volatile enhancements [13].

Hydrogen Measurements of Planetary Surfaces: Planetary neutron spectroscopy is the standard technique for quantifying hydrogen concentrations on planetary surfaces [14]. Neutrons are created by nuclear spallation reactions when high-energy cosmic rays strike the surface of an airless or nearly airless planetary body. The energies (E_n) of the resulting neutrons are typically divided into three ranges of fast ($E_n > 0.5\text{ MeV}$), epithermal ($0.5\text{ eV} < E_n < 0.5\text{ MeV}$) and thermal ($E_n < 0.5\text{ eV}$) neutrons. Hydrogen has a unique ability to moderate neutrons because hydrogen atoms and neutrons have the same mass, which allows a highly efficient momentum transfer between the two. This causes the number of epithermal neutrons to be strongly depressed where hydrogen is present so that epithermal neutrons can provide a highly sensitive measure of a soil's hydrogen content.

Polar hydrogen enhancements were first measured on the Moon using the Lunar Prospector Neutron Spectrometer (LP-NS)[3]. The LP-NS was an omnidirectional detector and as a consequence its spatial resolution was sufficiently broad ($\sim 45\text{ km}$) that individual hydrogen enhancements could not be conclusively tied to specific PSRs.

To address the need for higher spatial resolution measurements, the Lunar Reconnaissance Orbiter spacecraft carried a collimated neutron detector known as the Lunar Exploration Neutron Detector (LEND)[15,16], which was planned to quantify hydrogen concentrations at a spatial resolution of 10 km near both lunar poles. A dataset that meets this requirement would result in a significant improvement in our understanding of the lunar polar hydrogen distribution. Despite reports that claim the LEND instrument has met its spatial resolution requirements [17-19], there have been multiple studies using diverse and independent techniques that show the collimated neutron data have not successfully made hydrogen concentration measurements with 10 km spatial resolution [20-24].

In contrast to the collimated neutron measurements, other studies using LP-NS data have carried out spatial reconstruction analyses to obtain improved information regarding the spatial distribution of polar hydrogen concentrations [25,26]. These analyses of LP-NS data likely represent our current best knowledge of the lunar polar hydrogen distribution [24]. Nevertheless, there is still the need for improved data that can definitively identify crater locations of enhanced hydrogen.

With available technology, the two primary ways to obtain improved spatial resolution measurements of epithermal neutrons are to restrict the angle of detection using a collimator [16] or to make lower altitude measurements with an omnidirectional detector. The LEND instrument has illustrated the challenges of collimating epithermal neutrons, as the technique requires a large collimator mass, yet has a poor signal-to-background, and the background itself has a hydrogen spatial variability identical to that of uncollimated epithermal neutrons [21]. In contrast, if a mission concept can be designed where the altitude over one of the poles is lower than that of the LP-NS measurements, then the spatial resolution should be improved roughly by the ratio of the respective altitudes.

Lunar PLANE Mission: The Lunar Polar Low-Altitude Neutron Experiment (PLANE) can be accomplished with a single ^3He epithermal neutron sensor on a small spacecraft. The nominal mission scenario provides for low-altitude ($< 25\text{ km}$) passes

over the lunar south pole with higher altitude apoapsis (~200 km) values to provide orbital stability. To calculate the mission orbit, an order 50x50 lunar gravity model was used and Earth and Sun perturbations were included. A lunar south pole terrain map was used for low-altitude calculations. Figure 1 shows altitudes poleward of 70°S latitude versus time for the first three months of the Lunar PLANE mission. The average altitude poleward of 90°S latitude is 19 km. Figure 2 shows a map of the average altitudes on 0.5°x0.5° pixels. In comparison, Figure 3 shows an altitude map on 0.5°x0.5° pixels of the low-altitude portion of the Lunar Prospector (LP) mission. The average altitude poleward of 70°S for the LP-NS mission is 35 km. Figure 4 shows histograms of the south pole altitudes for the Lunar PLANE and LP missions. The LP mission shows a wide spread of higher altitudes, which results in a relatively broad spatial resolution. In contrast, the Lunar PLANE mission has both lower altitudes and a narrower altitude spread, which will result in improved epithermal neutron spatial resolution.

Based on this initial mission scenario, a simulated epithermal neutron count rate map will be derived using neutron simulation codes developed for neutron measurements at Mercury [9]. These codes explicitly account for the variable spatial resolution, sensor efficiency, spacecraft velocity effects, as well as statistical uncertainties. These simulation results will allow a full quantification of

the spatial resolution improvement to be determined for the Lunar PLANE mission concept.

References: [1] Watson, K. et al. (1961) *JGR* 66, 3033; [2] Arnold, J. R. (1979) *JGR* 84, 5659; [3] Feldman, W. C. et al. (1998) *Science*, 281, 1496; [4] Colaprete, A. et al. (2010) *Science*, 330, 463; [5] Spudis, P. D. et al. (2010) *GRL*, 37, 10.1029/2009GL042259; [6] Lucey, P. G. et al. (2014) *45th LPSC*, #2325; [7] Harmon et al. (2011) *Icarus*, 211, 37; [8] Neumann, G. A. et al. (2013) *Science*, 339, 296; [9] Lawrence, D. J. et al. (2013) *Science*, 339, 292; [10] Lucey, P. G. et al. (2009) *Elements*, 5, 41; [11] Crites, S. T. et al. (2013) *Icarus*, 226, 1192; [12] Paige, D. A. et al. (2013) *Science*, 339, 300; [13] Carpenter, J. D. et al. (2012) *Pl. Sp. Sci.*, 74, 208; [14] Feldman, W. C. et al. (1993), *Remote Geo. Ana.*, pp. 213 – 234. [15] Chin, G. et al. (2007) *Sp. Sci. Rev.*, 129, 391; [16] Mitrofanov, I. G. et al. (2010) *Sp. Sci. Rev.*, 10.1007/s/11214-009-9608-4; [17] Mitrofanov, I. G. et al. (2010) *Science*, 330, 483; [18] Boynton, W. V. et al. (2012) *JGR*, 117, 10.1029/2011JE003979; [19] Sanin, A. B. et al. (2012) *JGR*, 117, 10.1029/2011JE003971; [20] Lawrence, D.J. et al. (2010) *Astrobio.*, 10, 183; [21] Lawrence, D.J. et al. (2011) *Science*, 334, 1058; [22] Eke, V.R. (2012) *Ap. J.*, 747, 6; [23] Miller, R.S. et al. (2012) *JGR*, 117, 10.1029/2012JE004112; [24] Teodoro, L.F.A. et al. (2014) *JGR*, 10.1002/2013JE004421; [25] Eke, V.R. (2009) *Icarus*, 200, 12; [26] Teodoro, L.F.A. (2010) *GRL*, 37, 10.1029/2010GL042889.

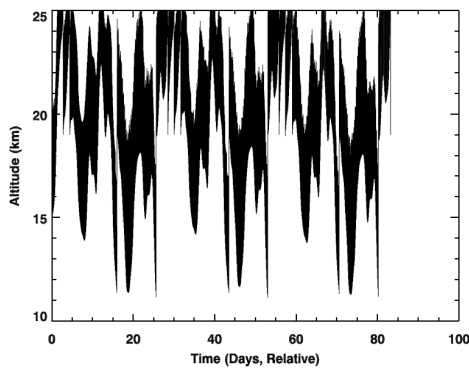


Figure 1: Altitude versus time for latitudes poleward of 70°S latitude for the Lunar PLANE mission.

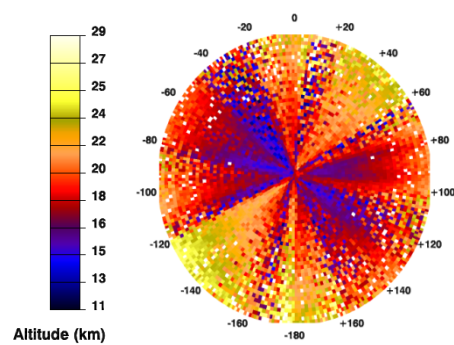


Figure 2: Average altitudes poleward of 70°S latitude on 0.5°x0.5° pixels for the Lunar PLANE mission.

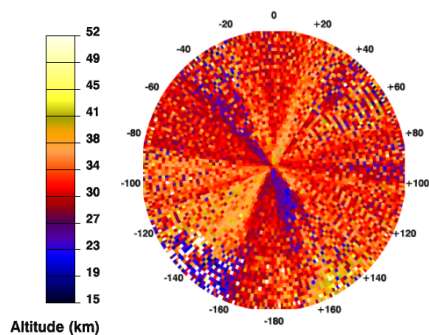


Figure 3: Average altitudes poleward of 70°S latitude on 0.5°x0.5° pixels for the Lunar Prospector low-altitude mission.

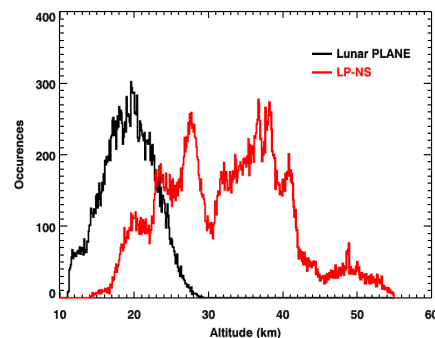


Figure 4: Altitude histograms for the Lunar PLANE and Lunar Prospector missions for latitudes poleward of 70°S.

IN SITU PYR-GC-MS CHEMICAL/ISOTOPIC ANALYSIS OF LUNAR SOIL : A GROUND TRUTH TO INTERPRET THE ANALYSES OF THE SAMPLES RETURNED FROM THE MOON. C. Szopa¹, P. Coll², M. Gerasimov³, P. Wurz⁴, L. Hofer⁴, M. Cabane¹, A. Buch⁵, A.G. Sapgir³, S.A. Aseev³, M.A. Zaitsev³, D. Coscia¹, the GAC team ¹LATMOS, University Paris 6-CNRS, Paris, France, ²LISA, Universities Paris 7 and 12-CNRS, Créteil, France, ³IKI, Moscow, Russia, ⁴Physikalisches Institut, University of Bern, Bern, Switzerland, ⁵Ecole Centrale Paris, Châtenay-Malabry, France (pcoll@lisa.u-pec.fr).

The chemical characterization of lunar samples will be of primary importance to assess their content in volatile species. These volatiles could reveal, for instance, part of the nature of : materials delivered to Earth from exogenous sources, minerals present in the Lunar regolith and surface rocks, and Lunar organic material. Even if the accuracy and sensitivity of the analytical instrumentation used in laboratory are very high to allow to thoroughly analyze the content of samples brought from the Moon, the journey of these samples in space, as well as their transportation to Earth environment, could change the nature of the sample volatiles (e.g. loss of chemical species, possible chemical reactions or contaminations).

For these reasons, an *in situ* chemical characterization of the samples could be of precious help for the interpretation of the results obtained in laboratory, and their transposition to the Moon surface environment. This is the reason why our team proposes an instrumentation to characterize *in situ* the content of volatiles in the lunar soil and rocks. This instrumentation would provide important reference data about the samples collected and returned to Earth. It is based on pyrolysis coupled with gas chromatography and mass spectrometry, and could have the capability to: extract volatile materials (either condensed or present in the minerals) from the solid samples, separate the volatile and analyze their structure for identification and quantification, and analyze isotopic ratios in a certain extent. This instrumentation is based on an inheritance of the GAP instrument that was present onboard the late Phobos-Grunt probe.

The instrumentation would be composed of : i. a pyrolyzer capable to heat the samples up to about 1000°C, and developed by IKI (Rus), which is also in charge to the whole instrument (PI M. Gerasimov); ii. a gas chromatograph devoted to separate and detect the volatile species released from the samples, developed by LATMOS and LISA (Fra.) (CoI C. Szopa & P. Coll); iii. a time of flight mass spectrometer for the structural identification of the molecules, developed by the University of Bern (Swi.) (CoI P. Wurz).

This instrumentation should allow the identification of inorganic volatile molecules and small organic molecules (up to about benzene). This communication aims at presenting this instrumentation that should be onboard the Luna Resource probe to the Lunar South pole, and it could

be used for a return sample mission to get ground truth data about the returned samples.

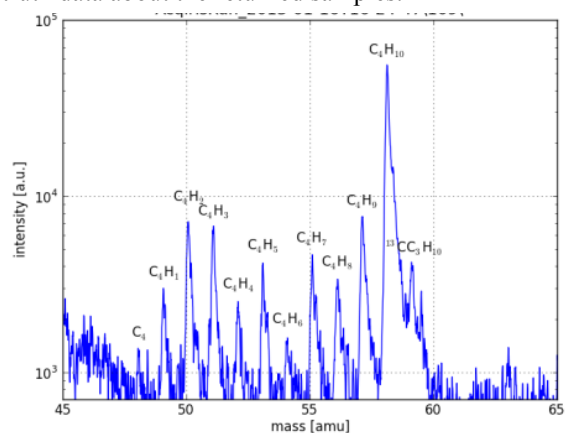


Figure 1: Mass sepctrum of C_4H_{10} recorded in the GCMS mode by coupling prototypes of the GC and the MS [Hofer et al., 2014].

L-VRAP: THE LUNAR VOLATILE RESOURCES ANALYSIS PACKAGE. S. Barber.

To follow...

TECHNOLOGICAL CHALLENGES FOR IN-SITU INVESTIGATION OF LUNAR RESOURCES.
P. Reiss¹, P. Hager¹, S. Parzinger², N. Henn³ ¹Institute of Astronautics, Technische Universität München, Boltzmannstr. 15, 85748 Garching, Germany, ²Institute of Thermodynamics, Technische Universität München, Boltzmannstr. 15, 85748 Garching, Germany, ³Deutsches Zentrum für Luft- und Raumfahrt – Space Administration, Königswinterer Str. 522-524, 53227 Bonn, Germany (p.reiss@tum.de).

Introduction: As extensive measurements either in-situ or on returned samples has shown, lunar regolith is composed of a multitude of oxides, minerals, and ores [1]. These components can be used as potential resources for future exploration missions and to enable sustainable presence on the Moon. Various approaches for the extraction of these resources exist, but require large efforts due to the necessary beneficiation and reduction of the initial regolith feedstock [2].

Recent remote measurements [3-6] support earlier assumptions that the regolith on the Moon also carries a number of volatile elements, among them noble gases, water and hydroxyl [7]. The observed temporal and spatial distribution of volatiles on the lunar surface indicates that their abundance is dependent on ambient temperature and solar radiation. Especially the stability of water and hydroxyl adsorption on the lunar regolith seems to be mainly affected by these parameters [8].

Lunar volatiles are and will be an important topic for future scientific investigations of the lunar surface [9]. The collection of lunar soil samples has a central role for research as well as in-situ resource utilization (ISRU). In this context the understanding of mechanisms for extraction, handling, and analysis of lunar resources are of paramount importance. Regarding lunar volatiles it is important to maintain pristine samples over the entire sampling process. Questions in terms of abundance, thermal stability, sample handling, and extraction need to be addressed for future in-situ or sample return missions.

In a project called LUISE (Lunar In-Situ Resource Experiment, funded by DLR under research grant no. 50JR1210), the Institute of Astronautics at Technische Universität München (TUM) investigates the technological aspects of lunar regolith handling and volatile extraction. The project partners include the DLR Institute of Planetary Science, the TUM Institute of Thermodynamics, and the company Kayser-Threde GmbH. The activities cover physical characterization of lunar regolith e.g. thermal conductivity, gas extraction processes, sample handling, subsurface penetration, and lunar environmental simulations.

Thermal Conductivity of Lunar Regolith: Experiments are being performed to measure the effective thermal conductivity of the lunar regolith simulant JSC-1A [10]. The results show a cubic increase of thermal conductivity as a function of temperature from $8 \cdot 10^{-3}$ W/(m K) at 150°C to $33 \cdot 10^{-3}$ W/(m K) at 650°C. The rise in thermal conductivity

is a result of the increasing contribution of the radiative term to the overall heat transfer, as is common in powders under vacuum conditions [11]. The effective thermal conductivity was measured as a function of gas pressure, temperature, porosity and grain size. Upon the results an analytical model to simulate heat transfer through lunar regolith was developed.

Gas Extraction Experiments: A demonstrator was built to test the capabilities of an in-situ heating concept. A cylindrical heater surrounded by a tube is pressed into lunar regolith simulant JSC-1A (Figure 1). The extracted volatiles are lead through the cylinder to an analysis device. The degree of sample manipulation is hence reduced to a minimum. In a first test assembly the difference between an open and a closed sample volume (heated tube) is being investigated to quantify the loss of extracted gases through deeper regolith layers. Preliminary tests showed that in the open system 45% less gas was recovered, i.e. more gas was lost through the surrounding regolith. The tests were conducted with the regolith simulant JSC-1A under pressures of 10^{-3} mbar in the heater tube and 10^{-5} mbar in the vacuum chamber. Up to now only the quantity of gas (most likely vaporized H₂O and CO₂) has been determined via restrictor measurement [12].

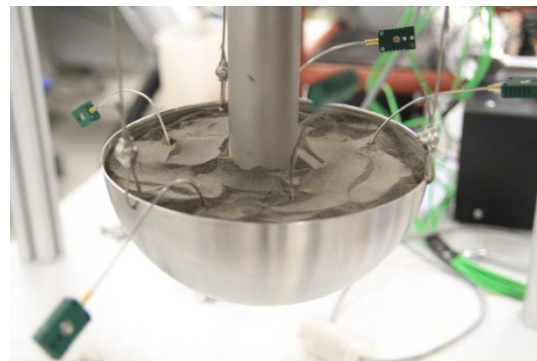


Figure 1: Heating rod pressed in lunar regolith simulant JSC-1A for gas extraction tests.

Sample Handling Experiments: The flowability of lunar regolith is a crucial factor for the design of conveying systems used in sampling instruments. Due to its physical properties, lunar regolith has the potential of arching and subsequently clogging hoppers, tubes, or similar devices. The reduced gravity on Moon further increases this risk. On the second ESA/CNES/DLR Joint European Partial-g Parabolic Flight campaign (JEPPF-2), the flowability of lunar regolith simulants JSC-1A and NU-LHT-

2M [13] through two-dimensional slotted hoppers was investigated under reduced gravity and vacuum conditions. The interdependency of the main influence parameters gravity, hopper inclination, and hopper outlet size was analyzed to understand the resulting scaling effects. It was found that the flow rate behaves mostly proportional to gravity and the outlet size of the hoppers. In order to maintain a constant flow rate under reduced gravity, the outlet size has to be scaled inverse with gravity. The inclination of the hopper showed an ambiguous effect on the flow rate. [14,15]. Additionally the compaction of both regolith simulants was measured under reduced gravity [16]. Several side effects were noted during the experiments and further investigation of this topic is ongoing.

Subsurface Penetration Experiments:

Sampling volatile-rich regolith will most likely require the access of the first sub-layers of the lunar surface. In order to map volatile distribution at different spots on the surface, and to avoid areas contaminated by the lander exhaust, a mobile platform, such as a rover, would yield the highest scientific output. However, the tools carried by a rover have tight constraints regarding their mass, and power consumption, as well as their dimensions. The most simple tool is a static penetrator, that is solely driven by the weight of the rover, or optionally agitated through vibrations. Several tests were performed to investigate the force required for penetrating into the lunar regolith simulant JSC-1A to a depth of 100 mm. The geometry of the penetrators was varied from flat and conical rods to tubes in different configurations. The outcome of the experiments are recommendations for optimized tool geometries in combination with the available penetration forces.

Lunar Thermal Environment Simulation: A thermal modeling tool (TherMoS) has been developed to simulate the thermal environment on the Moon. Several investigations concerning the transient thermal loads on a moving surface-craft (rover) in conjunction with the influence of surface features (boulders, craters, etc.) were performed [17]. Comparison with Lunar Reconnaissance Orbiter Diviner Lunar Radiometer Experiment data showed deviations of < 10% for craters Calippus and Marius A [18]. The determination of thermal loads on a regolith sample with highly volatile components was investigated regarding the requirements for a stable volatile transfer from excavation to an analysis device. Differences between transport in a closed containment (e.g. Mole) or an open system (e.g. scoop) were investigated [19]. The findings indicate that direct exposure of the regolith sample to sunlight must be avoided by all means, due to the high absorptivity of regolith. A total containment, as in case of the Mole, is less sensitive to heat fluxes

compared to an open scoop, and will yield in a more evenly distributed temperature in the sample. A Mole is less sensitive to infrared or solar heat peak loads with short exposure times. Furthermore, surface degradation of the collection device yield higher overall temperatures of the sample.

Ongoing and Future Work: The development of concepts for in-situ analysis of volatiles, as continuation of the described findings, is the main objective of the ongoing projects. Current investigations include novel in-situ heating concepts (simulation and test), thermal analysis of regolith samples in excavation devices, investigation of the mechanical loads on regolith during sample acquisition, penetration testing with lunar regolith simulants, further investigations on the flowability of regolith (effect of ambient pressure and electrostatic charging), evaluation of possible analysis methods and their integration into a coupled sampling and analysis instrument.

Although extensive work on regolith has been performed in the past, there is still much to learn and understand about effects related to transport, sampling, and handling of regolith in conjunction with engineering solutions and technological challenges.

References: [1] Heiken G. H. et al. (1991) *Lunar Sourcebook*. [2] Taylor L. A. and Carrier D. W. III. (1993) In: *Resources of near-Earth Space*, 69-108. [3] Colaprete A. et al. (2010) *Science* 330, 463-468. [4] Pieters C. et al. (2009) *Science* 326, 568-572. [5] Sunshine J. M. et al. (2009) *Science* 326, 565-568. [6] Clark R. N. (2009) *Science* 326, 562-564. [7] Fegley B. and Swindle T. D. (1993) In: *Resources of near-Earth Space*, 367-426. [8] Hibbitts C. A. et al. (2011) *Icarus* 213, 64-72. [9] Jaumann R. et al. (2012) *Planetary and Space Science* 74 (1), 15-41. [10] Orbitec (2007) *JSC-1A MSDS*, Rev. 4. [11] Parzinger S. et al. (2012) *Proc. 42nd ICES*, AIAA 2012-3430. [12] Parzinger S. et al. (2013) *Proc. 43rd ICES*, AIAA 2013-3524. [13] USGS (2008) *NU-LHT-2M MSDS*. [14] Reiss P. and Hager P. (2013) *EGU*, Abstract #2013-7741-1. [15] Reiss P. et al. (2014) *JTERRA* (under review). [16] Reiss P. and Walter U. (2013) *EPSC*, Abstract #2013-431-1. [17] Hager, P. and Walter U. (2012) *Proc. 42nd ICES*, AIAA 2012-3639. [18] Hager P. et al. (2014) *PSS*, <http://dx.doi.org/10.1016/j.pss.2014.01.011>. [19] Hager P. et al. (2014) *ASR* (under review).

LUNAR EXPLORATION AND SCIENCE IN ESA. J. Carpenter, B. Houdou, R. Fisackerly, D. De Rosa, B. Patti, J. Schiemann, B. Hufenbach, B. Foing, ESA ESTEC, Keplerlaan 1, 2201AZ, Noordwijk, The Netherlands (james.carpenter@esa.int).

ESA seeks to provide Europe with access to the lunar surface, and allow Europeans to benefit from the opening up of this new frontier, as part of a global endeavor. This will be best achieved through an exploration programme which combines the strengths and capabilities of both robotic and human explorers.

ESA is preparing for future participation in lunar exploration through a combination of human and robotic activities, in cooperation with international partners. Future planned activities include the contribution of key technological capabilities to the Russian led robotic missions, Luna-Glob, Luna-Resurs orbiter and Luna-Resurs lander. For the Luna-Resurs lander ESA will provide analytical capabilities to compliment the already selected Russian led payload, focusing on the composition and isotopic abundances of lunar volatiles in polar regions. This should be followed by the contributions at the level of mission elements to a Lunar Polar Sample Return mission.

This partnership will provide access for European investigators to the opportunities offered by the Russian led instruments on the missions, as well as providing Europe with a unique opportunity to characterize and utilize polar volatile populations. Ultimately samples of high scientific value, from as of yet unexplored and unsampled locations shall be made available to the scientific community.

These robotic activities are being performed with a view to enabling a future more comprehensive programme in which robotic and human activities are integrated to provide the maximum benefits from lunar surface access. Activities on the ISS and ESA participation to the US led Multi-Purpose Crew Vehicle, which is planned for a first unmanned lunar flight in 2017, are also important steps towards achieving this. All of these activities are performed with a view to generating the technologies, capabilities, knowledge and heritage that will make Europe an indispensable partner in the exploration missions of the future.

We report on the current status of the European elements in this cooperative scenario, with an emphasis on the investigations to be performed at the lunar surface. These investigations should generate knowledge that can be enabling for exploration in the future, and should also have a significant fundamental scientific return.

SPACE ARCHITECTURE FOR EXPLORATION AND SETTLEMENT ON OTHER PLANETARY BODIES – *IN-SITU* RESOURCE UTILISATION (ISRU) BASED STRUCTURES ON THE MOON. S. Lim¹, M. Anand^{2,3} ¹Department of Engineering and Innovation, The Open University, Walton Hall, Milton Keynes, MK7 6AA, UK, ²Department of Physical Sciences, The Open University, Walton Hall, Milton Keynes, MK7 6AA, UK. ³Department of Earth Sciences, The Natural History Museum, Cromwell Road, London, SW7 5BD, UK.

Introduction: Space Architecture is the theory and practice of designing and building an extraterrestrial environment for human habitation [1]. It combines engineering and aesthetics, requiring knowledge of space environments, space systems engineering, and the psychology of isolated and confined environments [2]. The Space Architecture field was incidentally established when, shortly after 1968 when humans left Earth's orbit for the first time, architect Maynard Dalton and industrial designer Raymond Lowy designed the interior of NASA's first space station, Skylab [3]. Other professionals then began to develop the theory and principles of Space Architecture, and it was finally officially established through a peer-reviewed Symposium at the World Space Congress (Houston) in 2002.

Building a human habitat in hostile environments on other planets requires locally sourced and manufactured construction materials, known as *In-Situ* Resource Utilisation (ISRU), and a fully automated construction assembly. Because ISRU is one of the most important concepts in the potential realisation of a deep-space exploration and space architecture, a significant amount of ISRU-related research has been carried out over the past 4 decades [4]. NASA has classified three types of extraterrestrial habitations as (i) Class I: pre-integrated hard-shell modules, e.g. the International Space Station; (ii) Class II: prefabricated and surface assembled modules, e.g. inflatable structures; and (iii) Class III: ISRU derived structures integrated with the Class I and II modules [3]. As more and more complex lunar missions are planned by various space agencies, the topic of ISRU will gain prominence, and be of fundamental importance for the viability of such ambitious undertakings. Thus, those involved in the Space Architecture field believe ISRU is particularly important for deep-space exploration; for example, ISRU on the Moon would produce propellant, shielding materials, water and oxygen which can reduce the amount of mass launched from the Earth to other planets such as Mars, thereby saving billions of dollars of the space budget. They thus contemplate robotised manufacturing technologies as key technologies in the construction of Class III human habitations and infrastructure, including radiation shields, surface paving, bridges, dust-shield walls and spacecraft landing fields, etc.

Background Technology. Additive manufacturing (AM) is defined by the American Society for Testing and Materials as “the process of joining materials to make objects from 3D model data, usually layer upon layer” [5]. Over the last 30 years, improvements in AM materials and processes have resulted in successful commercial realisation. AM is now an integral part of modern product development [6] and the technology has been commercialised to the extent where machines are now affordable for home use. The linear cost/production relationship for small-batch production is unique in the manufacturing sector providing a strong business case for mass-customisation or personalisation of components. For example, a comparison between AM and injection moulding demonstrates that AM can be cost-effective for smaller batches (up to 10,000x) [7].

In construction, the first attempt at using cementitious materials in an AM approach was suggested by Pegna [8]. Because of the slow adoption on new construction technologies and the relatively short history of AM in construction – less than two decades – only two large-scale AM processes focus on the built environment in the academic literature: Contour Crafting [9] and 3D Concrete Printing [10], and one in industry: D-Shape (Monolite) [11]. A range of construction forms has been identified where geometrical freedom has great potential for introducing mass-customisation in the construction industry, replacing the need to restrict component variability to the limits of how many moulds can be economically produced. These include major urban developments in the Middle East (e.g. Masdar city housing in Abu Dhabi) which would require an enormous number of detailed temporary formwork installations using conventional construction processes, to achieve the complex geometry envisaged for the building façade to control shading, solar gain and ventilation [10].

R&D on space Architecture: In industry, Beglow Aerospace signed a contract with NASA in January 2013 to explore options for a lunar base and public-private orbital outposts near the International Space Station. However, Beglow's habitation will be an inflatable module, Class II under NASA's classification. ESA and Foster+Partners (F+P) collaborated with D-Shape in 2010 to investigate the capability of the process to be used for Space Architecture (Top image in Fig. 1), and the team tested a closed-cell structure (Bottom image in Fig.

1) which both retains loose regolith and ensures shielding from cosmic rays and solar flares [12, 13]. However, such efforts to develop construction processes for Class III structures are still in their infancy and require further development to become a practical application.

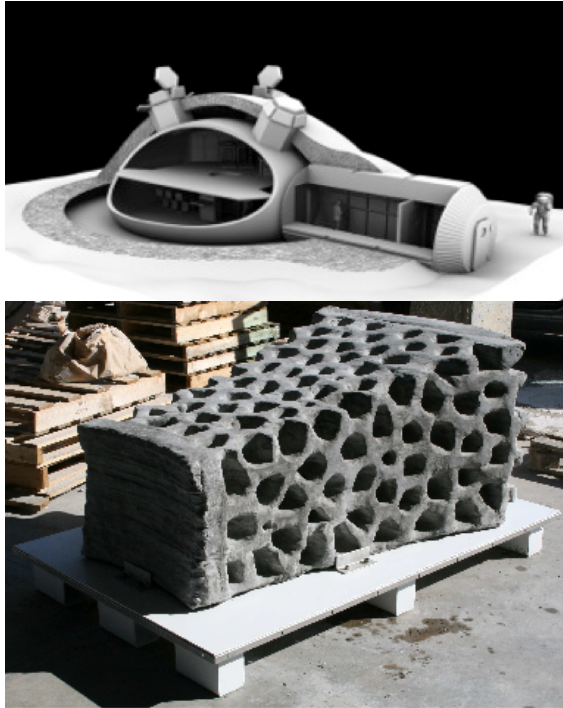


Figure 1: Top - Outpost design that shows a core and extendable modules covered by a lunar regolith shield (F+P) [12]; Bottom - Printed block using a Lunar simulant (D-Shape) [13]. The exact size of the block is unknown, however, the footprint of the block is estimated to be less than 1,000 by 2,000mm compared with the European pallet (800 by 1,200mm) beside of the block.

In academia, there is only one institution – Sasakawa International Centre for Space Architecture at the University of Houston – which focuses primarily on planning and designing Space Architecture. Moreover, despite a number of publications discussing the designs and deployment strategies of Lunar and Martian outposts [14, 15], few publications focus on the construction processes and technologies required to realise such designs.

Discussion: Over the last decade, Space Architecture has become an emerging issue for future space exploration, and is increasingly seen as a fundamental requirement for supporting long-term space exploration and settlement on other planets. However, despite this surge in interest and needs, awareness and understanding of Space Architecture are lacking, in both the academic and industrial built environment field; consequently, Space Architecture studies are still an under-researched and under-practiced discipline in the built environment field. Thus, developing a new research is both timely and

critical given the current upsurge of interest in Space Architecture, and the potential application of Space Architecture across multiple sectors including the Built Environment, Materials and Planetary Sciences because of the nature of its interdisciplinary research.

Lunar Application: The ESA test [13] shows the potential freezing of the binder and the related operation with a wet-mix based printing process under the extreme temperature changes of a lunar environment. In this case, a sintering-based printing process using microwave or laser power, which does not require any binder, could be a more appropriate technique. Nevertheless, there will be some challenges to material fabrication which need to be addressed, e.g., (i) vacuum tribology – friction, lubricant and wear – during the mechanical operations of fabrication, including material delivery, due to the presence of highly abrasive and electrostatic lunar dust and an almost non-existent atmosphere; and (ii) less self-compacted materials during deposition due to weak gravity. In addition, potential of a collaborative construction using smaller modular printing robots needs to be investigated, as a single printing system would require a longer construction period.

At the Open University, we are embarking on a multi-disciplinary research project to integrate our existing expertise in 3D Concrete Printing [10] and knowledge of ISRU potential on the Moon [16] to perform a series of experiments using lunar simulants to optimize 3D printing process and its potential application to building structures and components on the Moon in the context of future habitation of the Moon.

References: [1] SAW (2002) *Space Arch. W.* [2] Osburg, J. (2003) *ICES*. [3] Howe, A. S. and Sherwood, B. (2009) *AIAA*. [4] Anand, M. et al. (2012) *Planet. Space Sci.*, 74, 1, 42-48. [5] ASTM (2010) *ASTM*, F2792-10. [6] Hague, R. et al. (2003) *J. Mech. Eng. Sci.*, 217, 1, 25-30. [7] Hopkinson, N. and Dickens, P. (2003) *J. Mech. Eng. Sci.*, 217, 1, 31-39. [8] Pegna, J. (1997) *AIC*, 5, 5, 427-437. [9] Khoshnevis, B. et al. (2006) *Int. J. Ind. & Syst. Eng.*, 1, 3, 301-320. [10] Lim, S. et al. (2012) *AIC*, 21, 1, 262-268. [11] Dini, E. (2009) *Monolite UK Ltd.* [12] ESA (2013) http://www.esa.int/Our_Activities/Technology/Building_a_lunar_base_with_3D_printing. [13] Cesaretti, G. (2012) *ESA*, 3DP-ALT-RP-001. [14] Rousek, T. et al. (2012) *Acta Astronaut.*, 74, 98-111. [15] Doule, O. et al. (2011) *ICES*. [16] Anand, M. et al., (2012) *Planet. Space Sci.* 74, 42-48.

DEVELOPING THE GLOBAL EXPLORATION ROADMAP: EXPANDING THE “LUNAR VICINITY” SCENARIO. C. R. Neal¹, G. Schmidt², I. A. Crawford³, P. Ehrenfreund⁴ ¹Dept. Civil & Env. Eng. & Earth Sciences, University of Notre Dame, Notre Dame, IN 46556 USA (neal.1@nd.edu), ²SSERVI, NASA Ames Research Center, Moffett Field, CA, USA (gregory.k.schmidt@nasa.gov), ³Department of Earth and Planetary Science, Birkbeck College, University of London, UK (i.crawford@ucl.ac.uk), ⁴Elliott School of International Affairs, George Washington University, Washington DC 20052 USA (pehren@gwu.edu).

Introduction: The Global Exploration Roadmap (GER, [1]) has been developed by the International Space Exploration Coordination Group (ISECG – comprised of 14 space agencies) to define various pathways to getting humans beyond low Earth orbit and eventually to Mars. Such pathways include visiting asteroids or the Moon before going on to Mars. This document has been written at a very high level and many details are still to be determined.

In this presentation, we focus on developing the GER “Lunar Vicinity” scenario by mapping a number of recent reports/documents into the GER. These documents are in no way meant to be encompassing everything that is relevant to this process (indeed, others can and should be added, such as the soon to be published JAXA Space Exploration Roadmap). This exercise is intended to demonstrate that existing documents can be mapped into the GER despite the major differences in granularity, and that this mapping is a way to promote broader national and international buy-in to the GER.

The documents used here are: the Committee on Space Research (COSPAR) Panel on Exploration report on developing a global space exploration program [2], the Strategic Knowledge Gaps (SKGs) report from the Lunar Exploration Analysis Group (LEAG) [3], the Lunar Exploration Roadmap developed by LEAG [4], the National Research Council report Scientific Context for the Exploration of the Moon (SCEM) [5], the scientific rationale for resuming lunar surface exploration [6], and the astrobiological benefits of human space exploration [6,7].

A Summary of the Global Exploration Roadmap: The common goals as articulated in [1] are as follows:

- Develop Exploration Technologies & Capabilities.
- Engage the Public in Exploration.
- Enhance Earth Safety.
- Extend Human Presence.
- Perform Science to Enable Human Exploration.
- Perform Space, Earth, and Applied Science.
- Search for Life.
- Stimulate Economic Expansion.

With Mars being the goal there are three paths articulated - Exploration of a Near-Earth asteroid; Extended Duration Crew Missions; and Humans to the Lunar Surface. The GER gives 5 goals for the Lunar Surface scenario:

- Technology test bed (surface power systems, long distance mobility concepts, human-robotic partnerships, precision landing).

- Characterizing human health and performance outside Earth’s magnetosphere and in a reduced gravity environment.
- Conducting high priority science benefiting from human presence, including human-assisted lunar sample return.
- Advance knowledge base related to use of lunar resources.
- Explore landing sites of interest for extended durations.

The Mapping Process: For this activity, we did not try and map directly to the GER, but rather focused on important lunar science and exploration topics. Two example are reported here (and more will be presented at the workshop): Polar Volatiles and Technology Test Bed/Human Health.

1. Polar Volatiles: The discovery of volatile deposits at the lunar poles brought these areas into focus for future human exploration. The GER goal “Advance knowledge base related to use of lunar resources” certainly is important for this subject. The other documents [2-7] are detailed below using their reference number.

COSPAR [2]. Support studies and precursor activities toward “International human bases”; Sample return missions to the Moon, near-Earth asteroids and Mars.

LEAG-SKGs [3]. Composition/quantity/distribution/ form of water/H species and other volatiles associated with lunar cold traps:

- Map & characterize broad features of polar cold traps;
- Determine lateral & vertical extent of polar volatiles;
- Processes and history of water and other polar volatiles.

LEAG-LER [4]. Objective Sci-A-3: Characterize the environment and processes in lunar polar regions and in the lunar exosphere.

SCEM [5]. Priority 4 - The lunar poles are special environments that may bear witness to the volatile flux over the latter part of solar system history.

Scientific Rationale [6]. The Moon is the type locality to study volatile loss, transport, and retention on airless bodies; the polar deposits represent targets for in situ resource applications;

Astrobiology [6,7]. It is possible that some information concerning the importance of comets in “seeding” the terrestrial planets with volatiles and prebiotic organic materials. Lunar polar icedeposits will have been continuously subject to irradiation by cosmic rays and, as such, may have played host to organic synthesis reactions of the kind thought to occur in the outer Solar System and on interstellar dust grains.

2. Technology Test Bed/Human Health: The Moon represents a key asset for testing planetary exploration technologies and understanding the effect of the space exploration on human health because of its proximity to Earth and its hostile environment. The GER is quite expansive about such issues listing three main goals:

- Develop Exploration Technologies & Capabilities.
- Technology test bed (surface power systems, long distance mobility concepts, human-robotic partnerships, precision landing).
- Characterizing human health and performance outside Earth's magnetosphere and in a reduced gravity environment.

The test documents [2-7] map to these in the following ways.

COSPAR [2]. Synergies of robotic/human exploration; Robotic Village concept of ILEWG and ILRP.

LEAG-SKGs [3]. There are many SKGs highlighted that relate to this topic and these are: Solar event prediction; Radiation at the lunar surface; Biological impact of dust; Maintaining peak human health; Radiation shielding; Dust and Blast ejecta; Surface Trafficability; Plasma environment and charging.

LEAG-LER [4]. This roadmap is forward looking in that it proposes to use the Moon to go elsewhere. As such there are several goals and objectives that relate directly the technology and human health:

- **Objective Sci-A-4:** Understand the dynamical evolution and space weathering of the regolith;
- **Objective Sci-B-2:** Regolith as a recorder of extra-lunar processes;
- **Objective Sci-D-9:** Investigate the production of oxygen from lunar regolith in lunar gravity;
- **Objective Sci-D-14:** Study the fundamental biological and physiological effects of the integrated lunar environment on human health and the fundamental biological processes and subsystems upon which health depends;
- **Objective Sci-D-15:** Study the key physiological effects of the combined lunar environment on living systems and the effect of pharmacological and other countermeasures;
- **Objective Sci-D-16:** Evaluate consequences of long-duration exposure to lunar gravity on the human musculo-skeletal system;
- **Goal FF-A:** Identify and test technologies on the Moon to enable robotic and human solar system science and exploration.
- **Goal FF-B:** Use the Moon as a test-bed for missions operations and exploration techniques to reduce the risks and increase the productivity of future missions to Mars and beyond.
- **Goal FF-C:** Preparing for future missions to other airless bodies.

SCEM [5]. While this report focused on lunar science, understanding the pristine lunar environment is important for designing mitigation technologies in order to provide safe living and

working conditions. Therefore the SCEM maps into this through "Priority 8 - Processes involved with the atmosphere & dust environment of the Moon are accessible for scientific study while the environment is in a pristine state."

Scientific Rationale [6]. This document states in several places the importance of using the Moon to understand the effects of the space environment on human health, such as 1) Monitoring human adaptation to prolonged exposure to partial gravity may offer significant insights into vestibular disorders and a range of processes beyond associated in aging, disusepathology and lifestyle conditions such as the metabolic syndrome and cardiovascular disease; and 2) There would be much to learn about life support (e.g., bio-regenerative food, breathable air, and water closed-loops), and medical support provision, from human operations in a lunar base beyond research into partial gravity effects.

Astrobiology [6,7]. Use of the Moon to understand the long-term effects of the space environment (e.g., the radiation, microgravity, psychological aspects) is required because our knowledge is not sufficient. Several areas of investigation are highlighted:

- Study of the adaptation of terrestrial life to the lunar environment.
- Use of the lunar environment for panspermia experiments and as a test bed for planetary protection protocols.
- Use of the lunar environment as a test-bed for the development of bioregenerative life-support systems, for long-term use on the Moon and future long-duration deep space exploration missions.

Conclusions: There are many documents that describe the challenges and rewards of human space exploration. We have only scratched the surface in examining the "Lunar Vicinity" scenario of the GER, but our major conclusion is that while the GER has very broad goals that define a framework for international cooperation in human space exploration, detail from existing, well-established and community developed documents can be mapped to these goals. By broadening the scope of this mapping project to include other internationally developed documents and individual space agency roadmaps the GER can become an important long range planning document for human space exploration.

References: [1] Global Exploration Roadmap (2013) <http://www.globalspaceexploration.org>, 50 pp. [2] Ehrenfreund et al. (2012) *Adv. Space Res.* 49, 2-48. [3] Strategic Knowledge Gaps for the "Moon First" Human Exploration Scenario (2012) http://www.lpi.usra.edu/leag/GAP_SAT_03_09_12.pdf [4] Lunar Exploration Roadmap (2013) http://www.lpi.usra.edu/leag/ler_draft.shtml [5] National Research Council (2007) <http://www.nap.edu/catalog/11954.html> [6] Crawford et al. (2012) *Planet. Space Sci.* 74, 3-14. [7] Crawford (2010) *Astrobiology* 10, 577-587.

THE INTERNATIONAL LUNAR GEOPHYSICAL YEAR: 2017-2018. R. Cox¹, D. Dunlop², P. E. Clark^{1,3}
¹Flexure Engineering, USA, ²National Space Society, USA, ³Catholic University of America, USA
(Russell.Cox@Flexureengineering.com).

The Lunar Renaissance 2007 - 2020: After nearly thirty years of near total neglect an armada of spacecraft began to arrive at the Moon in 2007. Eleven spacecraft from many countries transformed our understanding of the Moon, from a dead, dry rock, to a dynamic destination rich with new scientific and commercial opportunities that can unlock the entire solar system in the twenty first century for all mankind. In 2017 - 2018, Russia, China, Korea and the US all plan to have active national missions in cislunar space. There are as many as twenty or more private missions being planned and there will be many secondary payloads and LunarCube missions riding along. Thus, there are going to be many nations, many organizations and many, many people involved in active missions in Cislunar space in the eighteen months from July 2017 to December 2018 the 60th anniversary of the International Geophysical Year 1957 - 1958.

Proposal: We are proposing to create The International Lunar Geophysical Year 2017 - 2018 (ILGY) to coordinate many of these activities. Like the International Geophysical Year (IGY) of 1957 - 1958, that launched the space age, the ILGY will focus on joint scientific collaboration and coordination while setting the stage for future political and commercial cooperation that will be critical for the peaceful and profitable exploration and exploitation of the cislunar environment for all mankind.

Initial Activities in 2014: Flexure Engineering and The Select Investor, Inc. will be providing the initial organization and promotion of the ILGY providing many opportunities for collaboration and discussion through the Lunar Initiatives.

The Lunar Initiatives

- The Lunar Workshops
- The Lunar Special Interest Groups (SIGs)
- The Lunar Challenges
- The Lunar Incubators
- The International Lunar Geophysical Year

In addition, we will create a public clearing house on the internet for missions, instruments and scientific objectives expected to be operational in the ILGY timeframe.

We will be establishing and running the monthly ILGY SIG that will explore these themes :

Scientific Collaboration

- Active Missions \ Scientific Objectives
- Terrestrial Scientific Collaborations
- Future Missions \ Scientific Objectives

Mission and Organizational Coordination

- National Missions
- Private or Commercial Missions
- Terrestrial Organizations

Political, Legal and Standards

- Treaties and other mechanisms to ensure open access for all mankind
- Legal framework for scientific and commercial activities
- Technical standards to encourage coexistence, interoperability and reuse

Activities in 2015 - 2016: Our goal will be to provide the information we have collected and the support systems we have created through The Lunar Initiatives to existing international political, professional and standards bodies to help in the creation of collaborative, coordinated strategies to deal with the tsunami of activity that is building now and will crash onto the Lunar shores in the second half of this decade.

Conclusions: The Lunar Renaissance is underway. In the next few years it will transform the Moon from the province of a few large national programs to a dynamic place with many programs large and small, public and private with participation from all over the globe, providing the technology and infrastructure to open The Lunar Frontier in 2020 and beyond. The ILGY would help smooth and accelerate global collaboration and exploration providing scientific and commercial benefits for all mankind.

References: [1] R. Cox et al, 2012, www.lpi.usra.edu/meetings/leag2012/presentations/cox.pdf; [2] Golden Spike, 2013, www.space.com/18800-golden-spike-private-moon-company.html; [3] P.E. Clark et al, 2012, www.lpi.usra.edu/meetings/leag2012/presentations/clark.pdf; [4] Google, 2012, www.googlelunarprize.org/teams.

"NASA'S SOLAR SYSTEM EXPLORATION RESEARCH VIRTUAL INSTITUTE" – INTERNATIONAL PARTNERSHIPS IN LUNAR SCIENCE. D. Daou¹, G. K. Schmidt¹, B. E. Bailey¹

¹Solar System Exploration Research Virtual Institute (SSERVI) (Doris.Daou@nasa.gov).

Introduction: The NASA Solar System Exploration Research Virtual Institute (SSERVI) has been pursuing international partnerships since its inception as the NASA Lunar Science Institute (NLSI), in order to both leverage the science being done by its domestic member institutions as well as to help lunar science and exploration become a greater global endeavor. The international partners of the Institute have pursued a broad program of lunar science stimulated by scientific partnerships enabled by the SSERVI community. Furthermore, regional partnerships have been formed such as the new pan-European lunar science consortium, which promises both new scientific approaches and mission concepts.

International partner membership requires long-term commitment from both the partner and SSERVI, together with tangible and specific plans for scientific interaction that will produce results of mutual benefit to both the institute's U.S. Teams and the international partner. International partners are invited to participate in all aspects of the Institute's activities and programs, on a basis of no exchange of funds. Through these activities, SSERVI researchers and international partners participate in sharing ideas, information, and data arising from their respective research efforts, and contribute to the training of young scientists.

This talk will present an overview of the Institute and the international nodes. We will also discuss the various processes to become a SSERVI partner as well as the opportunities available for collaborations with the SSERVI national teams.

Digital Formats:



LUNAR TEAM REPORT FROM A PLANETARY DESIGN WORKSHOP AT ESTEC. A. Gray¹, J. MacArthur², B. Foing³ ¹Blekinge Institute of Technology, Department of Mechanical Engineering, 371 79, Karlskrona, Sweden, ²Department of Physics and Astronomy, University College London, Gower Street, London WC1E 6BT, UK, ³European Space Research and Technology Centre, Keplerlaan 1, 2201 AZ Noordwijk, The Netherlands (amber.gray@bth.se).

Abstract: On February 13, 2014, GeoVUsie, a student association for Earth science majors at Vrije University (VU), Amsterdam, hosted a *Planetary Sciences: Moon, Mars and More* symposium. The symposium included a learning exercise the following day for a planetary design workshop at the European Space Research and Technology Centre (ESTEC) for 30 motivated students, the majority being from GeoVUsie with little previous experience of planetary science.

Students were split into five teams and assigned pre-selected new science mission projects. A few scientific papers were given to use as reference just days before the workshop. Three hours were allocated to create a mission concept before presenting results to the other students and science advisors. The educational backgrounds varied from second year undergraduate students to masters' students from mostly local universities.

The lunar team was told to design a mission to the lunar south pole, as this is a key destination agreed upon by the international lunar scientific community. This region has the potential to address many significant objectives for planetary science, as the South Pole-Aitken basin has preserved early solar system history and would help to understand impact events throughout the solar system as well as the origin and evolution of the Earth-Moon system, particularly if samples could be returned.

This report shows the lunar team's mission concept and reasons for studying the origin of volatiles on the Moon as the primary science objective [1]. Amundsen crater was selected as the optimal landing site near the lunar south pole [2]. Other mission concepts such as RESOLVE [3], LVRAP [4], ESA's lunar lander studies and Luna-27 were reviewed. A rover and drill were selected as being the most suitable architecture for the requirements of this mission.

Recommendations for future student planetary design exercises were to continue events like this, ideally with more time, and also to invite a more diverse range of educational backgrounds, i.e., both engineering and science students/professionals.

References: [1] R. Tartèse et al. (2013) *Geochimica et Cosmochimica*, Act 122, 58-74. [2] Kring D. A. & Durda D. D. (Eds) (2012) *LPI-JSC Center for Lunar Science & Exploration*, LPI Contribution No. 1694. [3] George J. A. et al. (2012) *LPSC XLIII*, 2583. [4] Wright I. P. et al. (2012) *Planetary & Space Science*, 74, 254-263.

Introduction: The Google Lunar XPRIZE, announced on September 13, 2007, is an incentive based prize with a cumulative purse totalling US\$30,000,000. The Google Lunar XPRIZE will provide cash prizes to privately funded teams that can land a robot on the surface of the Moon, explore the lunar surface by moving at least 500 meters from the landing site in a deliberate manner, and transmit back both near real-time and HD video and images known as “Mooncasts” from the lunar surface. Registered teams have until December 31, 2015 to achieve the requirements of the prize.

Currently there are 18, including 6 teams with a substantial presence in Europe. In the past year these teams have been focusing on fundraising, business development, and continuing their work on mission prototypes and flight hardware. Teams have also been looking at collaboration opportunities, both within the Google Lunar XPRIZE with other teams and outside the prize with commercial partnerships and contracts, in order to further their development and mission maturity.

Prior to the landing of Chang’e 3, a spacecraft had not soft landed on the Moon since 1973. The Google Lunar XPRIZE aims to enable future, regular missions to the Moon from the new commercial space sector, opening up lunar science and exploration beyond the preserve of government space agencies. Today we are already seeing the effects of this with Google Lunar XPRIZE teams selling payload capacity and complete missions.

In 2013 the Google Lunar XPRIZE announced the addition of the Terrestrial Milestone Prizes to identify and reward teams retiring key technical mission risks on Earth prior to their lunar mission in the categories of landing, mobility and imaging. In early 2014, 5 international teams were announced as finalist for the Terrestrial Milestone Prizes: Moon Express (USA), Astrobotic (USA), Indus (IND), the Part-Time Scientists (GER) and Hakuto (JPN). Throughout 2014 these teams will be completing testing and qualification to satisfy an independent judging panel that their systems have reached a predefined state of advancement towards Google Lunar XPRIZE mission flight readiness.

For these 5 teams, as well as the 13 others still competing for the Google Lunar XPRIZE Grand Prize, the upcoming year and a half will be critical not only for winning the competition, but ensuring the availability and capability of future lunar surface missions.

VORTICES: VOLATILES REGOLITH THERMAL INVESTIGATIONS CONSORTIUM FOR EXPLORATION & SCIENCE. D. B. J. Bussey¹ and the VORTICES team ¹Applied Physics Laboratory, Laurel MD, USA (ben.bussey@jhuapl.edu).

Introduction: The surface and near-surface of a planetary object is host to a wide variety of processes. It is the part of the body that interacts with impacts, solar and galactic energy to create or destroy volatiles, it is the part that we see with remote sensing instruments, and the part that will be sampled and tested by robots and astronauts. The VORTICES team has identified a set of interlocking themes considering the entire regolith-volatile system of the Moon and small planetary objects in the context of science and exploration. These themes are:

1) *Volatiles in the Solar System: Sources, Processes, and Sinks:* Understand how and where volatiles (e.g., OH and H₂O) form, how they interact physically and/or chemically with regolith, how they are transported across and within the regolith, and their ultimate fate - be it sequestration in a cold trap or lost from the body.

2) *Regolith: Origin and Evolution on Airless Bodies:* Understand how regoliths are formed and evolve, and how those formation and evolution processes vary across the inner solar system.

3) *Resources: Identification and Exploitation:* Understand how volatile and solar illumination resources are distributed and how they enable robotic and human exploration.

4) *Filling Strategic Knowledge Gaps:* Understand and address those unknowns in knowledge and technique needed to enable human exploration of the Moon, asteroids and the martian moons.

The proposed research is divided in to twelve synergistic tasks.

Task 1: Hydrogen Distribution on the Moon and Small Bodies (Lead: David Lawrence)

This task utilizes orbital geochemical techniques to obtain new insights into H concentrations of the Moon and Eros. The lunar investigation utilizes a new robust statistical analysis technique that leverages available neutron and gamma ray data. This comprehensive approach builds upon our recent identification of Shackleton Crater's unique hydrogen characteristic; ultimately it will enable application to the whole Moon. A separate subtask will constrain hydrogen concentrations on a near-Earth asteroid (Eros) using an advanced methodology to analyze gamma-ray spectroscopy data. The results from this task will be to enhance detection sensitivities and improve the inputs to volatile transport models.

Task 2: Modeling of Volatile Formation and Deposition (Lead: Dana Hurley)

We will improve understanding of the initial distribution of solar wind implanted elements in the regolith. We will account for two processes often neglected in calculating the access of the solar wind

to the surface: 1) the fact that regoliths topography is inherently uneven and 2) the change in fluence to the surface as a body travels through the planet's magnetosphere. If the solar wind implanted protons results in hydration of the regolith, these processes will affect observational signatures. They also provide a starting point for the distribution of volatiles that may subsequently migrate into the regolith or through the exosphere to cold traps. These results feed forward to Task 3, and complement the results of Task 8.

Task 3: Experimental Analysis and Modeling of Volatile / Regolith Interaction (Lead: Karl Hibbitts)

We will undertake laboratory experiments and the development of a three-part model to understand the migration of OH and H₂O through regolith. The laboratory component provides data on the energetics of interactions hydration of the regolith, measuring adsorption and desorption properties that are inputs into the migration models. The model utilizes lab experiments to simulate the molecular interactions and motions of OH/H₂O on single grains; output from the model will be inputs for the model of grain-to-grain migration of volatiles. The output from that model will then feed into a regional scale regolith diffusion model, that, coupled with a gardening model, this work will simulate the time evolution of volatiles as a function of depth.

Task 4 Thermal Characterization of the Surface and Near-Surface (Lead: Ben Greenhagen)

We will characterize the surface and near-surface thermal environments of the NEAs, Moon, Phobos, and Deimos through the SHERMAN thermophysical model. Model results will be analyzed from the perspective of identifying locations where volatiles may be stable. The existence of volatile reserves would be scientifically and operationally significant and therefore, areas of thermal stability are candidates for future exploration.

Task 5: Spectral Characterization of Volatile Species Interaction (Lead: Andy Rivkin)

We will characterize the spectral signature of adsorbed and structural H₂O and OH in anhydrous and hydroxylated materials, under ultra-high vacuum conditions and temperatures. Bi-directional reflectance measurements from the UV through the mid-IR (~140 nm to ~5 μm) make these measurements particularly relevant to telescopic as well as spacecraft observations. These measurements will enable us to better understand the hydration mechanisms that may occur and the abundances of the associated H₂O/OH. The modeling will enable better interpretation of existing and new laboratory spectra of materials under ambient (i.e., hydrated) conditions, by removing the spectral effects of

adsorbed terrestrial water.

Task 6: Regolith Generation by Thermal Fragmentation-Modeling and Experiments (Lead: KT Ramesh)

Our goal is to quantify the contributions of thermal fragmentation to regolith origin and evolution as a function of composition and environment. While impact-driven comminution is the canonical model for the formation of lunar regolith, such a process may not be applicable for asteroids. The typical lunar impact speed is high enough that the particles have sufficient energy to shatter and melt surface material. On asteroids, the impact speeds are much lower, with a significant fraction of impacts occurring more slowly. The lower impact speed (with only 10% the energy compared to lunar impacts) makes rock comminution much less efficient. Additionally, as the surface gravity is very low, material ejected by an impact at less than escape velocity will tend to be globally mixed. An alternative mechanism suggested to explain regolith formation on small bodies is thermal fracturing of the material due to thermal fatigue.

Task 7: Lunar and Asteroidal Regolith Properties (Lead: Jeff Plescia)

There is a diverse suite of data that asteroids are cratered and that a majority of asteroids are rubble piles - unconsolidated collections of material held together by their weak gravity and weaker cohesive forces. The objective of Task 6 is to model thermal fatigue and fracturing, thought to be critical to creating the fine-scale regolith seen on small bodies, and perhaps important on the Moon as well to a degree yet unappreciated. In order to evaluate the modeling and experimental results of rock fragmentation, we must understand the lunar and small body regolith, the goal of this task.

Task 8: Thermal and Irradiation Space Weathering Processes (Lead: Jeff Gillis-Davis)

Summary: We seek to improve understanding of the relative contributions of space weathering on asteroids and how the products of space weathering affect remotely sensed data. To this end, we will examine space-weathering processes on a range of appropriate target materials, to represent compositions from the Moon through small bodies. We examine the processes of: 1) micrometeorite bombardment, simulated by pulse laser irradiation; 2) H^+ implantation; and 3) interactions between the two. We will quantify the spectral changes including characterization of nanophase particles and any OH^- or H_2O produced/released during irradiation. Results of this task provide a framework for Task 5, and feed into Task 9.

Task 9: Search for Resources (Lead: Paul Spudis)

Evaluate and analyze the potential for resources of water and sunlight to develop new space faring capability. We will use an analytical model to search for and map ice deposits in the Moon's polar regions and develop scenarios for the incorporation of lunar

water into a resources-based architecture. New data sets for the lunar poles will be collated to derive resource maps of promising areas. An existing resource exploitation scenario will be extended, modified and quantified using the new data and information derived from the resource mapping. This operational scheme will be applied to model NEAs and the relative efficacies of lunar and asteroidal resources will be compared and evaluated. The results from this task will enable mission planners to assess the difficulty of incorporating resource prospecting and harvesting into future exploration scenarios and architectures.

Task 10. Illumination Characterization for Surface Operations (Lead: Ben Bussey)

Enhance our ability to characterize the illumination conditions on the Moon and small bodies in support of surface scientific and exploration activities. This includes high spatial and temporal analysis of illumination, exploring the value of photoclinometry, and developing a tool to determine routes that minimize darkness.

Task 11. Strategic Knowledge Gap Analysis (Lead: Jeff Plescia)

We will review the SKGs and determine which can be filled by the research to be undertaken by our VORTICES and other SSERVI teams. For those that cannot be closed with current data we will develop a strategy for closing them, including defining the objective, the required data, and the potential instruments needed to collect those data. The results from this task will aid HEOMD in planning instruments/missions to fill SKGs as a precursor to human exploration.

Task 12: Instrument / Mission Concepts (Lead: Paul Spudis)

The objective of this task is to consider what suites of instruments are required to fill SKGs that would enhance and enable exploration. The results of Task 11 will establish the basis to define the instrument manifests and exploration scenarios studied here. Such studies will provide a basis for HEOMD to formulate robotic missions to different targets to obtain the required information.



Poster presentations

RE-EXAMINATION OF APOLLO 17 LSPE DATA USING NEW LRO-BASED COORDINATES OF SEISMIC EQUIPMENT. A. Czeluschnke¹, M. Knapmeyer¹, J. Oberst^{1,2}, I. Haase² ¹German Aerospace Center (DLR), Inst. Of Planetary Research, Berlin, Germany, ²Technical University Berlin, Institute for Geodesy and Geoinformation Sciences, Germany (alexandra.czeluschnke@dlr.de).

Introduction: Our nearest neighbor in space, the Moon, is the only extraterrestrial body humans ever set foot on. Astronauts performed sophisticated scientific experiments on the lunar surface during the six Apollo missions from 1969 to 1972. Among others, the seismic measurements during these missions provided an inimitable resource of data which remains in the focus of scientific interest until today.

The Lunar Seismic Profiling Experiment (LSPE) of Apollo 17 represents the largest active seismic experiment to explore the Moon.

We re-examine the existing Apollo 17 LSPE data [1] with respect to new coordinates obtained through the combined use of lunar surface photography and high-resolution Lunar Reconnaissance Orbiter Camera (LROC) data [2].

LSPE and new LROC coordinates: The LSPE of Apollo 17 was used to explore the subsurface structure of the Moon. For the analysis of such seismic data sets it is necessary to know the exact positions of the geophones and seismic sources.

The Lunar Reconnaissance Orbiter (LRO) was launched on June 18, 2009. The LROC-Camera(LROC) mapped the surface of the Moon from orbit, at a best resolution of 25 cm/pixel. The images allow us a detailed mapping of the Apollo landing sites and a reconstruction of the geometry of the Apollo 17 seismic network.

In addition, we re-examined the surface photography taken by the astronauts during the extra-vehicular activities (EVA). Astronauts documented the deployment of equipment by using calibrated Hasselblad Electric Data Cameras. They took single shots with prominent features in the background or series of panoramic images while driving in the area of the deployed equipment.

By combined analysis of both high-resolution LROC orthoimages and Apollo surface images we determined geometrically accurate lunar-fixed ME-coordinates (Mean-Earth/Polar Axis) of the Apollo landing sites and equipment.

We find significant differences in point coordinates ranging from 1m up to 10m between previously published and new LROC-derived coordinates for geophone and seismic source locations [2]

Re-evaluation: Consequently, we are now in the process to re-evaluate the data from the Apollo 17 Profiling Experiment [3] with the new obtained coordinates, in order to obtain improved models concerning layering and seismic velocity structure of

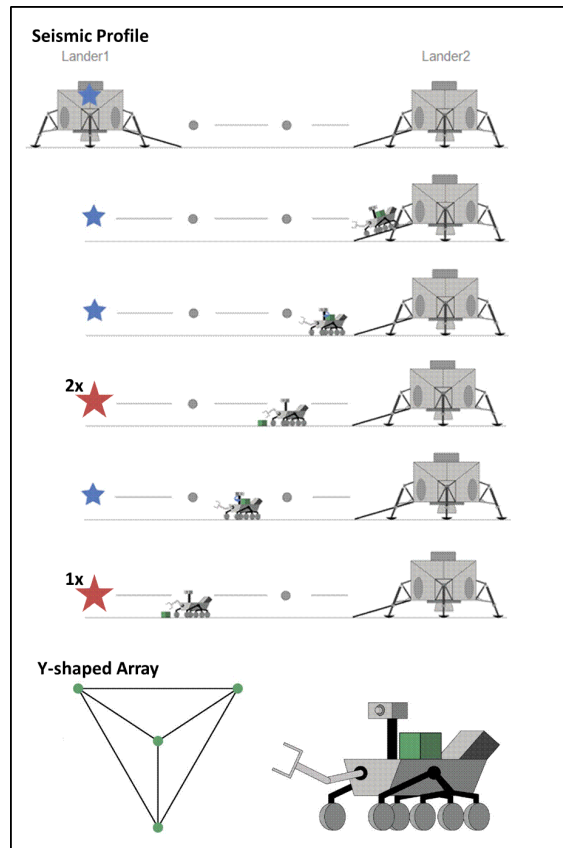
the lunar subsurface. Progress in this effort will be reported at the conference.

ROBEX-Alliance: This study is supported by the Helmholtz Alliance “Robotic Exploration of Extreme Environments – ROBEX”, which brings together space and deep-sea researchers. The project partners are jointly developing technologies for the exploration of highly inaccessible terrains.

For space, the ROBEX alliance aims to develop a new seismic experiment concept that can be conducted autonomously by robotic rovers on the Moon.

At the DLR Concurrent Engineering Facility (DLR Institute of Space Systems, Bremen) a first mission design was developed

The ROBEX – Active Seismic Network (ASN):



There are two phases of the mission being planned: (1) First, measurement of a seismic profile. Two landers shall land on the lunar surface at a distance of 10km (see figure). Lander1 will carry an active seismic source and Lander2 will carry a rover with a seismic sensor. On the way from one lander to the other, the rover shall deploy the seismic sensor for seismic recordings from several distances from Lander1. Via remote control, the rover shall fire and re-fire the active seismic source according to an on-

the-fly evaluation of the measured and stacked data, pick-up the sensor, drive to the next point on the profile, and so on. During the traverse, the rover shall map its surroundings using the Moonrise Context Imager pancam. (2) The second phase of the mission comprises the deployment of a Y-shaped array of sensors for passive listening mode and impact detection. Natural impacts can conveniently be used as seismic sources, if time and location of natural impacts are known by telescopic observation from Earth. These observation techniques and impact modeling are carried out in a separate work package of ROBEX. The array is also expected to observe other natural sources, like thermal moonquakes and shallow moonquakes.

References: [1] Michael R. Cooper et al. (1974) *Reviews of Geophysics and Space Physics, Vol. 12, No. 3*, 291-308. [2] I. Haase et al. (2013), LPSC XLIV, p. 1966 (abstract), [3] Matthew Brzostowski and Adam Brzostowski (2009) *The Leading Edge*, 414-416.

INFERRING THE PROPERTIES OF THE FIRST STARS AND GALAXIES FROM A RADIOMETER IN LUNAR ORBIT. G. J. A. Harker¹ ¹Marie Curie Fellow, University College London Department of Physics and Astronomy, Kathleen Lonsdale Building, Gower Place, London WC1E 6BT, UK (g.harker@ucl.ac.uk).

Introduction: A sensitive radiometer in lunar orbit will be able to see the imprint of the Universe's first stars on their surrounding hydrogen, using observations of the 21-cm hyperfine line [1]. Indeed, this seems by far the most promising (and perhaps the only) route to studying the epoch of 'cosmic dawn' within the next few years. A concept for an experiment to do so, the *Dark Ages Radio Explorer* (*DARE*) has been developed, and will be proposed as a Small Explorer mission for the upcoming Announcement of Opportunity.

The First Stars and Black Holes: UV radiation from the first stars couples the 21-cm hyperfine transition to the temperature of the gas, allowing it to be seen in absorption against the cosmic microwave background. Later, X-rays from the first accreting black holes heat the Universe's hydrogen, allowing it to be seen in emission. The observed frequency of the 21-cm line corresponds to a redshift and hence a specific cosmic epoch. During the cosmic dawn, the observed wavelengths are in the few metres range, so that a low-frequency radiometer can trace the history of the average UV and X-ray radiation field in the early Universe. We are developing accurate, efficient models to predict how different models for the Universe's first stars, galaxies and black holes affect the sky-averaged 21-cm signal. [2]

Overcoming the Foregrounds: We must contend with signals from the Galaxy, Sun and Moon which are orders of magnitude more powerful than the cosmological signal, and so extracting it requires extreme dynamic range, and an exquisite understanding of the instrument being used to measure it. Detailed circuit modelling of *DARE*, coupled with a novel calibration approach based on four-point switching between the antenna and an antenna emulating load, has allowed us to build a calibration and signal extraction pipeline based on a Markov Chain Monte Carlo technique. This also builds on an earlier version of the pipeline [3] by allowing us to perform rigorous, Bayesian selection between alternative models of the astrophysics of the cosmic dawn, as well as to infer parameters of these models. We can thereby approach fundamental, open

questions about this epoch, such as the nature (e.g. the mass) of the first, 'Population III' stars, and whether the predecessors of the supermassive black holes now seen in the centres of all galaxies were responsible for heating the early Universe.

Testing Our Approach from the Ground: A second-generation prototype of the *DARE* system has been deployed (as of end Feb. 2014) on the ground in the protected radio-quiet zone in Green Bank, WV, and is currently taking data. This system is being used to study the radio-frequency interference (RFI) environment and the effect of the Earth's ionosphere on the observations. Both of these present severe obstacles to detecting the cosmological signal from the ground, which is why *DARE* proposes to use the pristine radio environment of a low orbit over the lunar farside (indeed, the lunar farside is likely the best RFI environment in the inner solar system).

Validating the pipeline. The system is valuable, however, to study the astrophysical foregrounds, which will be the same in lunar orbit, to learn about the properties of the instrument (albeit without the environmental stability offered by a space mission), and to validate our data collection, RFI excision, calibration and signal extraction pipeline. Our Monte Carlo code is used to extract the properties of the foregrounds, instrument and ionosphere (and, for the full *DARE* experiment, the cosmological signal) simultaneously from the data, allowing for a full, rigorous error analysis and an objective measure of the suitability of our models. We present details of the pipeline, and show its application to synthetic data and to the first ground-based data from the new prototype system.

References: [1] Burns, J. O., Lazio, T. J. W., Bale, S., Bowman, J., Bradley, R., Carilli, C., Furlanetto, S., Harker, G. J. A., Loeb, A. and Pritchard, J. R. (2012) *Adv. Space Res.*, 49, 1070-1084. [2] Mirocha, J., Harker, G. J. A. and Burns, J. O. (2013) *Astrophys. J.*, 777, id. 118. [3] Harker, G. J. A., Pritchard, J. R., Burns, J. O. and Bowman, J. D. (2012) *Mon. Not. R. Astron. Soc.*, 419, 1070-1084.

THE RELATIONSHIP BETWEEN SOLAR WIND PARTICLE IMPACTS AND SPECTRAL MATURATION THROUGH SIMULATIONS AND OBSERVATIONS AT LUNAR MAGNETIC ANOMALIES. E.M. Harnett¹, G. Y. Kramer² ¹University of Washington, Earth and Space Sciences, Box 351310, Seattle, WA, 98195-1310, USA (eharnett@ess.washington.edu), ²Lunar and Planetary Institute, 3600 Bay Area Blvd, Houston, TX 77058, USA (kramer@lpi.usra.edu).

Introduction: Lunar swirls are high albedo regions on the lunar surface which appear to correspond to surface magnetic anomalies. (See review by [1]). While the origin of the lunar swirls is not yet resolved, one of the main theories is that the anomalous magnetic field deflects incoming ions, which would otherwise impact the surface and alter the spectral properties of the lunar regolith in identifiable ways through the creation of nano-phase iron [2]. These incoming particles may be completely deflected away from the surface or they may be deflected to other regions on the surface. It is thought that the dark lanes, regions of very low albedo adjacent to swirls, may correspond to locations of enhanced particle flux associated with the nearby partible deflection (For a more in depth discussion see [2]).

In this work, we present results of particle tracking studies following the interaction of ions and electrons with modeled 3D vector magnetic fields of actual magnetic anomalies, generated from satellite observations. Impact maps for each simulated anomalous region are generated and compared with spectral observations of the same regions. The objective is to assess the relationship between the surface pattern of the swirls and the difference in spectral changes resulting from the maturation of the high albedo swirls versus the dark lanes as they related to the flux of charged particles interacting with the magnetic field and density reaching the surface.

Method: Simulated anomalous magnetic field were generated by [3, 4]. The resolution of the magnetic field in all cases is 0.1° and map projection is simple cylindrical. The simulated region varied for each case, and included the full region plus several degrees surrounding. The results presented here are for the Ingenii, Gerasimovich, and Reiner Gamma anomaly regions. The total magnetic field simulated included just the anomalous magnetic field and the anomalous magnetic field plus a superposition of several different interplanetary magnetic fields ($B_{\text{vertical}} = \pm 2 \text{ nT}$, $B_{\text{horizontal}} = \pm 2 \text{ nT}$).

For the particle tracking studies, 400,000 non-interacting ions or electrons were launched at the magnetized surface for the variety of total magnetic field configurations. Particle trajectories were computed until all the particles either impacted the surface or left the simulation area. The velocity distributions for all cases are Maxwellians with a mean speed of 200 km s^{-1} and a thermal speed of 75 km s^{-1} .

Total densities and fluxes at the surface were computed by distributing the particles, in a weighted manner, on to a grid with the same resolution as the magnetic field data, and summing over the collected particles. Densities and fluxes were normalized so that the superparticle density in the initial launch region corresponded to $5 \text{ particles cm}^{-3}$, nominal solar wind densities at 1 AU.

Images and mapping of the swirls used Clementine multispectral data (Fig. 1), projected and co-registered to match the magnetic field maps. Qualitative analysis of surface maturity used the OMAT algorithm of [5]. Maps of Spectra are extracted from small, very fresh craters to approximate the composition of the fresh material beneath the regolith. These spectra are compared with spectra of the regolith surface to assess the changes in the spectra as the surface matures under the different particle flux conditions.

Results and Discussion: For all the anomalous regions simulated, maps of particle flux to the surface for each anomalous region showed little difference between the cases with an interplanetary magnetic field (IMF) and the case without an IMF, and little difference between the different IMF cases. The results shown here are for the cases without an IMF, in order to remove any magnetic field offset from the superposition.

Mare Ingenii. Figure 1 shows the results for the swirl region at Mare Ingenii. The strongest surface magnetic field ($\sim 35^\circ\text{S}$ and 160°E , Fig. 1b) is seen to correspond with a void in the flux (Fig. 1c) and the low particle densities at the surface (Fig. 1d). Not only is the number of particles impacting that region small, the speed of those that do, has been reduced. Central to this void region is the portion of the lunar swirl with the highest optical albedo (Fig. 1a). This corresponds with the brightest, bluest (flat spectral continuum), and most optically immature swirl surface at Ingenii.

Both to the north and south of this void are regions of enhanced surface flux and density. It is harder to correlate these regions of enhanced flux with dark lanes purely from the optical image alone in part because these locations are coincident with the rims of the mare-filled craters Thompson and Thompson M, which, being rich in the plagioclase, cannot darken like the dark lanes on the maria.

The simulations begin to describe the interactions that occur between the particles and the magnetic field that are manifested as complex patterns of bright and dark on the surface. This is demonstrated by comparing the simulation results and swirl

outlines within Thompson Crater. Unfortunately, the simulations stop short of describing the intricacy of the dark lanes observable in the optical images likely because of the coarser resolution of the magnetic field data.

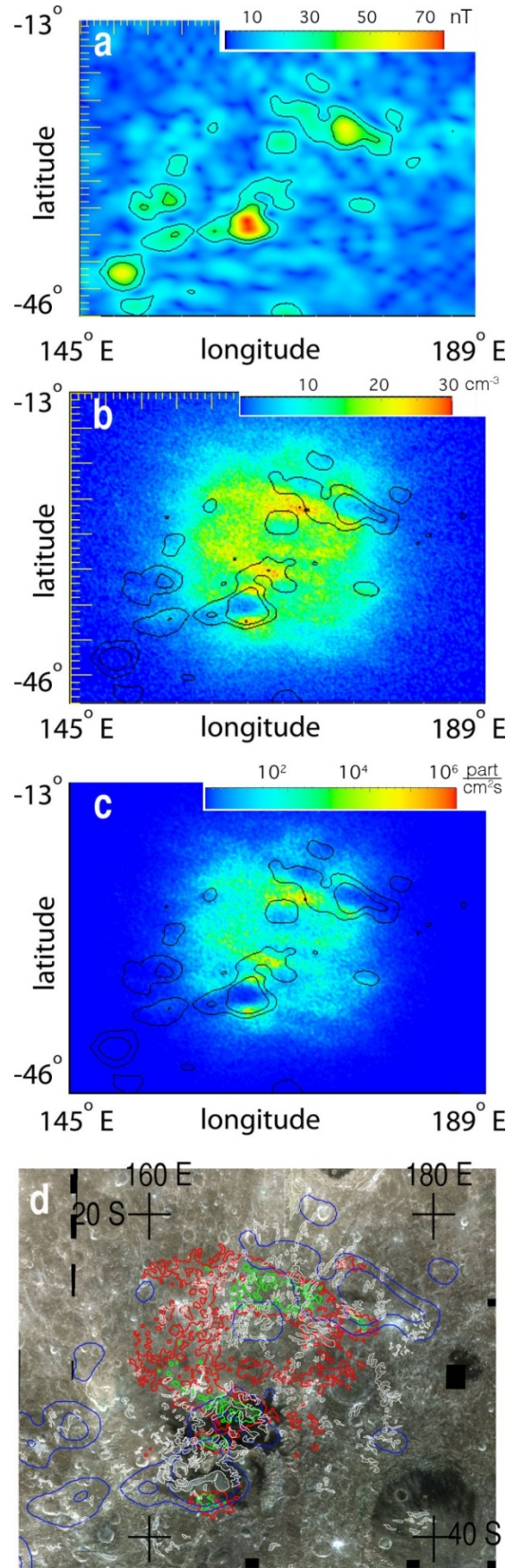
Reiner Gamma and Gerasimovich Similar to Ingenii, the particle tracking for both these cases shows reduced flux and density at the surface in the vicinity of the strongest magnetic field. The flux to the surface at the peak field strength at Reiner Gamma is not zero though, like the void region for Mare Ingenii. Instead it is on the order of 5×10^9 particles $\text{cm}^{-2} \text{s}^{-1}$, approximately 1/10th the peak flux seen in Figure 1c. For Gerasimovich, the flux at the region of strongest magnetic field is on the order of 10^{10} particles $\text{cm}^{-2} \text{s}^{-1}$, or 1/5th the peak flux in Figure 1c. This can not be explained by surface magnetic field strength alone as the peak magnetic field strengths at Gerasimovich are comparable to those at Mare Ingenii and approximately 20% stronger than the peak field strengths at Reiner Gamma.

Interpretation and Next Steps For all cases, the electrons show significantly more deflection than the ions. Taking this into account, means the flux maps for hydrogen ions shown here are worst case scenarios. In reality, an electric field would be generated as the electrons are stopped while the ions continue towards the surface. This electric field will pull the ions back towards the electrons, leading to more deflection of the ions than shown in these results. The next step will be to run simulations that incorporate this effect.

The results also point to the need for higher resolution magnetic field data. Many of the features in Figure 1d, particularly the dark lanes, are smaller than the 0.1° grid spacing of the magnetic field. 3D magnetic field data with much higher resolution than that currently available will be necessary to fully understand the formation of these structures.

References: [1] Blewett D. T. et al. (2011) JGR, 116, E02002, doi:10.1029/2010JE003656, [2] Kramer G. Y. et al. (2011) JGR, 116, E04008, doi:10.1029/2010JE003669, [3] Purucker M. E. and Nicholas J. B. (2010) JGR, 115, E12007, doi:10.1029/2010JE003650. [4] www.planet-mag.net/index.html. [5] Lucey et al. (2000) JGR 105, p.20,377.

Figure 1: (a-c) Simulation results for Ingenii swirl region. (a) Magnitude of the anomalous magnetic field at the surface (values in nT), (b) the particle flux at the surface (particles $\text{cm}^{-2} \text{s}^{-1}$), (c) the particle density at the surface (particles cm^{-3}). (d) Ingenii region showing outlines of the magnetic field at 15 and 30 nT (blue), the proton density $>15/\text{cm}^3$ (red), the proton flux $>104/\text{cm}^2\text{s}$ (green), and the swirls (white). Basemap is Clementine simulated true color (R=900 nm, G=750 nm, B=415 nm). Note that the extent of area shown in (d) is less than in (a-c).



LET'S SPICE THINGS UP: SIMULATING PLANETARY IGNEOUS CRYSTALLIZATION ENVIRONMENTS. J. D. Davenport^{1,2,3}, J. Longhi⁴, C. R. Neal^{2,3}, D. Bolster² and B. L. Joliff⁵ ¹Centre de Recherches Petrographiques et Geochimiques, 54500 Vandoeuvre-les-Nancy, France, ²Dept. of Civil and Environmental Engineering & Geological Sciences, University of Notre Dame, Notre Dame, IN 46556, USA, ³NASA Lunar Science Institute, U.S.A., ⁴Lamont-Doherty Earth Observatory, Palisades, NY 10964, USA, ⁵Dept. of Earth and Planetary Sciences, Washington University, St Louis, Missouri 63130, USA (jessedvnprt@gmail.com; neal.1@nd.edu).

Introduction: The MAGFOX [1], MAGPOX [2], BATCH [3], and FXMOTR [4] modeling codes were first developed in the early 1990s by experimental and lunar petrologist John Longhi to examine magma as it evolved via fractional and/or equilibrium crystallization. The programs were originally written using the cumbersome FORTRAN 77 programming language, but here they have been translated into the user friendly MATLAB programming environment.

The legacy of these programs is important: the FORTRAN versions of MAGFOX and MAGPOX, combined with geochemical and petrographic techniques, have been used repeatedly in the past to study lunar igneous suites and their implications for the evolution of the Moon (e.g., magma ocean crystallization, the petrogenesis of the lunar highlands, and mare basalt source regions). The programs have also been used to study igneous suites on the Earth and other terrestrial planetary bodies where olivine is initially on the liquidus.

The purpose and goals of this translation can be summarized in three points: 1) To break free from the cumbersome and outdated FORTRAN 77 programming language, 2) to bring these programs to a broader scientific audience by using a much more accessible programming language such as MATLAB and 3) provide access to these programs to users who have little to no programming experience via graphical user interfaces (GUIs). This new, user-friendly code, when combined with geochemical analyses, will be able to provide the phase relationships needed to better understand the petrogenesis of many igneous suites.

Copies of these programs are available from the authors and on the Lunar and Planetary Institute (LPI) website within the “Computational Tools” as a graphical user interface and windows executable file (<http://www.lpi.usra.edu/lunar/tools/crystallizationcalculation>). The programs are written in MATLAB, but the basic code can also be executed in the open source Octave programming language (located here: <https://www.gnu.org/software/octave/>).

The Programs: [5] and [6] give detailed information on the applicability of different programs on various magmas. SPICES provides a GUI that users with no programming experience can harness to model crystallization processes ([7]; Fig. 1). MAGFOX uses Rayleigh fractional crystallization, while MAGPOX uses equilibrium

crystallization in 1% crystallization steps — to calculate the major element oxide evolution of the liquid and mineralogy in several projections (e.g., the Ol-Pl-Wo-Sil system; e.g. Fig. 2). The programs can be used to derive crystallization sequences for different magmas (Fig. 3).

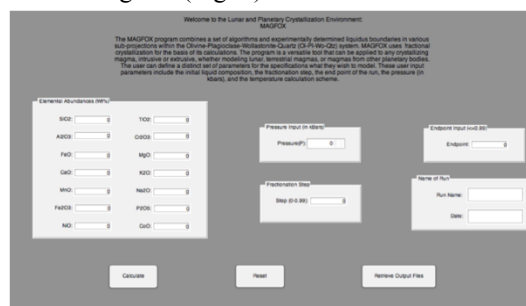


Figure 1: An image of the MAGFOX graphical user interface layout.

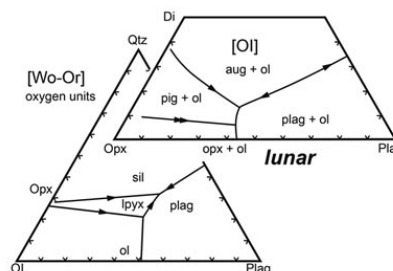


Figure 2: An example of the Ol-Pl-Wo-Sil system, from which the user can derive a crystallization sequence for a given magma.

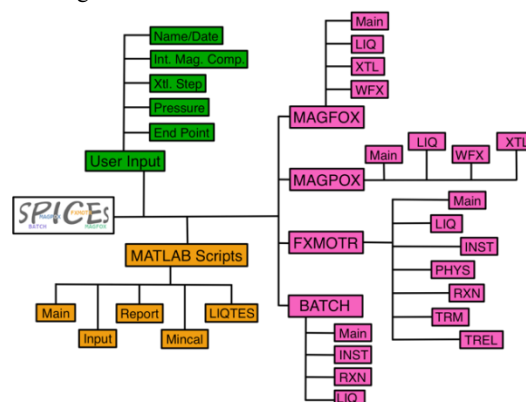
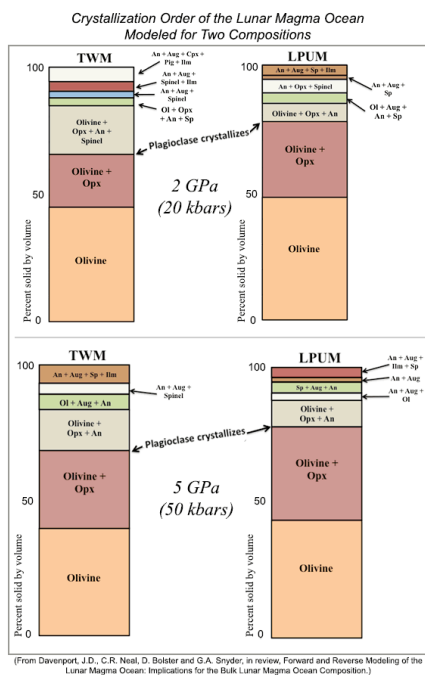


Figure 3: A schematic/flow chart describing the methods, process, and files of the SPICES programs.

FXMOTR uses a combination of equilibrium and fractional crystallization in 1% crystallization steps to calculate the evolution of major and trace elements of a liquid and crystallizing mineralogy.

BATCH is a high pressure version of MAGPOX. Consult [7] for more details on the organization of the code. Appendix A of [7] and references therein contain descriptions of all equations used in each program. [7] also details the construction of the GUIs (Fig. 2) for each program.

FXMOTR and the LMO, A case study: The Lunar Magma Ocean (LMO) has posed an interesting study ever since the return of anorthositic samples and the subsequent development of LMO theory. Despite several decades of LMO research, there are still a number of unsolved questions. For example, [8] sets the LMO depth at 400 km, while [9] sets the depth at 1000 km. This, coupled with variations in the initial LMO composition, produce variations in the mineralization sequences for LMO crystallization. Here, FXMOTR is used to calculate various mineralization sequences to crystallize the LMO assuming LMO depths of 400 km and 1000 km (20 and 50 kbar, respectively) and the TWM and LPUM LMO bulk initial compositions from the literature. Fig. 4 (below) highlights some of these results.



With the help of FXMOTR, it is found that an enrichment in alumina in the initial bulk LMO composition produces plagioclase on the liquidus much earlier than a less Al-enriched composition. Similar effects can be seen with increased LMO depth. Furthermore, with an increased Al and depth, garnet becomes present in small quantities (usually 1-5 wt.%; more to come in the future on this aspect).

Recent GRAIL data are consistent with a bulk Moon Al_2O_3 composition of ~4 wt.% with an average crustal thickness between 34-43 km [10]. However, this assumes that the majority of Al_2O_3 is sequestered in the lunar crust and does not indicate

the presence of an aluminous phase, i.e. garnet or spinel, in the lunar mantle. If garnet is present at depth, the bulk Al_2O_3 of the Moon must be increased. A higher Al_2O_3 content in the bulk Moon would facilitate earlier crystallization of plagioclase and other aluminous phases if the LMO was deeper than ~500 km. In turn, this would allow plagioclase to crystallize earlier and form the lunar crust earlier, thus yielding the inherent negative Eu anomaly in the mare source regions (requiring either a somewhat muted overturn of the cumulate pile or no overturn). Earlier crust formation would generate an insulating lid and promote a longer-lived LMO, as postulated by [11] and [9]. More recently [12], using MELTS, has proposed that the Moon is more enriched in FeO and Al_2O_3 than previously thought, consistent with the results here. They argue that bulk Moon FeO can be constrained to 1.3-1.8 xBSE (Bulk Silicate Earth) and Al_2O_3 between 1 and 1.5 xBSE.

Summary & Conclusion: SPICES has been an integral part in understanding the evolution of countless terrestrial, lunar, and other planetary magma compositions. The SPICES source code has been converted from the now outdated FORTRAN 77 language into the user-friendly MATLAB programming environment. The SPICES code allows the user to quickly calculate crystallizing phases of a magma based on its initial composition, pressure (depth), crystallization step, and model terminus. The examples presented within show that the SPICES code is a valid tool for understanding the evolution of a number of varied magmas on a variety of planetary bodies.

Future Work: One of the key aspects future studies should address is updating the partition coefficients for the major and trace element modeling, which will be a big, albeit very important job. It will have to use the compositions of the crystallizing phases to calculate the correct partition coefficients using research from the University of Notre Dame for plagioclase [13] and Brown University for pyroxene [14], among others. Other technique updates, appropriate for SPICES, will also be incorporated into the models.

References: [1] Longhi, J. (1991) *Am. Mineral.*, 76, 785-800 [2] Longhi, J. (1992) *PLPSC* 22, 343-353 [3] Longhi, J. (2002) *G³*, 1-33 [4] Longhi, J. (2006) *GCA* 70, 5919-5934 [5] Slater et al. (2003) 34th LPSC, Abstract #1896 [6] Thompson et al. (2003) 34th LPSC, Abstract #1881 [7] Davenport et al. in prep. for *Comp. Geosci.* [8] Snyder G.A. et al. (1992) *GCA* 56, 3809-3823 [9] Elkins-Tanton L.T. et al. (2011) *EPSL* 304, 326-336 [10] Wieczorek et al., (2013) *Science* 339, 671-675 [11] Borg et al. (2011) *Nature* 477, 70-73 [12] Sakai et al. (2014) *Icarus* 229, 45-56. [13] Hui et al. (2011) *GCA* 75, 6439-6460 [14] Sun and Liang (2013) *GCA* 119, 340-358.

CHARACTERISATION OF A TERRESTRIAL LOW-IRON SPINEL AS AN ANALOGUE TO SUPPORT THERMAL INFRARED OBSERVATIONS OF THE MOON. C. M. Marriner¹, K. L. Donaldson Hanna¹, N. E. Bowles¹, T. C. Prissel², C. R. M. Jackson², L. Cheek³, S. W. Parman², C. M. Pieters², P. J. Isaacson⁴, B. T. Greenhagen⁵ ¹Atmospheric, Oceanic & Planetary Physics, University of Oxford, Clarendon Laboratory, Oxford, OX1 3PU, UK, ²Dept. of Geological Sciences, Brown University, Providence, RI, USA, ³Astronomy Department, University of Maryland, College Park, Maryland, USA, ⁴HIGP, University of Hawaii, Manoa, Hawaii, USA, ⁵Jet Propulsion Laboratory, Pasadena, CA, USA (marriner@atm.ox.ac.uk).

Introduction: The Moon Mineralogy Mapper (M³) onboard the Chandrayaan-1 spacecraft has identified a new lunar rock type, spectrally dominated by Mg-spinel, in small exposures across the lunar surface [e.g. 1-4]. These exposures appear to be associated with regions of thinner crust and/or the inner rings of basins. This association indicates that the Mg-spinel likely originated in the lower crust/upper mantle before excavation to the surface during impact event(s) [1-4]; however, exposed lithologies suggestive of a mantle have yet to be observed [4]. In addition, these Mg-spinel exposures appear to be associated with feldspathic material, including identifications of pure crystalline plagioclase units nearby, with no observable mafic silicate signature in their spectra [4]. This is a distinguishing feature, as all spinel-bearing samples recovered from the Moon are associated with significant proportions of olivine +/- pyroxene [e.g. 5]. Thus, this new rock type has been termed a pink spinel anorthosite [1, 4].

The Fe-bearing Mg-spinel-rich exposures are identified spectroscopically in the near infrared (NIR) by a prominent absorption band near 2 μm and a lack of a 1 μm absorption band [1-4]. Recent studies have shown that synthetic spinels containing <5 wt. % FeO (high Mg) do not exhibit an absorption band near 1 μm in their NIR spectra suggesting Mg-spinels identified on the lunar surface may be low in FeO content [6]. Furthermore, experiments suggest Mg-spinel anorthosites (pink spinel anorthosites) may have formed during melt-rock interactions between Mg-suite magma and anorthositic crust, implying Mg-spinel anorthosites may be an uncollected member of the Mg-suite rocks [7].

The importance of wide wavelength coverage: NIR data can be used to uniquely identify exposures of Mg-spinel anorthosites as well as estimating the FeO content of the Mg-spinel [6]. Due to the non-linear nature of mixing in the NIR, it is difficult to determine the abundance of feldspathic material (plagioclase) in the Mg-spinel anorthosite exposures. However, the linear nature of mixing across thermal infrared (TIR) wavelengths may allow for the estimation of plagioclase abundance [e.g. 8]. Terrestrial and synthetic spinel samples must first be characterised at TIR wavelengths under Simulated Lunar Environment (SLE) before comparing resultant spectra to observations of Mg-spinel anorthosite exposures by the Diviner Lunar

Radiometer Experiment (Diviner) onboard NASA's Lunar Reconnaissance Orbiter (LRO) [9].

Key spectral features in the TIR, relevance to the Diviner compositional investigation: TIR spectra have several diagnostic features including the Christiansen feature (CF), reststrahlen bands (RB), and transparency feature (TF). The CF is an emissivity maximum where the refractive index of the material rapidly approaches the refractive index of the surrounding medium and is diagnostic of composition [10]. When the intensity of vibration bands are high, a mirror-like opacity is induced, and these are low emitting bands called RB. When no returned radiation has passed through some volume of the material before being backscattered to the observer the emittance is low from the sample, where the RB are the residual rays left after the strong reflectance from a smooth surface [10]. The TF is an emissivity minima caused by volume scattering in a spectral region of relative transparency between the principle RB [11]. While Diviner only maps the CF wavelength position the other spectral features are useful for future hyperspectral studies of the Moon and other airless bodies.

In this study, we analyse the TIR spectral properties of well-characterised pink spinels that are analogous to the spinel identified on the Moon by remote sensing. These lab measurements are the first in characterising lunar-like spinels across TIR wavelengths in an effort to understand current (Diviner) and future observations of Mg-spinel anorthosite exposures on the lunar surface.

Methodology: The rough spinel gemstones were ground into particulates (Figure 1). Several grains were chosen to verify elemental homogeneity and mineral chemistry using the FEI Quanta 600 FEG scanning electron microscope (SEM) using energy-dispersive X-ray spectroscopy (EDX) at the University of Oxford's Nanofabrication and Electron Microscopy Facility, and the Cameca SX-100 electron microprobe (EMP) at the Brown University Geological Sciences Electron Microprobe Research Facility to confirm that the samples are homogeneous and have low FeO content (<5 % FeO) making it a suitable lunar analogue.

The particulate spinel samples were further ground and sieved to particle sizes <45 μm . Fine particulate samples were measured across TIR wavelengths (5-25 μm or 400-2000 cm^{-1}) under ambient and SLE conditions in the Lunar Environment Chamber (LEC) at the University of

Oxford's Planetary Spectroscopy Facility [12]. Ambient or Earth-like conditions are simulated in the LEC by: heating the sample from below to ~350 K using a sample cup heater, holding the interior of the environment chamber to room temperature (~300 K), and the interior chamber pressure is held to ~1000 mbar of dry nitrogen gas (N₂). The near-surface lunar environment is simulated by: heating samples from below to ~280, 350, and 390 K, heating the sample from above using a solar-like halogen lamp, cooling the interior of the chamber to <125 K using a liquid nitrogen (LN₂) cooled radiation shield and the interior chamber pressure is evacuated to pressures < 10⁻⁴ mbar.

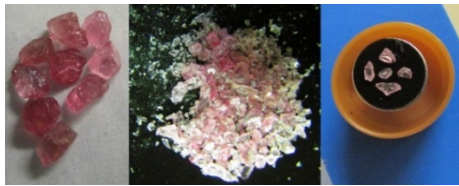


Figure 1: (Left) Rough pink spinel gemstones. (Centre) Crushed pink spinel sample. (Right) Largest grains for SEM EDX analysis.

Compositional Results: EDX and EMP analysis indicate the sample contains a large abundance of O, Mg, and Al, with little to no Fe detected, and is nearly pure, stoichiometric MgAl₂O₄ spinel with < 0.2 wt% FeO (see Table 1). Both techniques agree this is a Mg-rich spinel with low-Fe content (< 1 wt%), thus an excellent terrestrial sourced lunar analogue.

Table 1: Average of 20 points analysed (EMP).

| Molecule | Average Abundance (wt%) |
|--------------------------------|-------------------------|
| MgO | 28.7 ± 0.2 |
| Al ₂ O ₃ | 72.1 ± 0.4 |
| SiO ₂ | 0.057 ± 0.019 |
| CaO | 0.0025 ± 0.0026 |
| TiO ₂ | 0.013 ± 0.005 |
| Cr ₂ O ₃ | 0.14 ± 0.09 |
| MnO | 0.007 ± 0.004 |
| FeO | 0.15 ± 0.02 |
| Total | 101.17 ± 0.457 |

Spectral Emissivity Measurements under SLE: Two key observations for the spectral emissivity measurements of Mg-spinel under SLE (see Figure 2): (1) the CF shifts to higher wavenumbers when compared to ambient measurements, and (2) the spectral contrast between the CF and the RB is enhanced. These are consistent with spectral measurements of minerals, rocks, and lunar soils previously measured under vacuum and SLE conditions [e.g. 11-14]. The shifting of the CF position and the spectral contrast increasing under SLE conditions are due to a temperature gradient via solar heating and a reduction in the heat transport within the subsurface due to low thermal

conductivity of particulate samples and negligible convective transport to the vacuum pressures [12]. In the CF region the energy from greater depths in the sample is included in the emittance, whereas the radiation from the cooler surface layer dominates emittance in the RB region. While previous studies show the TF is significantly reduced under SLE (e.g. [10]-[11]), the TF for Mg-spinel under SLE remains relatively unchanged. Even though the spectral contrast between the CF and RB increases under SLE conditions, this increase in spectral contrast does not significantly affect the TF as it would in some minerals where the RB and CF contrast is greater [e.g. 14].

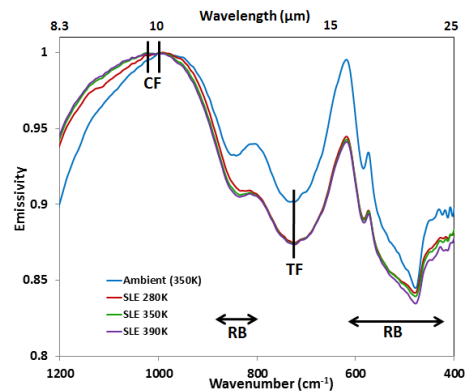


Figure 2: Emissivity spectra for low-Fe Mg-spinel under ambient (blue line) and SLE (280 K orange, 350 K green, and 390 K purple conditions).

Ongoing/Future Work: Lunar analogues like the low-Fe spinel sample in this study, as well as, a suite of well-characterised, synthesised spinel samples of varying Fe- and Cr-abundance will be measured across TIR wavelengths under SLE conditions to characterise spectral changes due to the lunar environment. TIR spectra under SLE will be compared to Diviner observations of Mg-spinel anorthosite exposures to provide initial estimates of the abundance of plagioclase in these spinel-rich regions. Understanding the spinel-to-plagioclase ratio in these exposures could provide insight into magmatic processes involved in spinel-production and the petrogenesis of spinel anorthosite lithologies on the Moon.

References: [1] Pieters C.M. et al., (2011), *JGR*, 116, E00G08. [2] Dhingra D. et al., (2011), *GRL*, L11201. [3] Lal D. et al., (2012), *JESS*, 121, 847-853 [4] Pieters C.M. et al., (2013), *LPSC44*, 2545. [5] Prinz M. et al. (1973). *Science*, 179, 74-76. [6] Jackson C.R.M. et al., (2012), *LPSC43*, 2335. [7] Prissel T.C. et al., (2012), *LPSC43*, 2743. [8] Ramsey M.S. and Christensen P.R. (1998), *JGR*, 103, 577-596. [9] Greenhagen B.T. et al., (2010), *Science*, 329, doi:10.1126/science.1192196. [10] Salisbury, J. W., Cambridge University Press, New York, 79-98, 1993. [11] Salisbury J. W. et al (1989), *JGR*, 94, 9192-9202. [12] Thomas I. R. et al., (2012) *Rev. Sci. Instrum.*, 83(12), 124502. [13] Logan L. M. et al. (1973), *JGR*, 78, 4983-5003. [14] Donaldson Hanna et al. (2012), *JGR*, 117, E1104.

THE ORIGIN AND EVOLUTION OF VOLATILES IN THE EARTH-MOON SYSTEM: A HALOGEN PERSPECTIVE. F. E. McDonald¹, K. H. Joy¹, P. L. Clay¹, R. Burgess¹ ¹School of Earth, Atmospheric and Environmental Sciences, University of Manchester, Oxford Road, Manchester, M13 9PL, UK (francesca.mcdonald@manchester.ac.uk).

Introduction: The volatile elements are an important constituent of planetary bodies, having a major influence on thermal and chemical processes such as melting, rheology and volcanism [1, 2]. Determining and comparing the volatile budgets of the lunar and terrestrial mantles will provide an understanding of volatile behaviour and distribution during the formation and evolution of the Earth-Moon system.

Volatiles Of The Earth-Moon System: The purported giant impact is widely believed to be the Moon forming event [3]. Such an impact can also explain the close similarity of the terrestrial and lunar oxygen isotope composition [4] and the current angular momentum of the Earth-Moon system [5, 6]. This event is also considered to have created a lunar magma ocean (LMO) [7, 8], which crystallised to form the current differentiated Moon. How the giant impact event and planetary differentiation affects the origin and evolution of the volatile elements on the Earth and the Moon is not currently well understood.

Accretionary versus later veneer. There are two main arguments concerning the origin of the volatile elements: either they were accumulated during the main planetary early accretion phase from solar and chondritic material [9, 10], or the giant Earth-Moon forming impact caused major degassing by hydrodynamic escape, with volatiles being subsequently acquired by both bodies as a “late veneer” of chondritic material, post-dating planetary formation and pre-dating mantle closure [11, 12, 13].

Processes affecting volatile evolution. Other factors to consider that affect the isotopic signatures and concentrations of the volatile elements are the role of impact erosion of an early crust [14], and with regard to the Earth, the role of recycling of volatiles at subduction boundaries [15, 16].

The Halogens As Tracers Of Volatiles: The halogens are very reactive due to their high electronegativity and show a range from moderate (F, Cl) to highly volatile (I) behaviour. However, because the halogens have such large ionic radii (particularly the heavy halogens, Cl, Br and I), they are highly incompatible. This means that their distribution is strongly influenced by fluid mobility and processes such as fractionation and degassing, making the halogens very good tracers for other volatile elements (e.g., H, C) [17].

Samples: To constrain the halogen composition of the primitive terrestrial and lunar mantles, we will target olivine hosted melt inclusions in ancient terrestrial komatiites and lunar mare basalts of comparable age. The volatile and halogen

composition of the melt inclusions should have remained relatively unaltered since their time of entrapment [18].

Terrestrial komatiites. A range of Achaean komatiites have been sourced from different greenstone belts around the world (i.e., Canada, S. E. Baltic Shield and South Africa). These locations provide a variety of geographic locations and flow depth and range in age from 3.3 – 2.4 Ga. This sample set will provide a global representation of the primitive terrestrial mantle and insight into its heterogeneity and evolution through time.

Lunar samples. Predominantly olivine rich mare basalts from a range of Apollo missions (age range from 4.2 – 3.2 Ga) have been selected to represent different lunar mantle source locations, depths and variation in chemistry (e.g., high and low-Ti and high-Al compositions). Analysis of picritic glass beads and some plutonic samples provide samples of mantle partial melts up to 4.2 Ga in age. They also potentially provide insight into degassing behaviour of volatiles on ascending to, erupting on, and ponding near to the lunar surface.

Research Plan: All samples will be petrographically and compositionally characterised using electron microscopy and microprobe techniques.

Halogen determination. The analytical technique used to determine halogens is Neutron Irradiation Noble Gas Mass Spectrometry (NI-NGMS). The initial neutron irradiation of samples converts the halogens Cl, Br and I into their respective noble gas isotopes, Ar, Kr and Xe, which are then readily measured by NGMS at the University of Manchester. CO₂ laser or furnace step heating releases the noble gas component for measurement, which is then used to determine the original halogen abundances. This analysis method is particularly sensitive and able to detect the least abundant and most difficult to measure halogen, iodine, which can be present at just 1 ppb per 1 mg of sample material.

Targeting melt inclusions. Laser ablation of melt inclusions hosted in individual olivine grains will provides access to halogen compositions representing the least unaltered and least degassed, primitive mantle compositions.

References: [1] Hirth, G. A. and Kohlstedt, D. (1996) *Earth Planet. Sci. Lett.*, 144, 93–108. [2] Saal, A. E. et al. (2008) *Nature. Lett.*, 454, 192–195. [3] Hartman, W. K. and Davis, D. R. (1975) *Icarus*, 24, 504–515. [4] Weichert, U. et al. (2008) *Science*, 294, 345–348. [5] Canup, R. M. and Esposito, L. W. (1996) *Icarus*, 119, 427–446. [6]

Canup, R. M. (2012) *Science*, 338, 1052-1055. [7]
 Taylor, S. R. (1975) *Pergamon Press, New York*, pp.390. [8] Warren, P. H. (1985) *Annu. Rev. Earth Planet. Sci.*, 13, 201-240. [9] Mukhopadhyay, S. (2012) *Nature. Lett.*, 486, 101-104. [10] Pepin, P. O. (1991) *Icarus*, 92, 2-79. [11] Tartèse, R. and Anand, M. (2013) *Earth Planet. Sci. Lett.*, 361, 480-486. [12] Marty, B. (2012) *Earth Planet. Sci. Lett.*, 313-314, 56-66. [13] Albarède, F. (2009) *Nature*, 461, 1227-1233. [14] Sharp, Z. D. and Draper, D. S. (2013) *Earth Planet. Sci. Lett.*, 369-370, 71-77. [15] Holland, G. and Ballentine, C. J. (2006) *Nature*, 441, 186-191. [16] Sumino, H. et al. (2010) *Earth Planet. Sci. Lett.*, 294, 163-172. [17] Kendrick, M. A. (2012) *Chemical Geology*, 292-293, 116-126. [18] Bucholz, C. E. et al. (2013) *Earth Planet. Sci. Lett.*, 374, 145-155.

Acknowledgements: For their generous donation of komatiite samples, I am most thankful to Gary Byerly, Igor Puchtel, Bernard Marty, Euan Nisbet and Mary McGee. We thank CAPTEM and NASA for allocation of Apollo basalts.

THE INDIGENEOUS VOLATILE CONTENT OF THE LUNAR INTERIOR: INVESTIGATING MARE BASALTS USING STEPPED HEATING TECHNIQUE. J. I. Mortimer¹, A. B. Verchovsky¹, M. Anand^{1, 2}, I. Gilmour¹, C. T. Pillinger¹ ¹Planetary and Space Sciences, Department of Physical Sciences, The Open University, Walton Hall, Milton Keynes, MK7 6AA, UK, ²Department of Earth Sciences, Natural History Museum, Cromwell Road, London, SW7 5BD, UK (james.mortimer@open.ac.uk).

Introduction: In recent years, the search for lunar volatiles has attracted renewed interest; while much of recent lunar volatile research has focused on analysis of water and its hydrogen isotopic composition (e.g. [1, 2]), less attention has been paid to the geochemistry of other volatile elements such as N, C and noble gases in lunar samples, especially in lunar basalts. Mare basalts provide an important window into the lunar interior, with indigenous lunar volatile components recorded into the basalts at crystallisation yielding data about the material from which the Earth-Moon system formed, and about the early geochemical evolution of the Moon.

In this new study, we combine stepped heating technique at higher resolution (multiple temperature steps, down to 50 °C) than previous studies (e.g. [3, 4]), with simultaneous collection of data for more element and isotope systems (N, C, He, Ne, and Ar) at each step, all from the same aliquot of lunar sample. Therefore, this new dataset represents a comprehensive, detailed inventory of volatiles in lunar basalts, building on and augmenting the results of previous studies.

Samples: Thirteen Apollo basalt samples (10017, 10057, 10072, 12040, 12047, 12064, 14053, 15386, 15555, 70017, 70035, 74275, and 75055) were selected for this study, spanning a range of crystallisation ages, cosmic-ray exposure (CRE) ages, and compositional variations, and covering each of the Apollo missions (except Apollo 16).

Methods: Approximately 250 mg of a single chip of each mare basalt was crushed using an agate mortar and pestle, to produce a homogenous powder, necessary for sub-sampling; around 5 mg aliquots of each sample were placed in cleaned Pt foil buckets, and subsequently crushed into spheres for analysis (following the procedures outlined in [5]). Samples were analysed using the custom-built multiple static-mode mass spectrometer system 'Finesse' at the Open University [5]. Samples were heated incrementally inside a double-walled quartz-ceramic furnace in 100 °C steps from 200 °C to 600 °C, 50 °C steps from 650 °C to 950 °C, and 100 °C steps from 1000 °C to 1400 °C. Gases released at each temperature were collected after each step and cryogenically separated using a system of liquid nitrogen cooled traps and molecular sieves. Gases were transferred within the machine along high vacuum lines, controlled by a system of automated pneumatic valves [5]. Ar and Ne were purified using Ti-Al getters. N abundances (recorded as ng of N) were measured *via* calibration of the dedicated N

mass spectrometer ion current at $m/z = 28$, and C abundances (recorded as ng of C) were calculated using the pressure of CO₂ measured on a calibrated MKS BaratronTM capacitance manometer. He and Ne were analysed using the quadrupole mass spectrometer, and Ar using one of two magnetic sector mass spectrometers within the 'Finesse' instrument, and noble gas abundances were measured *via* calibration of the mass spectrometer ion currents at the appropriate m/z values.

Results: *Identifying Indigenous Lunar Components:* Based on isotopic signature and C/N ratios, low temperature (typically < 500-600 °C) N and C components released from mare basalts are identified as being terrestrial organic contaminants, and thus these data are excluded when characterizing any indigenous lunar volatile components. Equally, at the highest temperature steps (typically > 950-1000 °C), N and C components released are dominated by cosmogenic isotopes, produced *in situ* during sample exposure to incident cosmic rays on the lunar surface, and hence are also excluded when characterizing indigenous lunar volatile components. However, this leaves a window at mid temperatures (variable between samples, but typically between 650-950 °C) where indigenous components within the samples are released without any masking from non-indigenous signatures, and where it is feasible to quantify the amount and isotopic composition of indigenous volatile components present.

Indigenous C/N ratios: Since both C and N were co-collected from the same aliquot, their release profiles for the same sample can be directly compared. Based on the similarities between these release profiles, it seems that C and N are co-located within the same phase, although the exact nature of this phase remains unidentified on the basis of release temperature alone. Since C and N are located in the same phase, it is possible to use the calculated C/N ratios for these indigenous volatile components to characterise the C and N properties of the lunar mantle, from which these basalts are derived. The average C/N ratios of the indigenous components (Table 1) are relatively tightly constrained. All the basalts in this study show indigenous C/N ratios between 4 and 22, much lower than those measured for the pre-sent-day terrestrial depleted mantle ($C/N_{\text{mantle}} = 535 \pm 224$ [6, 7]), or even for bulk silicate Earth (BSE) ($C/N_{\text{BSE}} = \sim 40 - 50$ (calculated from data in [6])). The range of C/N ratios seen in mare basalts is very similar to that of enstatite

chondrites (a possible proxy for primordial terrestrial mantle [8]).

| Sample | C/N Ratio |
|-----------------------------|---------------------|
| 10017 | 21 |
| 10057 | 16 |
| 10072 | 16 |
| 12040 | 6 |
| 12047 | 18 |
| 12064 | 9 |
| 14053 | 4 |
| 15386 | 10 |
| 70017 | 22 |
| 70035 | 11 |
| 74275 | 18 |
| 75055 | 17 |
| Terrestrial Depleted Mantle | 535 ± 224 [6,7] |
| Estatite Chondrites | 4.5 to 15 [9,10] |

Table 1: C/N ratios of samples compared with ratios for terrestrial depleted mantle and enstatite chondrites.

Indigenous Lunar Nitrogen: The weighted average N released across the mid-temperature indigenous ‘window’ for each basalt reveals a range of values ($\delta^{15}\text{N} = +24.6\text{‰}$ to -10.9‰), which fits well with previous analyses of indigenous lunar N [e.g. 11], and greatly expands the number of samples studied for this purpose. The weighted average $\delta^{15}\text{N}$ value for indigenous lunar N across all of the samples in this study is $+2.4 \pm 0.9\text{‰}$, only slightly heavier than terrestrial mantle N isotopic signatures [7], and also within the range of carbonaceous chondrites [7], highlighting the similarities between the materials forming the Earth, Moon and carbonaceous chondrites (Fig. 1).

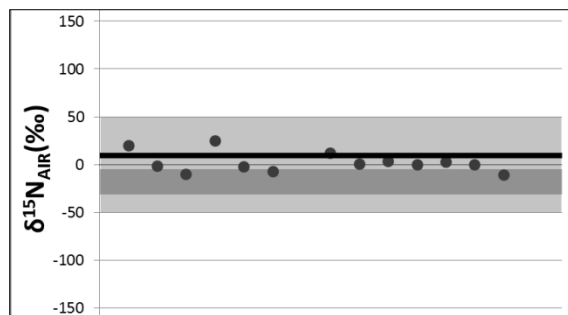


Figure 1: Indigenous lunar N (black circles and bar) with terrestrial mantle N (dark grey band) and carbonaceous chondrite N (light grey band).

Indigenous Lunar Neon: Most samples display binary mixing between a cosmogenic neon component and a terrestrial atmospheric component, a trend which disappears when the system blank is removed. One sample (12064) still shows mixing between cosmogenic and terrestrial-like Ne even after blank correction (Fig.2).

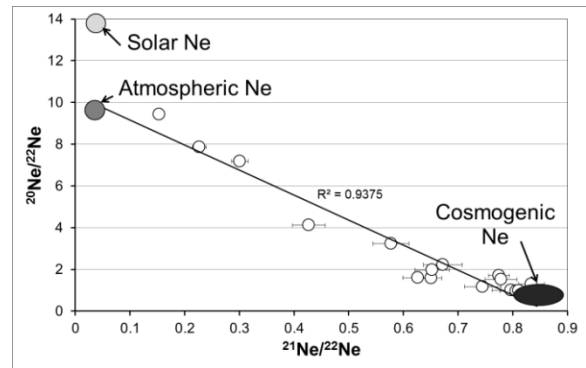


Figure 2: Neon components in sample 12064, displaying mixing between cosmogenic Ne and terrestrial-like trapped Ne components.

It is plausible that terrestrial neon is introduced during sample preparation, or terrestrial neon may be trapped within pseudo-inclusions generated via frictional heating and annealing of grain surfaces during crushing. However, trapping of terrestrial Ne cannot explain the observed mixing trend for several reasons:

- 1.) All samples were processed in the same way, yet terrestrial-like Ne is only seen in 12064.
- 2.) Other co-collected trapped components from the same aliquot do not show evidence for addition of terrestrial atmospheric gases. 134000 times less N is released from the same aliquot of 12064 than might be expected to be released based on the measured ^{21}Ne abundance and terrestrial atmospheric N/Ne ratio, while trapped ^{36}Ar abundances agree well with previous studies of uncrushed samples, suggesting no additional trapping of terrestrial atmospheric ^{36}Ar either.

Taking these factors into consideration, we propose that mare basalt 12064 contains a small amount of indigenous lunar Ne, the composition of which suggests that the source region for this particular basalt may have had indigenous Ne with a similar composition to the present-day terrestrial atmosphere.

References: [1] Saal A. E. et al. (2008) *Nature*, 454, 192-195. [2] Tartèse R. et al. (2013) *Geochim. Cosmochim. Acta*, 122, 58-74. [3] Des Marais D. J. (1978) *LPS IX*, 2451-2467. [4] Mathew K. J. and Marti K. (2001) *EPSL*, 184, 659-669. [5] Abernethy F. A. J. et al. (2013) *Meteoritics and Planet. Sci.*, 48, 1590-1606. [6] Halliday A. N. (2013) *GCA*, 105, 146-171. [7] Marty B. (2012) *EPSL*, 313-314, 56-66. [8] Javoy M. et al. (2010) *EPSL*, 293, 259-268. [9] Wasson J. T. and Kallemeyn G. W. (1988) *Phil. Trans. R. Soc. Lond. A*, 325, 535-544. [10] Thiemens M. H. and Clayton R. N. (1983) *EPSL*, 62, 165-168. [11] Barry, P. H. et al. (2013) *LPSC XLIV*, #2160.

GLOBAL DIVERSITY OF THE LUNAR CRUST: SCIENCE AND CHALLENGES OF LUNAR SAMPLE RETURN. K. H. Joy¹, J. Gross², T. Arai³, S. A. Russell⁴ ¹School of Earth, Atmospheric and Environmental Sciences, University of Manchester, Oxford Road, Manchester, M13 9PL, UK, ²The American Museum of Natural History, Dept. of Earth and Planetary Sciences, New York, NY 10024, USA, ³Planetary Exploration Research Centre, Chiba Institute of Technology, Japan, ⁴The Natural History Museum, Cromwell Road, London SW7 5BD, UK (katherine.joy@manchester.ac.uk).

Introduction: The lunar crust preserves an archive of planetary differentiation and early evolution, which is not easily accessible on other rocky planetary bodies.

Early history of the Moon: After its formation, the Moon had a well-mixed global lunar magma ocean (LMO) that initially crystallised at equilibrium [1-3]. This first phases precipitated were Mg-rich mafic minerals that, after ~50% total crystallisation, sank to form the lunar deep mantle [4-6]. The final stages of LMO formation were likely controlled by fractional crystallisation of a constantly changing and instantaneously homogenous residual magma [5]. After about 80% of LMO crystallisation, plagioclase was precipitated and floated to form a primary crust made of ferroan anorthosites [2-5]. In the classic LMO model all the plagioclase solidified would have originated from a chemically homogenous parent melt.

After the lunar highlands crust was formed, the lunar interior was still hot and partially melted. These melts intruded the crust and a formed suite of magmatic rocks (Mg-Suite and High Alkali Suite) and extrusive lava flows (KREEP basalts, high-Al basalts).

New insights from Apollo samples: Isotopic and chemical studies create complexities for FAN origin as primary crust formed from the primordial LMO. For example, variation in ϵNd values [7-8] and REE [9] suggest that FANs originated from a range source regions. Additionally some FANs have younger ages (~4.2 Ga [8]), that overlap with Magnesian Suite and High Alkali Suite intrusive magmatic rocks, suggesting that they formed through a similar period of lunar history.

New insights from lunar meteorites: Lunar meteorites are sourced from random localities on the surface and, thus, provide a global understanding of the geological diversity of the Moon, although their precise provenance is unknown [10,11]. Major element mineral compositions of anorthositic material in feldspathic lunar meteorites [12-14] do not fit well with the fields of Apollo highland rock suites [15]. Notably, anorthositic clasts in lunar meteorites are often more magnesian than their Apollo equivalents, suggesting unique parent melts [12-14]. Plagioclase mineral chemistry trace element data provide further evidence for compositional differences between the lunar nearside highlands, as sampled by Apollo 15 and 16 [9,16], and regions remote sampled by the lunar meteorites [17-19].

These critical observations potentially present complications for the proposed formation mechanisms of the lunar crust, and may support the view that the anorthositic highlands may have formed from different parent melts (e.g., asymmetric crystallisation or multiple magma oceans, serial magmatism, differentiated impact melt sheets [13]).

However, lunar meteorites are typically highly impact processed, and deconvolving the chemical and physical effects of impact from primordial signatures is a challenge [20]. It is unclear if all clasts in lunar meteorites are representative of large-scale lunar lithologies as their petrographic context has often been lost, including indication of true pristinity.

Sample return opportunities: Future exploration of the lunar surface [21] should seek to test models of lunar crust formation (e.g., [13, 22]). Any regolith / core drill samples returned from the lunar surface will likely contain small fragments of ancient crust, providing key insights to the chemical and chronological history of lunar differentiation. Direct sampling of crust within the farside Feldspathic Highlands Terrane will provide direct access of material with known geological context, helping to test models of crust formation [22]. It would be highly desirable to directly sample outcrops of pure anorthosite layers to compare their isotopic and petrological evolution compared with nearside FANs [23-25]. However, many of these sites are located in potentially technologically challenging landing sites (e.g., steep slopes, mountains), so roving capabilities from safer landing sites to collect material would enable bedrock sample access. Sampling floor materials in the South Pole-Aitken basin will help to investigate the products of differentiated impact melt ponds [22, 26], helping to test impact modification crust formation models.

References: [1] Tonks W. B. and Melosh H. J. (1990) *Origin of the Earth*. Oxford Univ. Press, New York, NY [2] Taylor S.R. (1982) Planetary Science: A lunar perspective. LPI Publication [3] Warren P. H. (1985) *Ann. Rev. Earth Planet. Sci.* 13, 201-40. [4] Snyder G. A. et al. (1992) *GCA* 56, 3809-3823 [5] Elkins-Tanton L. et al. (2011) *EPSL* 304, 326-336 [6] Elardo S. M. et al. (2001) *GCA* 75, 3024-3045. [7] Longhi J. (2003) *JGR* 108, 2-1 [8] Borg L. E. et al. (2009) *Nature* 477, 70-7 [9] Floss C. et al. (1998) *GCA* 62, 1255-1283. [10] Korotev R. L. et al. (2003) *GCA* 67, 4895-4923 [11] Joy K. H. and Arai

(2013) *Astronomy and Geophysics* 54, 4.28-4.32.
 [12] Takeda H. et al (2006) *EPSL* 247, 171–184 [13]
 Arai T. et al. (2008) *Earth, Planets, Space*. 60, 433–
 444 [14] Gross J. et al (2014) *EPSL* 388, 318-328
 [15] Warren P. H. (1993) *Am. Min.* 78, 360-376.
 [16] Papike J. J. et al. (1997) *GCA* 61, 2343–2350
 [17] Cahill J. T. et al. (2004) *MAPS* 39, 503–529.
 [18] Joy K. H. (2013) *LPSC XLIV* (Abst. #1033).
 [19] Russell S. S. et al (In Review) *Phil. Trans. R.
 Soc. A* [20] Warren P. H. (2012) Second Conference
 on the Lunar Highlands Crust (Abst.# 9034) [21]
 NRC (2007) The Scientific Context for the
 Exploration of the Moon ISBN: 0-309-10920-5 [22]
 Wetherill G. W. (1976) 7th *LPSC* 3245 [23] Ohtake
 M. et al. (2011) *Nature Geoscience*, 5, 384–388. [24]
 Ohtake M. et al. (2009) *Nature*, 461, 236-240 [25]
 Yamamoto S. et al., (2012) *GRL* 39,
 DOI: 10.1029/2012GL052098 [26] Hurwitz D. M.
 and Kring D.A. (2014) *LPSC XLV* (Abst. #1398).

THERMAL INFRARED STUDIES OF LUNAR SOILS: CHARACTERIZING SPECTRAL EFFECTS DUE TO SIMULATED LUNAR CONDITIONS AND PACKING. K. L. Donaldson Hanna¹, I. R. Thomas², N. E. Bowles¹, C. M. Pieters³, B. T. Greenhagen⁴ ¹Atmospheric, Oceanic and Planetary Physics, University of Oxford, Clarendon Laboratory, Parks Road, Oxford, UK, ²Belgian Institute for Space Aeronomy, Brussels, Belgium, ³Department of Geological Sciences, Brown University, Providence, RI, USA, ⁴Jet Propulsion Laboratory, Pasadena, CA, USA (DonaldsonHanna@atm.ox.ac.uk).

Introduction: Apollo mare and highland soils [e.g. 1-3] as well as basaltic rocks [4] have been well-characterized across the visible- to near-infrared (VNIR) wavelengths including the effects of particle size, mineralogy, mineral chemistries, ilmenite content and space weathering on their spectra. These laboratory analyses provided ground truth to remote sensing observations from Earth-based telescopic observations and spacecraft observations like those from Clementine, Galileo, Lunar Prospector, SELENE, and Chandrayaan-1 as well as providing key insights into the composition and evolution of the lunar surface. Recently the Diviner Lunar Radiometer, a thermal infrared (TIR) radiometer, was launched onboard the Lunar Reconnaissance Orbiter (LRO) making it necessary for the characterization of Apollo samples across TIR wavelengths. The near-surface vacuum environment of airless bodies like the Moon creates a thermal gradient in the upper hundred microns of regolith. Lab studies of particulate rocks and minerals as well as selected lunar soils under vacuum and lunar-like conditions have identified significant effects of this thermal gradient on thermal infrared (TIR) spectral measurements [e.g. 5-10]. Such lab studies demonstrate the high sensitivity of TIR emissivity spectra to environmental conditions under which they are measured. Further, TIR lab studies have demonstrated the spectral effects of packing on TIR spectral measurements [e.g. 5,11].

In this work, an initial set of thermal infrared emissivity measurements of the bulk lunar soil samples will be made in the Asteroid and Lunar Environment Chamber (ALEC) at Brown University and the Simulated Lunar Environment Chamber at the University of Oxford. These laboratory measurements of bulk lunar soil samples are compared with Diviner data to understand: (1) how to accurately simulate conditions of the near-surface environment of the Moon in the lab and (2) the difference between returned samples and undisturbed lunar soils in their native setting. Both are integral for constraining thermally derived compositions and properties of the lunar surface from current (Diviner) and future TIR datasets.

Experimental Setups: ALEC is a vacuum chamber in Brown University's RELAB [12] designed to simulate the space environment experienced by the near-surface regolith of the Moon and asteroids. The design details of the vacuum chamber have previously been discussed [13].

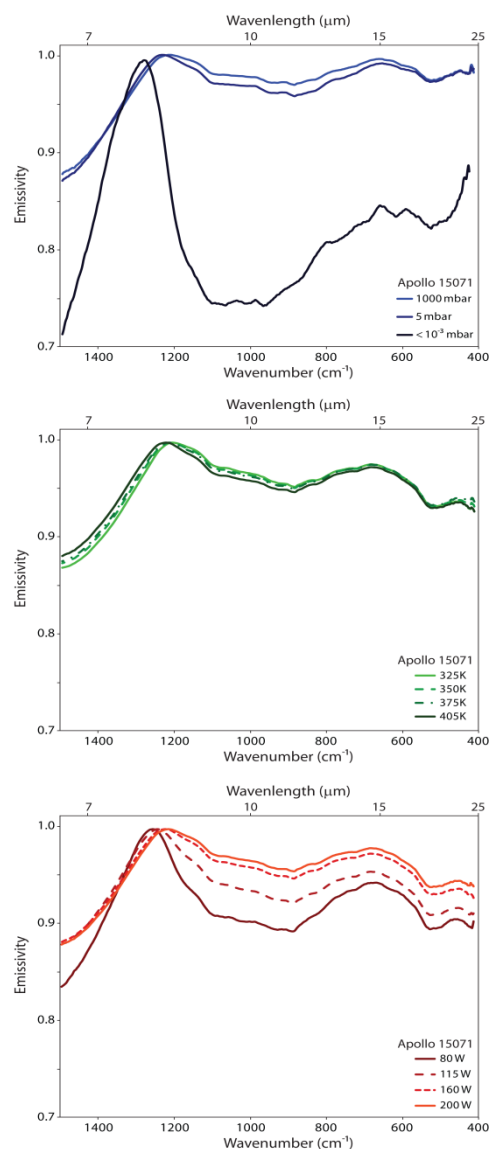


Figure 1: Bulk lunar soil 15071 measured under varying conditions in ALEC: **(Top)** Internal chamber pressure was varied between 1000 mbar and $<10^{-3}$ mbar, **(Middle)** Sample cup heater temperature was varied between 325 K and 405 K and **(Bottom)** Power of the solar lamp was varied between 80 W and 200 W.

ALEC is connected to RELAB's Thermo Nicolet 870 Nexus FTIR spectrometer which allows laboratory emissivity spectra to be collected at a resolution of 4 cm^{-1} over the $\sim 400 - 2000 \text{ cm}^{-1}$ spectral range. The Simulated Lunar Environment Chamber (SLEC) at the University of Oxford is described in more detail elsewhere [8]. Radiation emitted from the sample is reflected into a Brüker

IFS-66v/S FTIR spectrometer by a cooled collecting mirror positioned above the sample. Spectral measurements are collected at a resolution of 4 cm^{-1} over the $\sim 400 - 2400\text{ cm}^{-1}$ spectral range.

While the design and workings of each chamber is slightly different, the chambers are functionally the same. In each chamber, we simulate the lunar environment by: (1) pumping the chambers to vacuum pressures ($<10^{-3}$ mbar), which is sufficient to simulate lunar heat transport processes within the sample, (2) cooling the chambers with liquid nitrogen to simulate the cold space environment that the Moon radiates into, and (3) heating the samples from below, above, or both to set-up thermal gradients similar to those experienced in the upper hundreds of microns of the lunar surface. Sample material is spooned into the sample cup and the surface of the sample is prepared using four different methods: (1) tapped: the sample cup is tapped until the surface is relatively flat, (2) smoothed: the surface of the sample is smoothed by slightly pressing it, (3) flat edge: the a flat edge is taken across the surface of the sample to create a relatively flat and smooth surface, and (4) spooned: sample is simply spooned into the sample cup and no further prep is done to the sample.

Results: To best constrain the spectral effects of varying the environmental conditions, initial measurements were made of Apollo bulk sample 15071 in ALEC. The top plot in Figure 1 shows results for Apollo soil sample 15071 as the atmospheric pressure inside the chamber is systematically varied. The Christiansen Feature (CF), an emissivity maximum near $\sim 1250\text{ cm}^{-1}$, is observed to shift to higher wavenumbers (shorter wavelengths) and the spectral contrast of the CF relative to the reststrahlen bands (RB), spectral absorptions between ~ 1100 and $\sim 800\text{ cm}^{-1}$, is enhanced as the atmospheric pressure decreases from ambient (~ 1000 mbar) to vacuum ($<10^{-4}$ mbar) pressures. In the middle plot in Figure 1, no significant differences between spectral measurements made as the sample cup temperature is varied between 325K and 405K are observed. As the power of the solar-like halogen lamp is increased from 80 to 200 W, the CF shifts to lower wavenumbers (longer wavelengths) and the spectral contrast of the CF relative to the RB decreases as seen in the bottom plot in Figure 1. Changes in the pressure and halogen lamp power lead to competing spectral effects on the same scale. Whereas varying the sample cup temperature does not create any observable changes in the spectral measurements.

The spectral effects due to sample preparation were characterized by initial measurements of Apollo 15071 measured under simulated lunar conditions in SLEC. In Figure 2, minor shifts in the CF position are observed as the packing style

changes, however the other spectral features are observed at the same frequency (cm^{-1}) no matter the packing style. Differences in spectral contrast and slope between the packing styles are on the order of 1-2%. These results are consistent with previous lab studies of packing style [5,11].

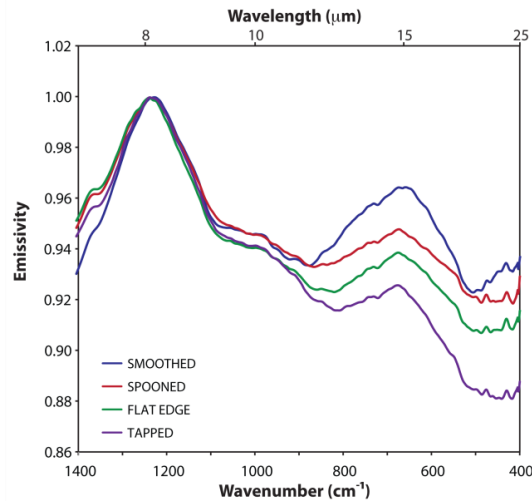


Figure 2: Spectra of Apollo 15071 measured under simulated lunar conditions in the SLEC. The sample was prepared using different methods: smoothed, spooned, flat edge, and tapped.

Discussion: Spectral measurements under varying environmental conditions and packing styles will be compared with Diviner TIR measurements to constrain the laboratory conditions that best simulate the lunar surface. Future work will focus on the measurement of a suite of Apollo bulk lunar soil samples that encompass a range of compositions and maturities. In addition, samples will be measured in a suite of environment chambers in an effort to better characterize the near surface environment of the Moon as well as understanding cross-laboratory measurement differences.

References: [1] Pieters C. M. et al. (2000) *LPS XXXI*, Abstract #1865. [2] Taylor L. A. et al. (2001) *MaPS*, 36, 285-299. [3] Taylor L. A. et al. (2003) *LPS XXXIV*, Abstract #1774. [4] Isaacson P. J. et al. (2011) *MaPS*, 46, 228-251. [5] Logan L. M. et al. (1973) *JGR*, 78, 4983-5003. [6] Salisbury J. W. and Walter L. S. (1989) *JGR*, 94, 9192-9202. [7] Henderson B. G. et al. (1996) *JGR*, 101, 14969-14975. [8] Thomas I. R. et al. (2012) *Rev. Sci. Instrum.*, 83(12), 124502. [9] Donaldson Hanna K. L. et al. (2012) *JGR*, 117, doi:10.1029/2011JE003862. [10] Donaldson Hanna K. L. et al. (2012) *JGR*, 117, doi:10.1029/2012JE004184. [11] Salisbury J. W. and Wald. A (1992) *Icarus*, 96, 121-128. [12] Pieters C. M. and Hiroi T. (2004) *LPS XXXV*, Abstract #1720. [13] Donaldson Hanna K. L. et al. (2013) *LPS XXXIV*, Abstract #2225.

COMPARISON OF MASS-WASTING FEATURES IN CRATERS ON ASTEROID 4 VESTA AND THE MOON. K. A. Otto¹, K. Krohn¹, J. Balzer^{1,2}, H. Hoffmann¹, R. Jaumann^{1,2} ¹Institute of Planetary Research, German Aerospace Center (DLR), Berlin, Germany, ²Freie Universität Berlin, Inst. of Geosciences, Planetology and Remote Sensing, Rutherfordstr. 2, 12489 Berlin, Germany (katharina.otto@dlr.de).

Introduction: Mass wasting on airless rocky bodies is driven by gravity and often triggered by seismic shaking of nearby impacts. We will analyze the similarities and differences of mass wasting features on the Moon and asteroid Vesta in relation to their gravity. Although the Moon's gravitational acceleration ($\sim 1.6 \text{ m/s}^2$) is about six times larger than asteroid Vesta's ($\sim 0.24 \text{ m/s}^2$) and both have different orbital properties, they show several similar mass-wasting features. Here, we focus on the mass-wasting processes in two famous craters: the Rheasilvia crater ($\sim 500 \text{ km}$ in diameter) on Vesta and the Tycho crater ($\sim 86 \text{ km}$ in diameter) on the Moon.

Asteroid Vesta: Vesta is the second most massive asteroid of the main asteroid belt between Mars and Jupiter and has been orbited by NASA's Dawn spacecraft in 2011 / 2012. Vesta is a differentiated oblate spheroid shaped proto-planet with a mean diameter of $\sim 525 \text{ km}$. One of Vesta's most prominent features is its $\sim 500 \text{ km}$ diameter south polar impact basin, called Rheasilvia [1, 2].

Methods: For comparison of Vestan and Lunar mass-wasting features we used the Low Altitude Mapping Orbit (LAMO) data from the NASA Dawn mission with a resolution of $\sim 20 \text{ m/pixel}$ [3, 4] and Wide Angle Camera (WAC) data from the Lunar Reconnaissance Orbiter (LRO) mission with a resolution of $\sim 100 \text{ m/pixel}$ [5]. For topographic analysis of the terrain, we used a Digital Terrain Models (DTM) of Vesta [6] and of the Moon [7], both with a spatial resolution of $\sim 100 \text{ m/pixel}$.

Results: Figure 1 shows differences and similarities between the Rheasilvia crater on Vesta and the Tycho crater on the Moon. We found intra-crater mass-wasting in both craters, such as slumps, slides and flow-like features.

The slides at Tycho can be divided into rock slides and debris slides [8], where rock slides are sheets of impact melt moving down a slope and debris slides are composed of displaced smaller sized grains. The slides on Vesta are predominantly debris slides forming landslide bodies of up to 100 km in length (Fig.1) [9]. Slides of this dimension in Tycho only occur outside the crater and are associated with impact ejecta.

Flow-like features are observable mainly between 35°E and 95°E in Rheasilvia and in the north and south of Tycho; however, they appear rarely (Fig. 1). They are slides of low friction or liquid behavior developing striations [8, 9]. They are often associated with impact melt or ejecta [9, 10].

Additionally, slumps form on the crater rims of Rheasilvia and Tycho. Slumps are characterized by a relatively short mass movement on a concave surface of rupture forming slumping blocks (Fig. 2). Slumping in Tycho is distributed along the entire crater wall, whereas in Rheasilvia the slumping areas are often eroded by later debris slides.

Conclusion: The study of Rheasilvia and Tycho shows similar mass wasting processes in both craters, such as slumps, slides and flow-like features. The different physical conditions, like gravity or surface material properties may cause differences in the morphology.

Rheasilvia shows a smooth transition between crater floor and crater rim, whereas the transition at Tycho is more distinctive. The most common degradation process in Tycho is slumping forming steep scarps. Rheasilvia has also been eroded by large debris slides forming a smooth transition between crater wall and floor.

Slumping is triggered when gravity forms a torque on the slumping body which exceeds the frictional forces. Therefore slumping develops more efficiently on bodies with higher gravity.

References: [1] Jaumann R. et al. (2012) *Science*, 336, 687-690. [2] Russell C. T. et al. (2013) *Meteoritics & Planet. Sci.*, 48, 2076-2089. [3] Russell C. T. et al. (2007) *Earth Moon Planets*, 101, 65-91. [4] Roatsch T. et al. (2013) *Planet. Space Sci.*, 85, 293-298. [5] Robinson M. S. et al. (2010) *Space Science Rev.*, 150, 81-124. [6] Preusker F. et al. (2012) *EPSC VII*, Abstract #428. [7] Scholten F. et al. (2011) *JGR*, 117, E00H17. [8] Xiao Z. et al. (2013) *Earth Planet. Sci. Lett.*, 376, 1-11. [9] Otto K. A. et al. (2013) *JGR*, 118, 2279-2294. [10] Williams D. A. et al. (2013) *Planet. Space Sci.*, in press.

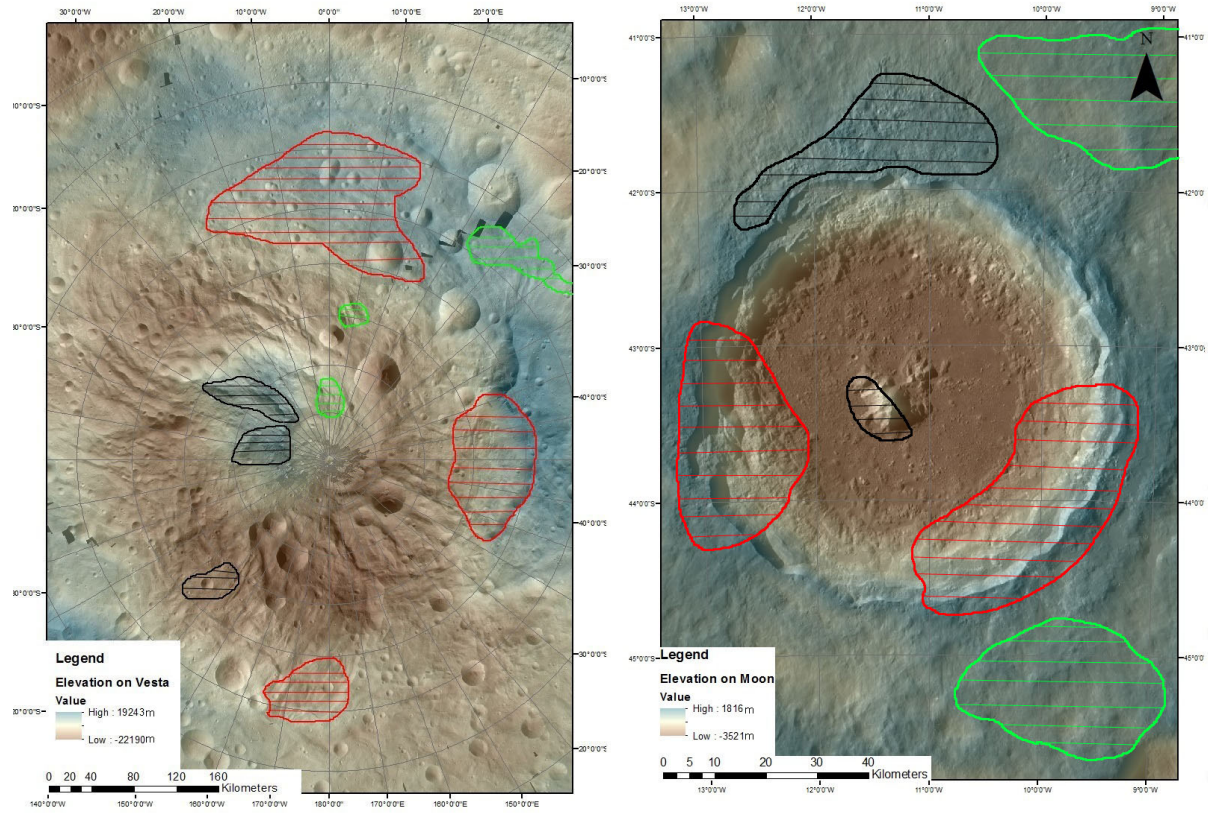


Figure 1: Distribution of slumping, sliding and flow-like areas inside Rheasilvia (left) and Tycho (right); red: slumps, black: slides, green: flow-like features.

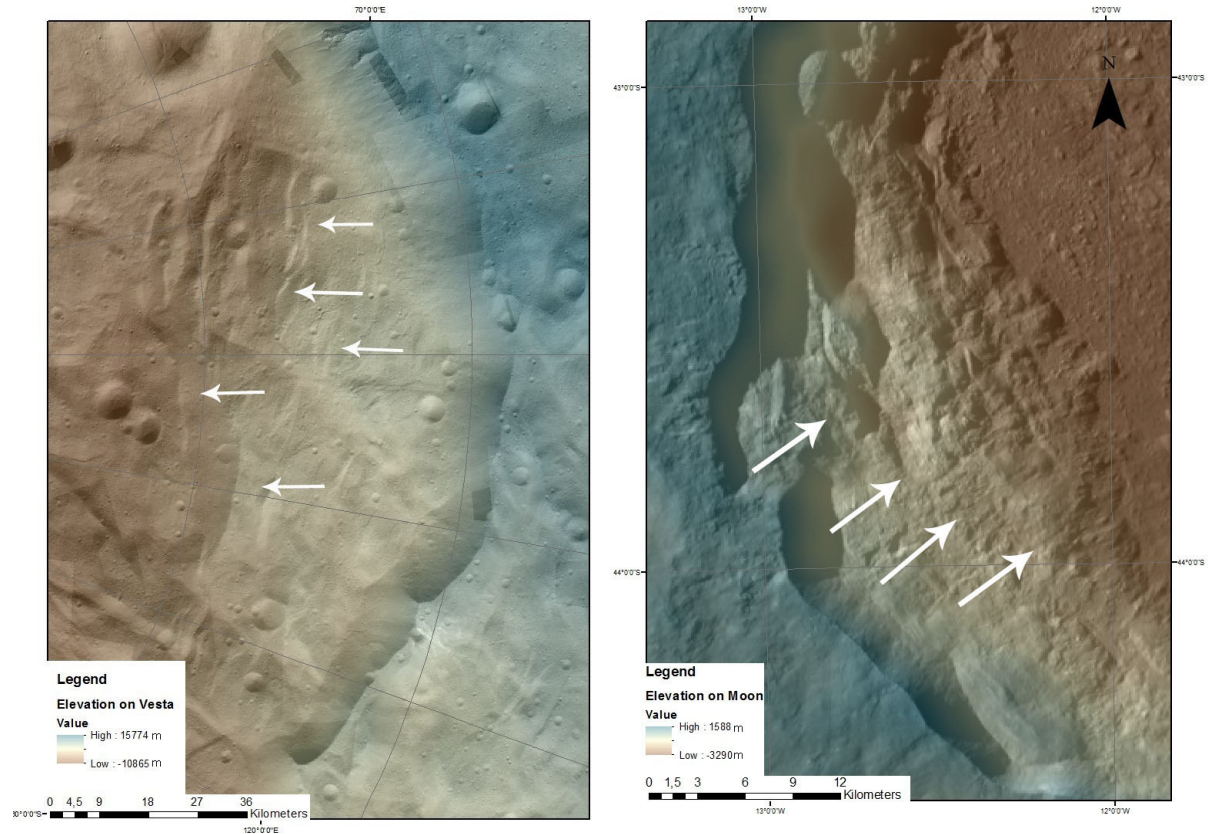


Figure 2: Slumping areas within Rheasilvia (left) and Tycho (right). The arrows indicate heads of slumping blocks.

AUTOMATIC ENDMEMBER SELECTION AND NONLINEAR SPECTRAL UNMIXING OF TERRESTRIAL MINERALS. D. Rommel¹, M. P. Felder¹, A. Grumpe¹, U. Mall², C. Wöhler¹ ¹Image Analysis Group, TU Dortmund University, D-44227 Dortmund, Germany; (daniela.rommel@tu-dortmund.de | marian.felder@tu-dortmund.de | arne.grumpe@tu-dortmund.de | christian.woehler@tu-dortmund.de), ²Max Planck Institute for Solar System Research, Max-Planck-Str. 2, 37199 Katlenburg-Lindau, Germany (mall@mps.mpg.de).

Introduction: Recent development in hyper-spectral remote sensing has dealt with the advanced mineralogical analysis of the surface by spectral unmixing (e.g. [1]). Commonly, due to the lack of ground truth data, spectral unmixing is applied to a certain data set, and the results are discussed (e.g. [2]). The goal of this study is the generation of laboratory ground truth samples of known mineral composition in order to evaluate a nonlinear unmixing algorithm, in the context of unmixing analysis of lunar spectra based on terrestrial analog materials.

Sample preparation: For this study, we have used an endmember catalog of seven samples from different groups of minerals: augite, diallagite, enstatite, eulite, two labradorites and olivine.

Powder generation: All minerals were mechanically crushed and sieved to produce grains at various sizes, i.e. <32 μm , 32-63 μm and 63-125 μm . Afterwards, impurities visible at microscopic inspection were removed by washing with solvents. Finally, the remaining impurities were removed manually.

Mixture preparation: In order to generate accurate mixtures, the corresponding powders were weighed using a high precision balance and mixed thoroughly by shaking the vessel containing all powders. Table 1 summarises the examined mixtures.

Reflectance measurement: The analysis within this work is restricted to a grain size of 32-63 μm . All powders were filled into a circular sample container and flattened. The sample was illuminated by an HL-2000-FHSH halogene light source and the spectral radiance in the wavelength range 600-2600 nm was then obtained using an Arcoptix FTNIR-U-06-026 spectrometer. According to lunar remote sensing standard geometry [3], we apply a nadir view setup with an incidence angle of 30°. To derive the reflectance of the sample, the obtained radiance spectrum was divided by the radiance spectrum of a diffuse reflectance standard. The resulting reflectance spectrum is thus relative to that of an ideally white Lambertian surface. The normalised reflectance of the surface according to the Hapke model [4] is obtained by multiplication by the cosine of the incidence angle. For the pure minerals, six different sample containers were filled and each quadrant of the container was measured. The resulting 24 spectra are averaged to reduce the effects of different powder compressions and filling heights which may arise from different pressures during the manual flattening of the samples. Fig. 1 shows the averaged endmember spectra (solid lines)

from our catalog and the standard deviation over all 24 measurements (dashed lines). In case of the mixtures, two samples were measured at nine distinct spots.

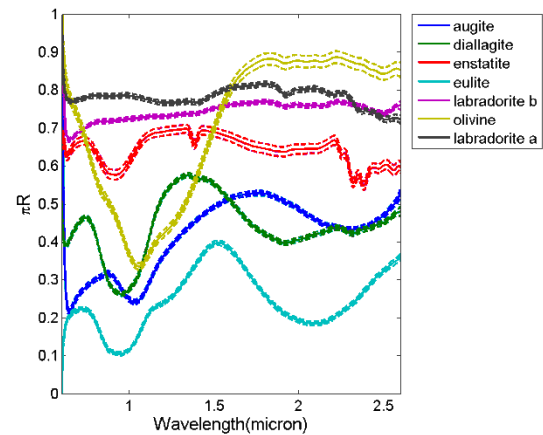


Figure 1: Endmember catalogue. Solid lines: average endmember spectra. Dashed lines: \pm standard deviation.

Non-linear unmixing algorithm: According to [5], nonlinear unmixing can be linearised based on the wavelength-dependent single-scattering albedo w of the Hapke model. We apply the full Hapke model including the anisotropic multiple scattering approximation [4, 6]. All parameters except the single-scattering albedo and the surface roughness parameter are adopted from [7]. The surface roughness is set to 0° due to the flattening during the sample preparation. The single-scattering albedo is then estimated by minimising the mean squared difference between the measured spectrum and the modelled reflectance for each spectral channel, respectively. The measured albedo spectrum is then linearly unmixed using albedo (w) spectra of the catalog endmembers by minimising the mean squared differences between the measured and the mixed spectrum. Additionally, the sum of the endmember coefficients is constrained to a constant. The closed interval [0;1] is traversed in steps of 0.01, and the constant with the minimal error is chosen. This strategy accounts for model inaccuracies and measurement errors as well as agglutinate produced by spaceweathering [8] in the case of our planned examinations of lunar minerals.

Endmember selection: Due to the limited number of endmembers in the catalog, we apply an exhaustive search to select endmembers from the catalog. For each possible combination, a fitness function is evaluated, respectively. The fitness function is adopted from [9]. It sums the squared difference between the measured and the mixed albedo spectrum and the squared difference of the

corresponding continuum-removed reflectances. Additionally, spectral parameters, e.g. the position, depth and width of absorption troughs at ~1000 nm, ~1300 nm and ~2000 nm, are computed and a normalised squared difference is added to the fitness function. Absorption features that are not present in the measured spectrum are penalised by adding a large constant.

Table 1: Examined mixtures.

| | mineral | wt% | mol% | estim. mol% |
|-----------------|---------------|-----|------|----------------|
| MP ₁ | enstatite | 30 | 30.6 | 25.6 |
| | labradorite a | 70 | 69.4 | 69.4 |
| | olivine | 0 | 0.0 | 0.5 |
| MP ₂ | enstatite | 70 | 70.6 | 73.5 |
| | labradorite a | 30 | 29.4 | 24.2 |
| | olivine | 0 | 0.0 | 0.5 |
| MP ₃ | enstatite | 10 | 10.2 | 0.0 |
| | labradorite a | 90 | 89.8 | 94.0 |
| MP ₄ | enstatite | 90 | 90.2 | 88.5 |
| | labradorite a | 10 | 9.8 | 11.5 |
| MP ₅ | enstatite | 30 | 30.0 | 26.5 |
| | labradorite a | 50 | 48.7 | 51.4 |
| | augite | 20 | 21.3 | 19.5 |

Results: The estimated mineral composition for each mixture, respectively, is given in Table 1. Notably, the estimated fractions do not sum to one. The remaining part may be interpreted as measurement uncertainty and absorbs possible modelling errors and/or different porosity caused by the manual flattening. The algorithm determines the correct endmembers. Only in case of MP₁ and MP₂ a negligible olivine fraction of 0.5 mol% is estimated.

The estimated fractions match the real fractions very well. The observed minor deviations may again be related to the reflectance modelling which influences the estimation of the endmember albedo spectra and the mixture albedo spectra. Thus, the results may be improved if multiple viewing and illumination geometries are considered.

Fig. 2 shows the reflectance spectra of the mixtures and the reconstructed reflectance spectra computed by the unmixing algorithm. The computed reflectance spectra of the estimated mixtures are in good agreement with the measured reflectance spectra. The mixture MP₃, however, is not well represented by the pure labradorite spectrum. Furthermore, the prominent enstatite signature near 1000 nm is missing in the measured reflectance of the mixture. Hence, it appears to be difficult to determine the presence of enstatite if its fraction is only 10 wt%. At this point it is not clear whether the effect of the missing absorption is not modelled by the reflectance model or if it is just not present at the examined observation geometry.

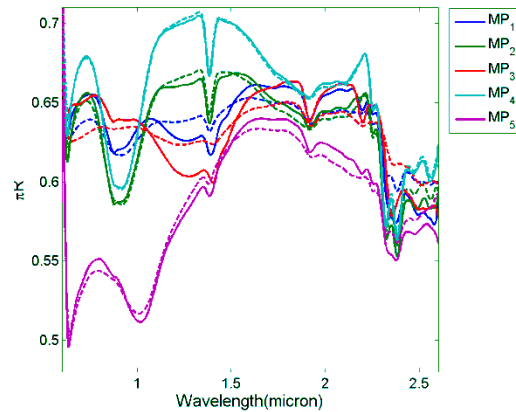


Figure 2: Reflectance spectra of the mixtures (solid lines) and the reconstructed spectra of the unmixing result (dashed lines).

Conclusion and Outlook: We have shown that, in general, the Hapke model can be applied to transform the nonlinear unmixing problem into the problem of linear unmixing of the single-scattering albedo (w) spectra. The obtained mineral fractions are in good agreement with the ground truth and show promising results. The endmembers were determined correctly from the available catalogue.

Further research will include the addition of further endmembers into the catalogue, e.g. ilmenite, which are known to have a strong influence on the reflectance of a mixture. Furthermore, the elemental composition of the catalogue minerals has been determined using electron microprobe analysis. Thus, the obtained mineralogical composition will allow for using to derive the elemental composition of the unmixed spectra.

The same experiments will be applied to measurements at different illumination and viewing directions to examine the influence of the illumination and derive an optimal set of incidence and emittance angles for the determination of the model parameters and the spectral unmixing result.

Acknowledgements: We thank Prof. Dr. G. Wörner and Dr. A. Kronz (University of Göttingen) as well as Prof. Dr. P. Walzel and G. Schaldach (TU Dortmund) for their technical support and valuable discussions.

References: [1] Keshava, N. and Mustard, J. F. *IEEE Signal Processing Magazine*, Jan. 2002, 44-57; [2] Heylen, R. and Gader, P. *IEEE Geoscience and Remote Sensing Letters*, in press; [3] Pieters (1999) *Workshop on New Views of the Moon II*, abstract #8025; [4] Hapke, B. (2002) *Icarus* 157(2), 523-534; [5] Mustard, J. F. and Pieters, C. M. (1989), *J. Geophys. Res.* 94, 13619-13634.; [6] Hapke, B. (1984) *Icarus* 59(1), 41-59; [7] Warell, J. (2004) *Icarus* 167, 271-286; [8] Mall, U. et al. (2012), *Geophysical Research Abstracts*, vol. 14, EGU2012-7852; [9] Felder, M. P. et al. (2013) *EPSC Abstracts*, vol. 8, EPSC2013-684.

AUTOMATIC SEGMENTATION OF PETROGRAPHIC GEOLOGIC UNITS BASED ON ELEMENTAL ABUNDANCE MAPS. A. Grumpe¹, C. Wöhler¹ ¹Image Analysis Group, TU Dortmund University, D-44227 Dortmund, Germany (arne.grumpe@tu-dortmund.de | christian.woehler@tu-dortmund.de).

Introduction: Geological units on planetary bodies are commonly defined by lithostratigraphy or chemostratigraphy. The definitions are based on manually selected criteria. Thus, the geological units may vary depending on the human that defines them. In contrast, automatic algorithms, e.g. cluster algorithms, may be applied to “learn” the defining criteria based on so-called features, e.g. topographic slopes or surface reflectance.

Motivation: Recent development in hyperspectral remote sensing has enabled an advanced mineralogical analysis of the surface e.g. by spectral unmixing [1]. In [2] a nonlinear spectral unmixing method is proposed that automatically selects end-members from a given catalogue. The runtime of that method, however, is too high to be applied at a global scale. The computational complexity, though, may be greatly reduced if homogeneous mineralogical units are known, such that the endmember selection needs to be executed only once per geological unit.

Related work: In a previous work [3], we have proposed a split-and-merge clustering algorithm which determines the geological units and compares the continuum-removed (CR) reflectance within each geological unit, respectively. If the spread within one geological unit is too large, the geological unit is split into several units. Afterwards, similar but independently found geological units are merged into single units. The proposed features therein were coefficients of a spectral decomposition based on the most distinct reflectance spectra.

Contribution: The obtained geological units are based on reflectance spectra and thus only contain indirect clues to the mineral composition of the surface. In order to produce geological units which are suitable for the unmixing approach, this work proposes a different feature set based on the petrographic properties of the surface.

Dataset: The proposed method is applied to our photometrically normalised global mosaic derived from hyperspectral data acquired by the Moon Mineralogy Mapper (M³) [4] instrument. All M³ images and the corresponding regions of the GLD100 digital elevation map [5] are resampled to 20 pixels per degree. The global mosaic covers a latitudinal range of $\pm 60^\circ$. The thermal emission component was estimated for each image and subtracted from the observed spectral radiances according to [6]. Afterwards, a channel-wise single-scattering albedo according to the Hapke model [7] was estimated for each pixel by minimising the mean-squared deviation between the modelled and the measured spectral reflectance over all overlapping images [8], where the GLD100 topographic data set was used to take into account

the influence of surface topography. The remaining parameters of the Hapke model were adopted from [9]. The normalised reflectance was computed by inserting the estimated single-scattering albedo and a standard illumination geometry of 30° incidence angle, 0° emission angle and 30° phase angle [10] into the Hapke model. Here, we downscale the global mosaic to two pixels per degree to reduce runtime.

Automatic clustering algorithm: We adopt the clustering algorithm of [3] to determine homogenous geological units. The proposed feature set, however, is changed to a petrographically motivated feature set.

Split-and-merge algorithm: According to [3], the spectra are grouped into 12 initial clusters using a self-organizing map (SOM) [11]. Afterwards, the median and the quartiles (25% and 75% quantiles) of the member spectra are computed for each cluster, respectively. The CR reflectance of the median spectrum and the quartile spectra are then compared and the cluster is split into three subclusters using the SOM if the correlation exceeds a threshold. Once the spread of the CR reflectance is homogenous in each cluster, similar clusters that originate from different original clusters are merged based on the correlation of the cluster's median spectra.

Feature extraction: The features proposed in [3] are based on the most distinct spectra within the whole mosaic. To select features that are more directly related to the mineral composition of the surface, we estimate the elemental abundances according to [12]. At a spatial scale of 0.2 pixels per degree, a linear regression model was trained to map spectral parameters, i.e. the continuum slope, the depth and wavelength of the absorption minimum and the width of the ferrous absorption trough at ~ 1000 nm and the continuum slope and the depth of the absorption trough at ~ 2000 nm, onto the Lunar Prospector Gamma Ray Spectrometer elemental abundance maps of the elements Ca, Al, Fe, Mg and O [13,14]. In the case of the element Ti, a quadratic regression model based on the continuum slope at ~ 1000 nm and the logarithm of the band depth ratio between ~ 1000 nm and ~ 2000 nm was determined [15]. From the estimated elements the most uncorrelated elements, i.e. Fe, Mg and Ti, are chosen. The correspondingly estimated weight percentages are used as features for the clustering algorithm.

Results: The clustering algorithm initially returned 143 geological units, but most returned clusters had only one member. Due to the split algorithm, each outlier is represented by its own cluster. Therefore, we removed all clusters with less than three members and obtained a set of ten

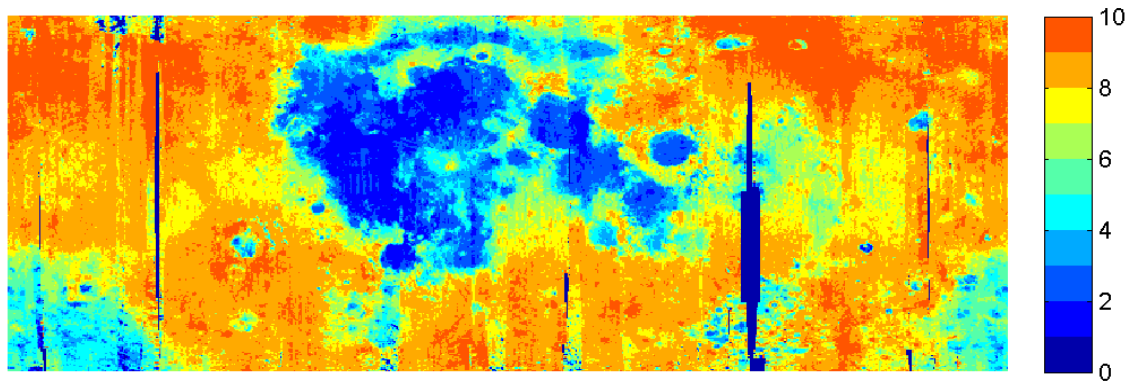


Figure 1: Result of the clustering algorithm for the M³ mosaic (selenographic latitude $\pm 60^\circ$). Colours denote cluster indices.

geological units that each contain several thousands of members.

Fig. 1 shows the global distribution of the clusters. The results are in good agreement with the basic types of lunar surface materials. The mare regions are clearly separated from highland areas. The corresponding prototype spectra show characteristic features for the corresponding region.

The mare prototypes (cf. upper graph of Fig. 2) exhibit deep absorptions near 1000 nm, indicating a high concentration of mafic minerals, while the highland prototypes (cf. lower graph of Fig. 2) show only weak absorptions. The minimum wavelengths of the mafic absorption troughs of the cluster 1-5 prototypes lie between 960 nm and 1000 nm and between about 1980 nm and 2200 nm, respectively. They reflect different pyroxene species containing different fractions of orthopyroxene vs. clinopyroxene (cf. e.g. [16]). The minimum wavelengths of the shallow absorption troughs near 1000 nm of the highland prototypes (clusters 6-10) are located between 970 nm and 1000 nm.

Notably, all prototypes show an absorption near 1300 nm which appears as an inflection feature for clusters 1-3. This absorption is usually attributed to the mineral plagioclase [17] but might also be a secondary absorption present in the spectra of some pyroxene species (cf. e.g. [18]). Since the clusters contain 5000-26000 members each and the prototypes are averaged spectra, this absorption feature is present all over the lunar surface.

References: [1] Keshava, N. and Mustard, J. F. (2002) *IEEE Signal Processing Magazine*, Jan. 2002, 44-57; [2] Felder, M. P. et al. (2013) *Proc. European Planetary Science Congress*, EPSC2013-684-3; [3] Felder, M. P. et al. (2013) *LPSC XLV*, abstract #2537; [4] Pieters et al. (2009) *Current Science* 96(4), 500-505; [5] Scholten et al. (2012) *JGR* 117, E00H17; [6] Wöhler, C. and Grumpe, A. (2013) In: M. Breuß et al. (eds.), *Innovations for Shape Analysis: Models and Algorithms*, Springer-Verlag, 467-492; [7] Hapke, B. (2002) *Icarus* 157 (2), 523-534; [8] Grumpe A. et al. (2013) *Adv. Space Res.*, in press; [9] Warell, J. (2004) *Icarus*, 167, 271-286; [10] Pieters (1999) *Proc. Workshop on New Views of the Moon II*, abstract #8025; [11] Kohonen, T. (1982) *Biological Cybernetics*, 43(1), 59-69;

[12] Grumpe, A. et al. (2012) *Proc. 3rd Moscow Solar System Symp.*, 180-181; [13] Lawrence, D. J. et al. (1998) *Science* 281(5382), 1484-1489; [14] <http://www.mapaplanet.org/explorer/moon.html>; [15] Bhatt et al. (2013) *LPSC XXXIV*, abstract #1590; [16] Smrekar, S. and Pieters, C. M. (1985) *Icarus* 63, 442-452; [17] Adams, J. B. and Goullaud, L. H. (1978) *LPSC IX*, 1-3; [18] Klima et al. (2005) *LPSC XXXVI*, abstract #1462.

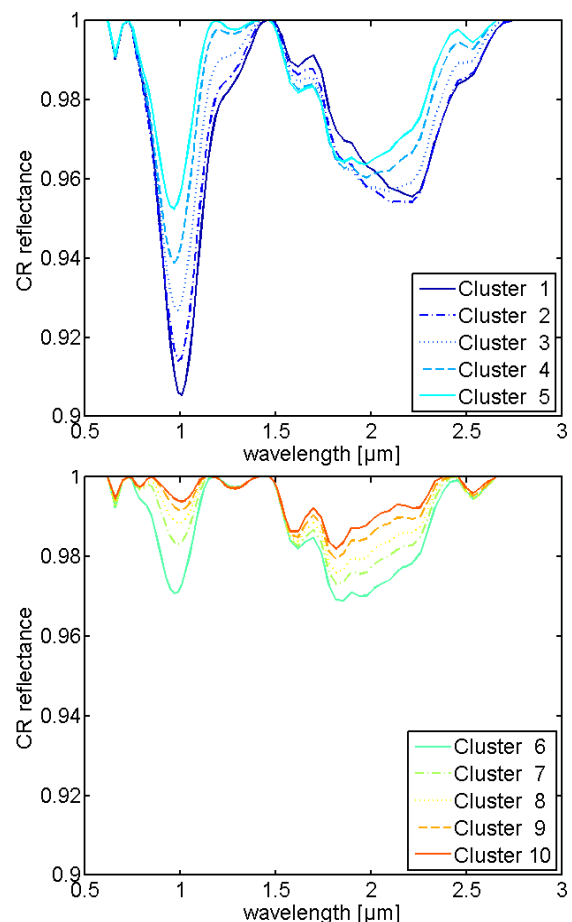


Figure 2: Continuum-removed prototype spectra. The spectra exhibit absorption troughs of variable depth near 1000 nm and 2000 nm. The position of the absorption band near 1000 nm varies across a wide range. Some prototype spectra show a shallow absorption band and others an inflection near 1300 nm.

NEW LABORATORY MEASUREMENTS TO HELP CONSTRAIN SURFACE ROUGHNESS EFFECTS IN THE LUNAR DIVINER RADIOMETER DATASET. T. J. Warren, N. Bowles, I. Thomas
Atmospheric, Oceanic and Planetary Physics, University of Oxford, Department of Physics, Clarendon Laboratory, Parks Road, Oxford, OX1 3PU, UK (warren@atm.ox.ac.uk, bowles@atm.ox.ac.uk, ian.thomas@aeronomie.be).

Introduction: Thermal infrared measurements can contain information on the surface properties of the Moon including the distribution of temperature and composition. The Diviner Lunar Radiometer (‘Diviner’) instrument is a nine-channel mapping radiometer on board NASA’s Lunar Reconnaissance Orbiter. It has been operated mainly in an orbit with an altitude of 50 km in a pushbroom-mapping mode, with a 320 m (in track) by 160 m (cross track) field of view (FOV). Diviner has channels ranging from the visible to the far infrared ($>400\mu\text{m}$) [1], with three mineralogy channels centered on the thermal infrared ($8\mu\text{m}$).

The thermal and far infrared measurements being made by Diviner contain compositional spectral features convolved with temperature dependent radiance. In order to determine the composition and temperature of the lunar surface, we must be able to separate the infrared signal due to the temperature and the composition. This can be achieved by having an accurate knowledge of the surface temperature [2].

Unfortunately the surface temperature of the Moon is not easy to determine because: 1) the regolith is very insulating and 2) the lack of an atmosphere means there is no convective heat transport. These properties ensure that radiation is the dominant mode of heat transport and because the surface is not smooth but full of large-scale ($>1\text{m}$) undulations – craters, ridges, boulders - huge thermal gradients ($>100\text{K}$) can exist between areas in direct sunlight and regions in shadow. The lunar surface is also very rough at the sub millimeter scale. Using pictures taken by the Apollo Lunar Surface Closeup Camera (ALSCC) the lunar surface has been shown to have average sub millimeter RMS slopes between 16° and 25° depending of the lunar terrain [3]. This small-scale roughness means that the huge thermal gradients can exist over just a few millimeters. The surface temperature of the moon is therefore very heterogeneous and subsequently, the Diviner FOV typically has a wide range of temperatures within it.

A simple model that assumes a single temperature for the surface inside the FOV cannot be used to de-convolve the composition from the temperature dependent radiance. Due to the non-linearity of the plank function, this will lead to a “blue slope in the resulting emissivity corrected reflectance spectra” [2] and could introduce false features in the corrected spectra.

A 3D thermal physical model [e.g. 4,5], which account for large-scale undulations by incorporating

LOLA topographical data, is therefore required to fully interpret the Diviner measurements. These models typically assume that infrared radiation is scattered isotropically from the lunar surface. Although generally the models are in very good agreement with Diviner measured brightness temperatures, there are some discrepancies particularly in permanently shadowed regions near the lunar poles [4]. One possible reason for these discrepancies is due to the sub millimeter-scale roughness of the regolith the lunar surface is not an isotropic scatter of TIR radiation as currently assumed in the models. Although significant progress is being made in determining the scattering properties of the lunar soil in the visible and near infrared [e.g. 6,7], there is still limited or no data available on the scattering properties in the thermal (TIR) or far infrared (FIR).

Therefore, we have developed an instrument known as the “Oxford Space Environment Goniometer” (OSEG – Figure 1). The OSEG is able to setup different viewing geometries (Figure 2) on a sample of Apollo regolith under simulated lunar thermal conditions i.e. under vacuum ($<10^{-6}$ mbar) whilst enclosed by a cooled (<150 K) radiation shield (Figure 3). The lunar like conditions helps induce the thermal gradient across the sample [9].

The OSEG described in more detail below is currently being used to investigate how the sub millimeter surface roughness affects the observed brightness temperature or emissivity for varying viewing angles (directional emissivity).

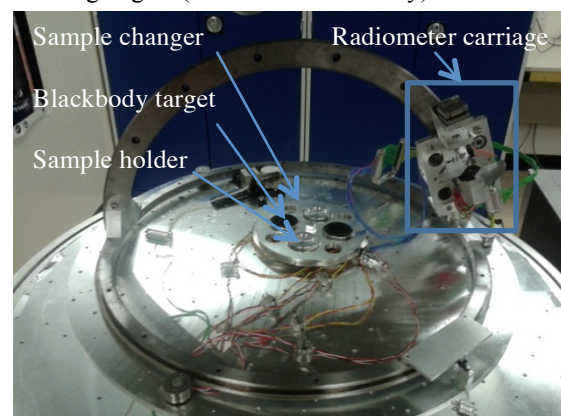


Figure 1: Photograph of the goniometer setup inside the vacuum chamber.

Infrared Goniometer Design: Currently the OSEG makes directional emissivity measurements of lunar simulant samples in the TIR and FIR by

heating the sample from below to $\sim 400\text{K}$. In the future the sample will be heated from above using a solar like lamp. The radiometer uses a high performance pyro-electric detector (Infratec LIE-312F) with a reference chopper and views of two calibrated blackbody targets with highly accurate thermometers to provide a traceable radiance calibration for thermal emission. Currently, a broadband KBr window provides wavelength selection. In the near future wavelength selection will be provided by spare Diviner filters [1].



Figure 3: (left) Photograph of the goniometer setup inside the vacuum chamber and (right) the cold shield surrounded in MLI (multi-layer insulation) inside the vacuum chamber.

Initial Directional Emissivity Results in the TIR and FIR: The first directional emissivity measurements have been made under vacuum of test surfaces that have a known directional emissivity.

These measurements have shown the setup to be working. Measurements are currently being made of rough surfaces under lunar like conditions.

Summary and Conclusions: The OSEG is now ready to study how the sub millimeter roughness (average RMS slope) affects the directional emissivity of lunar regolith analogue. This will then allow photometric parameters [e.g. 10] to be fitted to the measurements, creating a new library of directional emissivity measurements that can then be feed back into 3D thermo-physical models of the lunar surface. These models can be compared to measurements made by Diviner to investigate the surface properties and de-convolve the composition spectral features from the temperature dependent radiance.

Acknowledgements: We would like to acknowledge the UK Science and Technology Facilities Council (STFC) for supporting this work financially.

References: [1] Bandfield, J. L. (2014) LPSC XXXV abstract #1519. [2] Helfenstein, P. Shepard, M. K. (1999) Icarus 141. [3] Paige, D. A. et al. (2009), Space Sci. Rev.150, 125-160. [4] Paige, D. A. et al. (2010), Science, 330, 479. [5] Vasavada, A.R. et al., (1999), Icarus, 141, 179. [6] Foote, E. J. (2012) LPSC XXXIII abstract #2357. [7] Pommerol, A. et al. (2011), Planetary and Space Science., 59, 1601-1612. [8] Shepard, M. K. (2001) LPSC XXXII abstract #1015. [9] Thomas, I. et al. (2012) LPSC XXXIII abstract#2637. [10] Hapke, B. (1993), Cambridge Univ. Press.

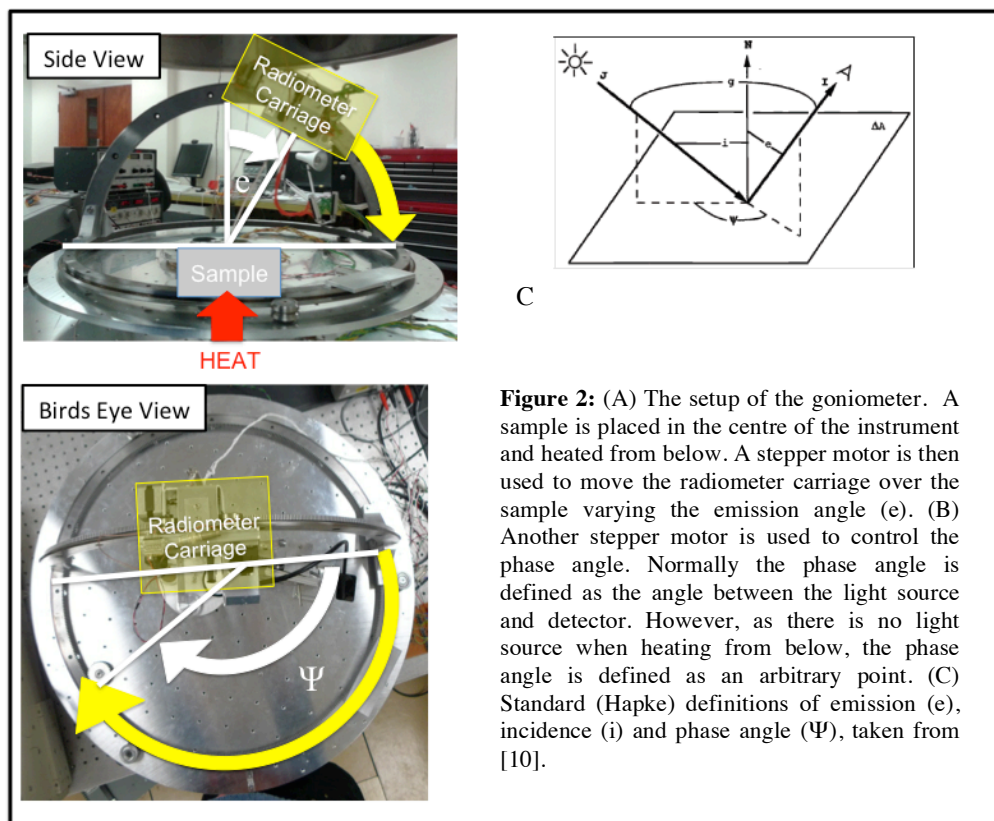


Figure 2: (A) The setup of the goniometer. A sample is placed in the centre of the instrument and heated from below. A stepper motor is then used to move the radiometer carriage over the sample varying the emission angle (e). (B) Another stepper motor is used to control the phase angle. Normally the phase angle is defined as the angle between the light source and detector. However, as there is no light source when heating from below, the phase angle is defined as an arbitrary point. (C) Standard (Hapke) definitions of emission (e), incidence (i) and phase angle (Ψ), taken from [10].

IDENTIFICATION (AND MISIDENTIFICATION) OF DARK-HALO CRATERS WITHIN THE TAURUS-LITTROW REGION OF THE MOON FROM MOONZOO DATA. K. G. Weilding, R. Bugiolacchi, I. A. Crawford Department of Earth and Planetary Sciences, Birkbeck University of London, London WC1E 7HX, UK (k.weilding2@ntlworld.com).

Introduction: MoonZoo is an online citizen science project, one of several of the Zooniverse Citizen Science Alliance. MoonZoo uses high spatial resolution images from the NASA Lunar Reconnaissance Orbiter (LRO) (Fig 1) [1], Narrow Angle Camera (LROC NAC) instrument [2].



Figure 1: Lunar Reconnaissance Orbiter (NASA).

Through the MoonZoo interface, citizen scientists are presented with NAC images of the surface of the Moon and they are asked to identify and annotate a wide range of geologic features. These features include crater sizing (the main research target) and counting, identifying rills and boulder tracks. MoonZoo has access to subsets of NAC images from three different zoom levels, representing the lunar surface at a scale from metres to kilometres (Fig 2).



Figure 2: The MoonZoo website and graphical interface for crater identification and measurement tasks [3].

No scale bars are provided on each image to prevent bias. Craters are identified down to a size of 20 pixels, which equates to a crater size of about 10 m in diameter in the highest resolution images (Fig 3).

Region of study: The Taurus-Littrow region, a steep-sided flat-floored valley, which is linked to the formation of the Serenitatis basin. Before the Apollo

missions, the dark surface areas were thought to represent pyroclastic materials originating from cinder cones [5]. Many of these presumed volcanic edifices have now been recognised as DHCs. One of the better known is Shorty crater, also in the region, where several patches of pyroclastic orange and black glass beads were found around the rim of the crater.

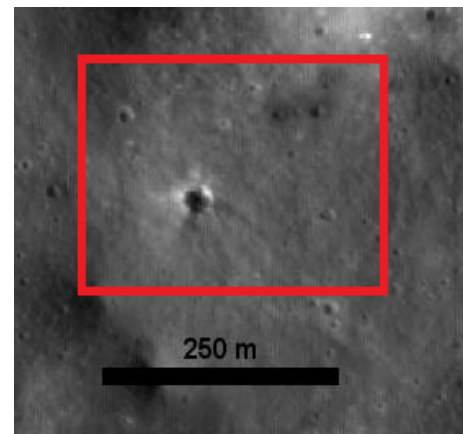


Figure 3: DRC identified by MoonZoo user.

Dark Halo Craters: This work focuses on Dark Halo Craters (DHC) and Dark Ray Craters (DRC), found within the Taurus-Littrow valley region, site of the Apollo 17 mission. The results show that, out of a total of 1018 possible identifications of DHCs by MoonZoo users, only 23 DHCs were correctly identified, and of these, only 4 were found to be unique, the others consisting of repeated identifications.

Consequently, this study suggests that a data validating routine should be implemented to scrutinise the output from MoonZoo; this could involve data assessment by experts, although this would be time consuming. Therefore more in-depth tutorials might improve detection skills of the citizen scientists.

In principle, by mapping dark-halo craters, it should be possible to estimate the thickness of the regolith. Small DHC may sample the top of the cryptomare, while larger ones would potentially sample materials below this layer, exhuming lighter coloured materials. To test this hypothesis a wide range of crater sizes from the same area is needed. The difference in excavation depths between these extremes can give an estimate of the cryptomare thickness [4]. The identification of DHCs can also provide information on the extent and volume of the cryptomare, a key aspect in the understanding of early volcanism on the Moon. If cryptomare were

found to be a common occurrence on the Moon, then our estimates of surface igneous distribution would need to be re-assessed. This would challenge aspects of the present understanding of the thermal history and evolution of the Moon, allowing for more prolonged periods of early volcanism than presently reckoned [4].

Method: The initial MoonZoo data coordinates were entered into the data handling program JMARS (Java Mission-Planning and Analysis for Remote sensing), a GIS developed by Arizona State University Mars Space Flight Facility to provide a free data analytical tool for NASA and the general public.

JMARS projects the MoonZoo crater coordinates on a generic Clementine map of the region (Fig 4).

Once the general location is established, the appropriate NAC stamp is identified and rendered. This stamp is then enlarged to evaluate DHC-DRC entries.

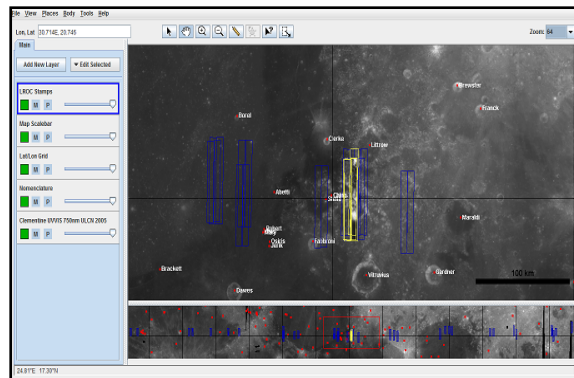


Figure 4: JMARS window showing Taurus-Littrow area and stamp boxes, yellow boxes indicate stamp rendered.

The depth of each crater was trigonometrically derived using the shadow length on the crater floor cast by the crater rim against the illumination angle of incidence. The shadow length was obtained by the measuring tool supplied by JMARS.

Results: The results show that out of a total of 1018 possible identifications of DHC made by MoonZoo users, only 23 craters were correctly identified, and of these only 4 were found to be unique, the others representing repeated identifications. The average thickness of the regolith within the Taurus-Littrow valley is approximately 14 m, as indicated by Apollo 17 field studies [6]. The DRCs observed so far fall into this approximate depth when uncertainties are considered (Table 1). Their excavation depths (i.e. one tenth of the crater diameter) are also compared in (Table 2) Only 2 out of the 4 identified DRC's were suitable for depth calculations. A much larger pool of DHCs-DRCs are needed to provide a clearer picture of the depth of the regolith along the Taurus-Littrow Valley.

Table 1: Mean depth and uncertainty values for two DRC's.

| <i>DRC Location</i> | <i>Mean Depth (m)</i> | <i>Crater Diameter (m)</i> | <i>Uncertainty</i> |
|----------------------|-----------------------|----------------------------|--------------------|
| 30.515E 21.136N | 11 | 26 | ± 4 |
| 30.499E 20.994N | 23 | 79 | ± 10 |
| *30.536E 20.970N | 0 | 30 | 0 |
| * 30.905E 20.759N | 0 | 11 | 0 |

* Insufficient data to produce mean depth.

Table 2: Comparison between mean and excavation depths.

| <i>DRC Location</i> | <i>Mean Depth (m)</i> | <i>Crater Diameter (m)</i> | <i>Excavation depth (m)</i> |
|---------------------|-----------------------|----------------------------|-----------------------------|
| 30.515E, 21.136N | 11 | 26 | 3 |
| 30.499E, 20.994N | 23 | 79 | 2 |

Conclusion: Our main objective is to identify DHCs within the Taurus-Littrow region by examining the data provided by citizen scientists through MoonZoo and validate their contributions. The indication so far is that a very large proportion of the DHC's-DRC's are misidentifications. The majority of highlighted craters are standard impact craters, which quite often show strong shadowing inside the crater and/or around the rim. The wrong interpretation of shadows for dark ejecta could be the main source of mistakes. More in-depth tutorials might improve detection skills by giving the observer a better understanding of what to look for.

To confirm the depths of the regolith within the Taurus-Littrow valley a much larger database of DHCs-DRCs is required covering a larger geographical area. Further, a wider investigation into DHCs-DRCs would allow for a better understanding of the extent of buried cryptomare.

Bibliography: [1] Chin, G.G. et al. 2007. *Space Science Revs* 129 391-419 [2] Robinson, M.S. et al. 2010. in *Lunar and planetary Science* XLI Abstr.no.1874. [3] Joy, et al. 2011. *A&G*, vol. 52, 2.11-2.12. [4] Antonenko, I. et al. 1995 *Earth, Moon and Planets* 69, 141-172 [5] Scott, D.H. 1972. *U.S. geol. Surv. Map* 1-1695. [6] Muenhlberger, W.R. 1992 *Lunar and Planetary Institute Technical Report* 92-09, part 1. 36-37.

Introduction: Lunar Fe (iron) and Ti (titanium) are two important elements distributed on the Moon. In the current study, visible to near-infrared reflectance data acquired by the Moon Mineralogy Mapper (M³) on Chandrayaan-1[1-3] are used to investigate the FeO and TiO₂ abundance of lunar surface at global scales.

The motivation for this study is to apply previous methods derived from the Clementine mission to a new data set. The M³, a high resolution, high precision imaging spectrometer, flew on board India's Chandrayaan-1 Mission from October 2008 through August 2009. Compared with Clementine data, M³ data is newer, contains a wider spectral range, and is similarly well calibrated. M³ acquired visible to infrared reflectance data at spatial and spectral resolutions capable of measuring discrete basaltic flows within the lunar maria[1-3].

Methods: After acquiring the data from the NASA PDS and re-sampling onto the same wavelength grid as the Clementine UV/Vis camera filters, we adopted the general approach of Lucey [4-8] using the following formula to estimate the FeO abundance,

$$\theta_{Fe} = -\arctan\left(\frac{R_{950}/R_{750} - 1.26}{0.01}\right) \dots\dots(1)$$

$$FeO\% = 17.83 \times \theta_{Fe} - 6.82 \dots\dots\dots(2)$$

Where theta is the characteristic angle, R750 and R950 are the reflectances at the 750 nm band and 950nm band, respectively. The design and principle of the TiO₂ inversion method is much more simple. Since the M³ dataset doesn't include the 415 nm waveband measured by Clementine, we used Shukuratov [9] model instead. Using a correlation diagram for FeO-TiO₂ on the lunar nearside, Shukuratov [9] has studied the relationship for FeO and TiO₂. The derived regression equation is:

$$\log(TiO_2[\%]) = 0.06 (FeO[\%]) - 0.54 \dots\dots(3)$$

We have also developed a preliminary model based on "ground truths" from Apollo and Luna sample-return sites to produce a titanium abundance map from M³ image cubes by conducting a similar analysis using the full spectral resolution M³ data and a characteristic angle approach in similar way to Lucey et al[4-7]. From the spectral shape of an ilmenite sample provided by Brown University's RELAB (sample number: PI-CMP-006/C1PI06), we used the presence of a broad absorption feature centered around 500 nm, which is assigned to the electron transition of Ti3+. We therefore used the M³ 540nm channel instead of the 415nm band to determine the characteristic slope in the spectrum. The chemical contents of the lunar soil samples returned by the Apollo and Luna missions are used

as ground truths for these abundance studies. We have attempted to correlate the laboratory TiO₂ contents of typical lunar soils with the remotely sensed multispectral images for individual sample stations using a technique based on Lucey et al. [6,7]. On the R750nm-R540nm/R750nm plane, the same trend of the different landing sites scattered point data also converge together in a optimized origin. After an extension of the scatter projections, the optimized origin's coordinate is calculated. The equations are:

$$\theta_{TiO_2} = \arctan\left(\frac{\frac{R_{540nm}}{R_{750nm}} - 0.57}{\left[\frac{R_{750nm}}{R_{750nm}} - 0.163\right]}\right) \dots\dots(4)$$

$$TiO_2\% = 0.1089 \times \theta_{TiO_2}^{6.6535} \dots\dots(5)$$

Results: According to formula (1-2), we have analyzed the FeO content based on M³ data, and show that lunar FeO content varies from 0 wt.% to 20 wt.%. However, the upper limit of 20% is a limitation of the Lucey et al model, related to the maturity of the soil (e.g. space weathering) effects obscuring the underlying mineralogy (typically sub micron-phase iron production etc. (Figure 1). As expected, we note that the iron distribution is much higher in mare regions than in the highlands.

According to equation (3), we analyzed the TiO₂ content based on M³ data, and show TiO₂ content distribution (Figure 2). Using equations (4-5), TiO₂ contents were also calculated and compared based on our own approach (Figure 3). In Table 1, we have also made a comparison with soils from the "Apollo," "Luna," and "Surveyor" Landing Sites[9]. Except for the titanium abundance from two extremely high samples (Surveyor 5 and Apollo 11), at all the other landing sites the M³ data matches the returned sample data with a deviation less than 15%.

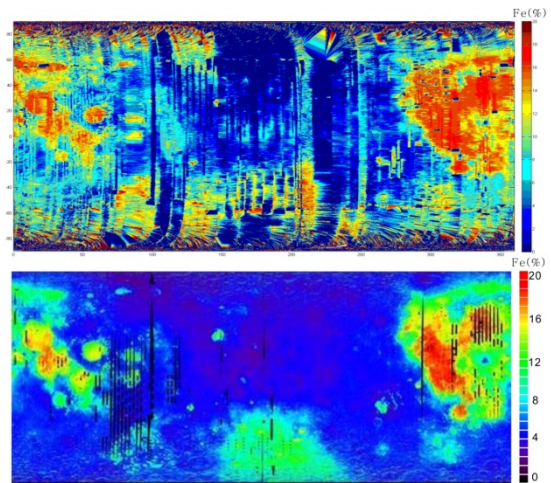


Figure 1: Comparison of FeO content retrieval result from M³ with Clementine Iron map (USGS Map-a-Planet).

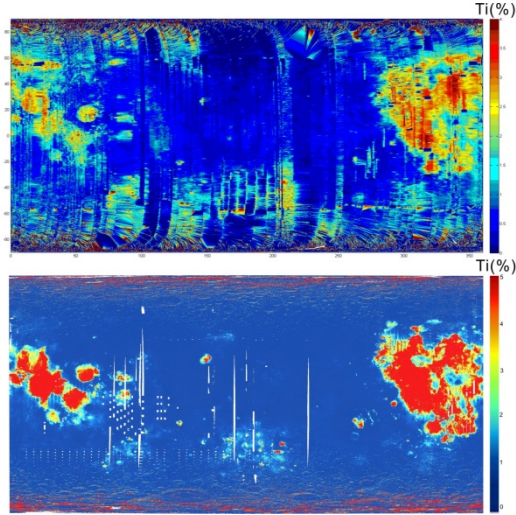


Figure 2: Comparison with Clementine titanium map[12].

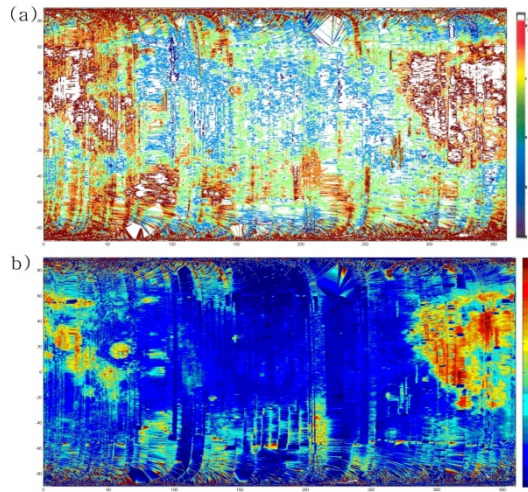


Figure 3: TiO₂ content retrieval result comparison (Labels: Fe %). This is a comparison of the two different M³ titanium approaches, where (a) is the result of 540-750nm prognosis (the second approach) and (b) is the map of Shkuratov prognosis (the first approach).

Conclusions: Data measured by the M³ instrument can provide FeO and TiO₂ abundances that are in broad agreement with “ground truth” with chemical analysis of returned samples. In a similar way to Clementine, the M³ data can be used to determine the FeO and TiO₂ composition of the lunar surface using these techniques at spatial resolutions appropriate for global maps. However, problems remain with the TiO₂ abundance due to the lack of shortwave M³ data, and future work will use the full spectral capability of the M³ instrument to provide additional constraints on these values.

References: [1] Clark R, Pieters C M, Green R O, et al. 2010, 1533: 2302. [2] Pieters C M, Goswami J N, Clark R N, et al. Science, 2009, 326(5952): 568–572. [3] Dhingra D, Pieters C M, Isaacson P, et al. In: 41st Lunar Planet Sci Conf, 2010, 1533: 2494. [4] Lucey P G, Blewett D T, Hawke B R. J Geophys Res, 1998, 103: 3679–3699. [5] Lucey P G, Blewett D T, Jolliff B L. J Geophys Res, 2000, 105: 20297–20305. [6] Lucey, P. G., G. J. Taylor, and E. Malar. Science, 1995, 268: 1150–1153. [7] Lucey, P. G., D. T. Blewett, J. R. Johnson G., J. Taylor, and B. R. Hawke. Lunar Planet Sci., 1996 XXVII, 781–782. [8] Boardman et al. Journal of Geophysical Research, 2011, 116: E00G14. [9] Shkuratov Y G., Kaydash V G., Opanasenko N V. Icarus, 1999, 137: 222–234. [10] Zhang W., Bowles N E. LPSC abstract, 2013, 1212. [11] Hapke, B. W. (1981) Theory, J. Geophys. Res. 86:3039–3054. [12] Shkuratov et al. Planetary and Space Science, 56(8), 2008, 1063–1078. [13] Shkuratov YG, Kaydash VG, Opanasenko NV. Icarus, 1999, 137, 222–234. [14] Bhatt M, Mall U, Bugiolacchi R. EPSC-DPS2011-441. [15] Nawa D F, Philpotts J A. Regolith from the Highland Region of the Moon, Nauka Press, 1979, 336–344. [16] Florensky K P, et al. Nauka Press, 1981. [17] Heiken G, Vaniman D, French B. Lunar Source-Book, Cambridge University Press, New York, 1991. [18] King E. Space Geology (an Introduction), Wiley, New York, 1976. [19] LSPET (Lunar Sample Preliminary Examination Team), Science, 1973, 183, 659–672. [20] Mason B, Melson W, The Lunar Rocks, Wiley, New York, 1970. [21] Korokhin V V, et al. Planetary and Space Science, 2008, 56, 1063–1078. [22] Pinet P C, et al., 28th Lunar and Planetary Science, 1997: 1431.

Table 1: Comparison with Soils from the “Apollo,” “Luna,” and “Surveyor” Landing Sites. Ref from [13].

| Landing site | Sample TiO ₂ (%) | M ³ TiO ₂ (%) | *Clementine TiO ₂ (%) | Sample FeO (%) | M ³ FeO (%) | *Clementine FeO (%) | References |
|---------------------|-----------------------------|-------------------------------------|----------------------------------|----------------|------------------------|---------------------|------------|
| Apollo 11 | 7.40 | 2.23 | 11.7±0.7 | 15.8 | 14.8 | 13 | [15–19] |
| Apollo 12 | 2.68 | 2.65 | 6.4±0.5 | 15.7 | 16.0 | 13.5 | [15–19] |
| Apollo 14 | 1.72 | 1.70 | 1.8±0.3 | 10.4 | 12.8 | 8.6 | [15,16,19] |
| Apollo 15(mare) | 1.64 | 2.32 | 1.7±0.6 | 15.2 | 15.1 | 12.9 | [15,17] |
| Apollo 16 | 0.55 | 0.88 | 0.8±0.1 | 5.0 | 7.8 | 4.0 | [15–17] |
| Apollo 17(highland) | 0.90 | 0.95 | 3.7±1.8 | 8.1 | 8.6 | 6.9 | [19] |
| Luna 16 | 3.36 | 2.71 | 6.4±0.6 | 16.7 | 14.8 | 13.0 | [16,17] |
| Luna 20 | 0.47 | 0.74 | 1.3±0.1 | 7.4 | 6.9 | 5.8 | [15–17] |
| Surveyor 5 | 7.60 | 2.01 | N/A | 12.1 | 13.8 | N/A | [20] |
| Surveyor 6 | 3.50 | 2.41 | N/A | 12.4 | 13.2 | N/A | [20] |
| Surveyor 7 | 0.50 | 0.75 | N/A | 5.5 | 6.9 | N/A | [20] |
| Luna 24 | 1.15 | 2.52 | 5.0±0.5 | 20.6 | 17.8 | 15.1 | [16], [17] |

*Clementine TiO₂ content values and errors are from [21] and Clementine FeO content values are from [22]. None of the authors provide Clementine FeO content retrieval errors in their papers [4–13]. The error range of Clementine and M³ should be of the same magnitude, as we applied almost the same method just on a different dataset that has been resampled to the same grid.

**NASA'S SOLAR SYSTEM EXPLORATION RESEARCH VIRTUAL INSTITUTE:
INTERDISCIPLINARY SCIENCE AND COMMUNITY DEVELOPMENT.** B. E. Bailey¹, Y. J. Pendleton¹, G. K. Schmidt¹, D. Daou^{1,2} ¹NASA Ames Research Center, USA, ²NASA Headquarters, USA (Brad.Bailey@nasa.gov).

Introduction: NASA's Solar System Exploration Research Virtual Institute (SSERVI) represents a close collaboration between science, technology and exploration that will enable deeper understanding of the Moon and other airless bodies as we move further out of low-Earth orbit. The new Solar System Exploration Research Virtual Institute (SSERVI) will focus on the scientific aspects of exploration as they pertain to the Moon, Near Earth Asteroids (NEAs) and the moons of Mars. The Institute focuses on interdisciplinary, exploration-related science centered around all airless bodies targeted as potential human destinations. Areas of study reported here will represent the broad spectrum of lunar, NEA, and Martian moon sciences encompassing investigations of the surface, interior, exosphere, and near-space environments as well as science uniquely enabled from these bodies.

We will provide a detailed look at research being conducted by each of the 9 domestic US teams as well as our 7 international partners. The research profile of the Institute integrates investigations of plasma physics, geology/geochemistry, technology integration, solar system origins/evolution, regolith geotechnical properties, analogues, volatiles, ISRU and exploration potential of the target bodies.

ROBEX-ASN – A CONCEPT STUDY FOR AN ACTIVE SEISMIC NETWORK ON THE MOON. A. Czeluschnke¹, M. Knapmeyer¹, F. Sohl¹, M. Bamberg¹, C. Lange², R. Luther², A. Margonis², R. Rosta³, N. Schmitz¹ and the “ROBEX ASN Study Team” ¹German Aerospace Center (DLR), Inst. of Planetary Research, Berlin, Germany, ²Institute for Geodesy and Geoinformation Sciences, Technical University Berlin, Germany, ³German Aerospace Center (DLR), Inst. of Space Systems, Bremen, Germany (alexandra.czeluschnke@dlr.de).

Introduction: The Helmholtz Alliance “Robotic Exploration of Extreme Environments – ROBEX”, brings together space and deep-sea researchers. The project partners are jointly developing technologies for the exploration of highly inaccessible terrains.

The research on the Moon and in the deep sea would answer different scientific questions but should be addressed by a common method (seismic surveys) and technological solution. The overall goal is to develop a combination of a stationary system and one or more mobile elements. The stationary system would provide the energy supply and the possibility to exchange data between the elements and the ground station. The mobile elements will perform the actual scientific exploration in the deep sea or on the Moon.

It is the overarching objective of the ROBEX Alliance is the equipment of these systems with innovative technologies for energy exchange and data transfer. Most processes should be conducted fully autonomously [1]. Science-critical decisions will be made semi-autonomously with Human-in-the Loop.

Robotic Exploration on the Moon: In the present study, we are developing the ROBEX – Active Seismic Network (ASN), a new mission concept that aims at conducting geological and geophysical experiments on the Moon with a high-level of autonomy. This will be done by the use of robotic rovers to inform about (i) the lunar surface, (ii) the crustal layering, (iii) the deep lunar interior and (iv) the source mechanisms of moonquakes and other natural seismic events. The main goal of the ASN is to perform geological investigations of surface properties and rocks, active and passive seismic studies, and gravity survey on the lunar surface. A first mission design involving two mission phases was developed at the Concurrent Engineering Facility (CEF) at the DLR Institute of Space Systems in Bremen. Two individual landed spacecraft were considered that would provide enough volume for lunar seismology equipment and additional scientific experiments, e.g., gravity measurements, and laser reflectors. Since each experiment is packed in exchangeable module boxes, the ROBEX mission scenario would be able to accommodate the postulated modularity.

(A) Mission Scenario for Active Profile Experiment: The two landers would be deployed on the lunar surface at distance of 10 km. Lander1 would carry an active seismic source (blue star label) to excite seismic waves that are sufficiently intense

to probe the lunar crust. Lander2 would carry a mobile element (rover), which is capable to carry, deploy and pick up a seismic sensor over a distance of at least 10 km, thereby obtaining data about the uppermost crustal layers. (Figure 1a). The rover would leave Lander2 using one of two available ramps (Fig.1b). The Geological Context Imager, largely based on the Moonrise Context Imager (MCI) [2] or Lunar PanCam [3] mounted on top of the rover would survey the surrounding on its way to the first profile point (Fig.1c). The Geological Context Imager is equipped with a High Resolution Camera and two Wide Angle Cameras for stereo and multispectral observations to perform 3D mapping and multispectral analysis of the lunar surface. The rover would deploy a Remote Unit (RU) for the first measurement. The RU comprises a seismometer with own batteries, data logger, on-board computer, antenna, and solar panel to work autonomously. The source would be fired for each measurement and, according to on-the-fly signal-to-noise evaluation, this process should be repeated in order to stack the signal (Fig.1d). Afterwards, the RU would be picked up again by the rover, and the Geological Context Imager would image the surrounding on its way to the next profile point (Fig.1e). The entire process would be repeated several times until the profile is completed [4].

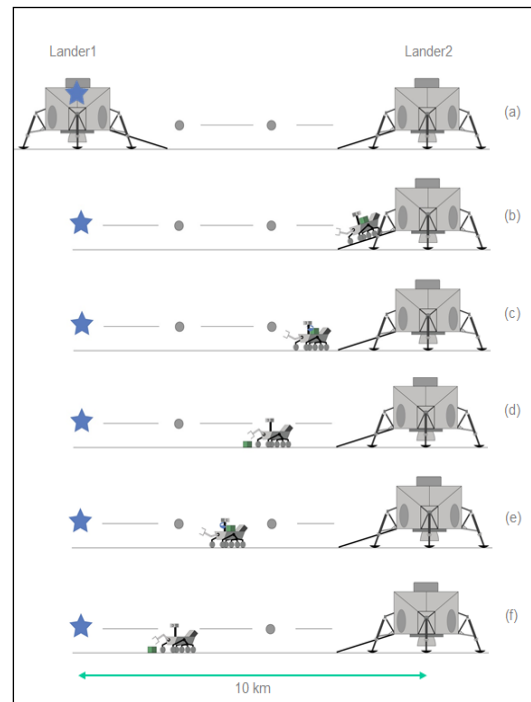


Figure 1: ROBEX-ASN Active Profile Experiment

(B) Mission Scenario for Passive Seismic Array: In addition to the active seismic survey, the mobile element would deploy a Y-shaped array of four seismic sensors for the passive seismic experiment. The array would be built up at a distance of at least 500 m to the lander to reduce equipment induced noise. The array would measure both signals caused by the active seismic source and by natural events such as moonquakes, microseismicity, and meteorite impacts. This array configuration resembles the Apollo 17 Lunar Seismic Profiling Experiment. In a separate contribution to this Symposium, a re-analysis of the Apollo 17 seismic record based on improved source and receiver coordinates is reported [5]. Natural impacts conveniently could be used as seismic sources, if time and location of these impacts were precisely known from space- or ground-based impact flash observations. The physical properties of the impactor can be inferred from the brightness of the flash and knowledge of the impact velocity. Additionally, confirmation of the impact event is guaranteed by simultaneously monitoring the lunar surface from different observation sites and subsequent search for fresh craters within the area of the impact flash based on spacecraft imaging data. Telescopic observational techniques and impact modeling studies are carried out in a separate work package of the ROBEX research alliance [6, 7].

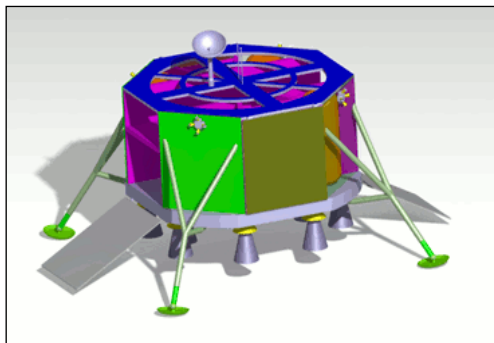


Figure 2: CEF Final Design of the ROBEX Lander

Landing Site: The proposed mission scenario would require two landing sites separated by 10 km, and a direct and smooth path connecting these locations. The lunar mare regions reveal excellent landing sites, due to their smooth volcanic surface. Small craters, wrinkle ridges, and sinuous rilles are common features within the mare areas [8, 9]. They need to be avoided as they would endanger the rover's safety. The mare consist of basalt layers of different thicknesses, indicating multiple flow events. Analyzing these flow features using the Geological Context Imager will also help to understand the volcanic history of the Moon.

Demo Mission: To demonstrate the feasibility of the concept, it is planned to conduct a demonstration mission in the field in the 2015/2016 timeframe. The

objective of the test will be to demonstrate that the intended science objectives can be met with the developed technology, and that the level of implemented autonomy, together with limited human intervention for science decisions, is suitable (and flexible enough) for high-quality science results.

For this purpose, at least one lander and one fully equipped rover (including the Geological Context Imager and a deployable Seismometer package) will be placed in a Moon-analogue environment. Part of the demo mission scenario will be the autonomous deployment of a seismic package by a rover, and a reduced active profile experiment. On the way from the lander to the deployment point of the seismic package, the rover will conduct geological context investigations with its Geological Context Imager. Criteria for a successful demo mission will be (a) the successful autonomous deployment of the seismic package by the rover, and the collection of geological context data on the way, and (b) the successful collection of scientifically meaningful data from both the seismic experiment and the Geological Context Imager.

Acknowledgments: This research has been supported by the Helmholtz Alliance ROBEX (HA-304).

References: [1] <http://www.robex-allianz.de/>. [2] Schmitz, N., et al. (2010): Geologic Context for Moon Sample Return: The Moon Rise Context Imager. In: 5th European Planetary Science Congress (EPSC) 2010, 19 – 24 September 2010, Rome, Italy. [3] A.J. Coates et al. (2012): Lunar PanCam: Adapting ExoMars PanCam for the ESA Lunar Lander, Planetary and Space Science 74 (2012) 247–253. [4] ROBEX ASN Study Team (2013), DLR CEF Report. [5] Czelusckke, A., M. Knapmeyer, J. Oberst and I. Haase (2014): Re-examination of Apollo 17 LSPE data with respect to new LRO coordinates (Poster), this conference. [6] Margonis A., F. Sohl, J. Flohrer, A. Christou, and J. Oberst (2012): Telescopic lunar observations using the SPOSH camera for impact flash detection. 7th European Planetary Science Congress (EPSC) 2012, 23.-28. Sep. 2012, Madrid, Spain. [7] Luther, R., A. Margonis, J. Oberst, F. Sohl and J. Flohrer (2013): Observation of lunar impact flashes with the SPOSH camera: System parameters and expected performance, 8th European Planetary Science Congress (EPSC) 2013, 8.-13. September, London, United Kingdom. [8] Hiesinger, H., Head, J.W. (2006): New Views of Lunar Geoscience: An Introduction and Overview. Reviews in Mineralogy & Geochemistry, Vol. 60. [9] Jaumann, R. et al. (2012): Geology, geochemistry, and geophysics of the Moon: Status of current understanding. Planetary Space Science, 74, 15-41.

REDUCTION, ANALYSIS AND APPLICATION OF ONE-WAY LASER RANGING DATA FROM ILRS GROUND STATIONS TO LRO. S. Bauer¹, J. Oberst^{1,2}, H. Hussmann¹, U. Schreiber³, D. Mao⁴, G.A. Neumann⁵, E. Mazarico⁵, M.H. Torrence⁶, J.F. McGarry⁵, D.E. Smith⁷, M.T. Zuber⁷ ¹DLR Berlin Germany, ²TU Berlin, Germany, ³Geodätisches Observatorium Wettzell, Germany, ⁴Sigma Space Corporation, Lanham, MD 20706 USA, ⁵NASA Goddard Space Flight Center, Greenbelt MD 20771 USA, ⁶SGT Inc., Greenbelt, MD 20770 USA, ⁷MIT, Cambridge, MA 02139 USA (sven.bauer@dlr.de).

Introduction: One-way Laser Ranging is being performed routinely from International Laser Ranging Service ground stations to the Lunar Orbiter Laser Altimeter, an instrument onboard NASA's Lunar Reconnaissance Orbiter. We developed software to process this novel type of tracking data and gathered information e.g. on characteristics and distribution in a preliminary analysis. By incorporating the high accuracy spacecraft range measurements into orbit determination, one expects the positioning and thereby the accuracy of further derived data products to improve. We used the one-way Laser Ranging measurements within the estimation software TUDAT for carrying out an orbit determination. Thereby the results from the preliminary analysis were used for various inputs into the estimation.

Background: The one-way LR (Laser Ranging) experiment provides high-accuracy range measurements over interplanetary distances between ILRS (International Laser Ranging Service) ground stations and the LOLA (Lunar Orbiter Laser Altimeter) instrument onboard NASA's LRO (Lunar Reconnaissance Orbiter). Furthermore, this data can be used for characterizing the LRO clock and monitoring its long-term behavior as well as referencing the MET (Mission Elapsed Time) to TDB (Barycentric Coordinated Time). Unlike ranging experiments to reflectors or transponders, LR to LRO is a one-way measurement (Figure 1). A ground station fires a laser pulse to LRO at a certain time and the received pulse is time stamped by the satellite. An optical receiver is attached to LRO's HGA (High Gain Antenna), which is always pointed towards Earth, and incoming Laser pulses are transmitted into the LOLA laser detector by a fiber optic cable. This permits ranging measurements to LRO simultaneously, while LOLA is ranging to the lunar surface [1].

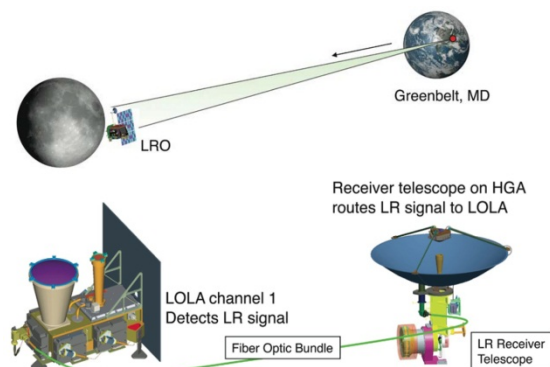


Figure 1: LR to LRO - basic principle [1].

By calculating the light travel time between the receiving and the firing time, a high precision range measurement with a typical RMS of 10 to 30 cm in case of this experiment is derived [3]. Currently the OD (Orbit Determination) for LRO is based on radio as well as altimetric crossover data and is provided in the form of the LRO SPK's (Spacecraft Positioning Kernels) with an accuracy of ≈ 14 m in total spacecraft positioning [2]. This, as well as the quality of Lunar remote sensing data products, is expected to improve with a successful incorporation of the LR data to the LRO nominal navigation data [1].

Summary: Beginning with the participation in an observation campaign at the Fundamentalstation Wettzell, we developed software to process one-way LR data from ground stations to LRO and carried out a preliminary analysis. We derived information on the LRO clock behavior as well as tracking data coverage, quality and quantity over a timeframe from beginning of CO until the end of ES03 mission phase (\sim July 2009 until December 2012). By incorporating the processed data into the estimation software TUDAT, we made an attempt to use the high accuracy LR data for the estimation of the LRO position. We compared, validated and improved the incorporated models as well as the results coming from the respective software systems. The results from the preliminary analysis were used to develop station specific weights for balancing the tracking data regarding quality and quantity, as well as for *a priori* covariance in order to stabilize the estimation solution.

We identified critical issues of the application of the one-way measurements within an OD and furthered our understanding of this novel type of tracking data. By further improving the incorporated models and the estimation setup, we intend to overcome the issues that are associated with this type of data and the experimental setup.

References: [1] Zuber, M.T., et al. (2010) *Space Science Rev*, Vol 150, No 1-4, pp. 63-80, The Lunar Reconnaissance Orbiter Laser Ranging Investigation. [2] Mazarico, E., et al. (2012) *J. Geod.*, 86, pp. 193-207, Orbit determination of the Lunar Reconnaissance Orbiter. [3] Mao, D., et al. (2011), *17th International Workshop on Laser Ranging, Bad Kötzing Germany*, <http://cddis.gsfc.nasa.gov>. Laser Ranging Experiment on Lunar Reconnaissance Orbiter: Timing Determination and Orbit Constraints. [4] TU Delft (March 2014) <http://tudat.tudelft.nl>

EVALUATION OF SMALL-SCALE PENETRATORS FOR LUNAR SUBSURFACE INVESTIGATION. P. Reiss¹, A. Hoehn¹ ¹Institute of Astronautics, Technische Universität München, Boltzmannstr. 15, 85748 Garching, Germany, (p.reiss@tum.de).

Introduction: One scope of lunar exploration is the investigation of the local regolith and its potential use as a resource. This is not limited to the mineralogical composition of the regolith itself, as recent remote sensing observations [1-4] show the evidence for small quantities of volatiles bound to the regolith. These appear mainly in shaded areas near the lunar poles, where the thermal environment may prevent the volatiles to desorb from the regolith surface. However, the knowledge about the existence of such lunar volatiles is so far only based on remote sensing measurements of probes, such as LCROSS, Chandrayaan-1, or Deep Impact. Verifying this data requires the collection of ground truth on the lunar surface, using landers and rovers for scientific sampling missions.

Using a lander-only approach limits the scientific value of a sampling mission, as the access to volatiles on the lunar surface is only possible within the reach of the landing site. The exhaust of the landing engines contaminates and alters the regolith properties significantly in this area (agitation of regolith layers, thermal disturbance, loss of adsorbed volatiles). Deeper regolith layers, which may not be affected by the exhaust, can only be reached with sample drilling devices. However, an examination of the pristine near-surface regolith is not possible at the landing site unless mobile elements are employed.

With the addition of a mobile rover, more remote, non-contaminated areas can be accessed. This not only enables the possibility of taking undisturbed samples further away from the landing site, but also to take samples at arbitrary locations. These could be sites that differ in their geological character, or in their thermal conditions. Samples could be taken from illuminated as well as shaded areas, for instance in front of a boulder and behind, in order to compare the influence of solar irradiation on the volatile content in the surface regolith. However, the payload capabilities of a mobile rover are restricted. Sampling tools that are carried onboard must be small, light-weight, and low in power consumption. The simplest tool is a static penetrator, which is driven into the regolith using only the weight of the rover. In a future application, this tool could be equipped with thermal, infrared, or electrical sensors to measure the physical properties of the regolith within the first few centimeters in depth.

Since the gravitational acceleration on the Moon is only 1.62 m/s^2 , the available force for static penetration is much smaller than on Earth. A relatively small rover with a mass of 10-20 kg (i.e. the proposed ESA Lunar Lander Mobile Payload Element [5]) would therefore only be able to exert a

force of approximately 16-32 N on the Moon. The penetration resistance mainly depends on the penetrator geometry (shaft and base resistance, surface roughness), and the regolith properties (cohesion, bulk density/compaction, gravity, friction angle, coefficient of lateral stress) [6]. Most of the material properties are highly variable for different locations on the Moon and variable with depth (varying particle shape, grain size, and compaction), and hence the prediction of penetration resistance is not trivial.

Two penetration tests series have been conducted at the Institute of Astronautics at Technische Universität München. The test results lead to a first estimation of maximum forces required for static penetration in lunar regolith to a depth of 100 mm. The tests covered the variation of penetrator geometries, including single solid rods with flat and conical tips (Figure 1), arrays of multiple rods, and tubes. The lunar regolith was simulated using the lunar mare analogue material JSC-1A [7].



Figure 1: Cylindrical test penetrators.

Previous studies: On the Apollo 14, 15, and 16 missions, various penetration tests have been performed in-situ by the astronauts. The penetration resistance was measured over depth using the Apollo Simple Penetrometer (ASP) and the Self-Recording Penetrometer (SRP).

The ASP had a base diameter of 9.5 mm and an apex cone angle of 30° . Three ASP measurements were done down to depths of 420 mm, 440 mm, and 500 mm. The resistance recorded for these measurements ranged between approximately 1,000 kPa and 1,900 kPa, which equals 70 to 135 N [8].

With the SRP on Apollo 16, two different cone diameters (12.8 and 20.3 mm) with an apex cone angle of 30° were examined [6,8-10]. The maximum reachable depth ranged from 213 to 740 mm. At a depth of 100 mm the recorded penetration resistance for the 12.8 mm base was between approximately 200 to 1,000 kPa, which corresponds with 25 to 129 N. For the 20.3 mm base at the same depth, the

resistance ranged from 300 to 600 kPa, or 97 to 194 N respectively [10].

Measurements with the cone-vane penetrometer PROP on the Lunokhod 1 rover were done only to depths of 80 mm. The tool had a base diameter of 50 mm and a conical tip of 60°. The maximum penetration force was 155 N at 80 mm depth for level intercrater regions, 200 N at 80 mm depth for crater wall regions, 200 N at 70 mm depth for crater slope regions, and 220 N at about 60 mm for regions covered with small rocks [6,8].

Recent examinations of the penetration resistance of regolith have been performed by [11-13], using different, mainly Martian analogue materials. The main influencing parameter was identified to be the bulk density and compaction of the regolith. A major problem encountered in laboratory tests is to prepare the regolith with a reasonably reproducible bulk density profile over depth. An evaluation of possible means to prepare the regolith was done by [13]. For a small sample container with a volume of 90 l the most reliable method proved to be using a small rake to loosen the regolith with straightforward movement and a board to level the surface. It was also found that this is the best method to achieve best reproducibility for varying test operators.

In contrast to the aforementioned investigations, the tests presented here focus on the particular application of small-scaled static penetrators that could be used on mobile rovers with limited resources. The reachable depth is restricted to 100 mm, which is considered to be sufficient for investigations regarding volatile content and physical properties of the lunar surface regolith. The variety of different penetrators tested under similar conditions also allows a direct comparison and the determination of interdependencies between the main influence parameters.

Test results: The penetrators shown in Figure 1 were pushed into a bucket filled with 8.5 l of lunar regolith simulant JSC-1A. The size of the bucket was chosen large enough (diameter 250 mm, depth 260 mm) to reduce edge effects and minimize the influence of container wall and bottom on the penetration process. The initial bulk density of the regolith simulant after filling into the bucket was approximately 1,800 kg/m³ (weighed mass divided by measured volume). After each penetration the simulant was loosened using a rake, trying to reproduce the same bulk density for each run. The advancing rate of the penetrator was held constant at 3 mm/s and the maximum depth was limited to 100 mm below the surface. The test was repeated at least 8 times for each penetrator. The necessary penetration force and depth were recorded via computer during penetration. The test machines were a custom-made Bevameter and a Zwick Z010 compression tester (load cell with 2 kN maximum force and accuracy class 0.05%).

The preliminary results for both solid rod and tubular penetrators are summarized in Table 1. As expected, the main influencing parameters are the cylinder diameter and cone angle.

Table 1: Tested penetrator types and resulting maximum penetration forces at 100 mm depth (*values in brackets are outer tube diameters).

| Type | Diameter* [mm] | Cone angle [°] | Force [N] at 100 mm |
|------|-------------------|-------------------|------------------------|
| Rod | 10 | - | 8 – 55 |
| Rod | 10 | 60 | 6 – 19 |
| Rod | 10 | 30 | 6 – 13 |
| Rod | 15 | - | 18 – 77 |
| Rod | 15 | 60 | 13 – 36 |
| Rod | 15 | 30 | 8 – 19 |
| Rod | 20 | - | 61 – 73 |
| Rod | 20 | 60 | 26 – 46 |
| Rod | 20 | 30 | 13 – 25 |
| Tube | 10 (14) | - | 17 – 38 |
| Tube | 20 (24) | - | 16 – 43 |
| Tube | 30 (34) | - | 27 – 81 |
| Tube | 39 (43) | - | 26 – 70 |
| Tube | 50 (52) | - | 25 – 103 |

The measured values can be used to make first recommendations for the minimum required mass of a rover to achieve penetration. It can be seen that most investigated penetrators require rover masses larger than 20 kg (i.e. 32 N equivalent force on the Moon) to reliably reach a depth of 100 mm. However, if not the entire weight of the rover can be transferred into driving force of the penetrator (e.g. through a lever or robotic arm), the minimum required rover mass will be higher. Further evaluation of the penetration tests, also with alternative penetrator geometries, is currently ongoing.

Acknowledgements: We thank the DLR Institute of Robotics and Mechatronics for the possibility to use the Bevameter test system. We also thank the TUM Institute of Lightweight Structures for making their commercial compression test facility available.

References: [1] Colaprete A. et al. (2010) *Science* 330, 463-468. [2] Pieters C. et al. (2009) *Science* 326, 568-572. [3] Sunshine J. M. et al. (2009) *Science* 326, 565-568. [4] Clark R. N. (2009) *Science* 326, 562-564. [5] Hofmann P. et al. (2011) *IAC, IAC-11-A3.2B.4*. [6] Heiken G. H. et al. (1991) *Lunar Sourcebook*. [7] Orbitec (2007) *JSC-1A MSDS*, Rev. 4. [8] Mitchell J. K. et al. (1974) *Space Sciences Laboratory Series 15*, Issue 7. [9] Zacny K. et al. (2010) *ASCE Earth and Space*. [10] Mitchell et al. (1972) In: *Apollo 16 Preliminary Science Report*, NASA SP-315. [11] El Shafie A. et al. (2010) *7th International Planetary Probe Workshop*. [12] El Shafie A. et al. (2009) *LPSC XL*, Abstract #1205. [13] Apfelbeck M. et al. (2011) *JTERRA*, 48/5, 360-371.

POTENTIAL FOR LUNAR EXPLORATION USING A STIRLING POWER CONVERSION SYSTEM (SPCS) POWERED BY A RADIOISOTOPIC HEAT SOURCE CURRENTLY BEING DEVELOPED FOR THE EUROPEAN SPACE AGENCY (ESA). J. Vrublevskis¹, A. Bate¹, D. Summers¹, C. Parfitt¹, R. Edwards¹, T. Bradshaw², M. Crook², G. Gilley², P. Bailey³, M. Dadd³, R. Stone³, B. Shaughnessy², A. Dowell², P. Jamotton⁴, E. De Cock⁵, M. Linder⁶, ¹SEA House, Building 660, Bristol Business Park, Coldharbour Lane, Bristol BS16 1EJ, UK (john.vrublevskis@sea.co.uk), ²STFC, Rutherford Appleton Laboratory, Harwell Oxford, Didcot, OX11 0QX, UK (tom.bradshaw@stfc.ac.uk), ³University of Oxford, Department of Engineering Science, Parks Road, Oxford OX1 3PJ, UK (richard.stone@eng.ox.ac.uk), ⁴Centre Spatial de Liège, Liège Science Park, Avenue du Pré-Aily, 4031 Angleur, Belgium (pjamotton@ulg.ac.be), ⁵QinetiQ Space nv, Hogenakkerhoekstraat 9, 9150 Kruibeke, Belgium (Ellen.DC@qinetiq.be), ⁶ESA-ESTEC, Keplerlaan 1, 2201 AZ Noordwijk, Netherlands (Martin.Linder@esa.int).

Introduction:

Compared to photovoltaic cells, electrical power generation from radioisotope heat sources offer enormous advantages to long duration lunar missions, especially those exploring Permanently Shadowed Regions (PSRs) of the Moon. The design of a breadboard power converter system for use with radioisotope heat sources will be described, highlighting its potential to the design of lunar missions and indicating the impact on surface operations due to its continuous, fixed energy output of heat and electrical power. This design is based on the Stirling cycle, taking advantage of long-life technologies developed for past European space cooler systems. Electrical output is a conditioned DC bus of approximately 100 W. The design consists of a Stirling Converter, Fuel Module, Thermal Control system, Support Structure and Power Conditioning Electronics. The critical functions of a future Stirling Radioisotope Power Generation system have been identified as Safety, Long-Life, Efficiency, Mass & Scalability and the breadboard (supported by 2 independent models) has been designed to investigate these areas fully and to raise their Technology Readiness Levels (TRLs). Manufacture of the breadboard is currently planned to start in 2014.

ASSESSING SAFETY AND POTENTIAL SCIENCE OF THE LUNA-GLOB LANDING SITE IN BOGUSLAWSKY CRATER, MOON. H. Hiesinger¹, M. Ivanov², J. W. Head³, A. T. Basilevsky², J. H. Pasckert¹, K. Bauch¹, C. H. van der Bogert¹, A. M. Abdrahimov² ¹Institut für Planetologie, Westfälische Wilhelms-Universität, Wilhelm-Klemm-Str. 10, 48149 Münster, Germany (hiesinger@uni-muenster.de), ²Vernadsky Institute, Moscow, Russia, ³Brown University, Providence, RI, USA.

Introduction: Although the main objective of the Russian Luna-Glob lander is to test landing techniques, it will also carry a small scientific payload. As primary landing site for the Luna-Glob mission, the floor of crater Boguslawsky (~95 km in diameter, centered at 72.9S, 43.26E) was chosen. In particular, two landing ellipses, 30x15 km each, were selected on the floor of the crater: Ellipse West is at 72.9S, 41.3E, Ellipse East is at 73.3S, 43.9E [1].

Data and Methods: For our assessment of the landing site safety and potential science return, we used data from the Lunar Reconnaissance Orbiter [Wide and Narrow Angle Camera images (WAC, NAC), Diviner temperature data, MiniRF radar data, laser altimeter data (LOLA)] and Chandrayaan (M³). We geologically mapped the crater, investigated its morphology and morphometry, performed crater size- frequency distribution (CSFD) measurements to derive absolute model ages, calculated temperatures and thermal inertia, derived rock abundances, and counted rocks in selected areas of interest.

We used CraterTools [2] to perform our crater counts and CraterStats [3] to plot the CSFDs. We used the production function (PF) and the lunar chronology of [4]. A detailed description of the technique of CSFD measurements is given by e.g., [5-7]. On the basis of LRO Diviner data, we calculate the relative rock abundance of Boguslawsky crater by analyzing temperature differences between fine material and exposed rocks during lunar night [8,9]. These temperatures are merged to a single observed temperature within the field of view. Due to the non-linearity of the Planck function, brightness temperatures are higher at lower wavelengths and approach the average at higher wavelengths. Using multispectral measurements the concentration of the two components within a field of view can be derived. Temperatures of the surface are modeled by using a 1-D thermal model [10].

Results: According to the geologic map of [11] the pre-Nectarian Boguslawsky crater (pNc) is superposed on pre-Nectarian rugged basin (pNbr) material. Secondary crater material of close-by Upper Imbrian (Ic2) Schomberger crater partly covers Boguslawsky and thus is younger [11]. The floor of Boguslawsky shows Nectarian terramantling and plains material (Ntp). Boguslawsky D is superposed on the eastern rim of Boguslawsky crater and is of Eratosthenian age (Ec). Boussingault crater, which superposes Boguslawsky crater in the NE is somewhat younger than Boguslawsky crater, but is still of pre-Nectarian age [11].

Using high-resolution LROC images, we identified six geologic units within Boguslawsky crater,

including smooth plains *fp*, rolling plains *rp*, secondary craters *sc*, the crater wall *w*, and the ejecta blanket of the 24-km sized crater Boguslawsky D (Fig. 1), which has been subdivided into ejecta on the floor of Boguslawsky (*ejf*), its wall (*ejw*), and outside the crater (*ejo*). The surrounding terrain of Boguslawsky was mapped as undifferentiated material (*ud*) [1].

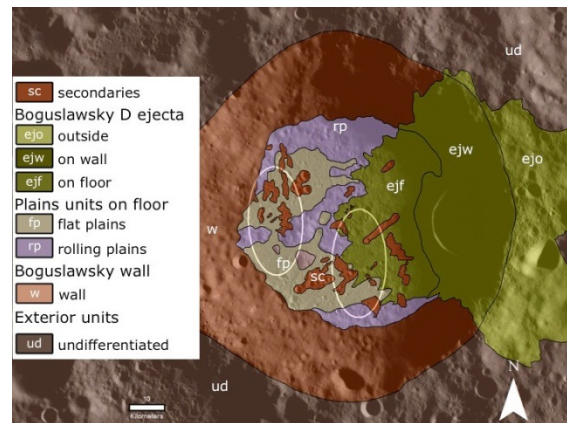


Figure 1: Geologic map of Boguslawsky crater. Landing ellipses are shown in white.

Within the western landing ellipse, units *fp*, *rp*, *sc*, *hu*, and possibly *cw* are accessible. There is a 58% chance to land on flat plains, a 22.5% chance to land on rolling plains, a 17.5% chance to land on secondary craters, and a 2% chance to land on wall material. The eastern landing ellipse covers unit *fp*, *rp*, *eb*, and *sc*. In this landing ellipse, the chance to land on ejecta material of Boguslawsky D is about 49.5%. Chances of landing on flat plains, secondary craters, and rolling plains are 22%, 17%, and 11.5%, respectively. The floor of Boguslawsky crater, as well as its south-western ejecta blanket shows numerous SW-NE oriented secondary craters, some of which might be related to the younger crater Schomberger and Schomberger A, consistent with the interpretation of [11]. Despite the large number of secondary craters, we were able to derive plausible absolute model ages for some of our geologic units. Based on our CSFD measurements, we favor a formation of Boguslawsky of at least 4 Ga ago. This model age is derived from a count area at the western crater wall, which might have been modified by mass wasting. Thus, our model age represents a minimum age, i.e., the crater might be older. Applying the stratigraphy of [14], we find Boguslawsky to be of pre-Nectarian age, consistent with the geologic map [11].

Our CSFD results indicate a model age of about 3.96 Ga for the rolling plains. Thus they are indistinguishable within the error bars from the

CSFD of the Boguslawsky wall. The smooth plains show a model age of 3.77 Ga, which is very similar to the model age of the ejecta blanket of Boguslawsky D (3.74 Ga). Compared to the geologic map [11], the crater floor appears to be somewhat younger and Boguslawsky D appears to be older, i.e., it is Imbrian in age.

Morphometric measurements of Boguslawsky and several large craters in its vicinity indicate that the depth/diameter ratio of Boguslawsky is rather low (Fig. 2). We interpret such a shallow morphology as the result of infill, most likely by ejecta of craters and basins [1].

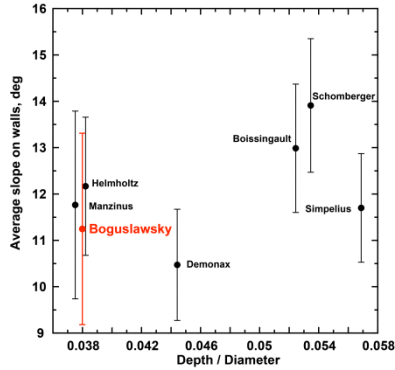


Figure 2: Depth/diameter ratios of Boguslawsky and large craters in its vicinity.

Slopes at ~30m base length within the two proposed landing sites are generally less than 5-10 degrees. However, local slopes associated with small impact craters (mostly <500 m diameter) can be up to 45 degrees (Fig. 3) [1].

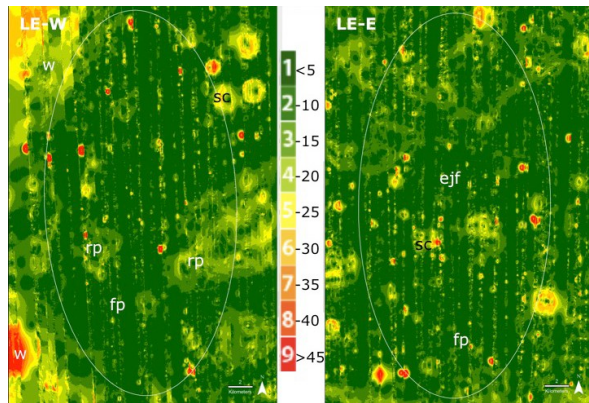


Figure 3: Slope map of the landing ellipses in Boguslawsky crater.

Both landing sites show about the same distribution of slopes (Fig. 4), although there are significant differences in slopes with respect to individual geologic units (Fig. 5) [1].

Our thermal model identified several areas with higher thermal inertia and, thus, rock abundances [1]. Although many of the areas are likely affected by temperature differences due to insufficient topographic correction, several areas with high rock abundances can not be explained by topographic effects. Manual boulder counts on LRO NAC images confirm a large number of boulders on the surface.

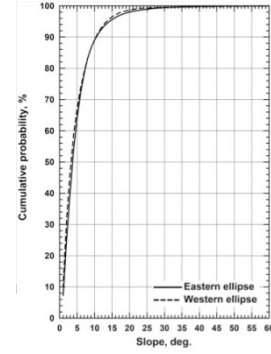


Figure 4: Slope distribution of the two landing ellipses.

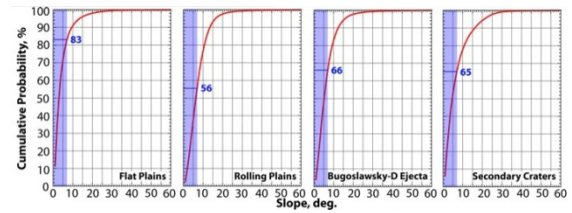


Figure 5: Slope distribution of geologic units. The blue box indicates slopes of less than 7 degrees; blue numbers indicate the percentage of surfaces that have slopes less than 7 degrees.

For example, in an area of about 4 km², we counted more than 16,000 boulders between ~0.5 m and up to 13 m in size. Radar data are either sensitive to ice or rocks in the upper few meters of the surface/subsurface. Although we see several areas with bright radar signals indicative of a higher roughness or blockiness, NAC images show a lack of larger boulders on the surface, suggesting that that most of the signal either comes from rocks below the NAC resolution, rocks buried in the regolith, or both.

Although one of the scientific objectives of Luna Glob is to search for water, LEND epithermal neutron counts at the landing sites in Boguslawsky crater are significantly higher (>9.8 counts per second, cps) than for hydrogen-rich regions such as, Cabaeus and Shoemaker craters (<9.8 cps), thus indicating lower abundances of hydrogen [15].

Results: Boguslawsky crater represents a scientifically interesting landing site that will allow us to study the complex geology of an old crater in detail.

References: [1] Hiesinger et al. (2014) LPSC 45; [2] Kneissl et al. (2011), PSS 59; [3] Michael and Neukum (2010) EPSL 294; [4] Neukum et al. (2001), Space Sci. Rev. 96; [5] Crater Analysis Working Group (1979), Icarus 37; [6] Hartmann (1966), Icarus 5; [7] Hiesinger et al. (2000), JGR 105; [8] Christensen, P.R. (1986), Icarus 68; [9] Bandfield, J.L. et al. (2011), JGR 116; [10] Bauch et al. Submitted to PSS, [11] Wilhelms et al. (1979) USGS I-1162; [12] Scholten et al. (2012) JGR 117; [13] Nozette et al. 2010, Space Sci. Rev. 150; [14] Wilhelms (1987) USGS Prof. Paper 1348; [15] Litvak et al. (2012) JGR 117.

